Proceedings of the 13th JPL Airborne Earth Science Workshop

Robert O. Green
Editor
Jet Propulsion Laboratory
California Institute of Technology

December 2004

Contents

Introduction

This publication contains the proceedings of the JPL Airborne Earth Science Workshop—a forum held to report science research and applications results with spectral images measured by the NASA Airborne Visible/Infrared Imaging Spectrometer (AVIRIS). These papers were presented at the Jet Propulsion Laboratory from March 31–April 2, 2004. Electronic versions of these papers may be found at the AVIRIS Web site noted below.

Note

Our budget this year allows for only a few color reproductions, even though they now often prove necessary for a complete understanding of figures presented here in black and white. For full color versions of the papers, please go to the AVIRIS Web site at http://aviris.jpl.nasa.gov and click on Documents.

A Method to Estimate Aerosol Load on a Pixel-by-Pixel Basis Using Airborne Hyperspectral Sensors: A Case Study over Santa Monica, California

Eyal Ben-Dor[1] and Bruce Kindel [2]

[1] The Remote Sensing and GIS Laboratories, Department of Geography
Tel-Aviv University, Israel

[2] Center for the Study of Earth from Space (CSES)
Cooperative Institute for Research in Environment Sciences (CIRES)
University of Colorado

INTRODUCTION

The advantage of hyperspectral technology is the ability to record small and narrow spectral features of both terrestrial and atmospheric components. Whereas terrestrial applications gained much attention and progress by many researchers, utilization of the atmospheric signals has not yet developed beyond the water vapor content current estimation. This is mainly due to the limited information the available hyperspectral (HRS) scanners can provide with reasonable signal quality as to the gas's spectral absorption. Extensive studies from HRS perspective and methodologies to depict water vapor content on a pixel-by-pixel basis have been developed by many researchers (e.g., Gao et al., 1993b, Richter, 2004). Knowledge of the water vapor content on a pixel-by-pixel basis enables better atmospheric correction and provides sharper HRS reflectance data. A recent work by Green (2001) showed also that the CO_2 content can be estimated using the absorption peaks at around 2.005 μm and 2.055 μm on a pixel basis. Using the CO_2 absorption features from an AVIRIS cube enabled Green (2001) to present good agreement between the topography and the CO_2 content over California's San Gabriel Mountains.

In flat terrain, excluding water vapor, all other atmospheric attenuations are considered to be constant. Whereas this consideration is mostly true for well-mixed gases such as O_2, CO_2 and O_3 it may not be the case for the aerosol load. Smoke, local dust or point particle emission to the air may hamper correct reflectance retrieval regarding the area in question. Furthermore, non-visible dust particles that may not be monitored spatially still can deteriorate air and life qualities. Determining the aerosols content on a pixel-by-pixel perspective using airborne data only (as done with the water vapor estimation) is still unavailable to the best of our knowledge. Ben-Dor et al. (1994) had shown that thin cirrus clouds can be spatially monitored in AVIRIS images using the oxygen peak at 0.76 μm and concluded that scattering effects of the non-visible ice particles contribute to the oxygen absorption response and affect its spectral signal. Based on this finding, and based on the understanding that AVIRIS data today is much better in its signal quality than the 1994 data, we propose in this study to examine a possible method at point estimation of aerosol load over an urban environment.

MATERIALS AND METHODS

In order to examine this idea we first generated a synthetic AVIRIS radiance scene composed of vegetation and urban materials with constant water vapor, constant concentration of other gases (O_3, O_2 and CO_2) and varying aerosol load. The synthetic AVIRIS cube was generated using the atmospheric radiative transfer code MODTRAN 4.0 (Berk et al., 1999). The code was run 100 times, corresponding to 100 aerosol load (visibility of 0–100 km) with water vapor content of 1.1 cm (estimated from authentic AVIRIS data of *Santa Monica 2000*). In order to generate the inputs for predicting the at-sensor radiance for each aerosol load, the code was run three times with constant albedos of 0.0 (the path radiance term), 0.5 and 1.0. Using these results, the two-way transmittance, path radiance, and spherical albedo were generated. With the addition of the surface reflectance and exoatmospheric solar spectrum, the at-sensor radiance was predicted. The solar geometry was chosen to replicate an "average" imaging spectrometer data collection, run with a solar zenith angle identical for an authentic AVIRIS scene selected later for further study. The MODTRAN code was set to the "mid-latitude summer" model, a constant surface elevation (0 km), changing visibility, constant water vapor level of 1.1 cm and a CO_2 mixing ratio of 360 ppm from altitudes of 20 km. The runs were performed with MODTRAN's two-stream DISORT and correlated-k algorithm ASDS (Ben-Dor et al., 2004).

The surface spectral information input to the synthetic data sets was obtained from two ASD-FR field spectra of urban and vegetation environments, acquired in typical urban areas (vegetation: mixture of grass and trees canopy; urban: mixture of concrete, asphalt, soil and dry wood). The vegetation and urban spectra were "mixed" linearly in 1% increments. The MODTRAN and ASD-FR spectra were convolved to an actual AVIRIS 2000 wavelength file (band centers and FWHM). The synthetic cube was constructed as follows: the 100 samples across the image are the 100 aerosol load values; sample 1 contains 0-km visibility and sample 100 contains 100-km visibility. The top line consists of 100% vegetation, and the bottom line of 99% urban (see Figure 1). The data were scaled by 10,000 and then converted to integer, and finally scaled by the AVIRIS scaling factors. Previous to this, all calculations were performed as floating point.

The authentic AVIRIS data that was selected for this study was of Santa Monica acquired on June 6, 2000 from an altitude of 20 km. The image was atmospherically corrected using ACORN code to yield an apparent reflectance cube and a water vapor image. Whereas the average water value of the scene (1.1 cm) was used in the synthetic data, the apparent reflectance image was processed to yield a "quick view" of the land use areas, as will be discussed later.

RESULT AND DISCUSSION

Ben-Dor et al. (1994) had shown that applying the parameter ln(A/R) to each pixel in the AVIRIS radiance/sun images (where A is the absorption of the oxygen peak at 0.760 μm and R is the reflectance at 0.760 μm if no oxygen absorption appears, i.e., the value on the continuum line of the oxygen peak) can extract a thin cirrus cloud image identified at 1.38 μm (A wavelength suggested by Gao et al. (1993) as a cirrus clouds marker in MODIS). Based on these findings we suggest using this parameter to further account for the aerosol loading on a pixel-by-pixel basis. Taking this challenge, we calculated the ln(A/R) over the synthetic image and segregated the calculated values to represent pure vegetation (100%), mixed vegetation-urban (50%) and pure urban pixels (100%).

Figure 2 shows the ln(A/R) values over these targets as a function of the visibility. As seen, a similar asymptotic trend was obtained for the three targets with an offset going from urban (low) to vegetation (high) targets. This offset is due to the spectral contribution of each target across the oxygen absorption peak and can be termed as the "albedo interference." The overall shape of the graphs presented in Figure 2 is based on the contribution of particle scattering to the oxygen absorption response at 0.760 μm. In reality, the oxygen, as a well-mixed gas, should provide a homogenous ln(A/R) image. Any variation from homogeneity may be related majorly to aerosol scattering appearance and/or minorly to the targets albedo variations. To reduce the albedo effect we used a look-up-table that was generated directly from Figure 2 and was set to represent 100% vegetation, 50% vegetation + 50% urban and 100% urban materials. Parallel to that we used the authentic AVIRIS image, which was first processed to remove the atmospheric attenuations by ACORN (2001) software (with a single visibility value of 25 km). The "atmospherically corrected" image was then interoperated using the SAM classifier for two end members, namely vegetation and urban material that were taken from the image. Each pixel in the authentic scene was characterized either as vegetation, urban or their mixture (excluding outliers), and then was classified to one of the three groups (100% vegetation(a), 50% vegetation + 50% urban(b) and 100% urban(c)). The ln(A/R) was calculated from the authentic AVIRIS radiance and then, was converted to present the visibility image. This was done by applying to each ln(A/R) calculated pixel a proper look-up-table that converts the data into visibility. The proper look-up-table for that purpose was selected based on the SAM classification and Figure 2. Adding all pixels together provided the visibility (albedo corrected) image of the area. Figure 3 shows a natural RGB image (a) of a Santa Monica, California, area side by side to the visibility image (b) of the same area, as was generated according to the process described above.

EVALUATION OF THE RESULTS AND FURTHER WORK

From Figure 2 it is seen that beyond ~30 km visibility the ln(A/R) values do not significantly change with increasing visibility. This suggests that a traditional visibility estimation, as done by an observer (for atmospherically rectifying remote sensing images), cannot be that precise; therefore, rough estimation is sufficient (e.g., 30 km or 40 km may provide similar ln(A/R) values). Nevertheless, on hazy days or over dusty areas, the visibility may be fairly low. In this regard, the ln(A/R) parameter is significantly affected by the aerosols load and can be used to precisely assess the correct visibility values over those pixels.

The histogram of the visibility image is given in Figure 4. It shows that an average of 30 km represents the entire scene. Several pixels however are characterized with lower visibility and can be seen in the image as darker tone areas (Figure 3b). The areas with low visibilities are those suspected to hold high aerosols load. From the image it is postulated that the lowest aerosol pixels are concentrated along a main strip (A in Figure 3b). As we have no ground truth data to validate this observation, we can only speculate that other areas are relatively contaminated with more fine particles in the air than the other areas. However, it should be remembered that this speculation has not been validated yet and more study in this direction has to be applied. Although this limitation may hamper a concrete conclusion, we believe that the suggested method has a favorable potential in depicting aerosol load on a pixel-by-pixel basis.

SUMMARY AND CONCLUSION

We presented here an idea and a first analytical step on how to account for the aerosol load on a pixel-by-pixel basis. The oxygen peak was used as a marker to pick the scattering effect of the aerosols and a look-up-table was set to reduce albedo effects of atmospherically studied components (aerosols and oxygen). The visibility image generated based on the suggested method showed a reasonable distribution over Santa Monica, California. Nevertheless, a proper validation process that can make such a method more concrete is still missing. More work in this direction is required and a combined research which will use low visibility data and ground truth information is strongly advised. Needless to say, only imaging spectrometry can provide such feasibility, and for that purpose, high quality data (e.g., AVIRIS) is a must.

REFERENCE

ACORN[TM], 2001, Atmospheric Correction Now. Analytical Imaging and Geophysics LLC, Version 3.12

Ben-Dor, E., A.F.H. Goetz, and A.T. Shapiro, 1994, Estimation of cirrus cloud and aerosol scattering in hyperspectral image data, *Proceedings of the International Symposium on Spectral Sensing Research,* 2:582–593, San Diego, California, USA

Ben-Dor, E., B. Kindel, and A.F.H. Goetz, 2004, Quality Assessment of Several Methods to Recover Surface Reflectance I using Synthetic Imaging Spectroscopy (IS) Data, *Remote Sensing of Environment* 90: 389–404

Berk, A., G.P. Anderson, L.S. Bernstein, P.K. Acharya, H. Dothe, M.W. Matthew, S.M. Adler-Golden, J.H. Chetwynd, Jr., S.C. Richtsmeier, B. Pukall, C.L. Allred, L.S. Jeong, and M.L. Hoke, 1999, MODTRAN 4 Radiative Transfer Modeling for Atmospheric Correction *Summaries of the Eighth JPL Airborne Earth Science Workshop* JPL-Pub 99-17: 23–31

Gao, B.C., A.F.H. Goetz, and W.J. Wiscombe, 1993a, Cirrus cloud detection from airborne imaging spectrometer data using the 1.38 mm water vapor band, *Geophysical Research Letters* 20(4): 301–304

Gao, B.C., K.B. Heidebrecht, and A.F.H. Goetz, 1993b, Derivation of Scaled Surface Reflectance from AVIRIS Data, *Remote Sens. Environ.* 44, 145–163

Green, R.O., 2001, Measuring the Spectral Expression of Carbon Dioxide in the Solar Reflected Spectrum with AVIRIS, *Proceedings of the 10th JPL Airborne Earth Science Workshop*, JPL Publication 02-1, Jet Propulsion Laboratory, Pasadena, California, 181–192

Richter, R., 2004, Atmospheric/Topographic Correction for Airborne Imagery (ATCOR-4), DLR report DLR-IB 565-02/04, Wesling, Germany
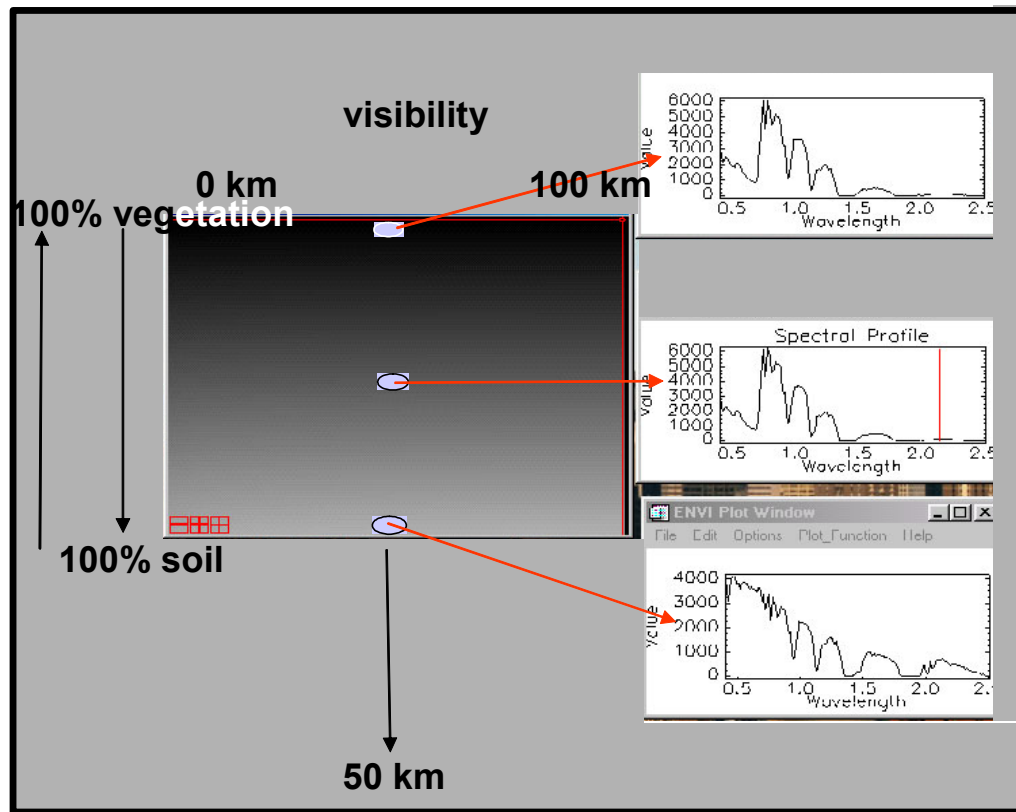
Figure 1: The synthetic radiance image and the spatial distribution of the visibility (X axis) and the urban and vegetation cover (Y axis).
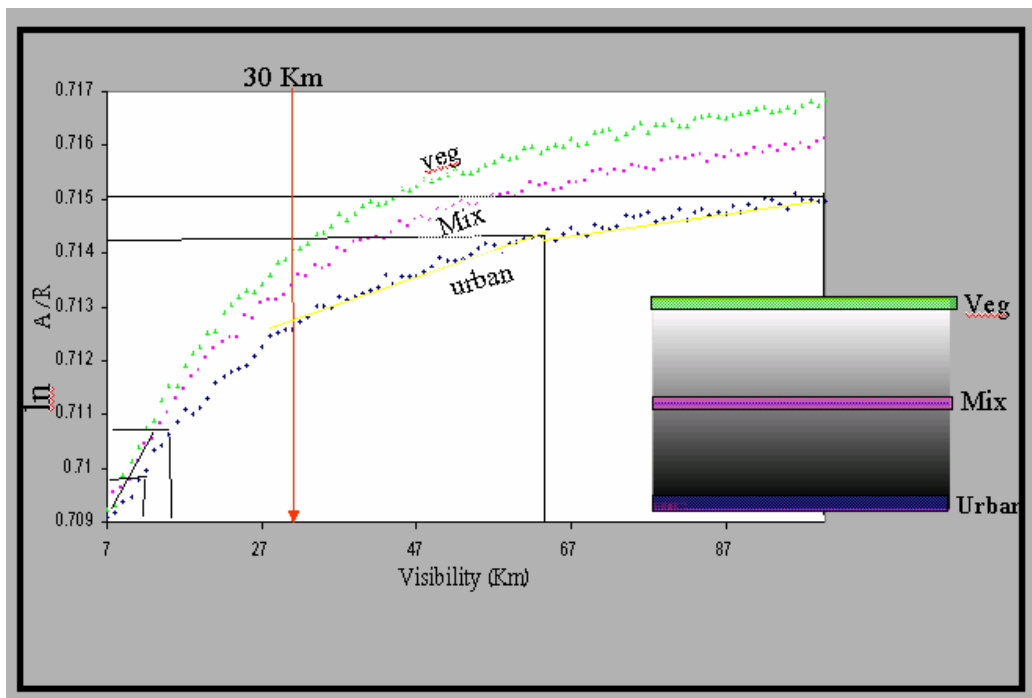
Figure 2: The ln(A/R) at 0.760 μm as a function of the visibility in the synthetic image for 100% vegetation, 50% vegetation + 50% urban and 100% urban targets.
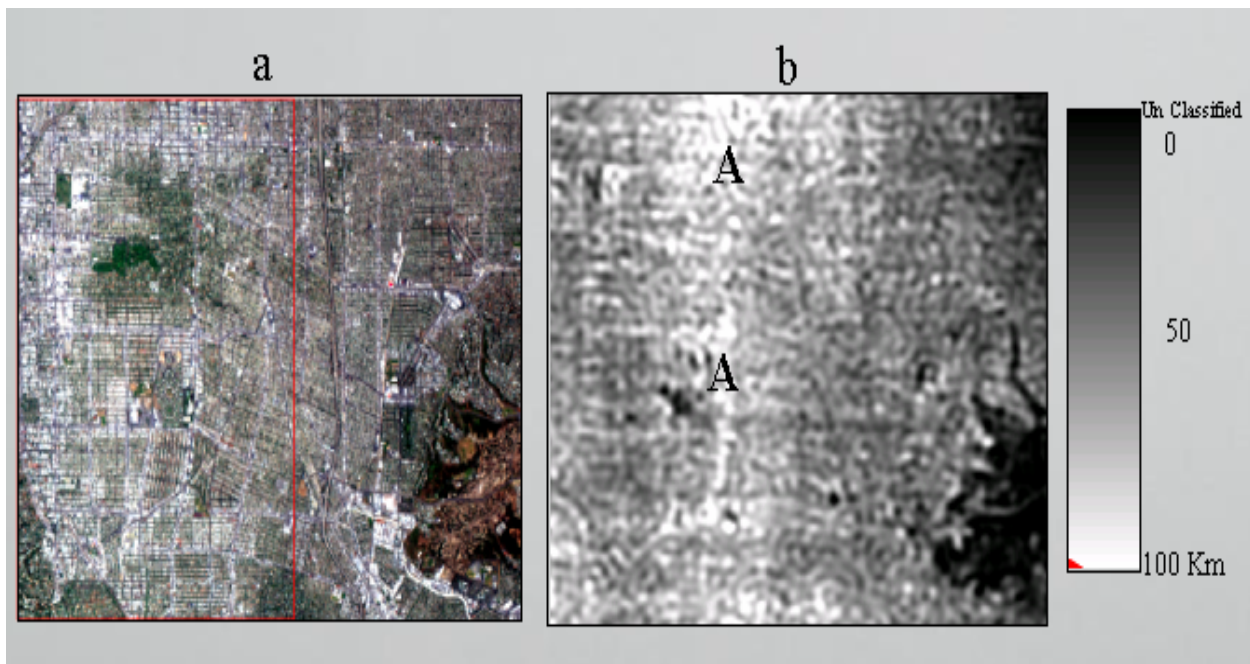
Figure 3: A natural color view of the area under study (a) and its visibility image generated according to the paper's suggested procedure (b).
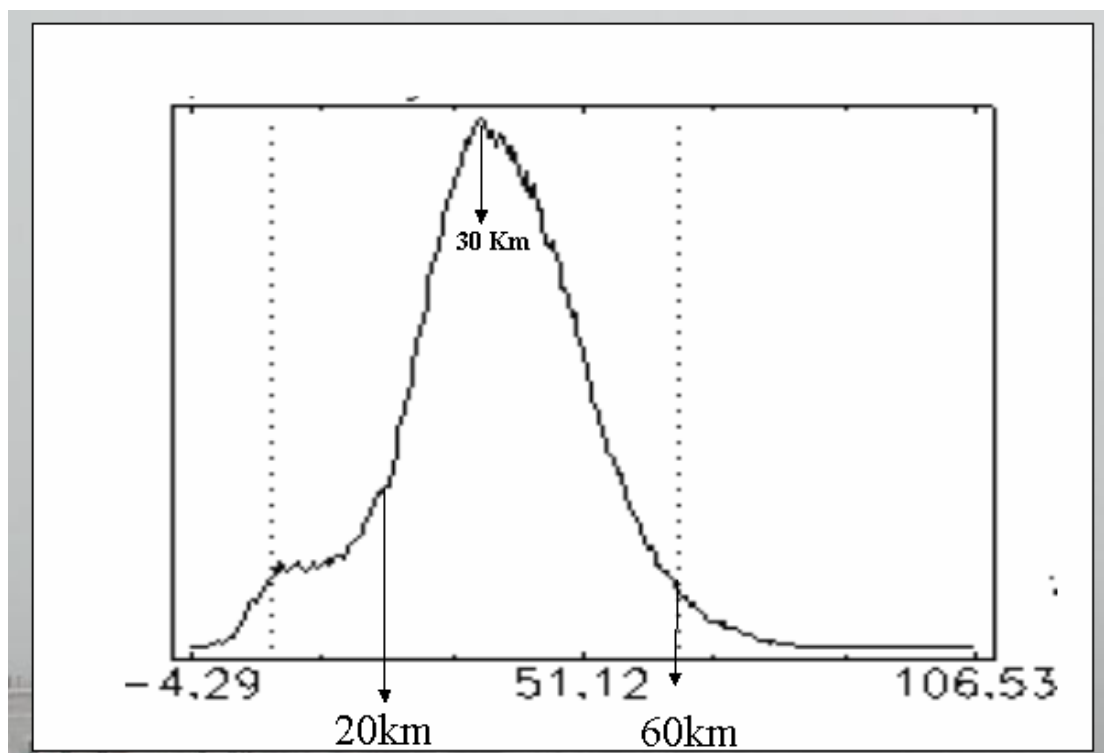
Figure 4: The histogram of the visibility image given in Figure 3a.

A NEW METHOD FOR ATMOSPHERIC CORRECTION AND AEROSOL OPTICAL PROPERTY RETRIEVAL FOR VIS-SWIR MULTI- AND HYPERSPECTRAL IMAGING SENSORS: QUICK ATMOSPHERIC CORRECTION

Lawrence S. Bernstein,[1] Steven M. Adler-Golden,[1] Robert L. Sundberg,[1] Robert Y. Levine,[1] Timothy C. Perkins,[1] Alexander Berk,[1] Anthony J. Ratkowski,[2] and Michael L. Hoke[2]

1.0 INTRODUCTION

A critical first step in the analysis of visible-SWIR hyperspectral or multispectral imagery (HSI or MSI) is atmospheric correction or compensation, in which atmospheric absorption and scattering effects are removed and the data are reduced to surface spectral reflectance (see Fig. 1). A number of atmospheric correction methods and algorithms exist, including algorithms based on first-principles radiation transport calculations (Gao *et al.*, 1993, 2000; Montes *et al.*, 2001; Green *et al.*, 1996; Miller, 2002; Adler-Golden *et al.*, 1999; Matthew *et al.*, 2000, 2003; Qu *et al.*, 2000; Richter and Schlaepfer, 2002), and empirical approaches such as the Empirical Line Method (ELM) (Roberts *et al.*, 1985; Kruse *et al.*, 1990), which relies on two or more known reflectances in the image. However, none of these methods provide the ideal combination of high accuracy, high computational speed, and independence from prior knowledge.
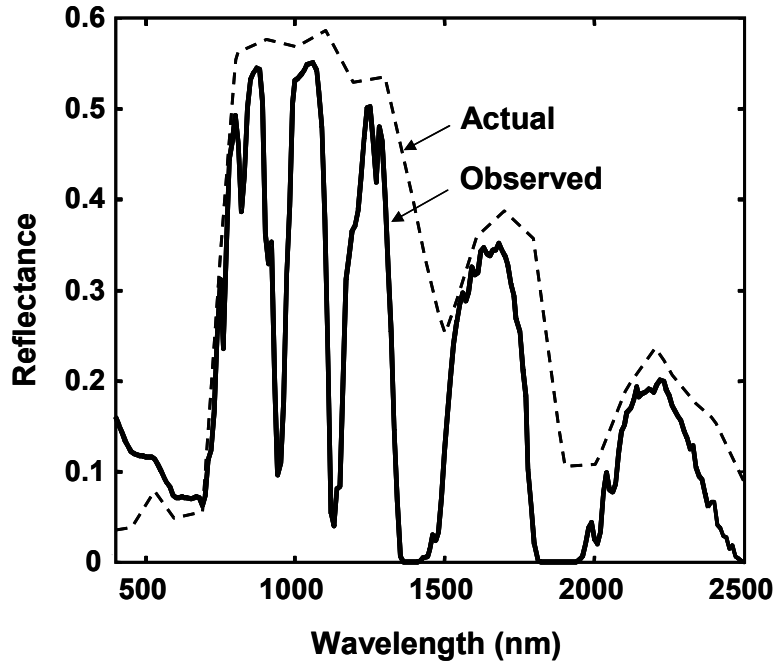
Figure 1. MODTRAN calculation of the apparent reflectance of a vegetation pixel as observed from space with nadir viewing, the Mid-Latitude Summer model atmosphere, and Rural aerosols with VIS=23km.

This paper presents a new, semi-empirical quick atmospheric correction method, dubbed QUAC, which also enables retrieval of the wavelength-dependent optical depth of the aerosol or haze and

---

[1] Spectral Sciences, Inc., 4 Fourth Avenue, Burlington, Massachusetts 01803-3304 (larry@spectral.com)
[2] Air Force Research Laboratory, Hanscom Air Force Base, Massachusetts 01731-3010

molecular absorbers. It allows the retrieval of approximate reflectance spectra even when the sensor does not have a proper radiometric or wavelength calibration, or when the solar illumination intensity is unknown, such as when a cloud deck is present. Computational speed is much faster than for the first-principles methods, making it potentially suitable for real-time applications. In tests to date, QUAC has yielded remarkably good agreement with a state-of-the-art first-principles algorithm. Like the ELM, QUAC assumes a linear relationship between spectral reflectance and measured radiance, which is considered to be a good approximation for most scenes.

The standard radiance equation may be written as (Matthew *et al.*, 2000, 2003)

$$\rho_j(\lambda) = A(\lambda) + \frac{B(\lambda)}{1 - S(\lambda) < \rho(\lambda) >} \rho_j^o(\lambda) + \frac{C(\lambda)}{1 - S(\lambda) < \rho(\lambda) >} < \rho(\lambda) > \tag{1}$$

where ρ_j is the observed reflectance (the radiance normalized by the surface normal component of the solar flux) for the *j*'th pixel at a spectral band centered at wavelength λ, ρ_j^o is the actual surface reflectance, $< \rho >$ is a spatially averaged surface reflectance. *A*, *B*, *C* and *S* are coefficients that describe the transmission and scattering effects of the atmosphere. Their physical origin is highlighted in Figure 2. The first coefficient, *A*, accounts for light that never encounters the surface, but is scattered and absorbed within the atmosphere. The second, *B*, accounts for the sun-surface-sensor path direct transmittance. The third, *C*, accounts for diffuse transmittance and gives rise to the "adjacency effect," a spatial blending induced by atmospheric scattering. The length scale of the adjacency effect is typically of order ~0.5 km, thus $< \rho >$ is typically a slowly varying function of position within a large image. *S*, the atmospheric spherical albedo, accounts for enhancement of the ground illumination by atmospheric reflection.
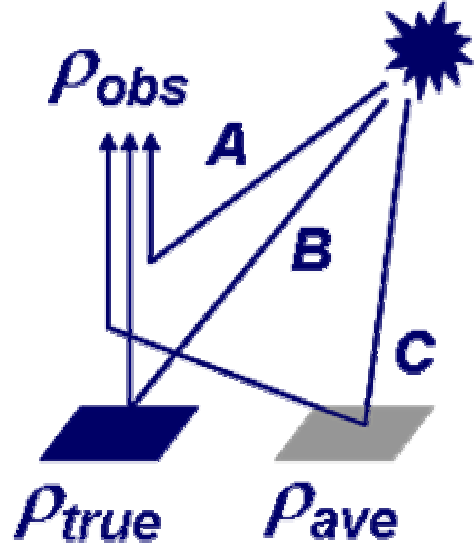
Figure 2. Radiation-transfer contributions to the observed apparent reflectance, ρ_{obs}.

Eq. (1) reduces to a linear form under many common conditions in which (1) $S < \rho >$ is small and when either, (2) the diffuse and direct transmittance terms can be combined with a single reflectance variable, or (3) the diffuse term can be combined with the backscattering term. Situation (1) occurs frequently, when the visibility is reasonably high or when the ground is dark in the visible (such as with vegetation, water, or dark soil). Situation (2) occurs when the pixels are very large, several hundred meters in size. Situation (3) occurs when the scene materials are fairly uniformly interspersed or when the image covers a small geographic area (< ~1 km), making $< \rho >$ nearly constant, or when the visibility is high, making the diffuse transmittance term small. When (1) and (3) apply, Eq. (1) reduces to the linear equation

$$\rho_j(\lambda) = A(\lambda) + B(\lambda)\rho_j^o(\lambda) + C(\lambda) < \rho(\lambda) > \tag{2}$$

With the linear Eq. (2), the aim of atmospheric compensation is essentially the determination of an offset, $A+C<\rho>$, and gain parameter, *B*, in order to retrieve the surface reflectance, ρ_j^o. Numerous

approaches to this problem have been developed. The ELM assumes that the radiance image contains some pixels of known reflectance. This method is not generally applicable, as in-scene known reflectances are often not available. In variants of the ELM, approximate gain and offset values are generated using pixels in the image that are treated as if their spectra were known. For example, in the Flat Field Method a single bright pixel is taken as having a spectrally flat reflectance and the offset is taken as zero; accordingly, dividing the image pixel spectra by the bright pixel spectrum yields approximate relative reflectances. In the Internal Average Relative Reflectance method, this procedure is followed using a scene-average spectrum rather than a single bright pixel spectrum. In general, neither the Flat Field Method nor the Internal Average Relative Reflectance methods are very accurate.

First-principles methods express the Eq. (1) or Eq. (2) parameters in terms of atmospheric physical variables, such as column water vapor and aerosol optical depth or visibility. For retrieving optical depth, methods are available that rely on modeling the aerosol backscatter over "dark" pixels such as vegetation and dark soil (Kaufman *et al*., 1997) or water bodies. However, difficulties in determining the optical depth arise when there is a lack of suitable dark pixels in the scene, or when the sensor is at a low altitude, within the aerosol layer, so that the backscatter it measures is a small (and generally unknown) fraction of the total.

Like many first-principles methods, QUAC determines the atmospheric compensation parameters directly from the information contained within the scene (observed pixel spectra), without ancillary information. However, unlike most other methods, its aerosol optical depth retrieval approach does not require the presence of dark pixels. The retrieved optical depth information can therefore be utilized to improve the accuracy of methods that use first-principles modeling. In particular, it can be used to set the optical depth of a model aerosol when dark pixels are unavailable, or to select from among alternative model aerosols to provide consistency with optical depths retrieved from a dark pixel method.

2.0 QUAC ALGORITHM DESCRIPTION

The underlying assumptions of the approach are:

- There are a number ($\approx$10 or more) of diverse pixel spectra (diverse materials) in a scene,
- The spectral standard deviation of ρ_j^o for a collection of diverse materials is a nearly wavelength-independent constant, and an additional, helpful assumption is that,
- There are sufficiently dark pixels ($\rho_j^o(\lambda)\approx0$) in a scene to allow for a good estimation of the nearly spatially invariant baseline contribution, $\rho_b=A+C<\rho>$

The first assumption is usually applicable, as it only requires that a handful of pixels out of typically $\sim10^5$ to 10^6 pixels display diverse spectra. The most notable exception would be a scene over completely open and deep water, in which case the material reflectance is well known *a priori*. The diverse spectra can be selected using any of a number of spectral diversity metrics and algorithms, such as endmembers. The second assumption appears to be generally true based on our empirical observation, and is likely related to the lack of spectral correlation between diverse materials. The third assumption is frequently applicable, as most scenes will contain a number of very dark pixels from such surfaces as water bodies, vegetation, and cast shadows. For the atypical cases that violate this assumption, there are alternative methods, described later, for estimating a reasonable baseline. The implementation of QUAC is straightforward and efficient, as highlighted in Figure 3. The atmospheric correction step just involves re-arranging Eq. (2) to solve for $\rho_j^o(\lambda)$ given B and the baseline. A key attribute of QUAC is its applicability to any sensor viewing or solar elevation angle.
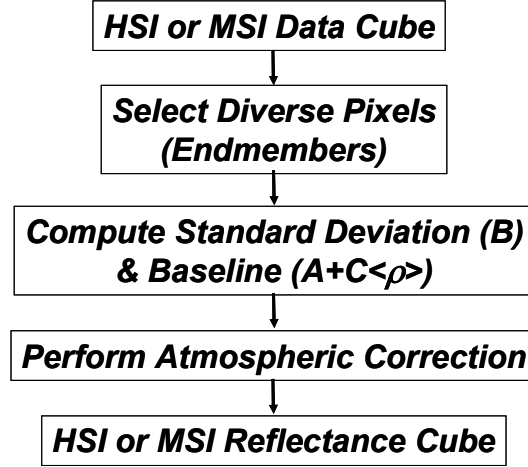
Figure 3. Overview of QUAC atmospheric correction data-processing flow.

Under the above-stated assumptions, the spectral standard deviation of Eq. (2) for a set of diverse pixel spectral can be expressed as,

$$\sigma\rho(\lambda) = B(\lambda)\sigma\rho^{\circ}(\lambda) \tag{3}$$

For reasons mentioned earlier, $A + C<\rho>$ can be taken as a constant in many, if not most, cases, so it makes no contribution to the standard deviation. In cases where it varies significantly within the scene, the image can be divided into smaller pieces, as discussed below. Since $\sigma\rho^{\circ}$ is assumed to be spectrally invariant, then to within a normalization factor, designated g_o, $\sigma\rho$ represents the correction factor, B. The actual surface spectral reflectance can be retrieved using the extracted in-scene-determined compensation parameters and re-arrangement of Eq. (2) to yield

$$\rho_j^{\circ}(\lambda) = \frac{\rho_j(\lambda) - \rho_b(\lambda)}{g_o\sigma\rho(\lambda)} \tag{4}$$

where $\rho_b = A + C<\rho>$ is the baseline contribution.

There are a number of ways in which the normalization factor, g_o, can be established. For many sensors there is at least one atmospheric window band, typically in the 1500–2500 nm region, for which $B(\lambda) \approx 1$ (inspection of Fig. 1 shows that $B=0.9$ is a good estimate for typical clear atmospheric conditions); thus, for this band

$$g_o = 0.9 / \sigma\rho \tag{5}$$

If a suitable window band is not available, the normalization factor, g_o, can still be extracted directly from the standard deviation curve. Two bands ($\lambda_2 > \lambda_1$) are selected which are outside of any water absorption region, insuring that the atmospheric extinction is due primarily to the aerosols. The ratio of the standard deviations of these bands is a direct measure of the difference in aerosol optical depth, τ, via,

$$-\ln\frac{\sigma\rho(\lambda_1)}{\sigma\rho(\lambda_2)} = \tau(\lambda_1) - \tau(\lambda_2) \tag{6}$$

Depending on the wavelengths of the selected bands, a generally small correction for molecular Rayleigh scattering may be required. For aerosols, the ratio of optical depths at two wavelengths is well approximated by the Ångström formula,

$$\frac{\tau(\lambda_1)}{\tau(\lambda_2)} = \left(\frac{\lambda_2}{\lambda_1}\right)^\alpha , \quad (\alpha > 0) \tag{7}$$

Combining Eqs. (6) and (7) allows one to convert the optical depth difference to an absolute optical depth at either wavelength,

$$\tau(\lambda_2) = \frac{-\ln\dfrac{\sigma\rho(\lambda_1)}{\sigma\rho(\lambda_2)}}{\left(\dfrac{\lambda_2}{\lambda_1}\right)^\alpha - 1}. \tag{8}$$

The normalization factor is now determined from

$$g_o = \exp(-\tau(\lambda_2))/\sigma\rho(\lambda_2) \tag{9}$$

It is noted that Eq. (9) is just a generalization of Eq. (5).

If neither the sensor radiometric calibration nor the solar illumination intensity is known, then $\sigma\rho$ is known only to within a scale factor and the normalization factor, g_o, must be estimated by a different method. One method is to set g_o such that that the maximum retrieved reflectance value for any wavelength and pixel is unity. This method is found to work reasonably in images containing a variety of man-made materials, such as urban scenes. Another method is to derive g_o by comparing the retrieved reflectance values with those in a library of material spectra.

For most scenes, the baseline curve is defined as the darkest observed signal for each band from among the diverse spectra. The presence of sufficiently dark pixels is indicated by at least one pixel spectrum with an apparent reflectance below ~0.05 for $\lambda > 1500$ nm. For the rare situation that a dark spectrum is unavailable, it is still possible to estimate a reasonable background. One such method is to use a radiative-transfer code such as MODTRAN (Berk *et al.*, 1989, 1998; Acharya *et al.*, 1999) to compute the baseline based on the retrieved aerosol and molecular optical properties.

While the focus of the previous discussion was on atmospheric compensation, it was noted that QUAC provides, to within a normalization factor, the sun-surface-sensor path transmittance, $B(\lambda)$, which in window regions provides the wavelength-dependent aerosol extinction curve. The process flow for retrieving the aerosol optical properties is highlighted in Figure 4. Analysis of B can provide quantitative measures (column amounts) of all the atmospheric attenuation sources, including aerosol scattering and absorption, molecular absorption, and Rayleigh scattering. This may be accomplished through spectral fitting with an accurate atmospheric radiative-transfer code (e.g., MODTRAN) or, alternatively, by analytical approximations such as the Ångström law discussed above.
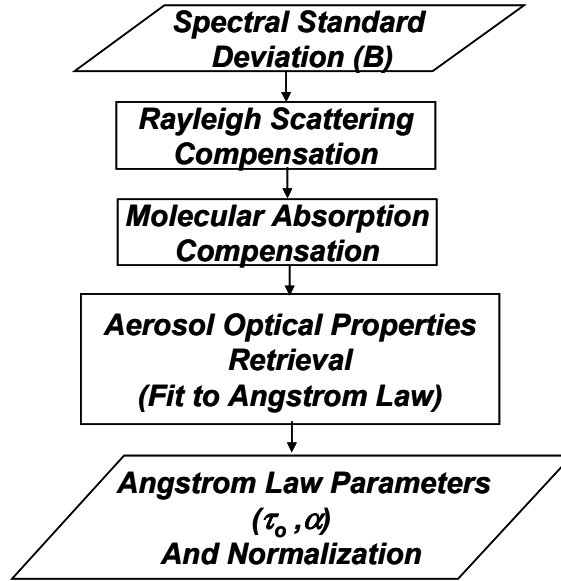
Figure 4. Overview of QUAC aerosol properties retrieval process flow.

Noting that the definition of a scene or image is flexible, the QUAC approach may be applied to individual sub-sections of a scene or image, if a sufficient diversity of pixel spectra exists within the sub-sections for computing a meaningful standard deviation and baseline. In this way, spatial variations in the adjacency-averaged reflectance $<\rho>$ and in the atmospheric parameters can be identified and taken into account in the atmospheric correction.

3.0 DATA ANALYSIS

QUAC was used to perform atmospheric correction and aerosol property retrieval on two very different hyperspectral AVIRIS (224 spectral channels from 400 to 2500 nm) data collects. As depicted in Figure 5, one corresponds to high visibility and low humidity, and the other to low visibility and high humidity. The NASA Stennis data is particularly useful because the Stennis site contains a large number of ground truth materials/panels (these are visible in the lower left corner of Figure 5).
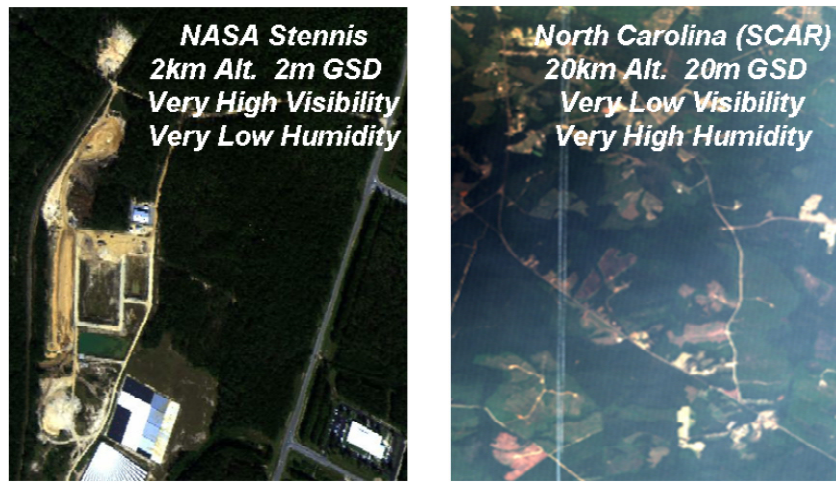
Figure 5. RGB image of the AVIRIS data sets used for evaluation of QUAC.

The first step in the process is the selection of diverse pixel spectra. For this analysis, we used the fast and automated SMACC (Sequential Maximum Angle Convex Cone) (Gruninger *et al.*, 2001) endmember code. To further speed the endmember-finding we used only ten window region wavelengths. The results for the NASA Stennis scene are displayed in Figure 6. It is evident that this set spans a wide variety of spectral shapes and reflectance values. Several endmembers are quite dark, and the lowest reflectance value for each channel defines the baseline spectrum.

The next step is to compute the standard deviation of the selected pixels. Before this is done, some refining of the initial selection usually occurs. This involves weeding out spectra with sharp features, mainly vegetation spectra that display a steep rise around 700 nm (the chlorophyll red edge). Pixels containing cirrus clouds, which can be easily discerned using established algorithms, are also rejected. The standard deviations for the NASA Stennis and North Carolina SCAR data are presented in Figure 7. The absorption due to the 940 nm H_2O band is clearly evident, and the much deeper feature seen in the North Carolina data is indicative of a much higher humidity level. Additional, weaker absorption features, such as the 840 nm H_2O and 760 nm O_2 bands are easily discernible. The general upper bounding envelope to these curves, formed by spectral regions outside of the absorption features, is a direct measure of the aerosol extinction for the L-shaped path from the sun to the surface to the sensor (i.e., the *B* coefficient). By inspection, it is quite obvious that the Stennis scene corresponds to a high visibility while the North Carolina scene displays approximately an order of magnitude more aerosol extinction and corresponds to a much lower visibility. The aerosol extinction is quantified below.

Figure 6. The first 20 endmembers selected by SMACC using the apparent reflectances from the NASA Stennis data.
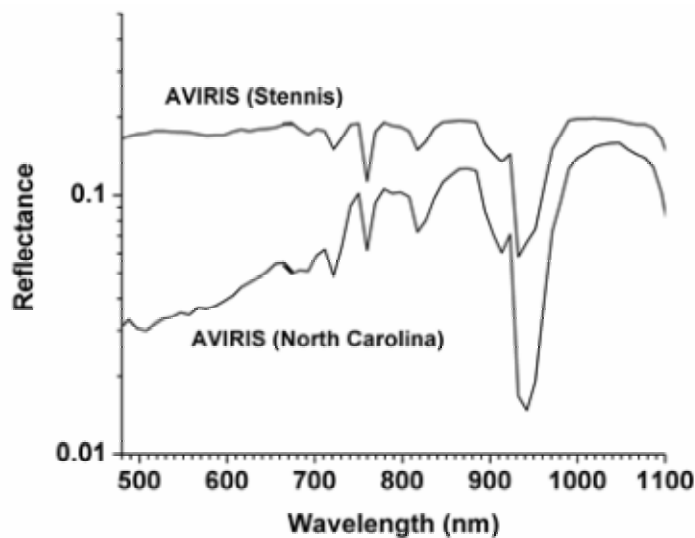
Figure 7. Spectral standard deviations based on the selected endmembers for the Stennis and North Carolina AVIRIS data sets.

From the above information, baseline and standard deviation, the entire data cube can be atmospherically corrected. Sample results for the Stennis data are shown in Figure 8 and include comparisons to FLAASH (Matthew *et al.* 2003, 2000) results and ground truth measurements. In this instance, and in general, QUAC compares well to FLAASH. The computational time required for the end-to-end QUAC process for an entire AVIRIS data cube (512 x 512 pixels and 224 spectral channels), as defined in Figure 8, is ~1 min on a 1.6 GHz Pentium IV PC. This is based on relatively slow IDL coding for the endmember selection and atmospheric correction steps. For comparison, FLAASH, which run a series of MODTRAN calculations, requires ~10min to perform the atmospheric correction.
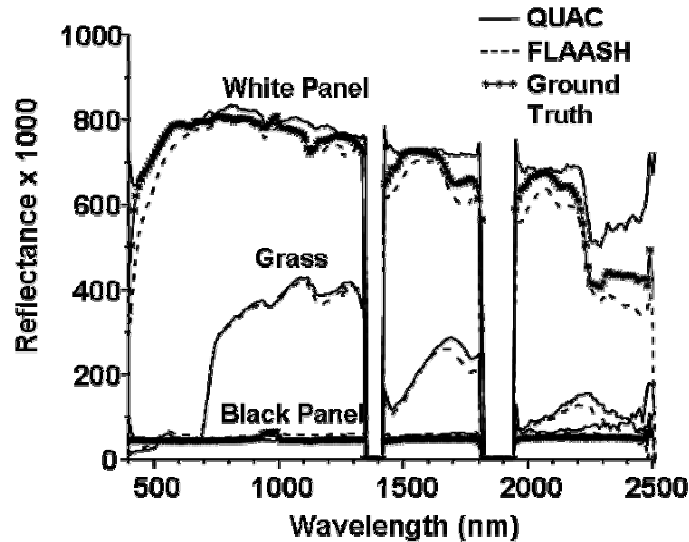
Figure 8. Comparison of QUAC atmospherically-corrected reflectances to those obtained from FLAASH and ground truth measurements for the Stennis data.

The key underlying assumption for QUAC is that the standard deviation of the endmember reflectances is independent of wavelength. This can be demonstrated by considering the FLAASH-corrected endmembers selected above by SMACC for the Stennis scene. It is noted that we cannot use the QUAC corrected endmembers since the assumption of a flat standard deviation is built into the approach, and in fact the standard deviation of the QUAC-corrected endmembers will be absolutely constant. However, no such assumption is built into FLAASH. The results are depicted in Figure 9. The effect of refining the endmember selection to wee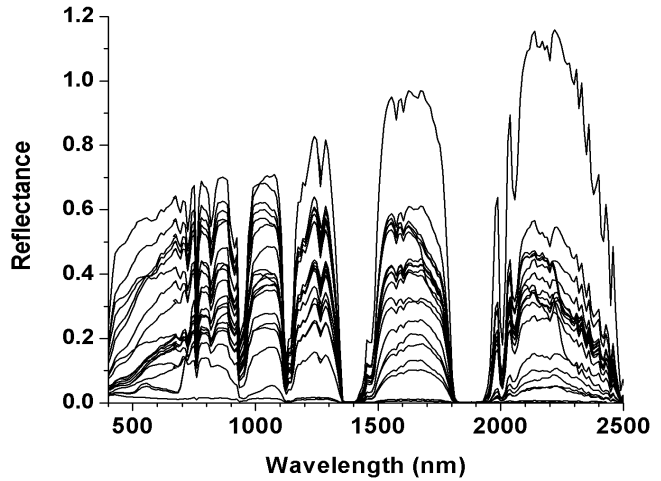d out vegetation and outliers (exceptionally bright pixels and glints) is also shown in Figure 9. We ascribe the non-flat behavior on the edges to possible calibration issues and/or imperfect atmospheric correction. In any event, for most of the spectral regime, ~500–2400 nm, the standard deviation is acceptably flat. We have produced similar curves for a number of different AVIRIS data sets and find similarly good, and sometimes better, behavior of the standard deviations.

An advanced implementation of QUAC could correct for the residual errors associated with the deviation from perfectly flat spectral behavior for the endmember standard deviation. The underlying assumption is that the basic QUAC approach yields a sufficiently good atmospheric correction to allow for a useful un-mixing of the corrected endmember spectra based on a material spectral library. The standard deviation may be computed for the library fit to the endmember spectra, and the resulting standard deviation curve from this fit used to further improve the atmospheric correction.
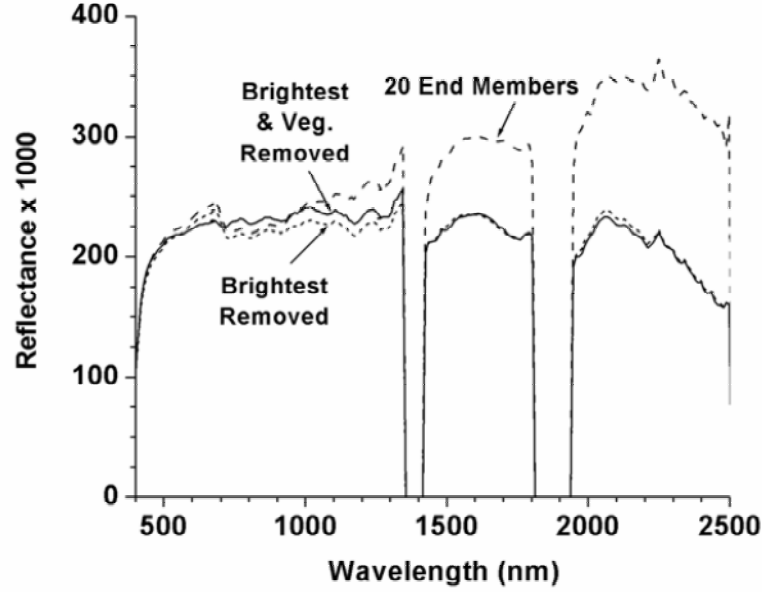
Figure 9. Standard deviation of the FLAASH-corrected endmembers for the Stennis scene.

QUAC was also applied to the multispectral satellite-based LANDSAT ETM+ sensor (6 broad bands, 450–2500 nm, 30 m GSD). The results with comparison to FLAASH are displayed in Figure 10.
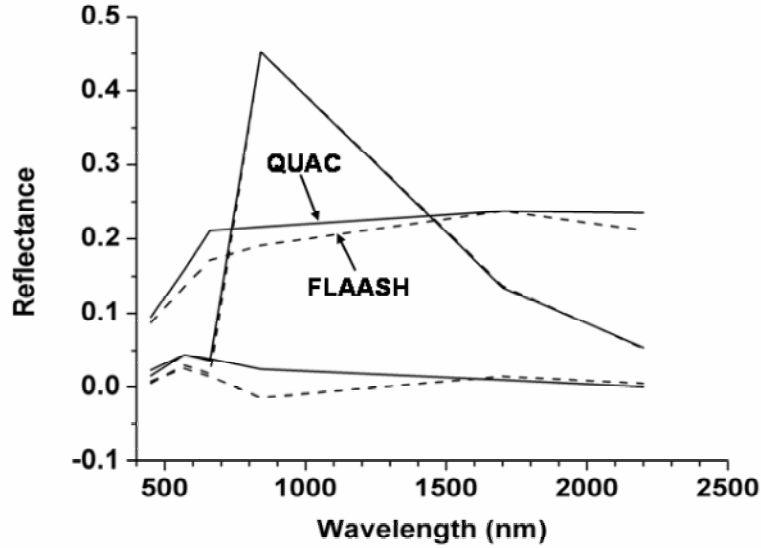
Figure 10. QUAC results and comparison to FLAASH for the multispectral LANDSAT ETM+ sensor.

The use of QUAC to retrieve aerosol optical properties following the process defined in Figure 4 is illustrated in Figure 11 for the Stennis and North Carolina data sets. An interesting result concerns the retrieved Ångström law exponent, α, which is indicative of aerosol type. For the North Carolina aerosol, α=1.5, which is identical to that for the MODTRAN rural aerosol model. For the Stennis data, α=2.4, which indicates a stratospheric aerosol type. This makes sense, as the small aerosol optical depth retrieved may all be attributed to a small residual stratospheric aerosol contribution as opposed to boundary layer aerosols.
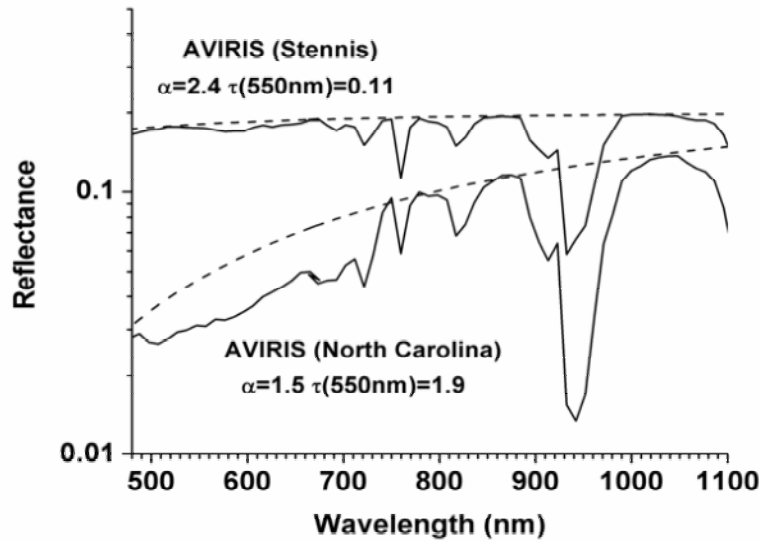
Figure 11. QUAC retrieval of aerosol optical properties based on an Ångström law fit (dashed lines) to the endmember standard deviations for the AVIRIS Stennis and North Carolina data sets.

Validation of the QUAC aerosol property retrieval approach is considerably more difficult to accomplish than the atmospheric correction approach because it requires complete characterization of the aerosol vertical profile concurrent to an HSI or MSI data collection. In lieu of such data, the next best validation approach is to use a high-fidelity HSI or MSI simulation code. We have recently developed such a code (Berk *et al.*, 2000a; Richtsmeier *et al.*, 2001), called MCSCENE, for this purpose. Briefly, it features a backward Monte Carlo multiple-scattering radiative-transfer approach utilizing MODTRAN spectroscopy, includes a fully 3D voxelized atmosphere, and models the surface at high spatial resolution allowing for topographical features and BDRFs (Bi-Directional Reflectance Distribution Function). We performed simulations for the satellite-based IKONOS sensor (4 broad bands, 450–800 nm, 2 m GSD) of the Stennis site. This included nadir and off-nadir viewing and variation of the solar zenith angle (forward and backward

Figure 12. Average reflectances (top curves) and standard deviations (bottom curves) for the endmembers selected for the IKONOS simulation. The square symbols on the bottom curves are the actual $B(\lambda)$ values used in the simulations.

aerosol scattering geometries). The Rural aerosol model with a visibility of 23 km was assumed. The results are presented in Figure 12. The QUAC derived aerosol optical properties are in close agreement with the actual ones used in the simulation. The off-nadir cases for the two solar azimuth/scattering

geometries display very different average reflectances (higher for forward scattering – 180° azimuth) but identical aerosol transmittance curves, $B(\lambda)$. Even though the solar azimuths are quite different, the total L-shaped path lengths are identical and thus, should yield identical extinction curves.

4.0 CONCLUSIONS AND RECOMMENDATIONS

A new semi-empirical algorithm, QUAC, for atmospheric correction and aerosol optical properties retrieval for VIS-SWIR HSI and MSI sensors has been developed. Initial applications of QUAC to atmospheric correction of HSI AVIRIS and MSI LANDSAT data sets show surprisingly good performance, nearly comparable to that of a first-principles physics-based code. The utility of QUAC for retrieving wavelength-dependent aerosol extinction, and by extension aerosol type, was demonstrated for several AVIRIS data sets. An initial validation of the aerosol optical properties retrieval method was accomplished through the use of a HSI scene simulation approach. Continued development and validation of QUAC is recommended using a wider variety of HSI and MSI data sets, including simulated data, and through field measurements involving full characterization of the aerosol column concurrent with airborne and/or satellite-based HSI and MSI observations. Computational speed-ups, automation, and eventually the development of an on-board data processing capability should also be explored.

5.0 REFERENCES

Acharya, P.K., A. Berk, N.F. Larsen, S.-C. Tsay, and K.H. Stamnes, "MODTRAN4: multiple scattering and bidirectional reflectance distribution function (BRDF) upgrades to MODTRAN," *SPIE 3756*, pp. 354–362, 1999.

Adler-Golden, S.M., M.W. Matthew, L.S. Bernstein, R.Y. Levine, A. Berk, S.C. Richtsmeier, P.K. Acharya, Anderson, G.P., G. Felde, J. Gardner, M. Hoke, L.S. Jeong, B. Pukall, J. Mello, A. Ratkowski and H.-H. Burke, "Atmospheric Correction for Short-wave Spectral Imagery Based on MODTRAN4," *Summaries of the Eighth Annual JPL Earth Science Workshop*, JPL Publication 99-17, pp. 12–23, Jet Propulsion Laboratory, Pasadena, CA, 1999.

Berk, A., L.S. Bernstein, and D.C. Robertson, "MODTRAN: A Moderate-Resolution Model for LOWTRAN 7," GL-TR-89-0122, Geophysics Directorate, Phillips Laboratory, Hanscom AFB, MA, 1989.

Berk, A., L.S. Bernstein, G.P. Anderson, P.K. Acharya, D.C. Robertson, J.H. Chetwynd and S.M. Adler-Golden, "MODTRAN Cloud and Multiple Scattering Upgrades with Application to AVIRIS," *Remote Sens. Environ.*, 65, 367–375, 1998.

Berk, A., P.K. Acharya, S.M. Adler-Golden, and L.S. Bernstein, "A 3-D Hyperspectral Imagery Simulation Test Bed for the Littoral Zone - Phase I Final Report", SSI-TR-356, Spectral Sciences, Inc., Burlington, MA, 2000a.

Berk, A., P.K. Acharya, L.S. Bernstein, G.P. Anderson, J.H. Chetwynd, and M.L. Hoke, "Reformulation of the MODTRAN band model for higher spectral resolution," *SPIE Proceeding, Algorithms for Multispectral, Hyperspectral, and Ultraspectral Imagery VI, Vol. 4049*, pp. 190–198, 2000b.

Gao, B.-C. M. J. Montes, Z. Ahmad, and C.O. Davis, "Atmospheric Correction Algorithm for Hyperspectral Remote Sensing of Ocean Color from Space," *Applied Optics,* 39, 887–896, 2000.

Gao, B.-C., K.B. Heidebrecht, and A.F.H. Goetz, "Derivation of Scaled Reflectances from AVIRIS Data," *Proceedings of the Fourth Annual JPL Airborne Geoscience Workshop*, Vol. I. pp. 35–36, 1993.

Green, R.O., D.A. Roberts, and J.E. Conel, "Characterization and Compensation of the Atmosphere for Inversion of AVIRIS Calibrated Radiance to Apparent Surface Reflectance," *Summaries of the Sixth Annual JPL Earth Science Workshop*, JPL Publication 96-4, Vol. 1, pp. 135–146, 1996.

Gruninger, J.H., M.J. Fox and R.L. Sundberg, "Hyperspectral Mixture Analysis using Constrained Projections onto Material Subspaces," *Proceedings of the International Symposium on Spectral Sensing Research*, Québec City, pp. 162–170, 2001.

Kaufman, Y.J., A.E. Wald, L.A. Remer, B.-C. Gao, R.-R. Li and L. Flynn, "The MODIS 2.1-μm Channel-Correlation with Visible Reflectance for Use in Remote Sensing of Aerosol," *IEEE Trans. Geosci. Remote Sens.*, 35, 1286–1298, 1997.

Kruse, F. A., K. S. Kierein-Young, and J. W. Boardman, "Mineral mapping at Cuprite, Nevada with a 63-channel imaging spectrometer," *Photogrammetric Engineering & Remote Sensing*, 56, 83–92, 1990.

Matthew, M.W., S.M. Adler-Golden, A. Berk, G. Felde, G.P. Anderson, D. Gorodetzky, S. Paswaters and M. Shippert, "Atmospheric Correction of Spectral Imagery: Evaluation of the FLAASH Algorithm with AVIRIS Data," *SPIE Proceeding,* A*lgorithms and Technologies for Multispectral, Hyperspectral, and Ultraspectral Imagery IX*, 5093, pp. 474–482, 2003.

Matthew, M.W., S.M. Adler-Golden, A. Berk, S.C. Richtsmeier, R.Y. Levine, L.S. Bernstein, P.K. Acharya, G.P. Anderson, G.W. Felde, M.P. Hoke, A. Ratkowski, H.-H. Burke, R.D. Kaiser, and D.P. Miller, "Status of Atmospheric Correction Using a MODTRAN4-based Algorithm," *SPIE Proceeding, Algorithms for Multispectral, Hyperspectral, and Ultraspectral Imagery VI*, *4049*, pp. 199–207, 2000.

Miller, C. J., "Performance assessment of ACORN atmospheric correction algorithm," *SPIE Proceedings, Algorithms and Technologies for Multispectral, Hyperspectral, and Ultraspectral Imagery VIII*, 4725, pp. 438–449, 2002.

Montes, M.J., B.-C. Gao, and C.O. Davis, "A new algorithm for atmospheric correction of hyperspectral remote sensing data," *SPIE Proceedings, Geo-Spatial Image and Data Exploitation II, Vol. 4383*, pp. 23–30, 2001.

Qu, Z., A.F.H. Goetz, and B. Kindel, "High-accuracy Atmospheric Correction for Hyperspectral Data (HATCH)," *Proceedings of the Ninth AVIRIS Earth Sciences and Applications Workshop*, JPL Publication 00-18, pp. 373–380, Jet Propulsion Laboratory, Pasadena, CA, 2000.

Richter, R. and D. Schlaepfer, "Geo-atmospheric processing of airborne imaging spectrometry data Part 2: atmospheric/topographic correction" *Int. J. Remote Sensing*, 23, 2631–2649, 2002.

Richtsmeier, S.C., A. Berk, S.M. Adler-Golden, and L.S. Bernstein, "A 3D Radiative-Transfer Hyperspectral Image Simulator for Algorithm Validation," *Proceedings of the International Symposium on Spectral Sensing Research*, Québec City, 2001. (Inadvertently missing from proceedings – available as a pdf at www.spectral.com)

Roberts, D. A., Y. Yamaguchi, and R. J. P. Lyon, "Calibration of Airborne Imaging Spectrometer data to percent reflectance using field spectral measurements," *19th International Symposium on Remote Sensing of Environment*, Ann Arbor, MI, 1985.

6.0 ACKNOWLEDGEMENTS

HYPERSPECTRAL MAPPING OF EARTH'S EARLIEST HYDROTHERMAL ACTIVITY IN AN ARCHEAN GRANITE-GREENSTONE TERRANE

Adrian J. Brown[1]

1   Introduction

As part of a joint Commonwealth Scientific and Industrial Research Organization (CSIRO)–Australian Centre for Astrobiology (ACA) project to map hydrothermally altered minerals in the East Pilbara Granite-Greenstone Terrane (EPGGT), mineral maps of epithermal activity in two regions of volcanic successions have been compiled using an airborne hyperspectral dataset. The differing mineral suites suggest epithermal activity characterized by high and low sulphidation, possibly at the Archean seafloor or in a shallow marine environment.

1.1   Motivation

In 2005, NASA will launch a hyperspectral visible/near infrared-short wavelength infrared-infrared (VNIR-SWIR-IR) instrument called the Compact Reconnaissance Infrared Spectrometer for Mars (CRISM) onboard the Mars Reconnaissance Orbiter (MRO) mission. In order to increase the probability of this mission encountering a Martian geobiological event of interest, this project is studying some of the oldest, best-preserved volcanic successions with life signs on Earth, at the Pilbara Craton, Western Australia. Three water-related signs of interest exist in the target terrain:

        a. pillow basalts,
        b. stromatolites, and
        c. serpentinized ultramafics.

The discovery of any of these water signs on Mars would be of great significance for the understanding of the geological development of the planet and verifying the existence of an extant or extinct Martian biosphere.

2   Geological Setting

The study area discussed herein lies in a region called the North Pole Dome (NPD) (see Figure 1), a succession of ovoid shaped volcanic units surrounding a central monzogranite, interpreted as a syn-volcanic laccolith (Van Kranendonk, 2000). The volcanic units form part of the 3.5-3.3 Ga Warrawoona Group, and include ultrabasic komatiite, mafic and felsic units (Brown *et al.*, 2004a) that dip 30–70 degrees away form the central monzogranite. A summary of the stratigraphy of the Warrawoona Group, along with associated fossil and stromatolite assemblages, is given in Table 1.

---

[1] **Australian Centre for Astrobiology, Macquarie University, NSW 2109, Australia.**
corresponding email: abrown@els.mq.edu.au
website: http://aca.mq.edu.au/abrown.htm
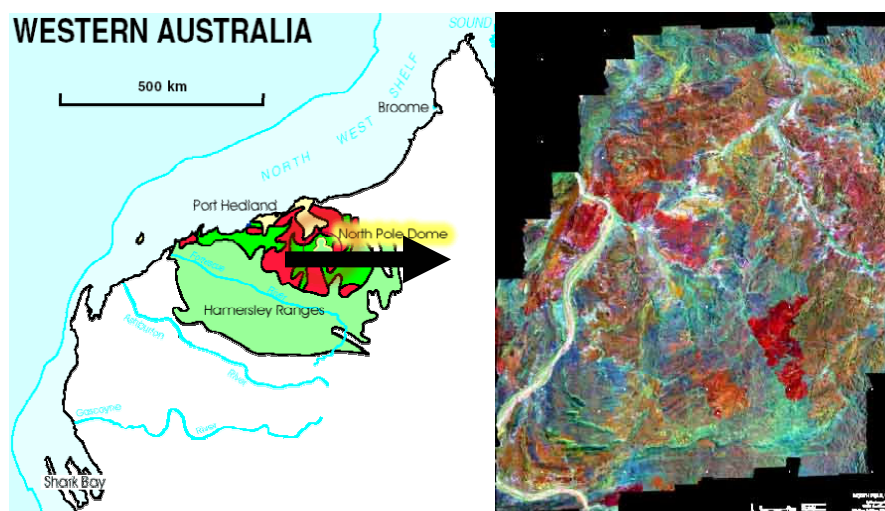
Figure 1 – Location map for the North Pole Dome and overall dataset. Central latitude and longitude of the dataset are 119°E 21°S. Dataset is approximately 27 km wide and north is up.

Table 1 – Stratigraphic column of Warrawoona Group units present at the North Pole Dome (Van Kranendonk, 2000). Dates are derived from U-Pb isotopes from zircons in the units and are accurate to approximately 3 million years; from Thorpe et al. (1992).

Age (Ga)	Unit	Fossil Assemblages
	Euro Basalt	
3.458	Strelley Pool Chert	Well-preserved conical stromatolites (Hofmann *et al.*, 1999)
	Panorama Formation	
	Apex Basalt	Microfossils within Apex Chert (Schopf, 1993)
3.470	Duffer Formation	
	Dresser Formation	Domical stromatolites and microfossils (Walter et al. 1980; Awramik et al. 1983)
	Mt. Ada Basalt	
3.515	Coonterunah Group	

2.1   Hydrothermal Alteration

Submerged hydrothermal vents have been posited as a possible setting for the genesis of life (Nisbet and Sleep, 2001). In the search for signs of life in early Archean terrains, such as the Pilbara, hydrothermally altered zones are an attractive location to commence looking. In addition to the ability of hydrothermal activity to sustain life, it also has the capability of preserving life signs (Walter and Des Marais, 1993). These principles would be as true for life on Mars as they are for life here on the early Earth.

2.1.1   Dresser Formation

There are two primary hydrothermal events in evidence at the North Pole Dome. The first event, terminating at the Dresser Formation, is characterized by subvertical black cherts leading up to a palaeo-surface, now replaced by chert, at the top of the Dresser Formation. The black cherts were first proposed as sedimentary features (Dunlop and Buick, 1981) but have now been interpreted as hydrothermal conduits (Nijman *et al.*, 2001), and carbon isotope geochemistry has led some researchers to propose them as an early niche for life (Ueno *et al.*, 2004). Barite accompanies the black chert throughout the unit, and has been proposed as a syn-depositional

exhalite product of the hydrothermal system (Van Kranendonk and Pirajno, in press). Domical stromatolites have been found at the extremities of Dresser Formation. This has led to some researchers suggesting the Dresser Formation was an early habitat of life (Groves *et al.*, 1981).

The style of alteration at the Dresser Formation is quite distinct from that found at a later horizon within the NPD, at the Strelley Pool Chert (SPC) level.

2.1.2   Strelley Pool Chert

The 3.2 Ga Strelley Pool Chert is a stromatolitic marker chert unit found in several regions throughout the Eastern Pilbara (Lowe, 1983). It outcrops distinctively at the outer extremities of the NPD, on top of the felsic Panorama Formation. It consists of carbonate and silicified stromatolites, black and white injection cherts and a succession of silicified clastic horizons. It is overlain by the pillow basalts of the Euro Basalt unit.

The presence of stromatolites (Hofmann *et al.*, 1999) and black and white injection cherts has lead some to propose a hydrothermal-based biosphere in the Early Archaean. This has been disputed (Lindsay *et al.*, 2003) but is an intriguing possibility. The underlying Panorama Formation is in places altered pervasively to pyrophyllite, and several sericite-rich veins lead up to the SPC level, cutting vertically through the underlying Apex and Panorama Formations. These will be discussed further below.

3   Methods

A VNIR-SWIR hyperspectral dataset covering 600 sq. km of the NPD region was collected on 22 October 2002. The dataset was collected with the HyMap instrument (Cocks *et al.*, 1998), which is analogous to the AVIRIS instrument. The Pilbara coverage was collected as 14 swathes, each 2 km wide. The instrument was flown at approximately 2.5 km, or 8200 ft above mean sea level (AMSL). Spectral coverage was between 450–2500 nanometers in 126 contiguous bands. The date of the collection was timed to coincide with the end of the local dry season, in order to minimize vegetation coverage. The spatial resolution of the dataset is approximately 5 m per pixel along track.

Mineral maps were produced using the continuum-removed SWIR region by applying the "spectral feature fitting" method in the ENVI software (www.rsi.com). Representative spectra were identified using a combination of spectral library comparison and ground testing through fieldwork. Hand samples were collected with the assistance of a PDA and GPS unit and were analysed using PIMA (portable infrared mineral analyzer: hand-held spectrometer), petrographic thin section, X-ray diffraction (XRD) and X-ray fluorescence (XRF).

4   Results

The dataset was delivered as radiance at sensor and was subsequently processed using the CSIRO-developed 'Hycorr' program, which is based upon the ATREM (ATmosphere REMoval) program, to give approximate surface reflectance. In addition, using the software program ENVI, the dataset was treated by a 'continuum removal' algorithm (Clark *et al.*, 1987). This enhanced the features in the 2.0-2.4 micron SWIR region, which are of most interest when detecting hydrothermally altered minerals.

Figure 2 displays representative continuum-removed spectra of five different hyodrothermal alteration minerals extracted from the HyMap dataset. Note the spectra appear similar in regions of the spectrum up to 2.0 microns. In the SWIR region, significant differences exist that enable them to be differentiated from each other.
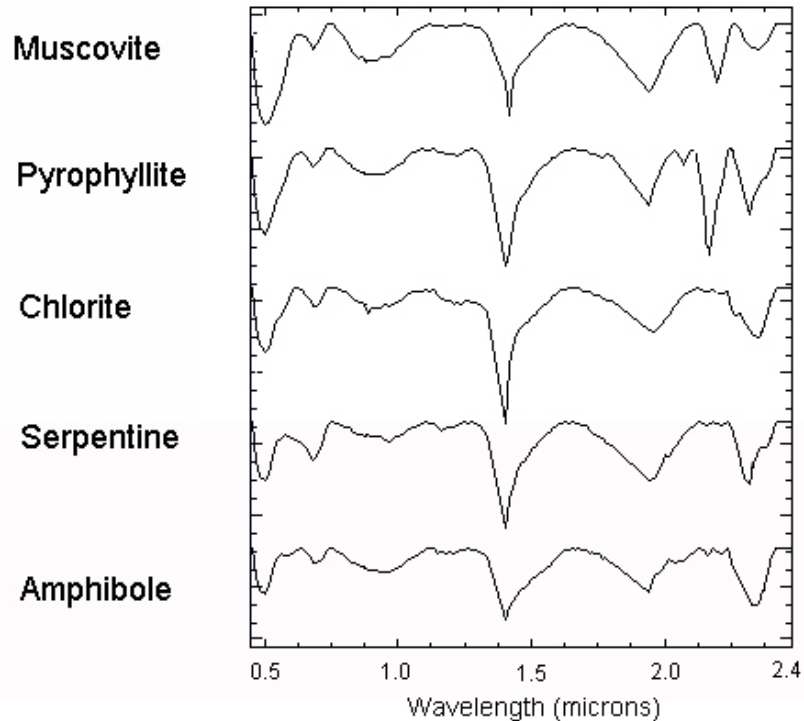
Figure 2 – Continuum-removed spectra of representative hydrothermal minerals extracted from the North Pole dataset. Each mineral is offset for clarity. Note differences between minerals are apparent in the 2.0–2.4 micron region.

Contrasting mineral assemblages were found at the Dresser Formation and Strelley Pool Chert levels; representative mineral maps are shown in Figures 3 and 4 below.

4.1   Dresser Formation

At the Dresser Formation level, it was possibly to discern an intense zone of sericitic alteration capped by a thin serpentinitic alteration layer, overlain by an intense chlorite layer. The region is also cut by several late quartz porphyry veins unrelated to alteration at this level. These are rich in sericite and are seen to cut through all horizons. From field mapping, it was determined that the intense sericitization was most likely due to pervasive and intense weathering of country rock basalts most likely affected through hydrothermal veins, now present as prominent black chert veins that cut through and terminate at a cap chert below the serpentine-rich horizon. The serpentine-rich layer was determined to be an ultramafic peridotite, most probably representing the basal layer of a komatiite succession (Brown *et al.*, 2004a). The overlying chlorite layer most probably represents seafloor alteration of the constituent basalts.

In addition to mapping the alteration minerals, black chert units that have been posited as feeder conduits for the Dresser Formation hydrothermal activity (Nijman *et al.*, 1998) can be

seen clearly in the visible region of the spectrum, often due to thin Fe-rich veneers that preferentially coat the chert. These are visible as east-west trending lineaments in Figure 3.

The hydrothermal activity that produced the sericite alteration most probably occurred in a low-pH environment. The presence of large barite deposits within and surrounding the vein testifies to an oxidizing fluid, if one is to accept that the Archean environment was generally reducing (Ohmoto, 1997; Holland, 1999). These locally oxidizing conditions may have been created by a primitive biosphere living in the hydrothermal vents.
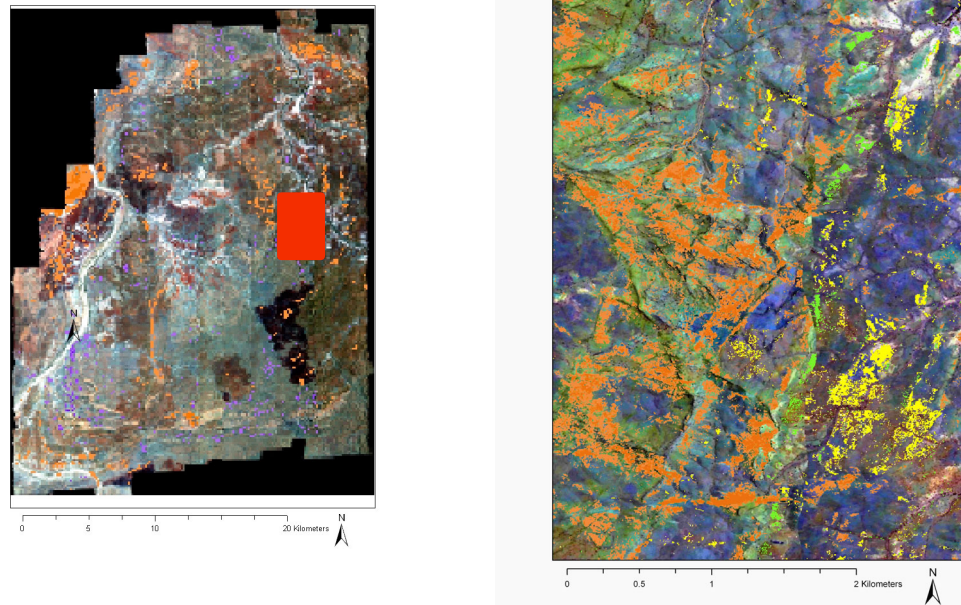
Figure 3 – Mineral map for the Dresser Formation region with context map on left showing coverage. Sericite is orange, serpentine light green (vertical strip in middle) and chlorite is yellow. East-west trending lineaments are massive black cherts, interpreted as feeder dykes for hydrothermal sites at the Dresser level (see text).

4.2   Strelley Pool Chert Mineral Assemblages

At the Strelley Pool Chert level, horizontal mineral assemblages of carbonate-chlorite are overlain by a thin but prominent sericite-pyrophyllite layer (at the Panorama felsic volcanic level), which is in turn overlain by a chlorite-rich layer. Sericite-rich veins grade into pyrophyllite and then terminate at the Strelley Pool Chert layer. Some layers within the Strelley Pool Chert display sericite signatures (Brown *et al.*, 2004b); however, there is no pyrophyllite within the Strelley Pool Chert.

It is hypothesized that this alteration style betrays the actions of an acid-sulfate hydrothermal system as described by previous researchers (White and Hedenquist, 1990). The presence of a thin continuous layer of pyrophyllite beneath a chert horizon and associated with sericite veins leading up to this horizon shows similarities with acid-sulfate Porphyry Cu argillic alteration, as portrayed in Figure 4 below (Bonham Jr. and Giles, 1983).
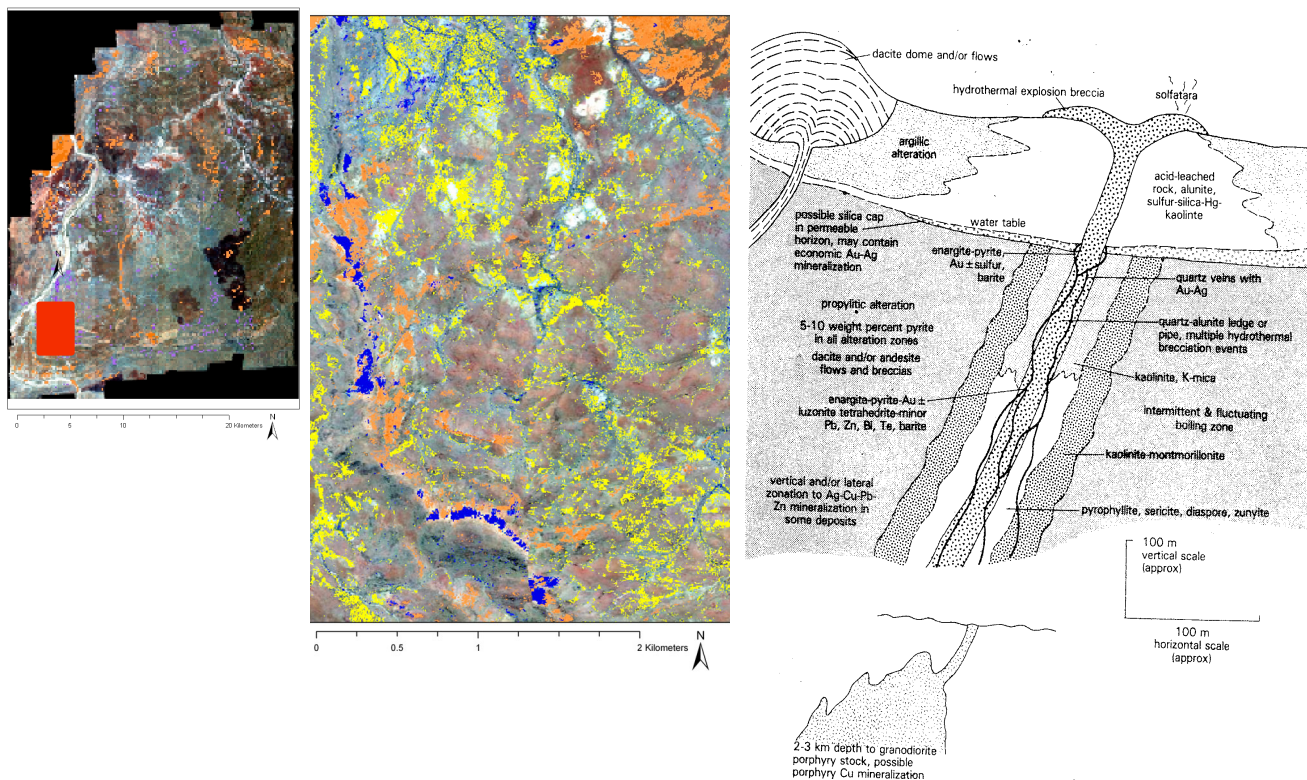
Figure 4 – Hydrothermal alteration at the Strelley Pool Chert level. Image on left shows coverage of central image. In central image, orange represents sericite, yellow chlorite and blue pyrophyllite. Image on right (from Bonham Jr. and Giles, 1983) shows typical mineral assemblages of an acid-sulfate epithermal vein.

5 Conclusion

This study into hydrothermal alteration amongst some of the best-preserved, oldest rocks preserved on this planet is continuing. Latest results are being published at the project website - http://aca.mq.edu.au/abrown.htm. Hyperspectral mapping has already demonstrated the ability to detect mineral assemblages that give vital clues to interpretation of the conditions within these hydrothermal systems.

In 2005, NASA will launch the hyperspectral VNIR-SWIR Compact Reconnaissance Infrared Spectrometer for Mars (CRISM) onboard the Mars Reconnaissance Orbiter (MRO). The instrument will have a spatial resolution of approximately 16 m in high-resolution mode (Murchie *et al.*, 2003). This will allow researchers to investigate signs of hydrothermal alteration using the critical SWIR region at scales approaching that expected for individual veins of an epithermal deposit. Application of the lessons learned from mapping volcanic terrains such as the Warrawoona Group in Western Australia will be of vital importance in informing the search for possible past or present habitats of life on Mars.

6 Acknowledgements

7 References

Awramik, S. M., Schopf, J. W., and Walter, M. R. (1983) Filamentous fossil bacteria from the Archean of Western Australia. *Precambrian Research*, 20, 357–374.

Bonham Jr., H. F. and Giles, D. L. (1983) Epithermal gold/silver deposits - the geothermal connection, pp. 384, Geothermal Resources Council.

Brown, A. J., Walter, M. R. and Cudahy, T. J. (2004a) Hypserspectral and field mapping of an Archaean Komatiite Unit in the Pilbara Craton, Western Australia: Applications for CRISM Mission, in *Lunar and Planetary Science Conference XXXV*, LPI, Houston, Texas.

Brown, A. J., Walter, M. R. and Cudahy, T. J. (2004b) Remote Mapping of Earth's Earliest Biosphere: Hyperspectral Imagery of the Pilbara Craton and applications for finding niches for life on Mars, in *International Journal of Astrobiology*, pp. 16–17, Special Supplement 1 - Abstracts from the Astrobiology Science Conference 2004, NASA Ames Research Laboratory, Mountain View, California.

Clark, R. N., King, T. V. V. and Gorelick, N. (1987) Automatic Continuum Analysis of Reflectance Spectra, in *Proceedings of the Third Airborne Imaging Spectrometer Data Analysis Workshop*, pp. 138–142, JPL Publication 87-30, Pasadena, California.

Cocks, T., Jenssen, R., Stewart, A., Wilson, I. and Shields, T. (1998) The HyMap Airborne Hyperspectral Sensor: The System, Calibration and Performance. *1st EARSeL Conference*, 37–42.

Dunlop, J. S. R. and Buick, R., (1981) Archaean epiclastic sediments derived from mafic volcanics, North Pole, Pilbara Block, Western Australia, in *Special Publication of the Geological Society of Australia*, edited by D. I. Groves and J. E. Glover, pp. 225–233, Geological Society of Australia, Perth, Western Australia.

Groves, D. I., Dunlop, J. S. R. and Buick, R. (1981) An early habitat of life. *Scientific American*, 245 (4), 56–65.

Hofmann, H. J., Grey, K., Hickman, A. H. and Thorpe, R. I. (1999) Origin of 3.45 Ga coniform stromatolites in Warrawoona Group, Western Australia. *GSA Bulletin*, 111 (8), 1256–1262.

Holland, H. D. (1999) When did the Earth's atmosphere become oxic? A Reply. *The Geochemical News*, 100, 20–22.

Lindsay, J. F., Brasier, M. D., McLoughlin, N., Green, O. R., Fogel, M., McNamara, K. M., Steele, A. and Mertzman, S. A. (2003) Abiotic Earth - Establishing a baseline for Earliest Life, Data from the Archean of Western Australia, in *Lunar and Planetary Science Conference XXXIV*, pp. 1137, LPI, Houston, Texas.

Lowe, D. R. (1983) Restricted shallow-water sedimentation of early Archean stromatolitic and evaporitic strata of the Strelley Pool Chert, Pilbara Block, Western Australia. *Precambrian Research*, 19 (3), 239–283.

Murchie, S., Arvidson, R., Beisser, K., Bibring, J.-P., Bishop, J., Boldt, J., Bussey, B., Choo, T., Clancy, R. T., Darlington, E. H., Des Marais, D., Fasold, M., Fort, D. E., Green, R. O., Guinness, E. A., Hayes, J., Heyler, G., Humm, D., Lee, R., Lees, J., Lohr, D., Malaret, E., Morris, R. L., Mustard, J., Rhodes, E., Robinson, M., Roush, T., Schaefer, E., Seagrave, G., Silverglate, P., Smith, M. D., Strohbehn, K., Thompson, P. and Tossman, B. (2003) CRISM: Compact Reconnaissance Imaging Spectrometer for Mars on the Mars Reconnaissance Orbiter, in *Sixth International Conference on Mars*, pp. 3062, LPI, Houston, Texas.

Nijman, W., de Bruijne, K. H. and Valkering, M. E. (1998) Growth fault control of Early Archaean cherts, barite mounds and chert-barite veins, North Pole Dome, Eastern Pilbara, Western Australia. *Precambrian Research*, 88 (1-4), 25–52.

Nijman, W., de Vries, S. T. and Houtzager, O. (2001) Earth's Earliest Sedimentary Basins: the Lower Archaen of the Pilbara and Kaapvaal compared, in *4th International Archaean Symposium*, edited by K. F. Cassidy; J. M. Dunphy and M. J. Van Kranendonk, pp. 520–522, AGSO, Perth, Western Australia.

Nisbet, E. G. and Sleep, N. H. (2001) The habitat and nature of early life. *Nature*, 409 (6823), 1083–1091.

Ohmoto, H. (1997) When did the Earth's atmosphere become oxic? *The Geochemical News*, 93, 12–27.

Schopf, J. W. (1993) Microfossils of the Early Archean Apex Chart: New Evidence of the Antiquity of Life. *Science*, 260, 640.

Thorpe, R. I., Hickman, A. H., Daris, D. W., Mortensen, J. K., and Trendall, A. F. (1992) U-Pb zircon geochronology of Archaean felsic units in the Marble Bar region, Pilbara Craton, Western Australia. *Precambrian Research*, 56, 169–189.

Ueno, Y., Yoshioka, H., Maruyama, S. and Isozaki, Y. (2004) Carbon isotopes and petrography of kerogens in ~3.5-Ga hydrothermal silica dikes in the North Pole area, Western Australia1. *Geochimica et Cosmochimica Acta*, 68 (3), 573–589.

Van Kranendonk, M. J. (2000) Geology of the North Shaw 1:100 000 Sheet, Geological Survey of Western Australia, Department of Minerals and Energy, Perth, Western Australia.

Van Kranendonk, M. J. and Pirajno, F. (in press) Geochemistry of metabasalts and hydrothermal alteration zones associated with ca. 3.45 Ga chert+/- barite deposits: implications for the geological setting of the Warrawoona Group, Pilbara Craton, Australia. *Geochemistry: Exploration, environment and analysis*.

Walter, M. R., Buick, R., and Dunlop, J. S. R. (1980) Stromatolites 3400–3500 Myr old from the North Pole area, Western Australia. *Nature*, 284, 443–445.

Walter, M. R. and Des Marais, D. J. (1993) Preservation of Biological Information in Thermal-Spring Deposits - Developing a Strategy for the Search for Fossil Life on Mars. *Icarus*, 101 (1), 129–143.

White, N. C. and Hedenquist, J. W. (1990) Epithermal environments and styles of mineralization: variations and their causes, and guideline for exploration. *Journal of Geochemical Exploration*, 36, 445–474.

Integrating Visible, Near-Infrared, and Short-Wave Infrared Hyperspectral and Multispectral Thermal Imagery for Geologic Mapping: Simulated Data

Xianfeng Chen, Timothy A. Warner, and David J. Campagna

Department of Geology and Geography
West Virginia University
Morgantown, West Virginia 26506-6300

1.   Introduction

Recent developments in VNIR/SWIR[1] hyperspectral and TIR multispectral remote sensing have greatly increased the potential for accurate geological mapping. Hyperspectral instruments, often referred as imaging spectrometers, acquire image data simultaneously in many narrow, contiguous channels (Goetz et al., 1985), generally spanning the reflected solar portion of the electromagnetic spectrum (0.4–2.5 µm) (Vane et al., 1993). The spectral bandwidths of hyperspectral image bands are generally less than 25 nm, in order to facilitate the identification of diagnostic absorption features of minerals (Clark, 1999). Hyperspectral data have a significant advantage over conventional multispectral data, such as Landsat Thematic Mapper imagery, in that with hyperspectral data, minerals can be identified by comparisons with generic library spectra (Clark et al., 2003). With hyperspectral data, it is therefore theoretically possible to map the surface mineralogy of an area without acquiring any ground data from the particular site.

In contrast to the many bands of hyperspectral instruments, TIR multispectral sensors measure surface radiance in a small number of broad bands. TIR imagery provides important information regarding temperature, thermal inertia, and emissivity of ground materials (Price, 1979; Kahle, 1987; Warner and Chen, 2001). Surface emissivity is potentially the most useful thermal property because it is an inherent characteristic of an object and is independent of illumination intensity and local temperature. Emissivity is defined as the ratio of the emitted radiation to that of a blackbody at the same temperature (Hook et al., 1992). Emissivity can be used to identify individual minerals and has been related to silica content of rocks (Lyon, 1972), thus offering the possibility of discriminating the silicate materials that make up much of the land surface.

Minerals tend to have characteristic spectral reflectance and associated emissivity features, which may potentially be used for remote identification (Clark, 1999; Hook et al., 1994). The characteristic spectral features are produced by the interaction of electromagnetic energy with the atoms and molecules of the minerals, which cause electronic transitions and vibrational processes. Electronic transitions tend to dominate mineral spectra in the visible and NIR, but are also found across the SWIR region (Clark, 1999; Goetz, 1989). Vibrational processes, dominating in SWIR and TIR region, produce particularly diagnostic absorption features in the spectra of silicate, hydroxyl, oxide, carbonate and water-bearing minerals (Vincent and Thomson, 1971; Hunt and Salisbury, 1974; Hunt, 1980; Hook et al., 1994; Clark, 1999).

---

[1] An unfortunate inconsistency has developed in the terms used by the remote sensing community for regions of the electromagnetic spectrum (Clark, 1999). In this study, the wavelength regions are defined as follows: **visible**: 0.4–0.7 µm, **near-infrared (NIR)**: 0.7–1.1 µm, **visible and near-infrared (VNIR)**: 0.4–1.1 µm, **short-wavelength infrared (SWIR)**: 1.1–2.5 µm, **mid-infrared** (**MIR**): 3–5 µm, and **thermal infrared (TIR)**: 8–14 µm (Goetz, 1989; Hook *et al.*, 2001).

The distinctive spectral features of silicates, as well as other important spectral features of most non-silicate minerals, including the carbonates, sulfates, phosphates, oxides, and hydroxide mineral groups, demonstrate the tremendous potential of the TIR region for geological mapping. Combining information from TIR spectral emissivity with measurement of spectral reflectance in the 0.4–2.5 μm region, which is particularly good for discriminating clays, iron oxides, and iron hydroxides (Clark, 1999), should provide a more comprehensive overview of rock compositional information than using data from only one of the two regions (Rowan, 1998).

In summary, the combination of VNIR/SWIR hyperspectral data and TIR multispectral data appears to have great promise for geological studies because of the complementary nature of information from the thermal and shorter wavelengths (Hook et al., 1999). Typically, iron oxide, hydroxyl, and carbonate minerals have absorption features in the visible or SWIR region, while the Si-O bonding of silicate minerals exhibit absorption features in TIR region. Nevertheless, combining VNIR/SWIR and TIR data has received very little prior attention, with the exception of Abrams and Hook (1991), who separately analyzed VNIR/SWIR hyperspectral and TIR multispectral data for lithological analysis at Cuprite, Nevada.

That no previous research has simultaneously analyzed VNIR/SWIR hyperspectral and TIR multispectral data is probably due to the fact that data from these spectral regions are rarely acquired simultaneously, and that coregistration of aerial imagery from different sources can be very challenging. However, modern aircraft-acquired data often include navigation information that can be used to remove non-systematic spatial distortions. Furthermore, in the future, with the increased availability of satellite data, which tends to have simpler geometry than aerial imagery, coregistration of different image products may become more routine. In fact, space-borne hyperspectral data is already being collected by the Hyperion instrument, and space-borne multispectral TIR data by the Advanced Spaceborne Thermal Emission and Reflection Radiometer (ASTER). Integrating imagery from different sensors may not even be necessary in the future; for example there are plans to fly an airborne hyperspectral sensor in 2005, Airborne Reflective Emissive Spectrometer (ARES), which has 160 image bands in the visible, NIR, SWIR, and TIR wavelength regions (Mueller *et al*., 2003).

This study investigated the potential value of integration of VNIR/SWIR hyperspectral analysis with TIR multispectral analysis, with the anticipation that such an approach should provide improved geological mapping. To test this hypothesis, simulated data were used to test the improvement in classification accuracy when the combination of VNIR/SWIR hyperspectral and TIR multispectral data is used, compared to an analysis that uses only the VNIR/SWIR or TIR regions on their own. In addition, the simulated data were used to evaluate the performance of automatic information extraction algorithms, including the conventional classification algorithms of minimum distance and maximum likelihood classification (Richards, 1993), as well as the hyperspectral analysis techniques of spectral angle mapper (Kruse et al., 1993a), binary encoding (Goetz et al., 1985), and spectral feature fitting (Crowley et al., 1989; Clark et al., 1990).

Simulated data have been demonstrated to be useful in developing general theories about how information is represented in images and spectra (Strahler et al., 1986). For example, simulated data have been used in many studies of image spatial properties (e.g., Woodcock et al., 1988, Jupp et al., 1989, Collins and Woodcock, 1999, Warner, 1999, Ferro and Warner, 2002), and spectral properties (e.g., Verhoef, 1984, Li et al., 1999, Pandya et al., 2000).

Simulated data were chosen for this study because with simulated data it is possible to evaluate accuracy with complete confidence in the reference data set. In contrast, ground checking of minerals for real hyperspectral analyses is challenging, especially when the minerals are fine grained. Although minerals can be identified through laboratory techniques, it is hard to generalize from small laboratory samples to 20 meter pixels, and especially difficult to estimate the proportions of minerals present in fine mixtures. Additional uncertainty is added by varying desert varnish, vegetation, weathering, and deposition of transported material in each pixel. Thus, in summary, it is close to impossible to produce a "truth map" for geological hyperspectral remote sensing; and indeed, we know of no previous quantitative assessment of accuracy of geological hyperspectral remote sensing classification.

A second reason for using simulated data is that this approach allows us to vary image properties in a controlled fashion, and thus potentially develop an understanding of the reasons behind the results we observe. We are also able to study what aspects of the scene model most affect the different methods, a key to developing improvements to the different methods. For example, if illumination variation were found to be a major source of error, then we would infer that illumination normalization methods should be researched further.

The third reason for using simulated data is that simulation provides a simplified, but reasonable, representation of real data as long as the major processes that result in a real image are included in the analysis. Simulated data are typically much simpler than reality. This does not necessarily negate the value of simulated data; indeed, the simplification can be an advantage, as discussed above.

In a future paper, the classification methods tested in this paper, as well as a specially developed expert system, will be applied to real data, comprising AVIRIS (Airborne Visible/Infrared Imaging Spectrometer) and MASTER (MODIS/ASTER Airborne Simulator) imagery of Cuprite, Nevada.

2. Methods

2.1   Classification algorithms

Image classification methods can be divided into two groups: **empirical classification algorithms** that use summary class statistics based on groups of image pixels, and **spectral analysis techniques** that match image spectra to previously acquired field or laboratory spectra, known as spectral libraries. With hyperspectral data, empirical classification approaches that rely on statistical measures tend to require excessive numbers of training samples for training the classifier (Landgrebe, 2000). The spectral library approach is attractive for hyperspectral image analysis because rocks and minerals tend to have distinctive and consistent spectral absorption features, as discussed above. Furthermore, the potential to identify surface materials without any local field data is clearly very attractive.

The two most common empirical classification methods used for geological mapping are minimum distance and maximum likelihood classification. Numerous additional spectral analysis methods have been developed for geological mapping (Mustard and Sunshine, 1999), including binary encoding, spectral feature fitting, and the spectral angle mapper. These three spectral analysis methods will be described briefly below.

Binary encoding (Goetz et al., 1985) is a fast spectral matching algorithm that compares summary measures of the spectral shapes of an unknown pixel and the reference spectra. The unknown pixel spectrum of n bands is represented by an n bit vector, with each bit set to 1 or 0 respectively, depending on whether the value of the spectrum for that band is above or equal to, or below the pixel mean.

Spectral feature fitting (SFF) (Crowley et al., 1989; Clark et al., 1990) is based on a comparison of the absorption features in the image and reference spectra. The continuum, defined as a convex hull fit over the top of each spectrum utilizing straight line-segments to connect local spectrum maxima (Clark et al., 2003; Kruse et al., 1993b), is removed by dividing the convex hull into the original spectrum. The continuum-removed pixel spectrum and reference spectra are compared at each absorption band using a least-square fit. The root mean square error indicates the relative goodness-of-fit of the two spectra.

Spectral angle mapper (SAM) (Kruse et al., 1993a) builds on the hyperspherical direction cosine method (Pouch and Campagna, 1990) by calculating the similarity between pixel spectra and reference spectra in terms of the angle between two n-dimensional vectors, where n is the number of bands of hyperspectral data.

2.2   Simulated data

The creation of the simulated data was carried out using the Interactive Data Language (IDL) (Research Systems, 2000). The spectra of 16 common minerals, rock types, and alteration types (Table 1) were chosen for this study because they represent the dominant lithological units and alteration types

typical of hydrothermal alteration areas such as Cuprite, Nevada (Abrams and Ashley, 1980). The library spectra were resampled to match the approximate spectral bandwidth and signal-to-noise of the AVIRIS and MASTER instruments. A brief introduction to the AVIRIS and MASTER instruments is given below (see also Table 2), followed by a more detailed discussion of the simulated data characteristics.

Table 1. Minerals, rock types, and alteration types used to create the simulated data

Type	Name
Minerals	Quartz, calcite, hematite, goethite, alunite, kaolinite, montmorillonite, muscovite, gypsum.
Unaltered rocks	Basalt, limestone, sandstone, siltstone
Altered rocks	Silicified rocks, opalized rocks, and argillized rocks.

The MASTER sensor was developed to support research prior to the launch of the Advanced Spaceborne Thermal Emission and Reflection Radiometer (ASTER) and the Moderate Resolution Imaging Spectroradiometer (MODIS) (Hook et al., 2001). MASTER has a total of 50 bands from 0.4–13 µm, including 10 TIR bands. In this study, simulated multispectral thermal data are based only on the 10 MASTER TIR bands (7.6–13 µm). AVIRIS, flown by NASA since 1987 (Green et al., 1998), acquires data in 224 narrow, contiguous spectral bands across the reflected solar energy region (0.4–2.5 µm), each band approximately 10 nm at full width, half maximum (FWHM).

Table 2. Summary characteristics of the MASTER and AVIRIS instruments

Characteristic	Sensor	
	MASTER	AVIRIS
Wavelength range	0.4–13 µm	0.4–2.5 µm
Number of spectral bands	50	224
Channel width	Varies, 40 to 650 nm	10 nm
Instantaneous field of view	2.5 mrad	1 mrad
Total field of view	85.92º	33º
Number of pixels	716	614
Platform	B200, ER-2, DC-8	ER-2, Twin Otter
Digitization	16-bit	12-bit

The simulated data were derived from the public domain spectral library included with ENVI (Research Systems, 2002): the Johns Hopkins University library of spectra of materials from 0.4 to 14 µm (Salisbury et al., 1991; Research Systems, 2002). Emissivities of minerals or rocks are calculated from Kirchoff's law, which states that spectral emissivity equals 1 minus the spectral reflectance.

To simplify the simulated data construction, the contribution of the atmosphere was not modeled directly. Nevertheless, the effects of the atmosphere were included indirectly, because noise was added on a band-by-band basis, equivalent to that found in typical AVIRIS and MASTER scenes that include atmospheric effects. In addition, the simulated AVIRIS bands in the atmospheric water absorption regions near 1.4, 1.9, and 2.5 µm were deleted, leaving a total of 188 out of the 224 bands for the analysis. Multiplying the spectral radiances with the inverse of the spectral signal-to-noise ratios for

AVIRIS and MASTER simulated the noise of the sensor system. The signal-to-noise ratio of AVIRIS was taken from Green et al. (1998), who measured in the laboratory the average and standard deviation of 3000 dark signal spectra, and 3000 illuminated radiometric calibration target spectra. The signal-to-noise ratio of MASTER was estimated using the ratio of the mean and standard deviation of a 7 by 7 moving window of MASTER imagery of Lake Mead, Nevada. An additional 0.015 variation in emissivity (Gillespie et al., 1998) was added to simulate the uncertainty due to the indeterminacy of the emissivity calculation from radiance data.

The library spectra were also combined in various proportions to simulate real pixels, which generally comprise mixed proportions of different surface materials:

$$L_\lambda = \sum_{i=1}^{n} (a_i R_{\lambda i}) + \varepsilon_\lambda \qquad (1)$$

Where

L_λ =   reflectance or emissivity at wavelength λ corresponding to a specific AVIRIS or MASTER band;

a_i =   the proportion of the endmember i in the pixel;

$R_{\lambda i}$ =   the reflectance or emissivity of endmember i at wavelength λ;

ε_λ =   the error term resulting from all sources of noise at wavelength λ.

Seven groups of simulated data with different levels of uncertainties were derived using equation 1 (Table 3). Each group includes three data sets designed to simulate AVIRIS data (188 bands between 0.4–2.5 µm, after the exclusion of the water absorption bands), MASTER thermal data (10 bands between 7.6–13 µm), and the combination of AVIRIS and MASTER multispectral thermal infrared data (a total of 198 bands between 0.4–2.5 µm and 7.6–13 µm). The simulated uncertainties include sensor system noise, mixing of vegetation and the other endmembers, and variation in solar illumination. Solar illumination uncertainty was applied only to the simulated AVIRIS data, assuming that topographic effects in thermal data are mostly suppressed when the emissivity is calculated. Solar illumination effects were simulated by varying the total radiance by 0 to 25 percent. The first group of data is a theoretical

Table 3. Simulated data with different levels of uncertainties*

| Group | Simulated Noise | | | |
| | System | Solar Illumination | Mixed pixels (proportion of cover type) | |
			Vegetation	Additional mineral/rock
1	X			
2	X	X		
3	X		0–5%	
4	X		0–5%	0–10%
5	X	X	0–5%	0–10%
6	X	X	0–5%	0–20%
7	X	X	0–10%	0–30%

*Empty boxes indicate uncertainties not included in the simulated data.

near-perfect data set, containing only reflectance or emissivity information and system noise of sensor instruments. The uncertainties of the second group include the system noise and solar illumination effects; in the third group, a random percentage of vegetation, up to 5 percent, is added; the fourth group has a random proportion, up to 5 percent, vegetation, and up to10 percent of another mineral or rock endmember, randomly selected from the 16 library spectra; the fifth group is similar to the fourth, except it also includes variations in solar illumination; the sixth group has up to 5 percent vegetation and up to 20 percent of another mineral or rock endmember, and the illumination effects; the seventh group has up to 10 percent vegetation, up to 30 percent another endmember, and illumination effects.

2.3   Analysis

All classification and spectral analysis methods were carried out with ENVI image analysis software (Research System, 2002). Binary encoding, SAM, and SFF were applied using endmember spectra derived from training data and also by comparing the image data directly with the spectral libraries. SFF is normally used with data of more limited spectral regions, and therefore SFF was also tested using the simulated AVIRIS bands from just the SWIR region (1.96–2.44 µm). Considering that SFF's focus on spectral absorption features makes the method inappropriate for use with minerals and rocks with spectrally flat curves, additional comparisons were made using only the nine minerals which exhibit absorption features in VNIR, SWIR, and TIR: alunite, calcite, goethite, hematite, kaolinite, montmorillonite, muscovite, quartz, and gypsum.

Data sets 5, 6 and 7 have comparatively high levels of uncertainty, and were found to produce notably low accuracies, especially for minimum distance and SAM classification. Therefore, additional preprocessing was carried out to evaluate whether the effect of the uncertainty could be reduced for these methods using the minimum noise fraction (MNF) transformation (Green et al., 1988). MNF was used to generate 13 MNF bands for each data set. MNF consists of two cascaded principal component transformations, and is usually used to suppress noise and reduce the number of bands prior to classification. The first transformation decorrelates and rescales the noise in the data, assuming the noise has unit variance and no band-to-band correlation. The second step is a standard principal component transformation applied on the noise-free data. The final transformed data includes two parts: one part associated with large eigenvalues representing most of the variance, and a second part with near-unity eigenvalues representing the noise-dominated data (Green et al., 1988).

Overall accuracies were calculated, and used to evaluate the degree to which the combined data aids discrimination by contributing to increased separability of the entire group of spectral classes. ENVI's confusion matrix procedure (Research Systems, 2002) was applied to all classified images to evaluate the performance of the classifications. The same approximately 10,000 pixels used for training the classifiers were used for classification assessment. In conventional accuracy assessment, different training and testing pixels are normally used. However, in this case, with a large random sample, there would be little difference in the results if a new data set was used for testing.

3.   Results

3.1.   Evaluation of combining VNIR, SWIR, and TIR spectral regions

The overall accuracies of classifications (Figure 1) were found to vary with the mapping methods and the data sets. With the exception of maximum likelihood, SFF, and all methods using the first uncertainty level data set, most methods applied to simulated MASTER data have higher accuracies than when applied to combined data sets (Figure 1, upper right). Although the simulated MASTER data has few bands, these bands have a higher signal-to-noise ratio than the simulated AVIRIS data due to MASTER's broad bands and the lack of variation in illumination in the simulated TIR data.

Figure 1 nevertheless provides evidence to support the hypothesis that the combination of AVIRIS and MASTER aids discrimination of minerals and rocks. First, for maximum likelihood classification, the combined data set always has the highest overall accuracy of the three data sets. The

combined data set also produced the highest accuracy for minimum distance classification and SAM applied to MNF transformed data (Figure 2).
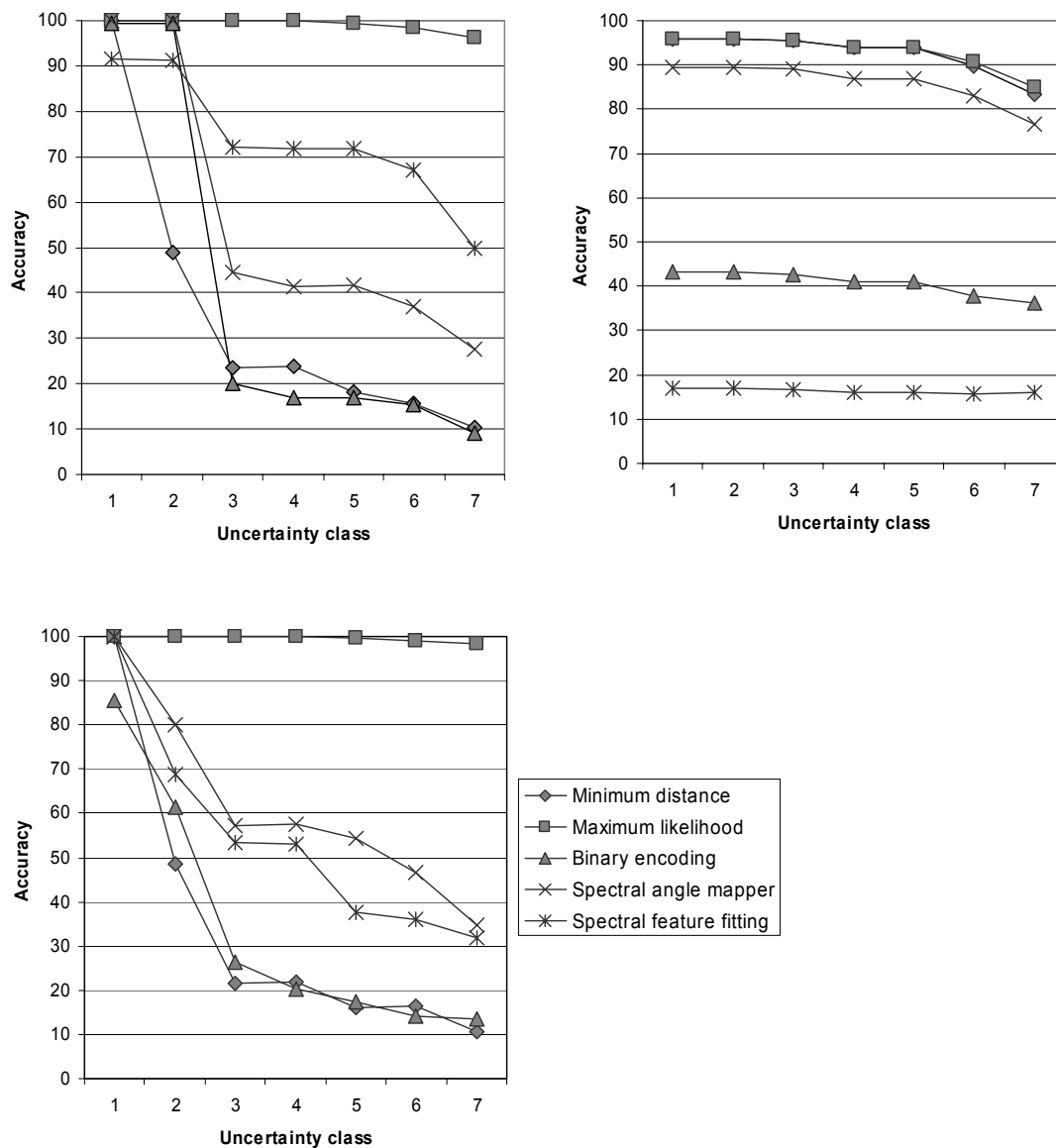

Figure 1. Comparison of the overall accuracies using five mapping methods on different noise level data sets of 16 mineral and rock classes. Upper left: AVIRIS data sets. Upper right: MASTER data set. Bottom: Combined data set.

Minimum Distance Classification

Spectral Angle Mapper

AVIRIS   MASTER   COMBINED
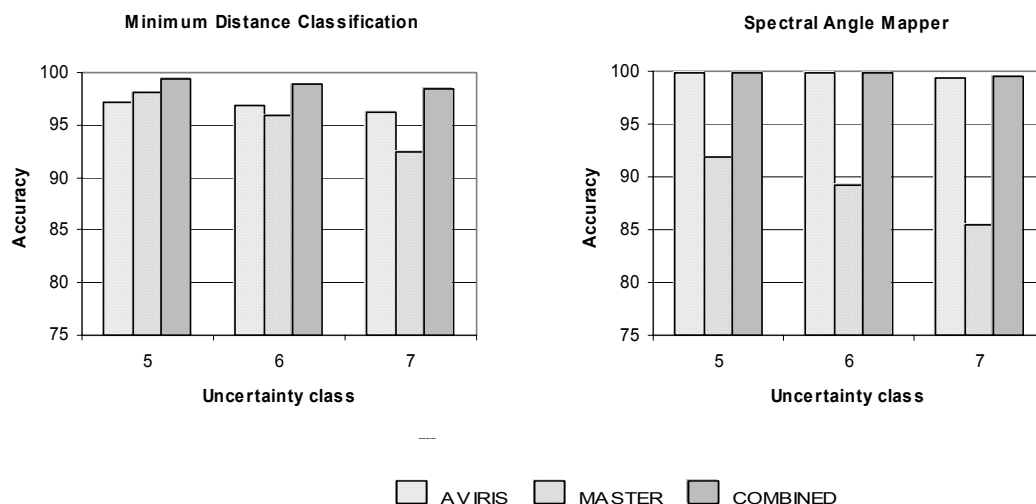
Figure 2. Overall classification accuracies of minimum distance classification and spectral angle mapping applied on MNF transformed data sets (Uncertainty levels 5, 6, and 7).

When the classifications are examined in more detail, some of the individual minerals and rocks can be seen to show large improvement in classification accuracy when the AVIRIS data set was combined with the MASTER data set (Table 4). For instance, basalt, calcite, and muscovite showed an improvement of almost 30 percent in either the producer's accuracy or the user's accuracy when SAM was applied to the combined data set. However, some minerals, such as alunite, montmorillonite, and kaolinite, showed little improvement, or even a decrease in accuracy. Most of the minerals that showed an improvement in classification accuracy with the combined data sets analyzed using SFF classification exhibit the characteristic absorption features in the thermal infrared wavelength region (Figure 3). For example, quartz and muscovite, which have deep Si-O absorption features around 9 μm, showed a marked improvement in classification accuracy using the combined data set. Likewise, goethite and hematite showed a higher classification accuracy with the combined data set because they have absorption features at 12.1 and 8.2 μm, respectively. On the other hand, basalt and kaolinite have relatively flat TIR spectra (Figure 3), so combining AVIRIS and MASTER reduced their classification accuracies. Calcite has only two relative weak absorption features in the 9 and 11 μm wavelength regions, which are diluted by mixing with other minerals or rocks. Therefore, calcite did not show any improvement in classification accuracy within the combined data set. Although alunite and gypsum are characterized by strong absorption features in the TIR, they are too close to be separated in the MASTER data, and therefore the combined data set did not enhance discrimination.

When SFF was applied to the AVIRIS SWIR bands alone (1.96–2.44 μm), the overall accuracy decreased, although some minerals with distinctive absorption features, such as kaolinite (Figure 3), showed a 55 percent improvement in user accuracy. However, some minerals with characteristic absorption features in the VNIR region, for instance, hematite and goethite (Figure 3), showed a large decrease in accuracy (e.g., 65 percent in user accuracy for hematite and 43 percent in producer accuracy for goethite). Thus, as might be expected, SFF applied to a relatively narrow wavelength region only enhances identification of the specific minerals or rocks which exhibit distinctive absorption features in that wavelength region.

Table 4. Classification accuracies of minerals and rock on data set 4 using SAM and SFF

| Mineral or rock | Accuracy: SAM | | | | Accuracy: SFF | | | |
| | AVIRIS | | COMBINED | | AVIRIS | | COMBINED | |
	Prod.*	User	Prod.	User	Prod.	User	Prod.	User
Alunite	30.43	100.00	38.14	92.00	92.38	97.17	44.91	76.67
Basalt	26.72	44.72	66.31	68.00	72.31	74.01	21.85	84.67
Calcite	19.00	52.80	43.19	80.05	79.49	99.94	74.03	96.06
Goethite	53.02	59.30	67.05	67.95	94.81	78.83	85.39	100.00
Hematite	65.90	65.46	69.85	68.98	76.75	95.96	100.00	100.00
Kaolinite	50.64	99.85	65.89	73.96	84.76	44.76	62.09	15.99
Montm.	36.06	53.95	52.69	64.26	81.39	95.58	37.63	99.61
Muscovite	26.19	11.76	61.12	21.93	43.36	62.99	44.43	100.00
Quartz	52.95	16.30	55.40	30.72	68.61	87.00	91.14	100.00
Gypsum	61.55	71.76	70.06	70.11	86.84	99.95	47.65	100.00

*Producer's accuracy of classification.

3.2.   Evaluation of classification algorithms

The major uncertainties added to the data sets include variable vegetation coverage, solar illumination effects, and mixing of the other minerals (Table 3). All the classification methods, with the exception of maximum likelihood classification applied to the simulated AVIRIS data sets, are generally very sensitive to the type and degree of uncertainty. For the near-perfect data set of the simulated AVIRIS with only instrumental system noise, all methods achieved relatively high classification accuracies, with maximum likelihood classification, binary encoding, and SAM obtaining 100 percent accuracy (Figure 1). When up to 5 percent mixing of vegetation is added to the data (Uncertainty Level 3), only maximum likelihood classification still resulted in 100 percent accuracy; the accuracies using the other methods dropped rapidly. This suggests that minimum distance classification, binary encoding, and SAM, are very sensitive to subpixel mixing. Although the overall accuracy of SFF dropped 20 percent, it obtained the second highest accuracy dealing with mixing pixels.

In terms of overall accuracy of the different methods, maximum likelihood classification is the best method for minerals and rocks classification using the simulated AVIRIS data (Figure 1, top left), followed by SFF and SAM; minimum distance classification and binary encoding have relative poor performance. Data sets 1 and 4 are similar to data sets 2 and 5, respectively, except that 2 and 5 have an additional uncertainty due to illumination effects. The accuracy for all methods applied to AVIRIS data, with the notable exception of minimum distance classification, declines only slightly from data sets 1 to 2 and from 4 to 5.

The results of the combined data sets are slightly more complex (Figure 1, bottom). In terms of overall accuracy, maximum likelihood classification almost achieved 100 percent accuracy for all uncertainty level data sets, and SAM resulted in the second highest accuracy. The accuracy of SFF method dropped to the third position. Minimum distance classification and binary encoding resulted in the worst accuracies. Curves of minimum distance and maximum likelihood classification follow the same trend as those from the AVIRIS data set, but the relative accuracies of the other methods differ greatly. Whereas with the simulated AVIRIS data illumination effects had little influence, with the combined data set, accuracy declined markedly when illumination was included. In fact, the illumination effects become the main factor reducing the classification accuracies. This may be a result of combining the analysis of spectra with illumination effects in the VNIR/SWIR and no illumination effects in the TIR.
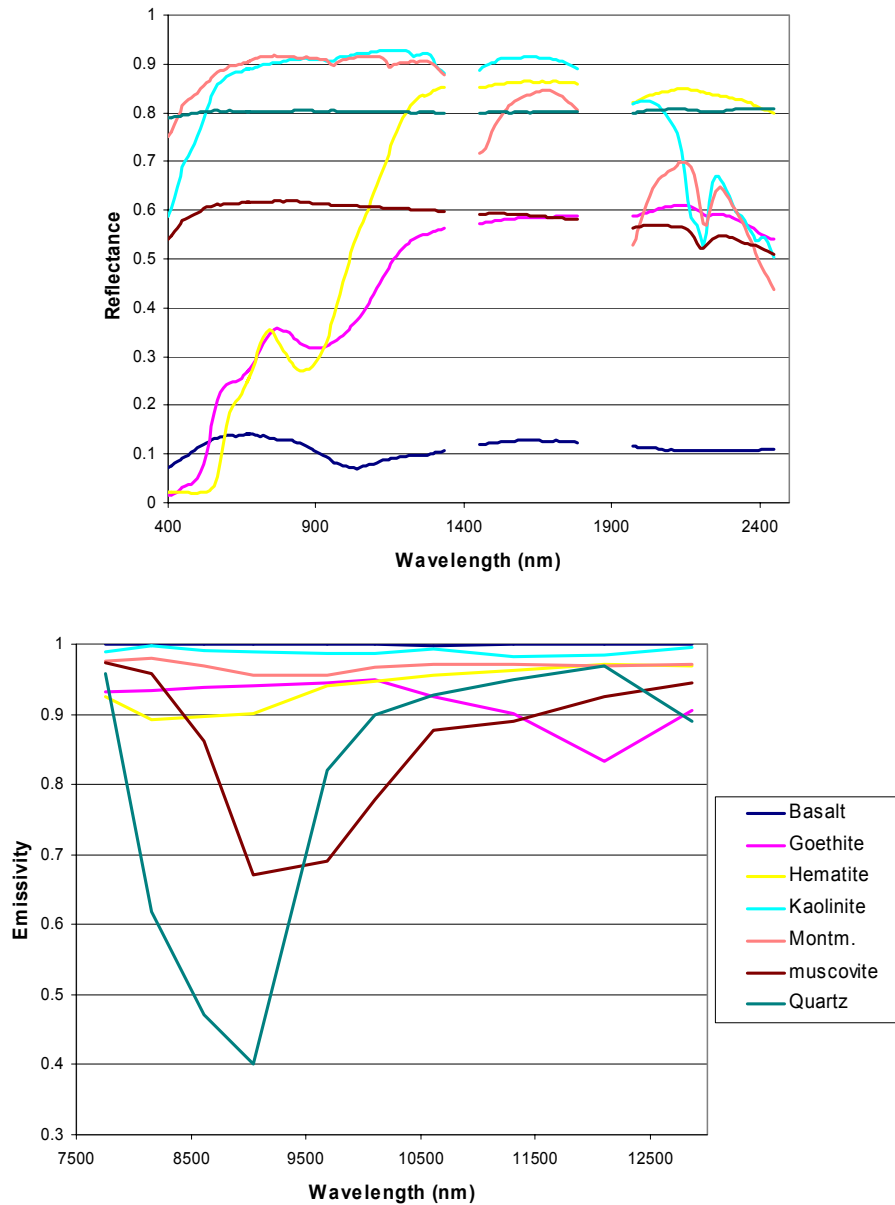
Figure 3. Laboratory reflectance spectra and emissivity spectra of minerals and rocks resampled to AVIRIS (top) and MASTER (bottom) wavelength bands. AVIRIS water absorption bands excluded from the analysis are indicated by the breaks in the spectral curves.

By comparison, maximum likelihood classification achieved the best performance on all data sets. Factors in the simulated data analysis that favor the maximum likelihood classification is the large and representative training sample of approximately 10,000 pixels, and that uncertainty in the data sets were modeled with normal distributions. In real applications, it can be difficult to select training data that completely characterize the classes of interest, and variability does not necessarily follow a normal distribution.

When the minerals and rocks with no distinct absorption features in the VNIR, SWIR, and TIR regions are excluded from the analysis, leaving just 9 minerals, the average results of the classifications (Figure 4) are similar in trend to the average results found with all 16 minerals and rocks (Figure 1), although in detail there are some important differences. Excluding the classes with relatively flat spectral

curves, including basalt, raised the accuracy of most methods, especially SFF. In fact, SFF achieved the second highest position in overall accuracy applying to the simulated AVIRIS data for the 9 minerals for the moderate to high uncertainty data sets (Figure 4, upper left). Although most of the selected minerals showed absorption features in the TIR region, SFF resulted in the worst accuracy for the simulated MASTER data (Figure 4, upper right). This poor result suggests that SFF is not good for classifying multispectral data with a relative broad bandwidth, like MASTER. The results of the combined data sets (Figure 4, bottom) showed that combining AVRIS and MASTER bands made a small but notable improvement for discriminating minerals using SAM in the moderate level uncertainty data sets. Quartz, goethite, and hematite, which have distinctive absorption features in the TIR region, showed a marked increase in classification accuracy for data set 3 and 4.

Figure 4. Comparison of the overall accuracies using five mapping methods on different noise level data sets of 9 mineral and rock classes with distinctive absorption features. Upper left: AVIRIS data sets. Upper right: MASTER data set. Bottom: Combined data set.

4. Summary and conclusions

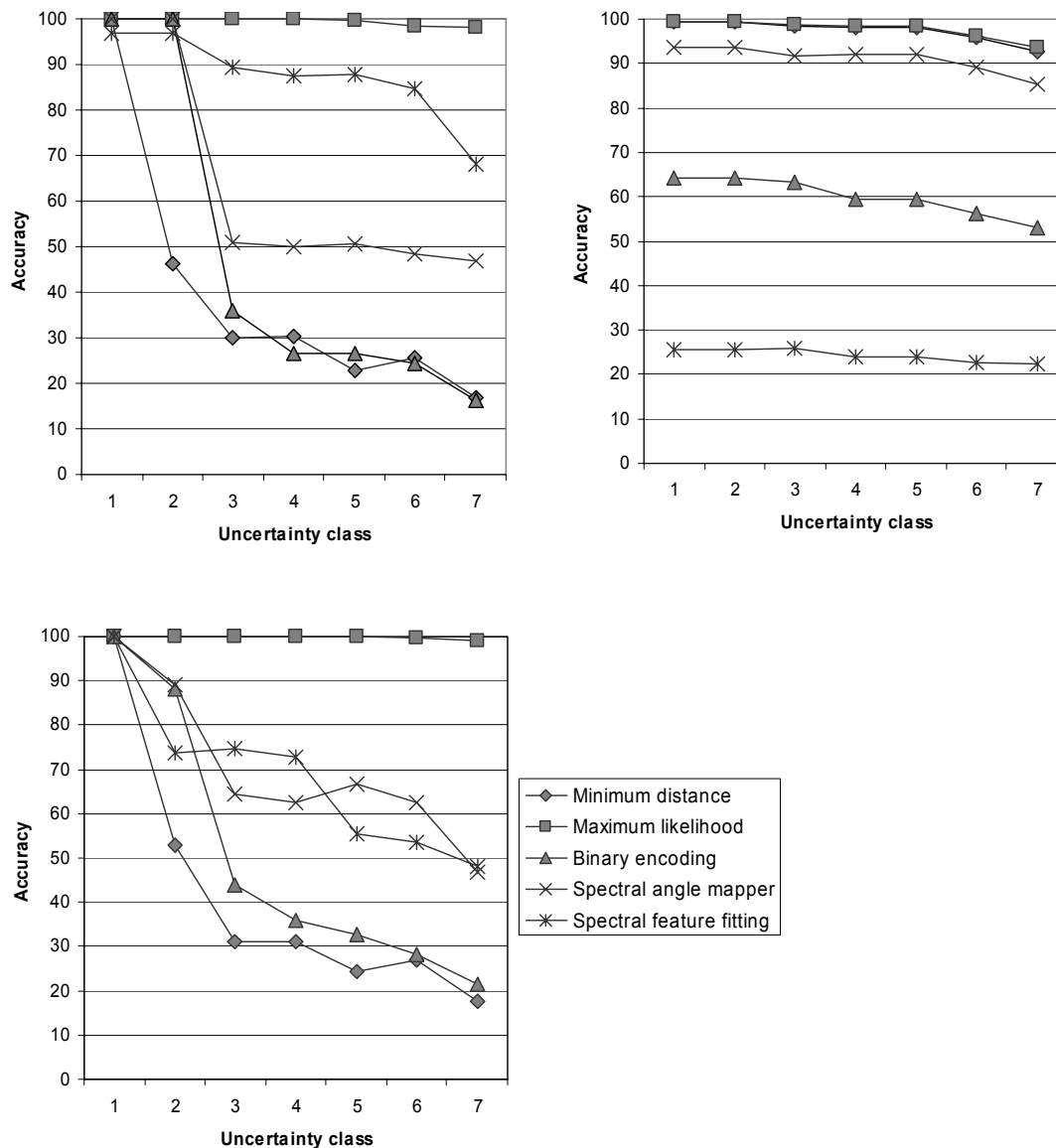A series of simulated data sets based on the characteristics of AVIRIS and MASTER sensors was created. The simulated data sets include surface reflectance and emissivity derived from library spectra of 16 common minerals and rocks occurring in Cuprite, Nevada. Five automatic classification algorithms, minimum distance, maximum likelihood classification, binary encoding, SAM, and SFF, were applied to all data sets. The classification results showed that combining AVIRIS with MASTER data sets can be useful for improving the accuracy of identifying the 16 selected minerals and rocks in some circumstances. First, most methods applied to the combined data sets, except SFF, achieved varying improvement in overall accuracy in comparison to these methods used with the AVIRIS data set alone. Second, some minerals and rocks showed a great improvement in their individual classification accuracies. Basalt, calcite, and muscovite, for instance, resulted in an improvement of at least 20 percent or greater in either the producer's or the user's accuracy using the combined data sets with SAM, and using the combined data set with SFF resulted in a large improvement in accuracy for goethite, hematite, quartz, and muscovite. Because SFF is an absorption feature based method, the combination of AVIRIS with MASTER with SFF only enhances discrimination of minerals and rocks exhibiting distinctive absorption features in the TIR region. Within the 16 minerals and rocks, only 4 minerals, goethite, hematite, quartz, and muscovite, have strong distinctive absorption features in TIR region. Adding uncertainty to MASTER tends to dilute absorption features. Therefore, for most minerals and rocks, combining MASTER TIR with AVIRIS bands degrades the performance of SFF.

Almost all methods used in this study are sensitive to mixing uncertainty. The only exception is maximum likelihood classification. SFF applied to the data set consisting of minerals exhibiting distinctive absorption features was found to be relative tolerant to mixing uncertainty. SAM, binary encoding, and SFF are less sensitive to illumination effects when they are applied to the simulated AVIRIS data sets. However, once illumination effects are applied to the simulated AVIRIS data in the combined data sets, there is a dramatic decrease of overall accuracy. This suggests that specific algorithms may need to be developed to integrate data with reflected and emissive characteristics, rather than simply applying previously developed methods to the combined data sets. Maximum likelihood classification is relatively robust in the presence of uncertainties, at least if sufficient training samples can be identified to estimate the probability distribution accurately. Generally however, it may not be possible to find a sufficient number of training pixels for the high dimensionality of AVIRIS data. Therefore, it may be necessary to perform feature extraction, for example with the MNF transformation, on the simulated AVIRIS and combined data sets before maximum likelihood classification is applied. The accuracy of minimum distance classification and SAM on MNF transformed data sets is almost 100 percent, indicating that the performance of MNF is very successful in suppressing the noise, and reducing the number of bands, at least for these simulated data.

In terms of overall accuracy of classification, maximum likelihood classification showed the best performance. However, prior knowledge about the study area is required in order to select training samples. Hyperspectral analysis methods like SFF have an advantage over maximum likelihood classification in that, at least potentially, external library spectra can replace in-scene training data. The simulated AVIRIS data showed that SFF is generally superior to SAM, although the accuracy of SAM applied to combined data sets is slightly better than that of SFF. SAM applied to the combined data sets increased classification accuracy for some minerals and rocks which do not exhibit distinct absorption feature in thermal infrared region, while for SFF, only the accuracy of minerals and rocks with characteristic absorption features in thermal infrared region was improved. Although binary encoding and minimum distance classification showed a relative poor performance on the simulated AVIRIS and combined data sets, binary encoding has some advantages, including a relatively simple algorithm, it is very fast, and is insensitive to illumination variation. Minimum distance classification is also relatively fast, only needs a small number of training samples, and achieves very high accuracy when it is applied to multispectral data sets. SFF is not good for multispectral data, whereas SAM can achieve relatively good performance with either hyperspectral or multispectral data.

6.   Acknowledgments

References

Abrams, M. J., and Ashley, R. P. (1980). Alteration mapping using multispectral images— Cuprite Mining District, Esmeralda County, Nevada. *U. S. Geological Survey Open File Report,* 80–367.

Abrams, M. J., and Hook, S. J. (1991). Combined use of TIMS and AVIRIS for alteration mapping: In *Proceedings of the third Thermal Infrared Multispectral Scanner (TIMS) Workshop*, JPL Publication 91-29, Jet Propulsion Laboratory, Pasadena, California, 54–64.

Clark, R. N. (1999). Spectroscopy of rocks and minerals, and principles of spectroscopy. In A. N. Rencz (Ed.), *Remote Sensing for the Earth Sciences: Manual of Remote Sensing,* 3rd ed., Vol. 3, Chapter 1 (pp. 3–58). New York: John Wiley & Sons.

Clark, R. N., Gallagher, A. J., and Swayze, G. A. (1990). Material absorption band depth mapping of imaging spectrometer data using the complete band shape least-squares algorithm simultaneously fit to multiple spectral features from multiple materials. *Proceedings of the Third Airborne Visible/Infrared Imaging Spectrometer (AVIRIS) Workshop*, JPL Publication 90-54, Jet Propulsion Laboratory, Pasadena, California, 176– 186.

Clark, R. N., Swayze, G. A., Livo, K. E., Kokaly, R. F., Sutley, S. J., Dalton, J. B., McDougal, R. R., and Gent, C. A. (2003). Imaging Spectroscopy: earth and planetary remote sensing with the USGS Tetracorder and expert systems. *Journal of Geophysical Research*, 108 (E12), 5131, doi:10.1029/2002JE001847.

Collins, J. B., and Woodcock, C. E. (1999). Geostatistical estimation of resolution dependent variance in remotely sensed images. *Photogrammetric Engineering and Remote Sensing*, 65, 41–50.

Crowley, J. K., Brickey, D. W., and Rowan, L. C. (1989). Airborne imaging spectrometer data of the Ruby Mountains, Montana: mineral discrimination using relative absorption band-depth images. *Remote Sensing of Environment*, 29, 121–134.

Ferro, C. J. and Warner, T. A. (2002). Scale and texture in digital image classification. *Photogrammetric Engineering and Remote Sensing,* 68, 51–63.

Gillespie, A.R., Rokugawa, S., Matsunaga, T., Cothern, J. S., Hook, S., and Kahle, A. B. (1998). A temperature and emissivity separation algorithm for advanced spaceborne thermal emission and reflection radiometer (ASTER) images. *IEEE Transactions on Geoscience and Remote Sensing*, 36, 1113–1126.

Goetz, A. F. H. (1989). Spectral remote sensing in geology. In: G. Asrar (ed.) *Theory and Applications of Optical Remote Sensing*, John Wiley & Sons, Inc., New York, Chapter 12. pp. 491–526.

Goetz, A. F. H., Vane, G. J., Solomon, E., and Rock, B. N. (1985). Imaging spectrometry for earth remote sensing. *Science*, 211, 1147–1153.

Green, A. A., Berman, M., Switzer, P., and Craig, M. D. (1988). A transformation for ordering multispectral data in terms of image quality with implications for noise removal. *IEEE Transactions on Geoscience and Remote Sensing*, 26, 65–74.

Green, R. O., Eastwood, M. L., Sarture, C. M., Chrien, T., Aronsson, G. M., Chippedale, B. J., Faust, J. A., Pavri, B. E., Chovit, C. J., Solis, M., Olah, M. R., and Williams, O. (1998). Imaging Spectroscopy and the Airborne Visible/Infrared Imaging Spectraometer (AVIRIS). *Remote Sensing of Environment*, 65, 227–248.

Hook, S. J., Abbott, E. Grove, A., C., Kahle, A. B., and Palluconi, F. (1999). Use of multispectral thermal infrared data in geological studies. In: A. N. Rencz (ed.), *Remote Sensing for the Earth Sciences*: *Manual of Remote Sensing*, 3rd ed., Vol. 3, Chapter 2 (pp. 59–110), New York: John Wiley & Sons.

Hook, S. J., Gabell, A. R., Green, A. A., and Kealy, P. S. (1992). A comparison of techniques for extracting emissivity information from thermal infrared data for geologic studies. *Remote Sensing of Environment*, 42, 123–135.

Hook, S. J., Karlstrom, K. E., Miller, C. F., and McCaffrey, K. J. W. (1994). Mapping the Piute Mountains, California, with thermal infrared multispectral scanner (TIMS) images. *Journal of Geophysical Research*, 99, 15,605–15,622.

Hook, S. J., Myers, J. J., Thome, K. J., Fitzgerald, M., and Kahle, A. B. (2001). The MODIS/ASTER Airborne Simulator (MASTER) – a new instrument for earth science studies. *Remote Sensing of Environment*, 76, 93–102.

Hunt, G. R. (1980). Electromagnetic radiation: the communication link in remote sensing. In B.S. Siegal and A.R. Gillespie (eds.), *Remote Sensing in Geology* (pp. 5–45). New York: Wiley.

Hunt, G. R., and Salisbury, J. W. (1974). Mid-infrared spectral behavior of igneous rocks. *Technical Report AFRCL-TR-75-0356*, US Air Force Cambridge Research Laboratory, Cambridge, Massachusetts.

Jupp, D. L., Strahler, A. H. and Woodcock, C. E. (1989). Autocorrelation and regularization in digital images. II. Simple image models. *IEEE Transactions on Geoscience and Remote Sensing*, 27, 247–258.

Kahle, A. B. (1987). Surface emittance, temperature, and thermal inertia derived from thermal infrared multispectal scanner (TIMS) data for Death Valley, California. *Geophysics*, 52, 858–874.

Kruse, F. A., Lefkoff, A. B., Boardman, J. B., Heidebrecht, K. B., Shapiro, A. T., Barloon, P. J., and Goetz, A. F. H. (1993a). The spectral image processing system (SIPS) – Interactive visualization and analysis of imaging spectrometer data. *Remote Sensing of Environment*, 44, 145–163.

Kruse, F. A., Lefkoff, A. B., and Dietz, J. B. (1993b). Expert system-based mineral mapping in Northern Death Valley, California/Nevada, Using the Airborne Visible/Infrared Imaging Spectrometer (AVIRIS). *Remote Sensing of Environment*, 44, 309–336.

Landgrebe, D. (2000). Information extraction principles and methods for multispectral and hyperspectral image data. In C. H. Chen (ed.), *Information Processing for Remote Sensing,* Chapter 1, New Jersey: World Scientific Publishing Co., Inc., River Edge.

Li, Z., Becker, F., Stoll, M. P., and Wan, Z. (1999). Evaluation of six methods for extracting relative emissivity spectra from thermal infrared images. *Remote Sensing of Environment*, 69, 197–214.

Lyon, R. J. P. (1972). Infrared spectral emittance in geologic mapping: Airborne spectrometer data from Pisgah Crater, California. *Science*, 175, 983–985.

Mueller, Richter, A., R., Habermeyer, M., Mehl, H., Dech, S., Kaufmann, H., Segl, K., Haschberger, P., and Strobl, P. (2003). ARES: a new reflective/emissive imaging spectrometer for terrestrial application: In *Proceedings of the 13th Airborne Visible/Infrared Imaging Spectrometer (AVIRIS) and Hyperion Workshop*, Jet Propulsion Laboratory, Pasadena, California.

Mustard, J. F. and Sunshine, J. M. (1999). Spectral analysis for earth science: Investigations using remote sensing data. In A. N. Rencz (ed.), *Remote Sensing for the Earth Sciences*: Manual of Remote Sensing, 3rd ed, Vol. 3, Chapter 5 (pp. 251–306), New York: John Wiley & Sons.

Pandya, M. R., Dadhwal, V. K., and Navalgund, R. R. (2000). Effects of WiFS viewing geometry on crop reflectance: A simulation study using SAIL model. *International Journal of Remote Sensing*, 21, 1931–1938.

Pouch, G. W. and Campagna, D. J. (1990). Hyperspherical direction cosine transformation for separation of spectral and illumination information in digital scanner data. *Photogrammetric Engineering and Remote Sensing*, 56, 475–479.

Price, J. C. (1979). Surface temperature variations as measured by the Heating Capacity mapping Mission. *Proceedings of the Thirteenth International Symposium on Remote Sensing of the Environ*ment (pp. 765–770). Ann Arbor, Michigan: Environmental Research Inst. of Michigan.

Richards, J.A (1993). *Remote Sensing Digital Image Analysis: An Introduction*. New York: Springer-Verlag, 340p.

Research Systems (2000). *Using IDL, IDL Version 5.6*. Research Systems, Boulder Colorado, 716p.

Research Systems (2002). *ENVI User's Guide, ENVI 3.6*. Research Systems, Boulder Colorado, 1042p.

Rowan, L. C. (1998). Analysis of simulated advanced spaceborne thermal emission and reflection (ASTER) radiometer data of the Iron Hill, Colorado, study area for mapping lithologies. *Journal of Geophysical Research D: Atmospheres*, 103, 32,291–32,306.

Salisbury, J. W., Walter, L. S., Vergo, N., and D`Aria, D. M. (1991). *Infrared (2.1–25 micrometers) Spectra of Minerals*. Johns Hopkins University Press, 294p.

Strahler, A. H., Woodcock, C. and Smith, J. A. (1986). On the nature of models in remote sensing. *Remote Sensing of Environment*, 20, 121–139.

Vane, G., Green, R. O., Chrien, T. G., Enmark, H. T., Hansen, E. G., and Porter, W. M. (1993). Airborne Visible/Infrared Imaging Spectrometer (AVIRIS). *Remote Sensing of Environment*, 44, 127–143.

Verhoef, W. (1984). Light scattering by leaf layers with application to canopy reflectance modeling: The SAIL model. *Remote Sensing of Environment*, 16, 125–141.

Vincent, R.K., and Thomson, F. J. (1971). Discrimination of basic silicate rocks by recognition maps processed from aerial infrared data. *Proceedings of the Seventh International Symposium on Remote Sensing Environment* (pp. 245–251). Ann Arbor, Michigan: University of Michigan.

Warner, T. (1999). Analysis of spatial patterns in remotely sensed data using multivariate spatial correlation. *Geocarto International,* 14: 59–65.

Warner, T. A. and Chen, X. (2001). Normalization of Landsat thermal imagery for the effects of solar heating and topography. *International Journal of Remote Sensing*, 22, 773–788.

Woodcock, C. E, Strahler, A. H., and D. L. Jupp (1988). The use of variograms in remote sensing: I. Scene models and simulated images. *Remote Sensing of Environment,* 25, 323–348.

ESTIMATION OF HAWAIIAN ISLANDS FIRE FUEL PARAMETERS FROM HYPERSPECTRAL IMAGERY

Matthew L. Clark,[1] Dar A. Roberts,[1] Margaret E. Gardner,[1] and David R. Weise[2]

1. Introduction

Wildland fire has played a role in the development of some of the flora and fauna of the Hawaiian Islands given the volcanic nature of the archipelago's origin. However, the current floral and faunal composition of the major islands (Kaua'i, O'ahu, Moloka'i, Maui, and Hawai'i) is quite different from the biota that were present when humans first settled the islands circa 600 A.D. Large percentages of the land area on the major islands have been transformed by human activity, drastically altering fire regimes. For example, invasive non-native grass species have increased the occurrence and extent of wildland fire (D'Antonio and Vitousek, 1992). Fire can be detrimental to some native plants in Hawaii thereby jeopardizing survival and leading to loss of biodiversity (Mehrhoff, 1998). However, some native species appear to respond well to low intensity fires.

Fire behavior computer models are useful tools to understand the function of vegetative fuel types in propagating fire and predicting the effectiveness of fire management techniques in protecting and restoring native vegetation. These models (e.g., FARSITE (Finney, 1998)) require maps of fuel models, which are the quantitative description of the vegetation fuel bed in two or three dimensions. There is little vegetative fuels information available for the Hawaiian Islands. A recent advancement was the completion of the U.S. Forest Service stereo-photograph series and vegetation plots which quantitatively describe fuel properties in a range of grassland, shrubland, woodland and forest vegetation types at 36 sites across five of the islands (Wright et al., 2002).

Remote sensing has immense potential for fire behavior modeling in that it can provide larger extents and more frequent measurements of fuel-load parameters than what is currently available. The objectives of this study were to: 1) assess the utility of AVIRIS spectral features for per-pixel estimation of fuel parameters, and 2) compare the relative benefits of narrowband (i.e., AVIRIS) and broadband (i.e., Landsat ETM+) formulations of vegetation indices in estimating fuel properties.

2. Data acquisition and processing

The study was focused on the islands of Hawai'i, Kaua'i, Moloka'i, O'ahu and Maui in the Hawaiian archipelago (Fig. 1). Field data from 24 vegetation sampling plots (Fig. 1) were collected in November 1999, July 2000 and February 2001 (Wright et al., 2002). There were 9 grassland, 3 shrubland, 7 woodland and 5 tree-plantation plots sampled from 47 to 2037-m elevation. Tree plantations were dominated by *Casuarina equisetifolia*, *Pinus radiata*, *Pinus pinaster*, or *Pinus elliottii*. Thirteen of the plots were on Hawai'i island, mainly on the drier side of the precipitation gradient that runs from east to west across the island. Fuel parameters measured included percent canopy cover and the biomass of dead and live materials. Dead-wood biomass was classified into diameter classes: <0.64 cm, 0.65-2.5 cm, 2.6-7.6 cm and > 7.6 cm.
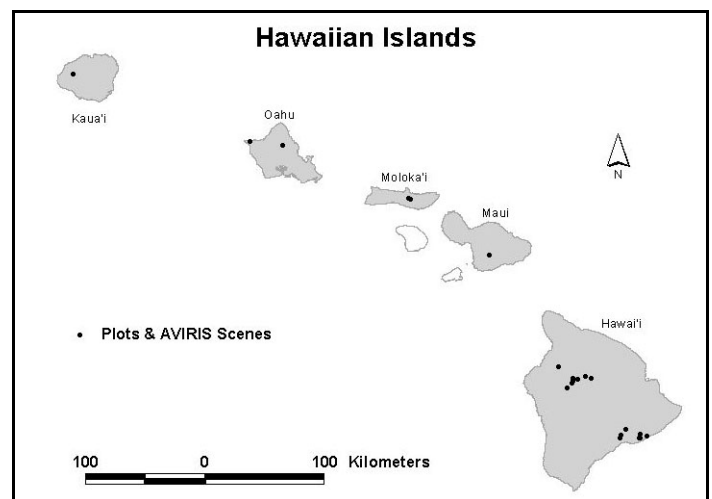

Figure 1. Study islands (shaded) and associated, co-located plot and AVIRIS scene locations.

[1] Department of Geography, University of California, Santa Barbara, California

[2] Forest Fire Laboratory, Pacific Southwest Research Station, USDA Forest Service, Riverside, California

These size classes correspond to 1-hr, 10-hr, 100-hr and 1000-hr fuel moisture time-lag classes, respectively, which are commonly used in fire models (Anderson, 1982). Other dead materials included litter and duff. Live-material biomass included herbaceous components (i.e., forbs, ferns and graminoids) and woody shrubs. Canopy cover had tree, shrub and herbaceous components and is important because it is used in fuel moisture and wind reduction calculations in fire modeling (Albini and Baughman, 1979; Rothermel et al., 1986).

High-altitude AVIRIS data were collected in April, 2000 with a 20-m Ground Instantaneous Field of View (GFOV). Runs were processed to apparent surface reflectance with the MODTRAN radiative transfer model (Green et al., 1993). Reflectance from several field calibration spectra (beaches) were used to remove artifacts in modeled reflectance spectra (Dennison et al., 2001). Calibrated AVIRIS scenes had to be georegistered so that field plots could be located for the sampling of image pixels. Georegistered base information included vector road layers (State of Hawaii, Office of Planning, 1998) and Landsat ETM+ imagery registered to the road vector layer. We georegistered a total of 13 AVIRIS scenes to the UTM projection (Zone 4, Datum WGS 84) with first-order polynomial transformations and nearest-neighbor, 20-m resampling. Transformation equations were built by visually matching points within the AVIRIS imagery to registered points in the Landsat images or the road layer. Root-mean-square error ranged from 0.5 to 1.8 m, using between 5 to 14 points.

Field plots were located in georegistered AVIRIS scenes based on plot-center GPS coordinates. Due to georegistration errors, plot-center location errors, and cloud coverage, the image sampling locations of 10 plots were shifted between 30 to 500 m to locate more appropriate sampling locations. Care was taken to locate the adjusted plot centers in the same vegetation patch.

3. Hyperspectral features analyzed

Spectral mixture analysis (SMA) of AVIRIS data was performed using a 4-endmember (EM) model consisting of green vegetation (GV), non-photosynthetic vegetation (NPV), soil and photogrammetric shade reference EMs. Following techniques outlined by Roberts et al., (1998a), reference EMs were selected from an AVIRIS-convolved library of field spectra (Dennison et al., 2001) according to the criteria that they produced low root-mean-square error (RMSE) and physically-reasonable fractions.

Several vegetation liquid water indices were calculated from AVIRIS reflectance spectra. Equivalent Water Thickness (EWT; Roberts et al., 1998b) was calculated using the water absorption feature between 865 and 1065 nm. The Water Band Index (WI; Peñuelas et al., 1993; Sims and Gamon, 2003) was calculated as R_{900} / R_{970} (the ratio of reflectance (R) at 900 and 970 nm, respectively). The Normalized Difference Water Index (NDWI; Gao, 1996) was calculated as $(R_{860} - R_{1240}) / (R_{860} + R_{1240})$.

Narrowband vegetation indices included the Vegetation Index (VI = R_{800} / R_{680}; Sims and Gamon, 2003), Normalized Difference Vegetation Index (NDVI = $[R_{800} - R_{680}] / [R_{800} + R_{680}]$; Sims and Gamon, 2003), Soil-Adjusted Vegetation Index (SAVI = $1.5 * [R_{800} - R_{680}] / [R_{800} + R_{680} + 0.5]$; Huete, 1988), and the Photochemical Reflectance Index (PRI = $[R_{531} - R_{570}] / [R_{531} + R_{570}]$; Gamon et al., 1997). Landsat ETM+ broadband imagery was simulated using AVIRIS reflectance spectra and the ETM+ spectral response functions for the 6 optical bands. Broadband vegetation indices were then calculated from simulated ETM+ data. These indices included ETM_VI (R_{830} / R_{660}), ETM_NDVI [$(R_{830} - R_{660}) / (R_{830} + R_{660})$], and ETM_SAVI [$1.5 * (R_{830} - R_{660}) / (R_{830} + R_{660} + 0.5)$]. ETM+ indices had the 20-m spatial resolution of the AVIRIS reflectance data.

4. Statistical Analyses

Mean and standard deviation values for reflectance spectra, indices, and SMA output (fractions and RMSE) were calculated from a 3x3-pixel kernel (60 x 60-m = 3600 m^2) centered on each plot. Single- and multiple-regression analyses were used to assess the relationship between field-measured fuel parameters (e.g., 1-hr fuels) and hyperspectral features (e.g., EWT, GV fraction). Analyses included the square-root (SQRT) transformation of the dependent variables (i.e., fuel parameters). SQRT was included as the final model if the adjusted-r^2 value was higher than that without the transformation. For

multiple-regression, the S-Plus 2000 LEAPS step-wise procedure (Mathsoft Engineering & Education, Inc., Cambridge, MA) was used with a minimum Mallow's-C_p criteria to select the best model using all independent variable (i.e., hyperspectral features) combinations. Regression models from LEAPS with fewer variables than the minimum-C_P model were also considered. A lower-variable model was selected if 1) it was significant according to the F statistic ($\alpha = 0.05$) and 2) a comparison against a higher-variable model was not significant (F-statistic, $\alpha = 0.05$).

Figure 2. Dead fuels summarized by vegetation type

5. Results and Discussion

There were significant differences in fuel parameters among the four vegetation types—grasslands, shrublands, woodlands and plantations—for all fuels except for live forb biomass and percent cover of forbs and ferns (Kruskal-Wallis tests; $\alpha = 0.05$). As is expected, there was a consistent increase in 10-hr, 100-hr, 1000-hr fuels and litter biomass in a gradient of increasing woody vegetation in the grasslands-shrublands-woodlands-plantation sequence (Fig. 2). As would be expected, live-fuel biomass in grasslands was dominated by grasses and dominated by shrubs in shrublands (Fig. 3). Live fuels in woodlands were a mixture of fuel types, and plantations had little live fuels below the tree canopy (Fig. 3).

Figure 3. Dead fuels summarized by vegetation type.

The G-01 grassland plot was a 1972 pahoehoe lava flow and had trace amounts of vegetation and so its albedo was very low (<10% reflectance; Fig. 4a, G-01). As percent-cover of grass increased, grasslands plot spectra incorporated more grass signal and less soil/lava signal (Fig. 4a). Because grasses were mostly senesced due to an extended El-Niño drought during the April AVIRIS campaign, there was only slight expression of near-infrared (NIR, 700-1300 nm) water absorption features and there was little chlorophyll absorption at 680 nm (Fig. 4a). Shrubs were also strongly affected by the drought during the AVIRIS campaign. Spectra from shrublands plots were dominated by NPV, from exposed branches and twigs, and soil (weathered lava) which was 12-25% exposed (Fig. 4b). There was no evidence of liquid water absorption in the NIR to shortwave infrared (SWIR, 1500-2508 nm) regions, and slight lingo-cellulose absorption was expressed in SWIR (Fig. 4b). Woodlands were a mix of grasses, shrubs and trees. For some plots the dominant spectral signal was from senesced shrubs and grasses (Fig. 4c, W-02, W-04, W-05), similar to shrublands plots. One plot (Fig. 4c, W-06) was located on the wetter southeast side of Hawai'i island and its spectral signal had a strong chlorophyll absorption in visible (VIS, 374-700 nm) and NIR and SWIR water absorption features from Asian swordfern (*Nephrolepsis multiflora*, 92% cover) leaves with high liquid water content. Tree plantation spectra were dominated by radiance that was multiple-scattered in the leaves (mostly needles) of overstory trees (Fig. 4d). There was strong blue (500 nm) and red (680 nm) absorption by chlorophyll, deep expression of NIR liquid water bands (near
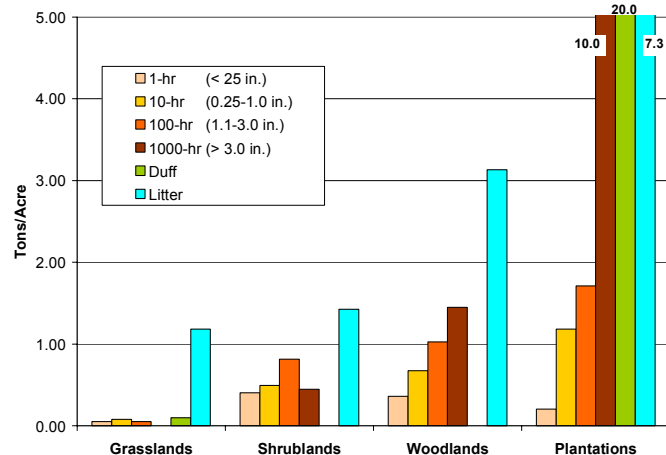
975 and 1200 nm), and broad absorption by liquid water in SWIR (Roberts et al., 2004). For plantations, non-photosynthetic dead fuels on or near the forest floor (Fig. 2) are generally shielded by the optically-thick photosynthetic overstory after crown closure has occurred.

Pearson correlation coefficients were calculated by relating dead-fuel parameters to reflectance on a band-by-band basis. Coefficients closely followed the pattern of a photosynthetic overstory canopy (Fig. 5a). For example, red absorption (i.e., lower 680 nm reflectance) associated with chlorophyll tended to be negatively correlated with dead fuels. As mentioned, dead fuels generally increased along the grassland-shrubland-woodland-plantation sequence (Fig. 2), especially for litter, duff and the size-class fuels ≥ 0.65 cm (i.e., ≥ 10 hr). Coincident in this sequence was an increase in overstory volume of photosynthetic material exposed to the sensor. Thus, as overstory cholorphyll increased, so did dead fuel biomass; and subsequently, red reflectance decreased, thereby creating a negative relationship between reflectance and dead fuels. Also, volumetric scattering will increase from grasslands to plantations due to more structure and photosynthetic foliage (e.g., higher leaf area index, LAI) in the plantation overstory. This gradient in scattering will result in increasing NIR reflectance from grasslands to plantations, thereby creating a positive relationship between dead fuel biomass and NIR bands. Because very fine dead materials (< 0.64 cm 1-hr fuels) did not show a strong increase in the grassland-plantation sequence (Fig. 2), these fuels had the weakest correlations across the spectrum (Fig. 5a). There were weaker correlations when considering live fuels (Fig. 5b). Graminoid (i.e., grasses) biomass was strongly positively correlated (r > +0.6) in SWIR bands (1500-2350 nm). There was a negative relationship between tree percent cover and graminoid percent cover, and more tree canopy tended to reduce SWIR reflectance due to water absorption
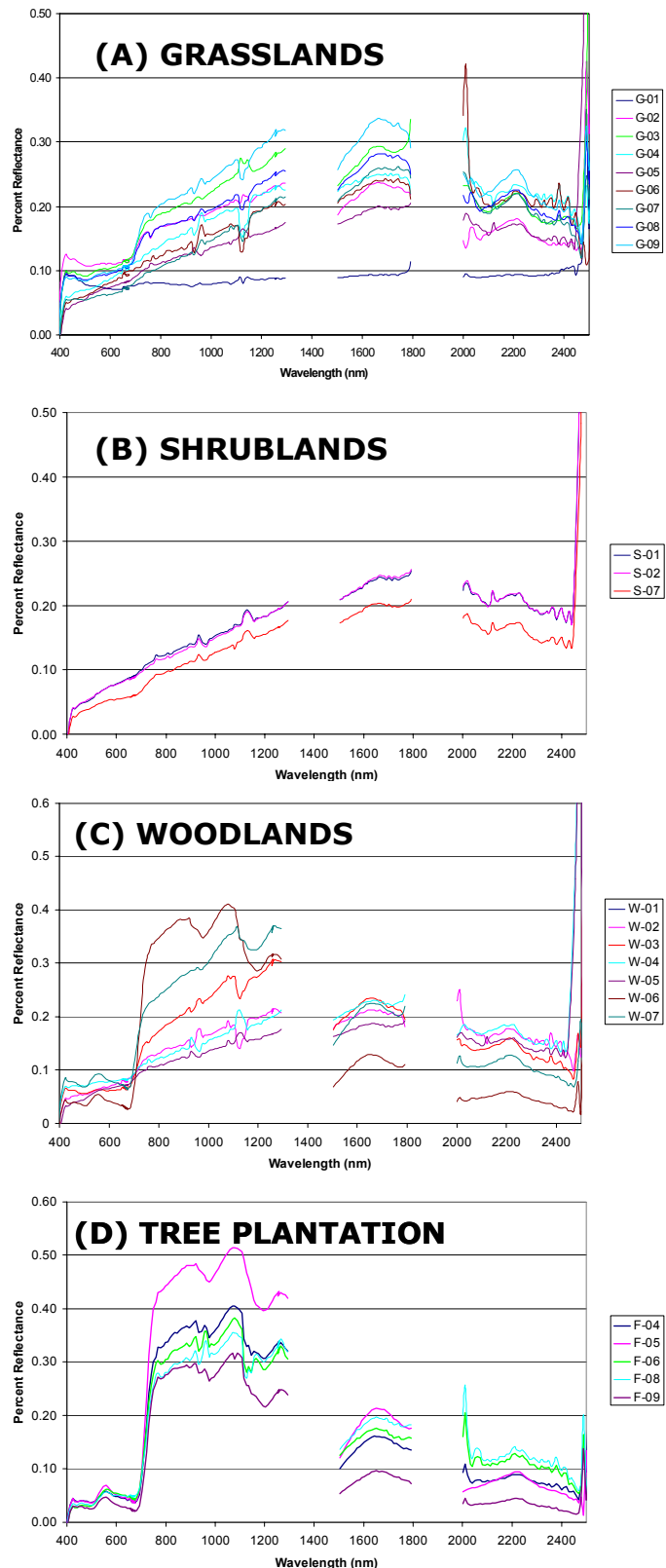

Figure 4. AVIRIS reflectance spectra from plots (average of 9 pixels in 3x3 kernel) for a) grasslands, b) shrublands, c) woodlands, and d) tree plantations.

(Fig. 4d). There is thus a positive relationship between graminoid biomass and SWIR reflectance—with less tree cover, there is more grass cover and more SWIR reflectance.

Relating single AVIRIS-derived variables to fuel parameters, r^2 values ranged from 0.17 to 0.65 (Table 1). The best correlation was +0.80, between litter and NDVI (Fig 6a). This was stronger than the best single-wavelength correlation for litter (r = +0.73, 760 nm, Fig. 5a). NDVI takes advantage of strong spectral contrast seen between 680 and 800 nm wavelengths (Fig. 5a). In ecological terms, higher NDVI may be associated with high LAI (Gong et al., 1995) and more ground litter; and thus, an indirect and positive correlation exists between NDVI and litter biomass.   Similar indirect relationships exist for 10-hr and 100-hr fuels, where higher NDVI values are positively correlated with increased structural branches that support plantation overstory leaves (Table 1). These branches are inputs to the layer of dead fuels ≥ 0.65 cm on the surface, thereby creating a positive, indirect relationship between large dead fuels and NDVI (Fig. 6b). A similar argument can be made for the correlation between 1000-hr fuels and PRI, however PRI is expected to be more negative with increasing photosynthetic overstory (Gamon et al., 1997), thus explaining the negative relationship between the variables (Table 1). Duff was associated with plantations (Fig. 2a) and negatively related to NPV (Table 1), indicating that plots with higher percent tree cover shielded more NPV from the sensor.

There was a significant -0.70 correlation between live grass fuels and NDWI (Table 1). If the AVIRIS imagery had been acquired in the wet season, NIR liquid water absorption would be expected to be deeper (higher NDWI) in plantations relative to grasslands due to the multiple-scattering environment of tree canopies, which tend to amplify water absorption features (Roberts et al., 2004). Grass biomass, which decreased from grasslands to plantations (Fig. 2b) would thus be negatively related to NDWI. This relationship may be even stronger in this drought imagery because grass was senesced and so had very low NIR liquid water absorption (Fig. 4a). A similar argument is
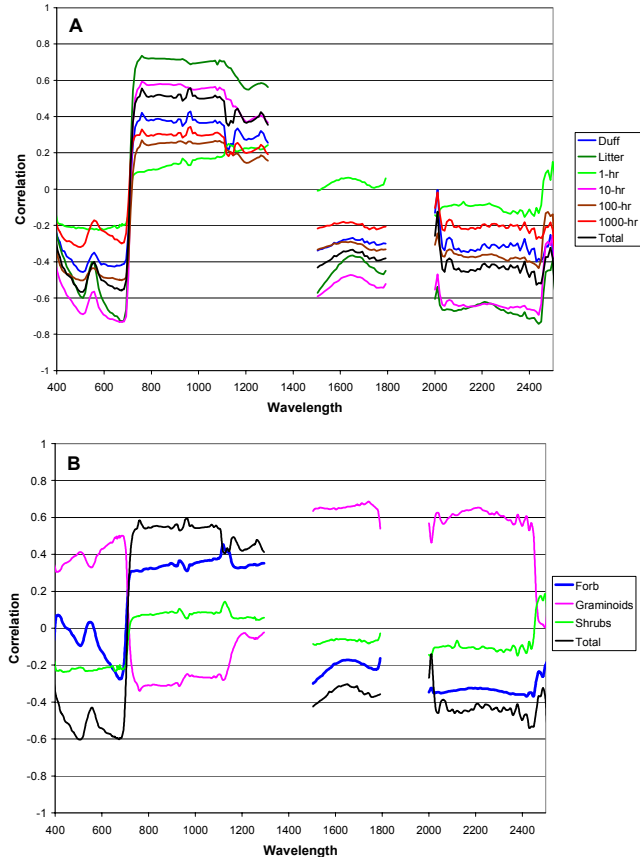

Figure 5. AVIRIS reflectance Pearson's correlation with a) dead fuels and b) aboveground biomass (n=24 plots).
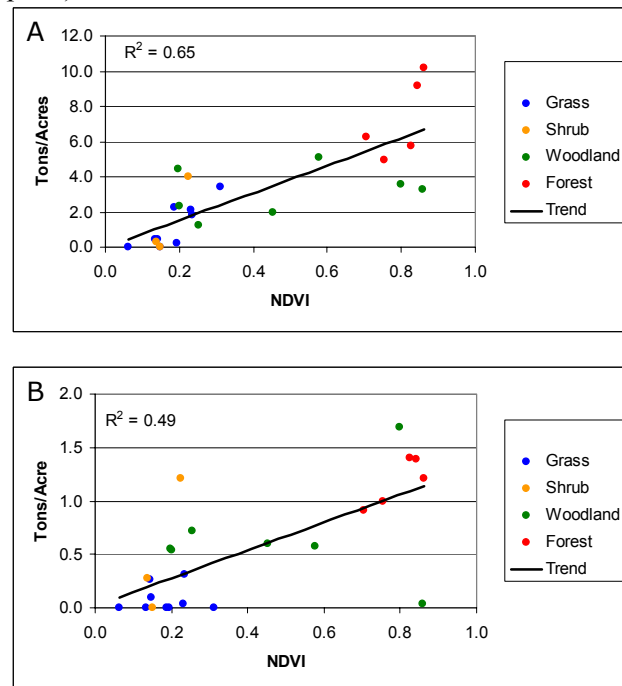

Figure 6. Relationship of narrow band NDVI to a) litter aboveground biomass, b) dead fuels 0.25 to 1 in. biomass.

49

valid for the strong negative correlation between graminoid percent cover and NDWI (Table 1). As expected, percent tree cover was positively correlated (r = +0.80) to NDVI—with more tree canopy, NDVI increased because there were more photosynthetically-active leaves.

Table 1. Single-variable regression of fuel parameters and AVRIS spectral features.

Dependent	Transform	Independent	R	r^2	Sig
DEAD BIOMASS					
1-hr	None	SOIL	-0.50	0.25	*
10-hr	None	NDVI	0.70	0.49	***
100-hr	Sqrt	NDVI	0.44	0.20	*
1000-hr	Sqrt	PRI	-0.56	0.32	**
Duff	Sqrt	NPV	-0.67	0.44	***
Litter	None	NDVI	0.80	0.65	****
Total	Sqrt	NDVI	0.72	0.52	****
LIVE BIOMASS					
Shrub	Sqrt	SOIL	-0.49	0.24	*
Forb	None	GV	0.52	0.27	**
Graminoid	Sqrt	NDWI	-0.70	0.49	***
Total	Sqrt	SOIL	-0.51	0.26	*
PERCENT COVER					
Tree	Sqrt	NDVI	0.80	0.63	****
Shrub	Sqrt	SOIL	-0.59	0.35	**
Forb & Fern	None	GV	0.41	0.17	*
Graminoid	Sqrt	NDWI	-0.77	0.59	****

Significance levels: * p≤ 0.05, ** p≤ 0.01, *** p≤ 0.001, **** p≤ 0.0001, ns= not significant

There were 225 single-variable regression analyses performed (15 dependent vs. 15 independent variables). In terms of the number and significance of correlations against the fuel parameters, NDVI, NPV and PRI were the most useful AVIRIS-derived features (Table 3). NDWI outperformed the WI and EWT liquid water indices and NPV was the best SMA endmember. The Landsat ETM+ (broadband) versions of NDVI (ETM_NDVI) had similar performance as to narrowband NDVI, and ETM_SAVI outperformed narrowband SAVI in terms of the number and significance level of correlations (Tables 2 and 3). There may be other wavelengths to calculate NDVI that could better isolate the red absorption and NIR plateau and outperform the broadband NDVI, however such a sensitivity analysis was beyond the scope of this research. Contrary to expectations, SAVI was not as useful as NDVI for single-variable predictions. It may be that the SAVI soil-baseline parameters need to be better calibrated for the relatively dark lava-derived soil found in our study areas.

The square root transformation of the dependent (fuel) variable improved most multiple-regression equations. Adjusted-R^2 values ranged from 0.22 to 0.83 (Table 4). Equations contained one to four variables and the most common spectral variables used were NDVI, SOIL, RMSE, PRI and SOIL. RMSE was a minor component to the models, but its presence suggests that there is an unmodeled spectral component that is related to the dependent variables. For 1-hr and 10-hr fuels, there was a negative relationship with VI yet a positive relationship with NDVI. It was expected that these variables would provide equivalent information, and it is not clear why they are contradictory. The percent tree cover relationship is the most instructive model. The relationship is associated with negative PRI, positive EWT and negative NPV. As tree cover increases, photosynthetic leaves increase and there is thus less exposed NPV, less PRI, and more water absorption (high EWT).

Table 2. Single-variable regression of fuel parameters and simulated ETM+ vegetation indices.

Dependent	Transform	Independent	R	r^2	Sig
DEAD BIOMASS					
1-hr	None	ETM_NDVI	0.17	0.03	ns
10-hr	None	ETM_NDVI	0.72	0.52	****
100-hr	Sqrt	ETM_NDVI	0.47	0.22	*
1000-hr	Sqrt	ETM_NDVI	0.46	0.21	*
Duff	Sqrt	ETM_NDVI	0.61	0.37	**
Litter	None	ETM_NDVI	0.81	0.65	****
Total	Sqrt	ETM_NDVI	0.73	0.54	****
LIVE BIOMASS					
Shrub	None	ETM_VI	0.40	0.16	ns
Forb	Sqrt	ETM_NDVI	-0.60	0.36	**
Graminoid	None	ETM_NDVI	0.17	0.03	ns
Total	None	ETM_NDVI	0.07	0.00	ns
PERCENT COVER					
Tree	Sqrt	ETM_NDVI	0.79	0.63	****
Shrub	None	ETM_NDVI	0.17	0.03	ns
Forb & Fern	None	ETM_VI	0.40	0.16	ns
Graminoid	Sqrt	ETM_VI	-0.66	0.44	***

Significance levels: * p≤ 0.05, ** p≤ 0.01, *** p≤ 0.001, **** p≤ 0.0001, ns= not significant

Table 3. Summary of significant independent variables in single-variable regression analyses.

	$p \leq 0.05$	$p \leq 0.01$	$p \leq 0.001$	$p \leq 0.0001$	Total
NARROWBAND VEGETATION INDICES					
NDVI	2	2	2	4	10
VI	1	5	2	1	9
SAVI	1	2	4	2	9
PRI	3	4	2	1	10
LIQUID WATER INDICES					
EWT	1	1			2
NDWI	1	3	3	1	8
WI		2			2
SPECTRAL MIXTURE ANALYSIS FRACTIONS					
GV	7	2			9
NPV	2	4	2	2	10
SOIL	5	3			8
SHADE	1				1
RMSE	4	1			5
BROADBAND VEGETATION INDICES					
ETM_NDVI	2	2	1	5	10
ETM_VI		4	2	2	8
ETM_SAVI	2	2	1	5	10

Table 4. Multiple-regression analyses of hyperspectral features.

Dependent	Independent Variables	Adj-R^2	Sig.
DEAD BIOMASS			
1-hr*	0.320 - 0.107 x VI + 1.930 x NDVI – 0.002 x RMSE	0.53	**
10-hr*	1.645 - 0.112 x VI + 3.837 x NDVI - 0.014 x GV - 0.005 x RMSE	0.68	***
100-hr*	6.393 - 12.793 x NDWI + 2.936 x NDVI - 0.068 x NPV - 0.004 x RMSE	0.53	**
1000-hr*	-0.529 - 23.293 x PRI	0.32	**
Duff*	-7.180 - 31.428 x PRI + 0.054 x SOIL	0.69	****
Litter*	-0.499 - 4.034 x NDWI + 3.882 x NDVI	0.69	****
LIVE BIOMASS			
Shrub*	3.965 - 0.026 x SOIL	0.24	*
Forb	-3.181 + 0.034 x GV	0.27	**
Graminoid*	-5.497 + 0.193 x VI - 2.901 x NDVI + 0.051 x NPV + 0.006 x RMSE	0.79	****
Total Live*	8.625 - 0.072 x SOIL + 0.010 x RMSE	0.43	**
PERCENT COVER			
Tree	92.774 - 489.078 x PRI + 3.290 x EWT - 0.872 x NPV	0.75	****
Shrub*	11.981 - 0.0790 x SOIL	0.35	**
Forb & Fern	-31.160 + 0.344 x GV	0.22	*
Graminoid	-442.127 + 112.268 x SAVI + 434.492 x PRI + 2.847 x NPV + 1.238 x SOIL	0.83	****

6. Conclusion

In this study we sought to find spectral features that may be useful for estimating important fuel properties as potential per-pixel inputs for fire behavior models. The sizes and spatial distribution of dead surface fuels are the most important components to characterize in these models. In the Hawaiian Islands landscapes analyzed in this study, we found that these dead fuels tended to increase in size and quantity along a grasslands-shrublands-woodlands-tree plantation sequence of vegetation types. Because AVIRIS scenes were acquired during a drought, grasses and shrubs were mostly senesced while tree canopies were green, and so photosynthetic materials exposed to the sensor increased in volume and vigor along the same grasslands to plantation sequence. As tree overstory canopy cover increases, the spectral component of dead surface fuels are a smaller component in the radiance signal reaching the sensor. Therefore, most dead fuels are not directly "sensed" by the sensor, and there is an indirect relationship between reflectance properties of overstory photosynthesis and dead fuel biomass. For this reason, we observed that both narrowband and broadband NDVI was positively correlated with increasing dead fuel size and quantity.

Live-fuel biomass and percent cover were not as well predicted as dead-fuel biomass, even with the inclusion of more variables in the regression models. Grass biomass and cover were well predicted using NDWI with regressions that explained 49% and 59% of the variance, respectively. The negative relationship between moisture content and quantity of grasses exists because grasses were senescent and plantations were not. The relationship would likely be less distinct in wet-season AVIRIS scenes because photosynthetically-active grasses would have deeper NIR liquid water absorption features.

For 10-hr and 100-hr dead fuels, duff, litter, and tree cover, narrowband NDVI provided single-variable models that explained 20% to 65% of the variance. Models were equal or slightly better with broadband ETM_NDVI, indicating that a multispectral satellite may provide adequate sensitivity to these fuel parameters. This is important in an operational sense in that ETM+ data over the whole Hawaiian archipelago are much cheaper and easier to process for producing island-wide fuels maps. For other fuel parameters, such as grass cover, 1000-hr fuels, and duff, we found that features based on AVRIS data were important in single-variable regressions. Multiple regression equations, which used AVIRIS-derived variables, appear stronger based on adjusted-R^2 values. Some variables in these equations, such

as PRI, NDWI and EWT can not be calculated from ETM+ data due to the limited band resolution and/or position. Although SMA fractions can be estimated with ETM+, they should be more accurate when estimated from hyperspectral data. At this stage in our research, we found AVIRIS useful for exploring different indices. However, more field data are required to test model estimation error and establish the relative advantage of hyperspectral data for vegetation fuel estimation. Here we estimated individual fuel parameters (e.g., 10-hr dead biomass), whereas current fire behavior models take more generalized fuel models or types as inputs (Riaño et al., 2002). Future research should focus on methods to map fuel types on a per-pixel basis from estimated fuel parameters, possibly with a decision tree classifier.

7. Acknowledgements

8. References

Albini, F. A. and Baughman, R. G. (1979). Estimating windspeeds for predicting wildland fire behavior. USDA Forest Service Res. Pap. INT-221.

Anderson, H. E. 1982. Aids to determining fuel models for estimating fire behavior. USDA Forest Service Gen. Tech. Rep. INT-122.

D'Antonio, C. M. and Vitousek, P. M. (1992). Biological Invasions by Exotic Grasses, the Grass Fire Cycle, and Global Change. *Annual Review of Ecology and Systematics*, *23*, 63–87.

Dennison, P. E., Gardner, M. E., Roberts, D. A., and Green, R. O. (2001). Calibration and vegetation field spectra collection for the 2000 AVIRIS Hawaii deployment. *Summaries of the Tenth Annual JPL Airborne Geoscience Workshop*, Pasadena, California: Jet Propulsion Laboratory.

Finney, Mark A. (1998). FARSITE: Fire Area Simulator—Model development and evaluation. USDA Forest Service Res. Pap. RMRS-RP-4.

Gamon, J. A., Serrano, L. and Surfus, J.S. (1997). The photochemical reflectance index: an optical indicator of photosynthetic radiation use efficiency across species, functional types, and nutrient levels. *Oecologia*, *112*(4), 492–501.

Gao, B. C. (1996). NDWI - A normalized difference water index for remote sensing of vegetation liquid water from space. *Remote Sensing of Environment*, 58(3), 257–266.

Gong, P., Pu, R. L., and Miller, J. R. (1995). Coniferous forest Leaf-Area Index estimation along the Oregon Transect using Compact Airborne Spectrographic Imager data. *Photographic Engineering and Remote Sensing*, 61(9), 1107–1117.

Green, R. O., Conel, J. E., and Roberts, D. A. (1993). Estimation of aerosol optical depth and additional atmospheric parameters for the calculation of apparent reflectance from radiance measured by the Airborne Visible/Infrared Imaging Spectrometer. *Summaries of the Fourth Annual JPL Airborne Geoscience Workshop*, Pasadena, California: Jet Propulsion Laboratory.

Huete, A. R. (1988). A Soil-Adjusted Vegetation Index (SAVI). *Remote Sensing of Environment*, 25(3), 295–309.

Mehroff, L. A. (1998). Endangered and threatened species, in Atlas of Hawai'i, 3rd ed., eds. S. P. Juvik and J. O. Juvik,. University of Hawai'i Press, Honolulu, pp. 150–153.

Peñuelas, J., Filella, I., Biel, C., Serrano, L., and Save,R. (1993). The reflectance at the 950–970 nm region as an indicator of plant water status. *International Journal of Remote Sensing*, *14*, 1887–1905.

Riaño, D., Chuvieco, E., Salas, J., Palacios-Orueta, A., and Bastarrika, A. (2002). Generation of fuel type maps from Landsat TM images and ancillary data in Mediterranean ecosystems. *Canadian Journal of Forest Research*, *32*(8), 1301–1315.

Roberts, D. A., Ustin, S. L., Ogunjemiyo, S., Greenberg, J., Dobrowski, S. Z., Chen, J., and Hinckley, T. M. (2004). Spectral and structural measures of Northwest forest vegetation at leaf to landscape scales. *Ecosystems*, *in press*.

Roberts, D. A., Batista, G. Pereira, J., Waller, E, and Nelson, B. (1998a). Change identification using multitemporal spectral mixture analysis: Applications in eastern Amazonia, *in* Remote Sensing Change Detection: Environmental Monitoring Applications and Methods, eds. C. Elvidge and R. Lunetta, pp. 137–161, Ann Arbor Press, Chelsea, Michigan.

Roberts, D. A., Brownz, K., Green, R., Ustin, S., and Hinckley, T. (1998b). Investigating the relationship between liquid water and leaf area in clonal Populus. *Summaries of the Seventh JPL Airborne Earth Science Workshop.* Pasadena, California: Jet Propulsion Laboratory.

Rothermel, R. C, Wilson, R. A.,Morris, G. A. and Sackett, S. S. (1986). Modeling moisture content of fine dead wildland fuels input to the BEHAVE fire prediction system. USDA Forest Service Res. Pap. INT-359.

Sims, D. A. and Gamon, J. A. (2003). Estimation of vegetation water content and photosynthetic tissue area from spectral reflectance: a comparison of indices based on liquid water and chlorophyll absorption features. *Remote Sensing of Environment*, *84*(4), 526–537.

State of Hawaii Office of Planning. (1998). Hawaii Statewide Geographic Information System. http://www.hawaii.gov/dbedt/gis/ (last accessed 11/01/04).

Wright, C. S., Ottmar, R. D., Vihnanek, R. E., and Weise, D. R. (2002). Stereo photo series for quantifying natural fuels: Grassland, shrubland, woodland, and forest types in Hawaii. USDA Forest Service Gen. Tech. Rep. PNW-GTR-545.

EXAMINING SEASONAL CHANGES IN CANOPY MOISTURE
USING AVIRIS TIME SERIES DATA

Philip E. Dennison[1] and Dar A. Roberts[2]

1. Introduction

Canopy moisture content has both ecological importance as indicator of vegetation response to drought stress and importance in terms of fire danger, as canopy moisture is a major determinant of the ability of fire to propagate through vegetation canopies. Imaging spectrometer data are well-suited to measuring canopy water moisture using water absorption features in the near- and shortwave- infrared. This paper examines the use of Airborne Visible Infrared Imaging Spectrometer (AVIRIS) and Moderate Resolution Imaging Spectrometer (MODIS) data for mapping and monitoring canopy moisture content in chaparral in the Santa Monica Mountains of Southern California.

2. Background

Canopy water content is measured as live fuel moisture for fire danger assessment (Countryman and Dean, 1979). Live fuel moisture is the mass of liquid water divided by the mass of dry vegetation:

$$M = \frac{m_w - m_d}{m_d} \tag{1}$$

where M is the live fuel moisture, m_w is the measured mass of a fresh, undried sample, and m_d is the measured mass of a dried sample. Live fuel moisture in chaparral typically follows a seasonal trend, with high live fuel moisture in the winter and spring and low fuel moisture in summer and fall (Figure 1). Live fuel moisture peaks between 130-160% in chamise (*A. fasciculatum*), a species common in Southern California chaparral. Live fuel moisture declines through the summer and fall to reach approximately 60%, a level that is referred to as the "critical" live fuel moisture. At this level, fire will readily propagate through chamise canopies by the combustion of live fuels. The ability to monitor changes in live fuel moisture and identify the onset of critical live fuel moisture could permit more efficient allocation of personnel and resources in fire prone areas.

Canopy water content measures in the near-infrared are based on weak water absorption features centered around 970 nm and 1200 nm wavelength. Equivalent water thickness (EWT) is a measure of canopy water content that can be easily derived from hyperspectral data (Gao and Goetz, 1995). EWT models reflectance (ρ_λ) as a linear function of wavelength (λ) multiplied by an absorption function:

$$\rho_\lambda = (m\lambda + b)e^{-t\alpha_\lambda} \tag{2}$$

[1] Department of Geography, University of Utah
[2] Department of Geography, University of California, Santa Barbara

where *m* and *b* are coefficients that determine the slope and intercept of the linear function, α_λ is the absorption coefficient of liquid water, and *t* is the equivalent water thickness (Gao and Goetz, 1995; Green, 2003). Thus EWT is the equivalent amount of water that would be necessary to reproduce the water absorption feature in the reflectance spectrum. An alternative measure of canopy water absorption, normalized difference water index (NDWI) is portable to multispectral data. NDWI (Gao, 1996) uses a normalized difference index to compared the reflectance measured in the 1200 nm water absorption feature and reflectance measured in a reference band. For MODIS data, NDWI is calculated as:

$$\text{NDWI} = \frac{\rho_{857} - \rho_{1241}}{\rho_{857} + \rho_{1241}} \tag{3}$$

where ρ_{857} is the reflectance in a near infrared reference band and ρ_{1241} is the reflectance at the edge of the 1200 nm water absorption band (Gao, 1996).
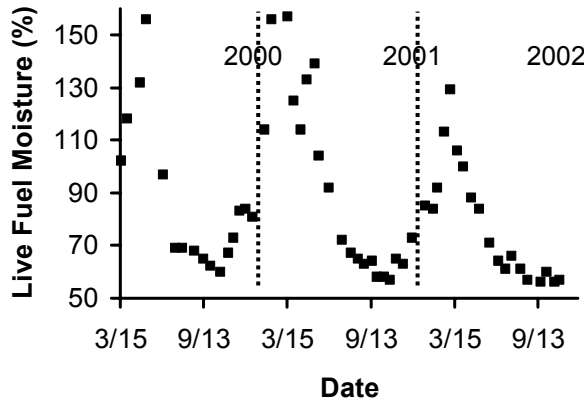

Figure 1. Seasonal trends in chamise live fuel moisture as measured by the Los Angeles County Fire Department at Clark Motorway, March 2000-October 2002.

Several studies have demonstrated relationships between spectral measures of water absorption and canopy moisture. Sims and Gamon (2003) compared the ability of water indices to estimate vegetation water content. They found indices based on the 970 nm and 1200 nm water absorption bands to be the best predictors of canopy water content. Serrano et al. (2000) compared water index (WI), NDWI, and EWT calculated from AVIRIS data to relative water content in chaparral. WI and NDWI accounted for most of the variation in canopy relative water content, but the relationship between these indices and relative water content was found to be species dependent. Roberts et al. (1997) and Ustin et al. (1998) identified seasonal changes in EWT that were dependent on changes in canopy moisture in chaparral. Peñuelas et al. (1997) used time series field spectrometer data to relate WI to the relative water content of Mediterranean plant seedlings. Zarco-Tejada et al. (2003) modeled EWT from a Moderate Resolution Imaging Spectrometer (MODIS) time series and found a good correlation with field-measured relative water content.

3. Methods

Two methods were used to demonstrate remote sensing retrieval of canopy water content in chaparral: 1) EWT was calculated for an AVIRIS time series, and then compared to live fuel moisture sampled by the Los Angeles County Fire Department (LACFD) and to cumulative water balance index (CWBI), a relative measure of drought stress; and 2) NDWI was calculated for an MODIS time series, and was compared live fuel moisture sampled by the LACFD.

AVIRIS Time Series

Fifteen high-altitude AVIRIS images acquired over the Santa Monica Mountains, California between 1994 and 2002 were used to construct a time series. AVIRIS data were corrected to apparent surface reflectance using MODTRAN (Green et al., 1993). Images were registered to an orthorectified SPOT image sampled to a resolution of 20 meters. EWT was calculated for each pixel by fitting equation (2) to the 850-1100 nm spectral region using non-linear least squares. CWBI was calculated for each date by cumulatively summing precipitation and reference evapotranspiration measured by a California Irrigation Management Information System (CIMIS) station in Santa Monica, California (Dennison et al., 2003).

EWT and live fuel moisture from the LACFD Clark Motorway site were compared using linear regression. A mean EWT value was determined for the site by extracting EWT values from a polygon containing homogeneous vegetation cover around the coordinates of the site. Homogeneity was determined using a 1 meter resolution orthophotograph. A sigmoidal function was used to compared EWT for each pixel within the time series and CWBI:

$$EWT = a + \frac{b}{1 + e^{-(c + d \cdot CWBI)}} \tag{4}$$

where *a* is the minimum EWT, *b* is the range in EWT, and *c* and *d* control the slope and timing of the sigmoidal function. Four AVIRIS dates were excluded from the time series fit with equation (4), with three dates excluded due to registration errors and one date excluded due to extremely high precipitation during the winter of 1998, which skewed the CWBI calculated for that date.

MODIS Time Series

Terra MODIS data acquired between March 2000 and October 2002 were used to construct a time series for Southern California. The MODIS 500-meter resolution daily surface reflectance product (MOD09GHK version 4; Vermote et al., 1997) was used to create 10-day cloud masked composites. Median reflectance within the masked 10-day window was calculated for each band and for each pixel in the time series. NDWI was calculated for each 10-day composite using equation (3). NDWI was extracted for a single pixel containing the Clark Motorway live fuel moisture site. Since LACFD does not report actual sampling dates, the date of the actual report was used to determine the date of the composite used for comparison.

4. Results

EWT demonstrated a strong, linear relationship with live fuel moisture measured at the Clark Motorway site (Figure 2). A linear regression of live fuel moisture against EWT produced a R^2 of 0.83. NDWI calculated from MODIS data was also positively correlated with live fuel moisture measured at the Clark Motorway site (Figure 3). A linear regression of live fuel moisture against NDWI produced a R^2 of 0.73.
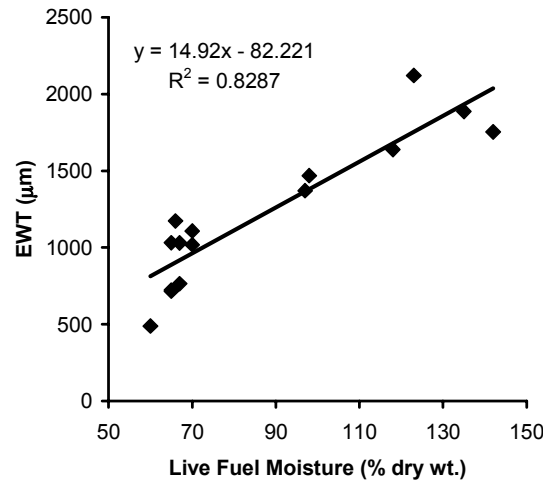
Figure 2. Live fuel moisture vs. EWT for the Clark Motorway chamise site.
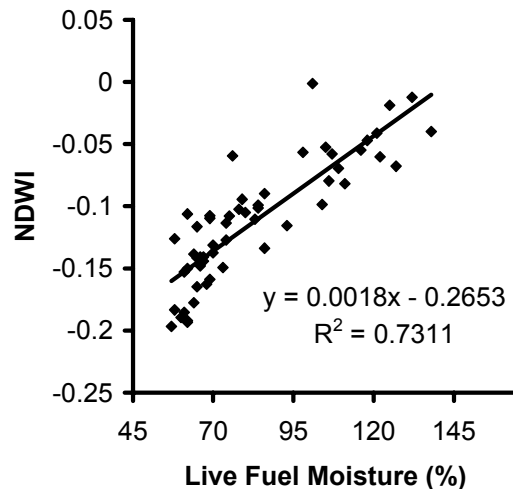
Figure 3. Live fuel moisture vs. MODIS NDWI for the Clark Motorway chamise site.

Fit parameters derived from Equation 4 for CWBI and EWT are shown in Figure 4. RMSE of the model fits was below 0.3mm in most naturally vegetated areas, and higher in residential and agricultural areas surrounding the Santa Monica Mountains (Figure 4a). RMSE was highest in pixels with temporal vegetation disturbances such as wildfire or human activity. Fire scars from the 1993 Green Meadow Fire (G), 1996 Calabasas Fire (C), and 1993 Topanga Fire are clearly visible in Figure 4a. Minimum EWT (Figure 4b) and maximum EWT (Figure 4c) define the baseline and upper limit canopy water absorption. The minimum and maximum EWT values are highest in high elevation areas outside of the fire scars. The modeled inflection points demonstrated

several important spatial trends (Figure 4d). The most rapid change in EWT occurred at small negative CWBI values in lower elevation grassland and chaparral areas in the northern and eastern Santa Monica Mountains (Figure 4d). Inflection points occurred at more negative CWBI values in higher elevation, inland areas of the Santa Monica Mountains.
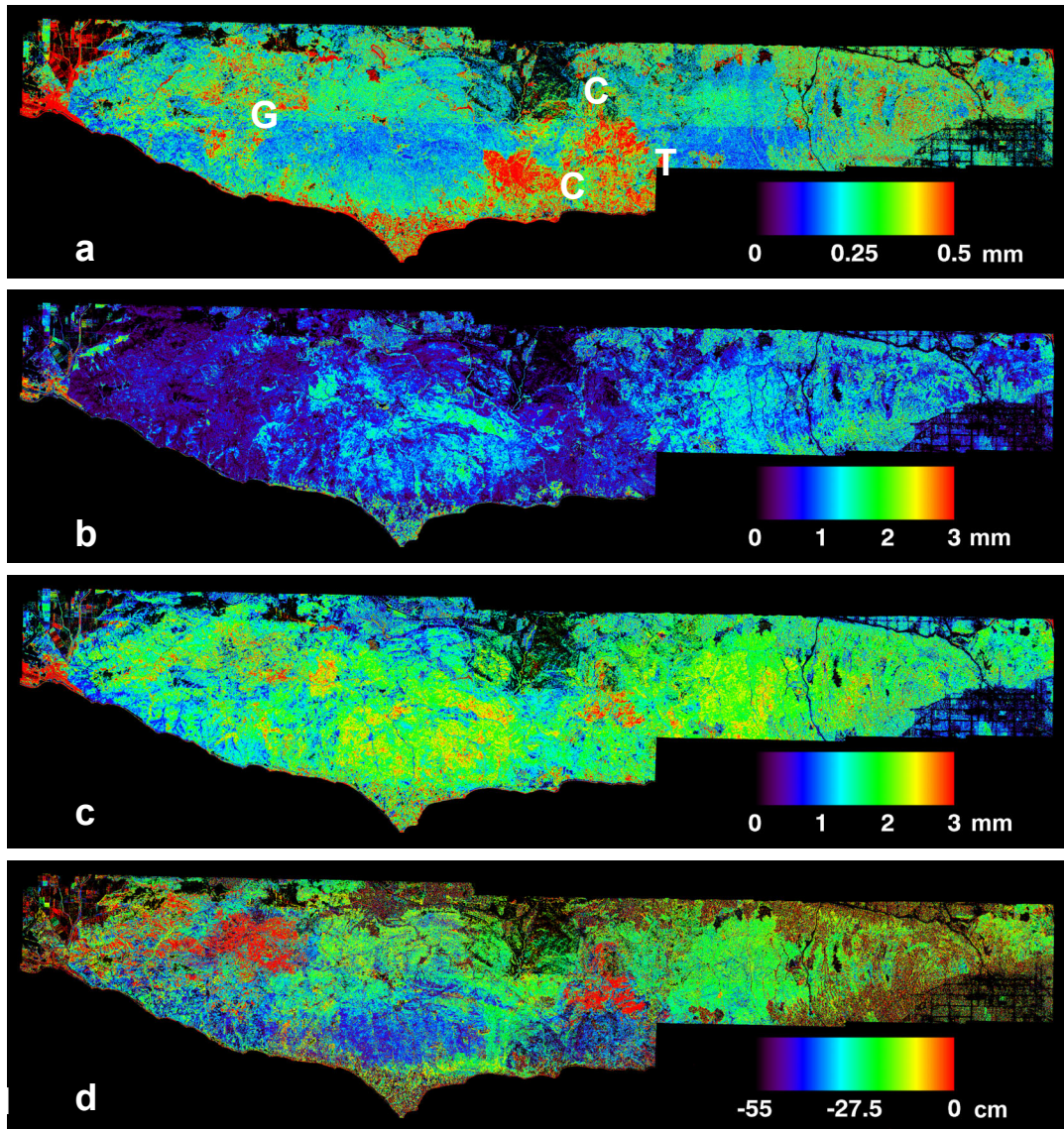
Figure 4. Sigmoidal model fit parameters for the time series: a) root mean square error, b) minimum EWT, c) maximum EWT, and d) inflection point. Fire scars are marked in the RMSE image as the 1993 Green Meadow Fire (G), the 1993 Topanga Fire (T), and the northern and southern halves of the 1996 Calabasas Fire (C).

Both the minimum and maximum EWT were closely related to aboveground biomass (Figure 5). Minimum and maximum EWT were compared to biomass measured at seven chaparral sites in the Santa Monica Mountains (Regelbrugge and Conard, 1997; Dennison et al., 2003). The two linear regressions between biomass and EWT had similar slopes, but the intercept term for maximum EWT possessed

an intercept 0.87 mm higher than the intercept for minimum EWT. Minimum EWT had the strongest correlation with biomass, with an R^2 of 0.88 (Figure 5).

Figure 5. Live aboveground biomass versus the minimum and maximum EWT.

5. Discussion

Both AVIRIS EWT and MODIS NDWI demonstrate strong relationships with live fuel moisture measured at a single sample site. The correlation between NDWI and live fuel moisture is somewhat weaker than the correlation between EWT and live fuel moisture. Differences in the strengths of the two relationships may be due to difference in spatial resolution. While the actual size of the sample 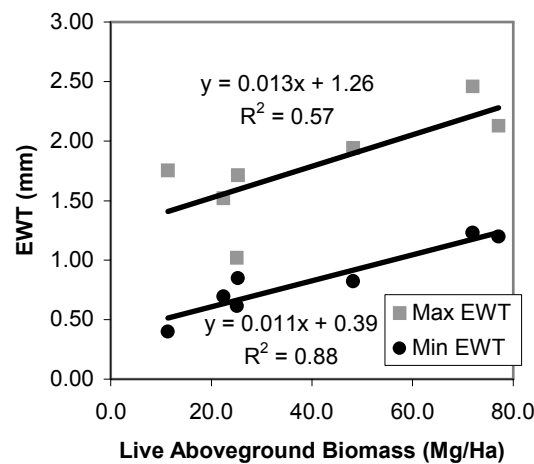site is unknown, Countryman and Dean (1979) recommended that frequently sampled sites possess a size of approximately 3-4 hectares. In contrast, a 500 meter MODIS pixel contains 25 hectares, within which significant variation in land cover type and topography can occur. Twenty-meter AVIRIS data were averaged for the comparison of live fuel moisture and EWT, which may have reduced spatial variation in spectral characteristics.

Both Figures 2 and 3 show higher variability in EWT and NDWI at the critical live fuel moisture of 60%. While live fuel moisture does not drop below 60% in live chaparral, extreme drought stress may lead to a reduction in leaf area or partial die-back of chaparral canopies. Changes in canopy biomass are difficult to discriminate from changes in canopy moisture using any method of quantifying spectral water absorption (Gao, 1996). Where reduction in canopy biomass occurs, EWT and NDWI may underestimate live fuel moisture. An index with greater range at high drought stress, such as CWBI, may be more appropriate for characterizing changes in canopy moisture during periods of extreme drought.

Time series EWT modeled by CWBI reveals spatial differences in EWT minima, maxima, and inflection points. Conditions that may cause spatial variation in drought stress may include the prevalence of vegetation species, soil depth and water capacity, and topographic variability of solar insolation and precipitation. Higher elevation areas in the Santa Monica Mountains receive higher precipitation, and portions of the range

closer to the Pacific Ocean may receive reduced evapotranspiration and additional moisture from marine fog. These factors may delay the onset of drought stress at higher elevation and coastal sites.

6. Conclusions

Both EWT calculated from AVIRIS data and NDWI calculated from MODIS data were found to be related to chaparral live fuel moisture measured in the Santa Monica Mountains. Using CWBI, spatial trends in the minimum and maximum EWT values and the CWBI inflection point were observed. The results of this work point to different roles for a high resolution hyperspectral sensor such as AVIRIS and a coarse resolution multispectral instrument such as MODIS. AVIRIS data can best be used for the detailed spatial analysis of vegetation response to drought stress. A small number of well-timed data acquisitions could reasonably characterize seasonal changes in canopy moisture, as shown with the Santa Monica Mountains time series. An airborne hyperspectral sensor can not provide a means for active monitoring of changes in canopy moisture. This is a role better suited to MODIS, which allows frequent (daily-to-weekly) retrieval of vegetation response to drought stress.

7. Acknowledgements

8. References

Countryman, C.M., and Dean, W.A., 1979, Measuring moisture content in living chaparral: a field user's manual. U.S. Dept. of Agriculture, Forest Service, Pacific Southwest Forest and Range Experiment Station, Berkeley, California.

Dennison, P.E., D.A. Roberts, S.R. Thorgusen, J.C. Regelbrugge, D. Weise, and C. Lee., 2003, "Modeling seasonal changes in live fuel moisture and equivalent water thickness using a cumulative water balance index." Remote Sensing of Environment, 88: 442–452.

Gao, B.-C., 1996, NDWI – A Normalized Difference Water Index for Remote Sensing of Vegetation Liquid Water from Space, Remote Sensing of Environment, 58(3): 257–266.

Gao, B.-C. and Goetz, A.F.H., 1995, Retrieval of equivalent water thickness and information related to biochemical components of vegetation canopies from AVIRIS data, Remote Sensing of Environment, 52:155–162.

Green, R.O., 2003, Understanding the three phases of water with imaging spectroscopy in the solar reflected energy spectrum. Dissertation, University of California Santa Barbara, Santa Barbara, California.

Green, R., Conel, J., and Roberts, D., 1993, Estimation of aerosol optical depth and additional atmospheric parameters for the calculation of apparent surface reflectance from radiance as measured by the Airborne Visible-Infrared Imaging Spectrometer (AVIRIS). Summaries of the Fourth Annual JPL Airborne

Geosciences Workshop, Jet Propulsion Laboratory, Pasadena, California, pp. 73–76.

Peñuelas, J., Pinol, J., Ogaya, R., and Filella, I., 1997, Estimation of plant water concentration by the reflectance water index (WI) (R900/R970). International Journal of Remote Sensing, 18:2869–2875.

Regelbrugge, J.C., and Conard, S.G., 1997, Biomass and Fuel Characteristics of Chaparral in Southern California. Fire in California Ecosystems: Integrating Ecology, Prevention, and Management, November 17–20, 1997.

Roberts, D.A., Green, R.O., and Adams, J.B., 1997, Temporal and spatial patterns in vegetation and atmospheric properties from AVIRIS. Remote Sensing of Environment, 62:223–240.

Serrano, L., Ustin, S.L., Roberts, D.A., Gamon, G.A., and Penuelas, J., 2000, Deriving water content of chaparral vegetation from AVIRIS data. Remote Sensing of Environment 74:570–581.

Sims, D.A., and Gamon, J.A., 2003, Estimation of vegetation water content and photosynthetic tissue area from spectral reflectance: a comparison of indices based on liquid water and chlorophyll absorption features. Remote Sensing of Environment, 84:526–537.

Ustin, S.L., Roberts, D.A., Pinzon, J., Jacquemoud, S., Gardner, M., Scheer, G., Castaneda, C.M., and Palacios-Orueta, A., 1998, Estimating canopy water content of chaparral shrubs using optical methods. Remote Sensing of Environment, 65:280–291.

Vermote, E.F., El Saleous, N.Z., Justice, C.O., Kaufman, Y.J., Privette, J., Remer, L.C., and Tanre, D., 1997, Atmospheric correction of visible to middle infrared EOS-MODIS data over land surface, background, operational algorithm and validation. Journal of Geophysical Research, 102: 17131–17141.

Zarco-Tejada, P.J., Rueda, C.A. and Ustin, S.L., 2003. Water content estimation in vegetation with MODIS reflectance data and model inversion methods. *Remote Sensing of Environment*, 85: 109–124.

INCREASED SPATIAL AND TEMPORAL CONSISTENCY OF LEAFY SPURGE MAPS FROM MULTIDATE AVIRIS IMAGERY: A MODIFIED, HYBRID LINEAR SPECTRAL MIXTURE ANALYSIS/MIXTURE-TUNED MATCHED FILTERING APPROACH

Kathleen Burke Dudek,[1] Ralph R. Root,[2] Raymond F. Kokaly,[3] Gerald L. Anderson[4]

1. INTRODUCTION

Imaging spectroscopy has been predominantly used for research-oriented studies, although more recently there has been increased interest in exploiting imaging spectroscopy to address applied problems. Applied work has lagged behind in part due to the complex, interactive processing that hyperspectral imagery requires and to the associated "learning curve." Land managers may be aware of the potential benefits of the technology for ecological monitoring, but are most often not well versed in hyperspectral processing and analysis. Current processing methods require specialized training or advanced experience in remote sensing in order to determine the most appropriate methods to use, to make informed decisions during interactive processing, and to determine whether results are realistic and accurate.

The intent of this work was to develop specific strategies to facilitate and streamline analysis, and eliminate interactive steps that require in-depth knowledge of the ground to guide processing decisions. If the need for advanced training or experience can be minimized, imaging spectroscopy may become a more widespread tool for ecological and other applied work. In the application tested here, the suitability of multi-temporal AVIRIS data for monitoring change in *Euphorbia esula* L. (leafy spurge) over a two-year period was evaluated. High altitude AVIRIS data were collected 6 July 1999 and 21 June 2001 over Theodore Roosevelt National Park (THRO) (Figure 1). A specific goal was to determine which methods are most appropriate for applied work, as well as evaluate problems that are unique to multi-temporal imaging spectroscopy. Successful management of leafy spurge over time, and monitoring of ecosystem characteristics in general, requires reliable identification of plants over time and space. This necessitates processing methods that are explicitly defined and repeatable, and that yield accurate and consistent results. Imaging spectroscopy has been used previously to map invasive species including leafy spurge (DiPietro et al., 2002; Kokaly et al., 2001; O'Neill et al., 2000; Parker-Williams and Hunt, 2002; Root et al., 2002). Relatively few studies, however, have used multi-temporal imaging spectroscopy, and fewer still have focused on problems that are uniquely encountered with multi-temporal hyperspectral data processing. Primary applications of remote sensing in general include monitoring and change detection, yet imaging spectroscopy has been underexploited in these areas.

Leafy spurge is an aggressive perennial invasive that was introduced into the U.S. and Canada in the early 19th century and has since spread throughout much of North America (Anderson et al., 2003; Dunn, 1979, 1985). It is a particularly serious problem in the northern Great Plains States and Prairie Provinces of Canada, where it has serious economic and environmental consequences (Bangsund et al., 1993; Beck, 1996; Leitch et al., 1994; Wallace et al., 1992). It is difficult to monitor due to a relatively non-selective habitat, ranging from dry hills to swampy riparian habitats throughout remote rangelands, wildlands, and cultivated and disturbed areas (Callihan et al., 1990; Galitz, 1994). The weed requires a substantial effort to control, with greatest success realized when small, emergent patches are treated within the first years of establishment (Lajeunesse et al., 1997). Imaging spectroscopy has been suggested as a means for locating smaller, nascent patches that are often fragmented and difficult to locate, as well as for temporal monitoring of treatments that have been applied over larger established infestations.

To streamline, refine, and automate current processing, standard hyperspectral mapping methods were tested and modified within a commercially available software package, Environment for Visualizing

---

[1] Dept. of Forest, Rangeland, and Watershed Stewardship, Colorado State University (kaydudek@cnr.colostate.edu)
[2] Deceased
[3] USGS Spectroscopy Laboratory
[4] USDA, ARS, Northern Plains Agricultural Research Laboratory

Systems (ENVI). Specific objectives for the refinement included: decreasing the influence of analyst decisions or bias; decreasing the need for expert knowledge or advanced training; decreasing the need for ground support or reference data; and decreasing the need for conclusive *a priori* knowledge of the target endmember spectrum. The ultimate goal of the project is to produce accurate and *consistent* multi-temporal maps and avoid misinterpretations due to apparent change (e.g., changes that are a reflection of differences in processing over time rather than real landcover change).
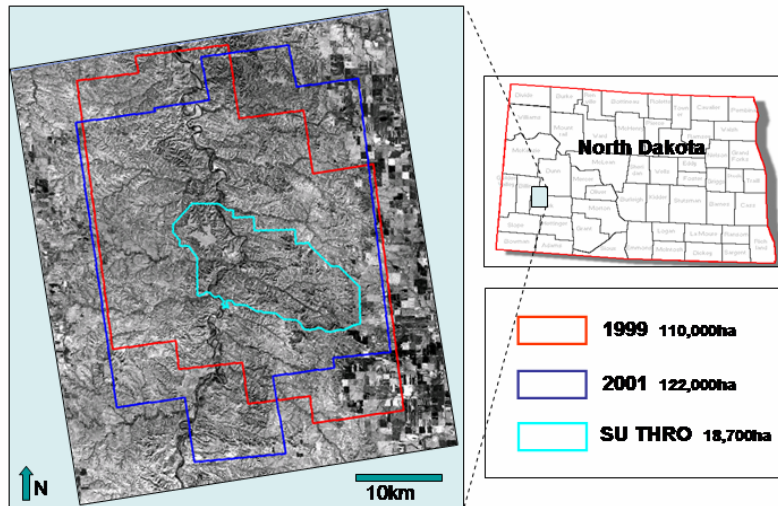

Figure 1. Study area: South Unit THRO and adjacent National Grasslands, South Unit outlined in cyan. AVIRIS coverage indicated in red (1999) and blue (2001), 4 flightlines per date with 35-40% sidelap.

2. PREVIOUS WORK

The potential impact of differences in processing methodology was suggested by initial test maps. These maps of leafy spurge were produced using several different algorithms, including spectral angle mapper (SAM) (Kruse et al., 1993), linear spectral mixture analysis (SMA) (Adams et al., 1993), spectral feature fitting (SFF) (Clark et al., 1990), and mixture-tuned matched filtering (MTMF) (Boardman, 1998). The results indicated that the proportion of leafy spurge that was mapped varied dramatically depending on the algorithm that was used (Figure 2). The map results were also sensitive to threshold decisions as well as some preprocessing steps including band editing, cross-track illumination correction, and image masking. The source and quality of the spectral library also impacted the results (see discussion in Dudek, 2005). The variability of the results produced from identical data that were associated strictly with processing differences suggests that change maps produced from independently-processed, multi-temporal hyperspectral imagery could therefore include spurious results and a misleading representation of change. Apparent change could instead represent an artifact of processing rather than true temporal differences in landcover. This in turn could lead to erroneous interpretation of the effect of controls and the advance and decline of infestations, which could result in inappropriate decisions regarding treatment effects and future management decisions.

3. METHODS

Standard hyperspectral preprocessing and processing methods were applied and have been described previously (Root et al., 2002). These included, for example, calibration to reflectance using ACORN software (Atmospheric Correction Now) and georeferencing using a thin plate spline model (Geomatica User Guide, 2003).
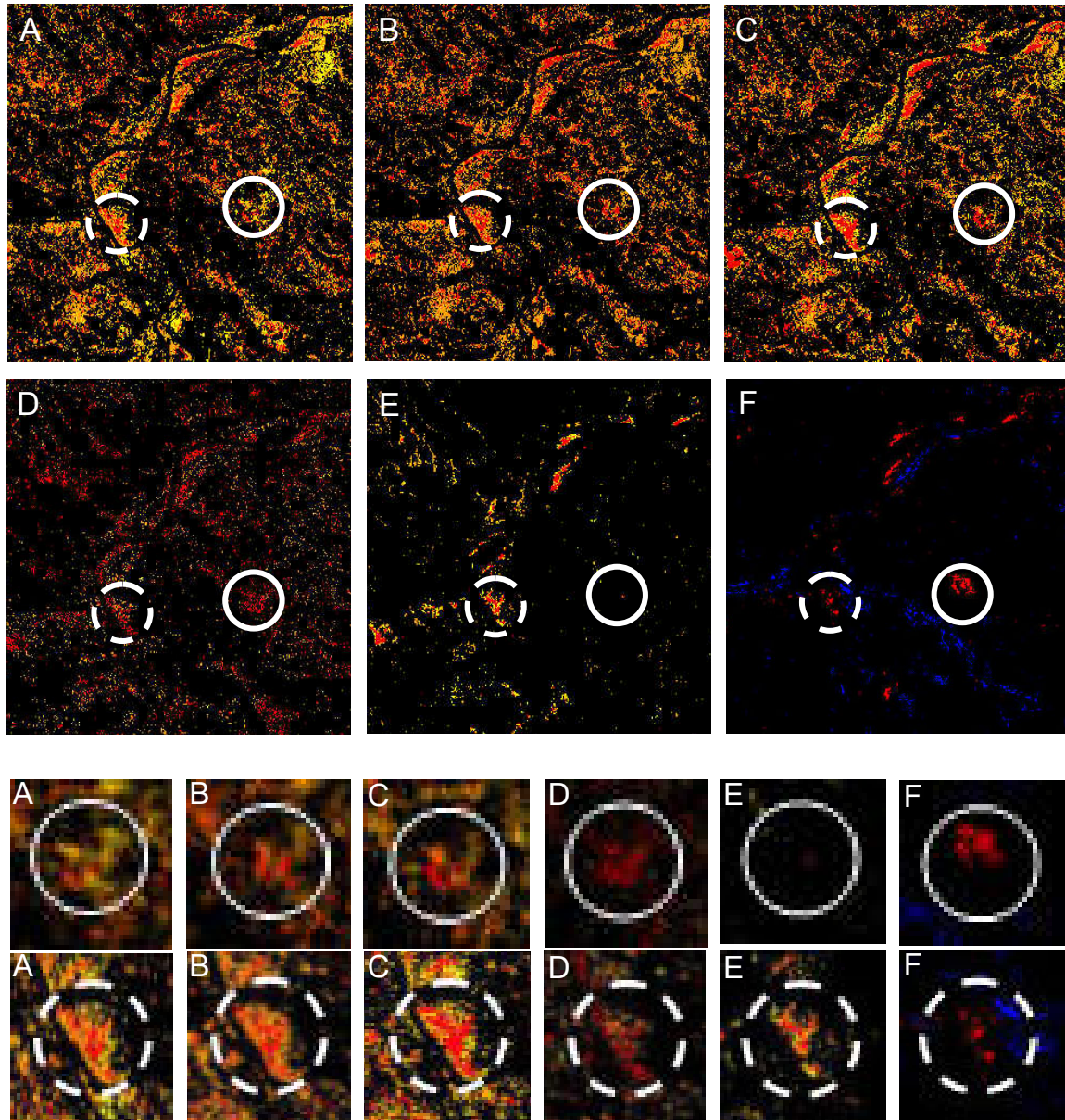
Figure 2. Leafy spurge test maps from identical data. All methods except E incorrectly mapped the assemblage within the solid circles as leafy spurge. The area of known leafy spurge (broken circles) was mapped with all methods but was over-classified in A, B, and C; under-classified in F; and slightly under-classified in E. E is considered most accurate overall and therefore was the method selected as a starting point for the modifications and refinements.

Preprocessing steps that were crucial for accurate mapping included: cross-track illumination correction (ENVI User's Guide, 2003; Kennedy et al., 1997) and liberal editing of bands, including removal of bands displaying anomalous spikes within the chlorophyll absorption region. The MTMF algorithm in conjunction with an image-derived endmember library produced the most accurate results and was therefore selected for all additional processing and refinement (see Figure 2E).

Once preprocessing was completed, the mapping technique generally followed the "hourglass" mapping scheme (CSES, 2000), but with several modifications (Figure 3). These included: 1) a two-step endmember selection: first, for general landcover classes, followed by collection of vegetation

endmembers only from an NDVI-masked image; the collection strategy was modified for the masked image endmember selection; 2) for each additional flightline on a given date (in a scene), a minimum noise fraction (MNF) re-transformation of the spectral library derived from a single flightline; 3) hybrid application of the MTMF algorithm: input all possible endmembers; solve for all endmember fractions; 4) modified application of the MTMF algorithm: eliminate threshold decisions by first using rule classification to assign MF thresholds, then using +1 sigma from the mean noise units as a standard threshold for infeasibility score refinement. These steps are described in detail below.
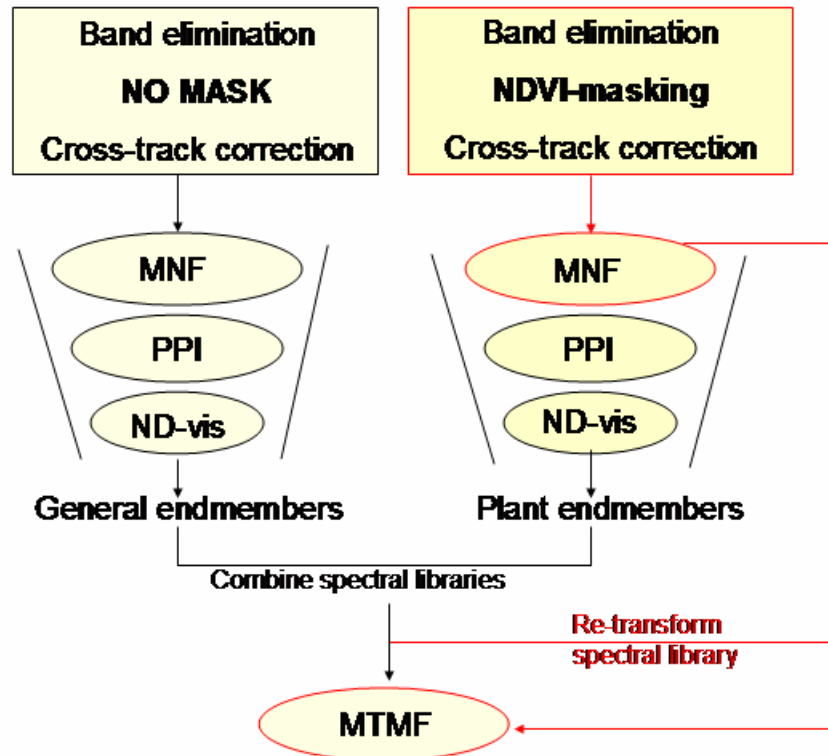

Figure 3. Modified hourglass processing: two-stage endmember collection for the initial flightline, with the added second step indicated in darker yellow; additional steps for subsequent flightlines on each date are outlined in red. Critical preprocessing steps are indicated in the two boxes, listed in the order applied.

3.1 Two-stage endmember library collection

For mapping, two endmember libraries were derived independently from the image. It was necessary to extract a full set of general landcover endmembers from the full image in order to correctly derive endmember fractions in vegetation-dominated pixels containing inert materials as a minor component. Initially, the full non-masked image was transformed with the minimum noise fraction (MNF) to decrease noise and reduce the dimensionality of the data set (Green et al., 1988). With the pixel purity index (PPI), the most spectrally unique individual pixel spectra were isolated and input to the n-dimensional visualizer in ENVI to collect a set of general landcover endmembers (Figure 4A) (ENVI, 2003). Twenty-two input MNF bands were sufficient to represent the variance of, and therefore isolate, these major landcover classes.

For the collection of the plant endmembers, pixels that were dominated by vegetation were isolated by applying an NDVI-based mask to the image. The threshold for the mask was set to differentiate between dominantly vegetation and non-vegetated landcover, at a value of .40. This value was based on empirical tests of several thresholds on this data set. The threshold effectively excluded large (>> 1 pixel) soil-dominated areas, but retained portions of small roads that were adjacent to vegetated areas that

displayed vegetation signatures resulting from mixing of vegetation with pavement or soil. This effectively included all significant vegetation within the scene in the masked "vegetation-only" image. All 35 coherent MNF bands were input to the n-dimensional visualizer for selection of the plant endmembers (Figure 4B).
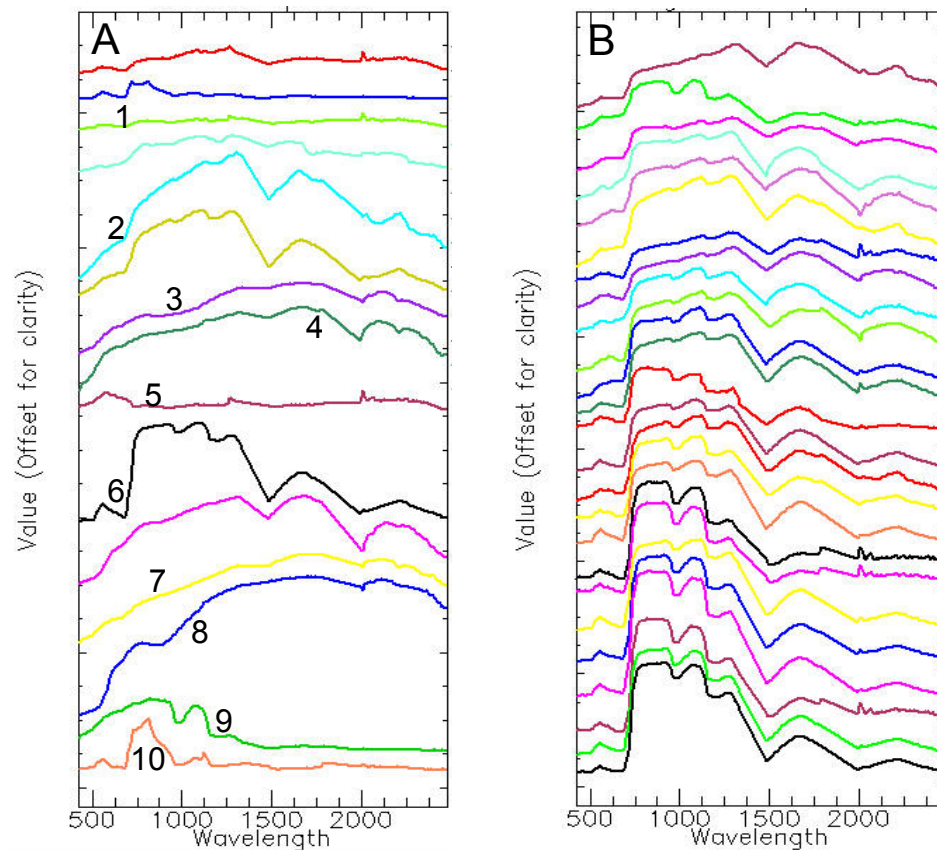

Figure 4. A sample of the general endmember spectra (derived from full image) is shown in A, including examples of shadow (1), senescent vegetation (2), soil and rock classes (3,4,7,8), water (5), vegetation (6), silty water (9), and eutrophic water (10). B includes sample vegetation endmember spectra (derived from the NDVI-masked image).

3.2 Modified strategy for endmember collection

Generally, when endmembers are selected using the n-dimensional visualizer in ENVI, aggregates of pixels are selected at the outer extremes of spectrally well-separated extensions from the central pixel cloud (ENVI, 2003). This strategy was used to select the general landcover endmembers (Figure 5A). Because the pixels from the masked image were dominated by vegetation, however, the pixel cloud was spectrally homogeneous, and presented very few unique, well-defined extensions in spectral space. A different strategy was used, therefore, to select the vegetation endmember set. Only the most extreme few pixels on the ends of small protrusions from the more homogeneous pixel cloud were selected to represent potential species endmembers (Figure 5B). There were many more of these subtle extensions than the number of input MNF bands, however, and any possible unique set of pixels on these extensions was collected. The selection of potential endmembers continued until no additional extreme pixels could reasonably be obtained. Sixty-one potential vegetation endmembers were collected, and it was assumed that a complete set of endmembers had been extracted for this scene. Both the vegetation and general landcover spectra were edited for consistency, redundant classes were removed, the mean spectrum for each class was calculated and then added to the spectral library. The two libraries were combined, with

the final complete libraries containing 62 (for 1999) and 63 (in 2001) total endmembers. All endmembers were input to the MTMF algorithm, however, the classified scenes were dominated by only 20-25 classes, with several classes represented by only a few pixels in all the flightlines.
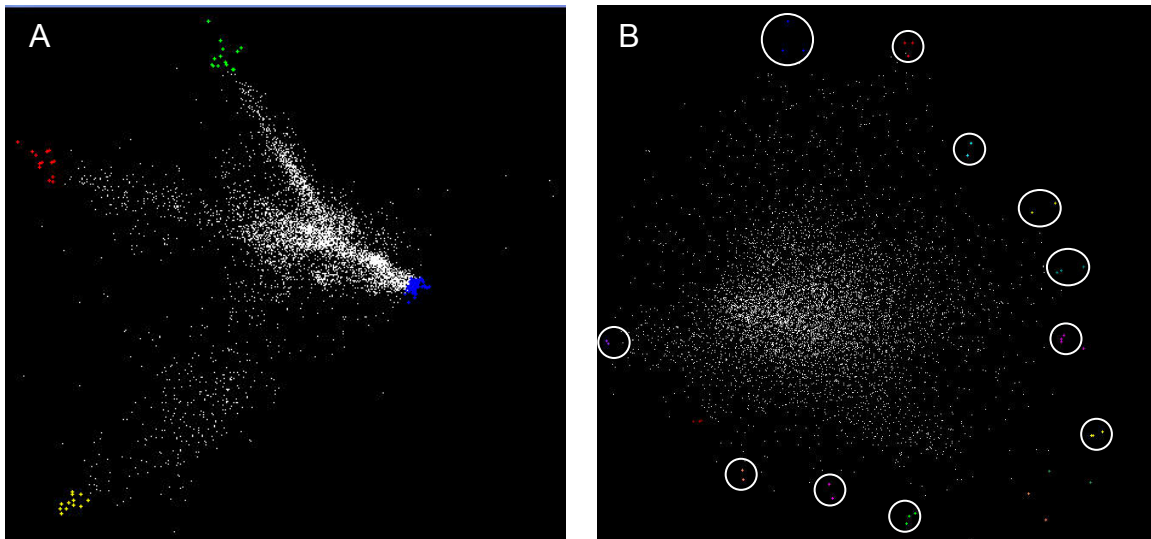

Figure 5. Two-step selection of endmembers from ND-visualizer scatter plots. A: general landcover class selection using large clusters of isolated extreme pixels from full image; B: vegetation endmember selection from small, subtle extensions from the more homogeneous, centralized vegetation cloud, using small groups of pixels (generally 2-5 pixels per class) from masked image.

3.3 Spectral libraries for multiple flightlines: comparisons and retransformations

To map multiple flightlines, two options can be used for the input image-derived spectral library: 1) a single library, derived from one flightline then applied to all other flightlines or 2) individual spectral libraries, derived independently from each flightline, and used to map that respective flightline. To test which approach was more appropriate for multi-flightline, multi-temporal mapping and change detection, test maps were produced using both options. With 35-40% sidelap between flightlines, it was possible to test the consistency of maps from one flightline to the next for the spectral library options by comparing classifications of identical areas from adjacent, overlapping flightlines. Figure 6A indicates the maps of identical areas classified on flightlines 1 and 3 that were produced using two unique libraries (i.e., one library was derived from and used to map flightline 1, and a second from flightline 3). Overall landcover was consistent within the coverage of the two test flightlines; therefore, it was expected that the endmember classes extracted from each of the flightlines would be similar. Roughly equivalent groups of pixels were defined as distinct classes on the two flightlines. It was difficult to directly compare the results, however, because the libraries were not identical and class codes varied. Seamless mosaics could not be produced without recoding and re-coloring equivalent classes between flightlines. With several flightlines and many endmembers, recoding all flightlines to the identical class codes (and colors) would be cumbersome and time consuming.

To avoid coding problems, a single spectral library, derived from flightline 1, was applied directly to map all four flightlines from a single date. The results from flightlines 1 and 3 are shown in B. Because the identical library was used to map both flightlines, the green endmember class should indicate leafy spurge in both images. It is correctly mapped on flightline 1, but incorrectly on flightline 3 (see Figure 6, B1 vs. B3). It is difficult to identify a single spectral class that represents leafy spurge in the classified image from flightline 3. The remaining vegetation classes also do not correspond well between the two flightlines.
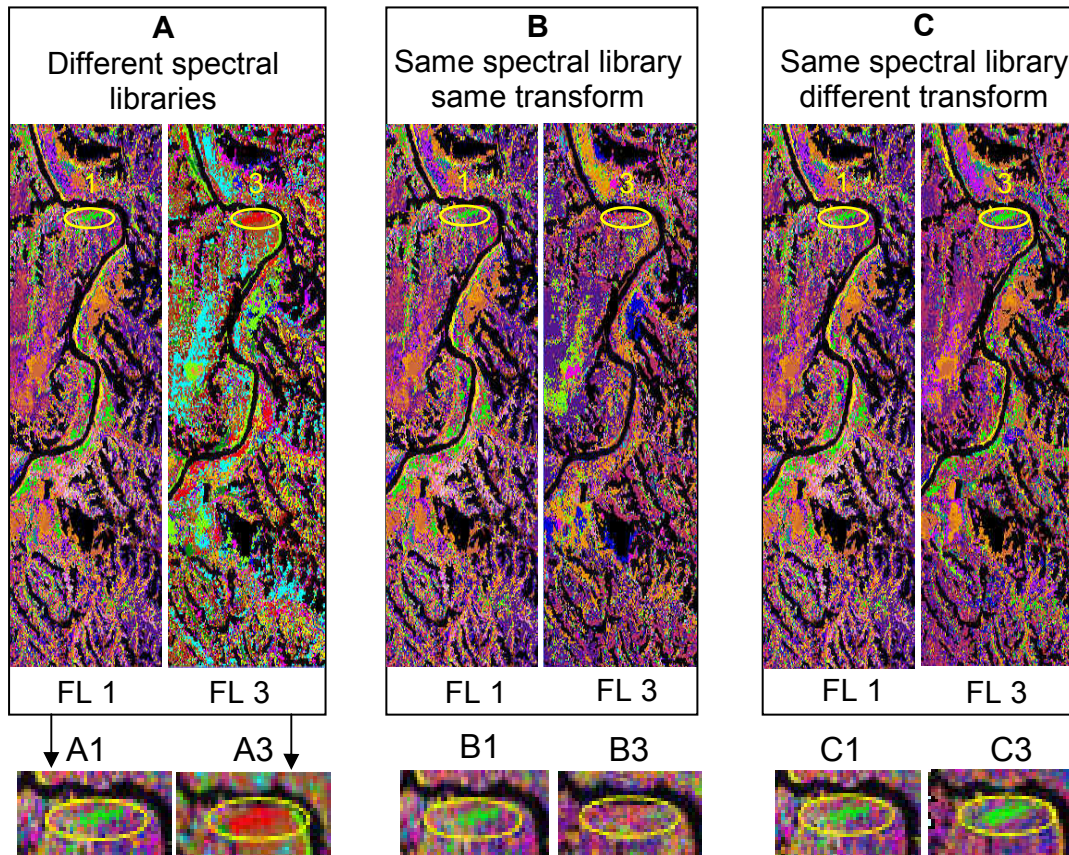
Figure 6. Spectral library effects between flightlines. The area of leafy spurge circled in yellow is enlarged below each corresponding flightline. Green pixels indicate a known leafy spurge patch in A1, B1, and C1 (which are identical classifications). Spurge is well-defined in the corresponding flightline 3 area for A3 and C3, but poorly classified in B3. Comparisons are difficult between A1 and A3 due to mismatched codes between the 2 separate libraries. C (same library, different transformation) provides the most consistent, interpretable results between flightlines.

If the original single spectral library derived from the single flightline is inverse transformed, however, then re-transformed using the MNF statistics files that were generated during the MNF transformation of each individual flightline, and then used to classify that flightline , very good class correspondence is obtained from one flightline to the next (see Figure 6, C1 and C3). Using this single, re-transformed spectral library allows processing to be streamlined by eliminating the need to extract spectral libraries from each flightline, or to adjust codes following classification. Mosaicing and analyses between flightlines are facilitated because the original input spectra are the same, all classes are identical, and coding is consistent from one flightline to the next.

3.4 Modified, hybrid MTMF application

Modifications of the MTMF application focused on reducing interactive decisions during processing, and specifically included altering the input endmembers, as well as developing a new strategy for post-classification thresholding. A hybrid approach used the logic of linear spectral mixture analysis (SMA), while the MTMF algorithm was applied for the actual mapping.

A critical modification involved running the MTMF algorithm with all possible endmembers, using an approach that amounts to a hybrid between linear SMA and MTMF. It is generally considered an advantage of the MTMF that it requires only one to a few target endmembers to map specific materials.

To use this approach, however, the target endmember spectrum must be unequivocally identified prior to mapping. This can be difficult for plant species or assemblages, particularly when a large number of similar endmembers have been extracted from an image. For this reason a hybrid approach was used. All possible endmember classes were input to the algorithm, similar to linear SMA mapping in which all endmembers must be represented in order to simultaneously retrieve the endmember fractions (Adams et al., 1993). With SMA, however, the total number of endmembers is actually restricted to the number of input bands plus 1. Based on homogeneity of spectral plots as well as visual absence of spatial patterns in the imagery, 34-36 MNF bands (depending on flightline) were considered coherent enough to use for mapping in this study. This would mathematically restrict the number of endmembers to 35-37, if the SMA algorithm was used. If there appeared to be additional endmembers, they would not be used for mapping and the target endmember could be excluded. The exhaustive endmember set collected from this data, for example, contained 63 possible endmembers, and if SMA was used, nearly half of these would be discarded. With the modified MTMF, by inputting all endmembers, no *a priori* decision regarding the most appropriate target spectrum was required. Once mapping was completed, however, the target class and endmember spectrum were readily identified by using a GIS overlay of vegetation polygons, including leafy spurge patches, on the classified image. These polygons were delineated by continuously collecting GPS point locations while circumscribing the perimeter of vegetation patches in the field.

The method for selecting MTMF thresholds was modified by automating the process using: 1) a rule classification to establish the MF threshold; and 2) applying a standard +1 sigma for selecting the infeasible threshold. The output of the MTMF algorithm is a matched filter (MF) score image and an infeasibility image for each endmember. In the traditional application of this algorithm, maps are produced from the MTMF results by selecting hard thresholds for the target class(es) from a graphics display of MF score versus infeasibility score (Boardman, 1998). Pixels with high MF and low infeasibility scores represent the most suitable values for accurately defining a class. These are selected manually by defining a region of interest (ROI) around the selected combination of MF and infeasible values. This approach is subjective, however, and thresholds will vary from one analyst to another, one time to another, as well as between flightlines. Even within a single flightline the selection will vary because the graphical method only applies the threshold to those pixels that are within the currently displayed image window. A test of this standard method indicated that minor variations in the ROI produced critical differences in leafy spurge maps (Figure 7). An accurate map could be produced with this method (i.e., Figure 7C), but to do so required several manual adjustments of the ROI until the resulting map corresponded to known occurrences of leafy spurge on the ground.

A different approach was developed to remove subjective boundary decisions on the part of the analyst. Initially a post-classification "rule classifier" (ENVI, 2003) was used to produce a fully classified, thematic map similar to the output from traditional multi-spectral classifiers (Lillesand and Kiefer, 2000). All 63 endmember matched filter images were included in the rule classification, with the assignment of the dominant class based on the highest of the 63 MF scores for each pixel. This allowed a map of the dominant material within each pixel to be produced, without requiring a decision on an absolute, single threshold. With this technique, manual adjustment of thresholds based on intimate knowledge of the ground was not required, and the threshold was automatically determined individually for each pixel rather than forcing the selection of a single image-wide threshold.

A map of the leafy spurge target class was produced from the classified map by masking and isolating pixels that mapped as leafy spurge as the dominant class. This leafy spurge map was then refined using a standardized infeasibility threshold. Based on several test thresholds, +1 sigma above the mean infeasibility score from the target image was selected as the standard. This was determined to be an appropriate boundary for leafy spurge, for all eight flightlines classified in this study; however, this boundary was not tested on other vegetation classes. The +1 sigma value placed the thresholds for each image at a value that eliminated most known false positives, while no large or obvious known patches of leafy spurge were omitted. By applying this as the standard threshold no interpretive decision was required by the analyst to establish the infeasible threshold.
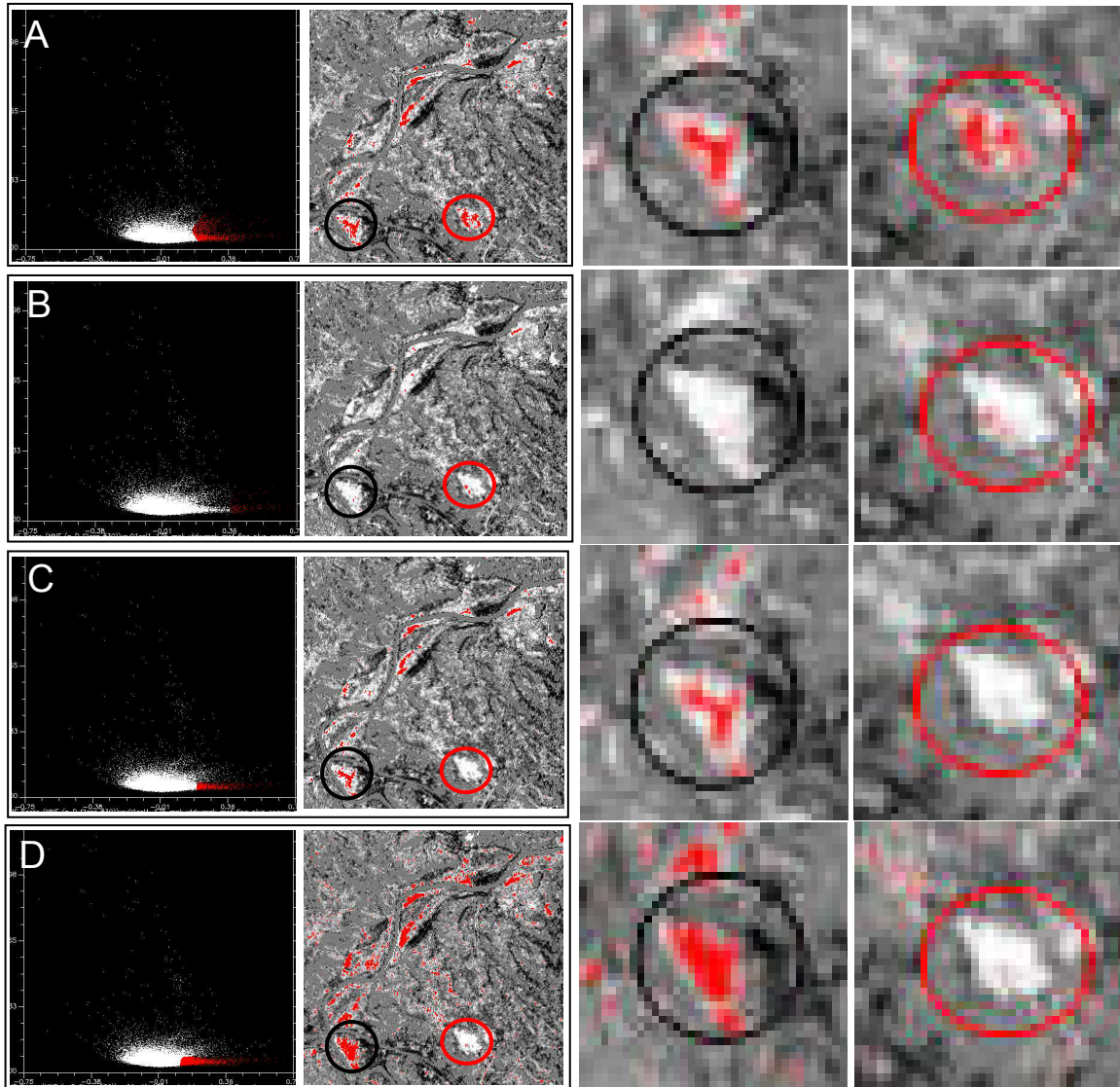
Figure 7. User-defined graphical selection of thresholds. Red pixels are those that have been labeled leafy spurge, based on the corresponding scatter plot ROI to the left. The area circled in black contains a known dense infestation of spurge; the red circled area is known to be free of leafy spurge. In A, C, and D the ROIs have correctly included MF/infeasible values to map the spurge (see black circles); the A and B ROIs have also incorrectly included values within the leafy spurge mapping threshold for other types of vegetation as well and therefore required adjustment (see red circles). C and D are close to the known occurrence of leafy spurge in the field, but D is overclassified (black circle); while C is slightly underclassified (black circle). Ground reference data was required to adjust the ROIs until the map fits the correct distribution.

The maps produced with the hybrid, modified MTMF method successfully defined known patches of leafy spurge, while at the same time spectrally similar vegetation that had been easily confused with leafy spurge using other classification strategies was effectively excluded (see Figure 8). The black and red circled areas in this figure correspond to those in Figure 7, and show a similar distribution to the map in 7C, the most correct classification obtained by manually and repeatedly adjusting ROI thresholds; however, the automated, modified mapping method produced a qualitatively accurate classification, without requiring decisions, interpretation, or manual adjustments to produce the best fit to known ground

locations. By using standardized, automated thresholds, results will be more comparable temporally, rather than reflect artifacts due to differences in selected thresholds or manual adjustments by image analysts.
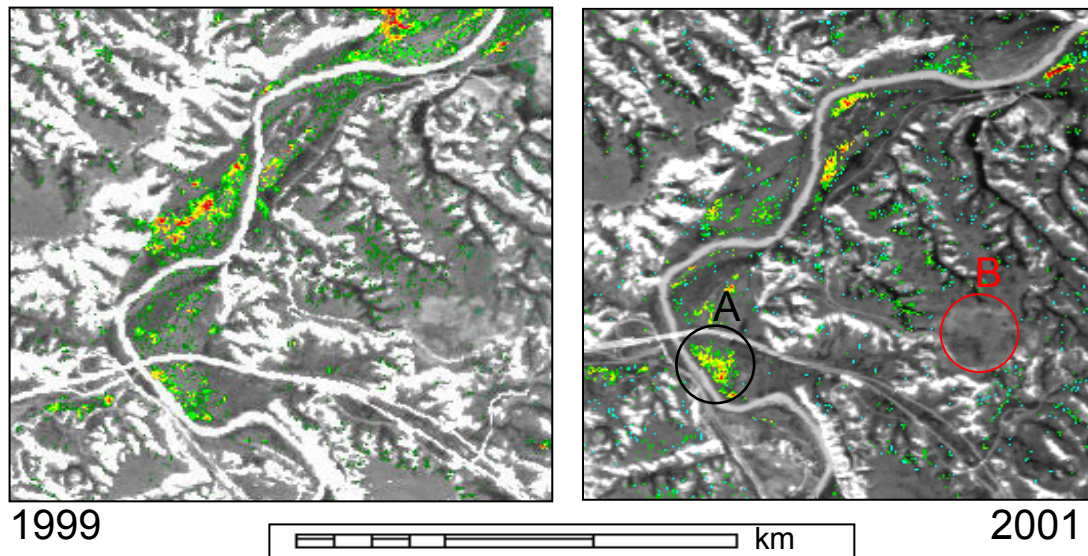
Figure 8. 1999 and 2001 leafy spurge maps produced from modified MTMF. Only pixels in which spurge represents the dominant component are mapped. The relative fraction (abundance?) is indicated by color. Red is highest fraction, followed by orange, yellow, then greens/cyan represent the lowest fraction, leafy spurge classified pixels. On the 2001 map, the black circle labeled A encloses a known area of dense leafy spurge; B (red circle) is an area known to be devoid of spurge.
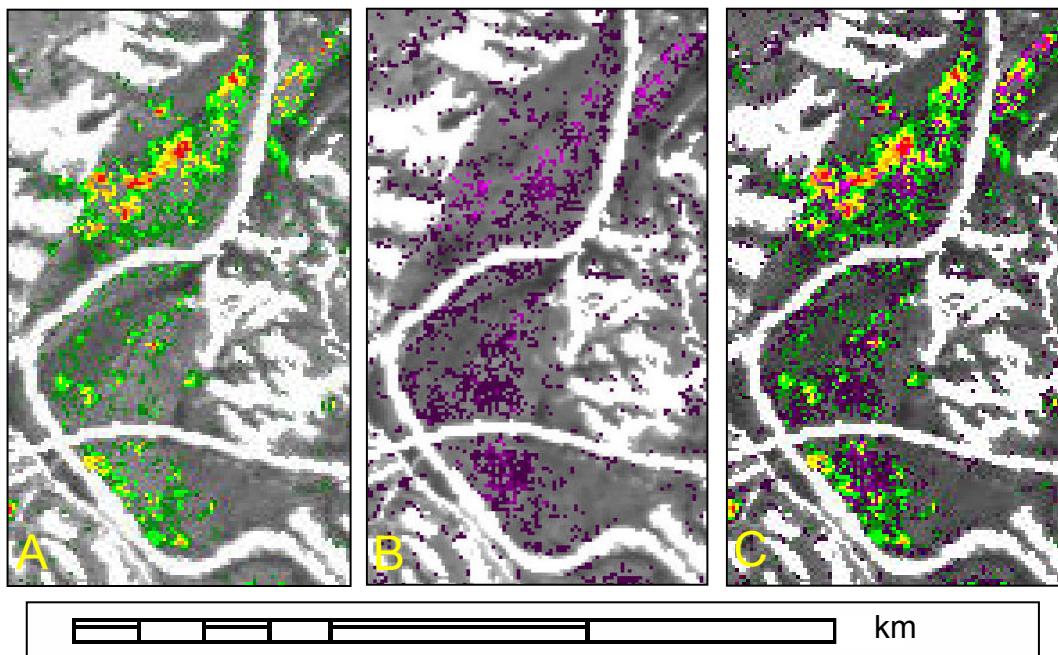
Figure 9. 1999 leafy spurge maps. A: density-sliced categories of primary map (leafy spurge the dominant component of mapped pixels); B: density-sliced map of secondary map (leafy spurge fractions in pixels where weed is a subordinate component); C: primary and secondary density-sliced leafy spurge

maps combined. Lightest magenta: highest fraction; deep magenta lowest; Red: highest fraction, decreasing from orange through yellow, green, and dark green.

Figure 10. A and C: binary (presence/absence) maps of leafy spurge, 1999 and 2001; B: density sliced map of leafy spurge as subordinate fraction of pixels (lightest magenta represents the highest fraction, deep magenta the lowest fractional abundances).

The final binary leafy spurge maps from 1999 and 2001 were density-sliced, using equal interval MF scores to produce maps that approximate the relative abundance of leafy spurge in those areas where it represented the dominant vegetation within a pixel. The MF score is assumed to represent a surrogate measurement of abundance. The 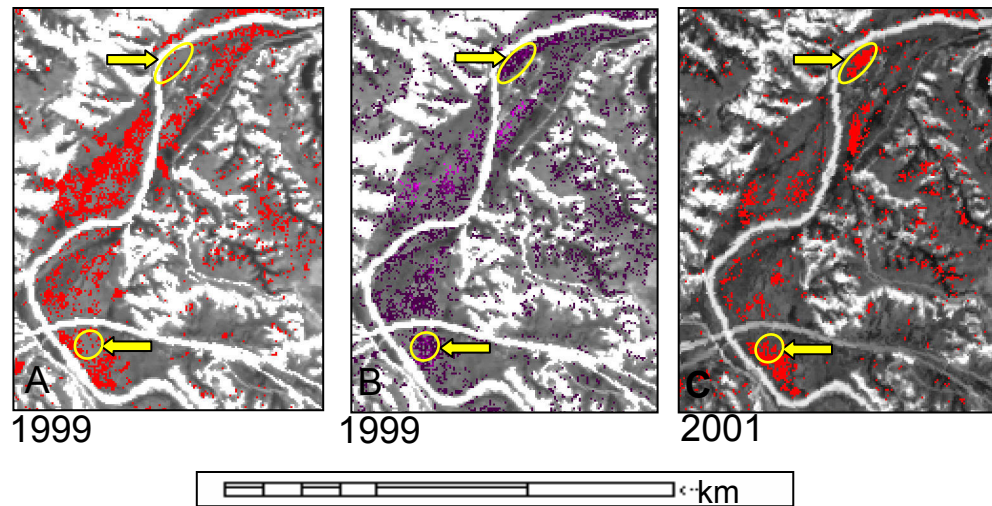method above yields maps indicating the relative abundance only in pixels in which leafy spurge represents the dominant fraction (Figure 8).

These maps will underestimate the occurrence of leafy spurge, because they do not include the fractional abundance of leafy spurge for pixels in which the weed is a subordinate, yet still significant component of a pixel. To address this problem a secondary leafy spurge map was created using the identical density slice range from the leafy spurge MF image for all pixels that did not map leafy spurge as the dominant class (Figure 9). In Figure 10, areas circled in yellow indicate pixels that did not map as leafy spurge dominant in 1999, but were classified as leafy spurge in 2001. The same areas contain continuous patches of leafy spurge as low fraction, non-dominant components of these same pixels in the 1999 secondary map. Such areas may prove useful as predictors of areas prone to future heavy infestations.

3.5 Rapid, automated vegetation mapping

An intermediate product of the process was a full scene vegetation map for all non-masked pixels (Figure 11, B for 1999 and C for 2001). These maps compared favorably to a published vegetation map (see Figure 11, A) produced from 1:10,000 scale aerial photography (Anderson et al., 1996). The modified MTMF is an alternative to manual photo-interpretation for vegetation mapping, and the maps from 1999 and 2001 compare favorably to the photo-interpreted map, but are more detailed, as it will map the dominant vegetation within 17 m² versus the standard 1- or 5-acre minimum mapping unit used by vegetation mapping programs. This technique also generates significant savings in time and effort for area-wide vegetation mapping.
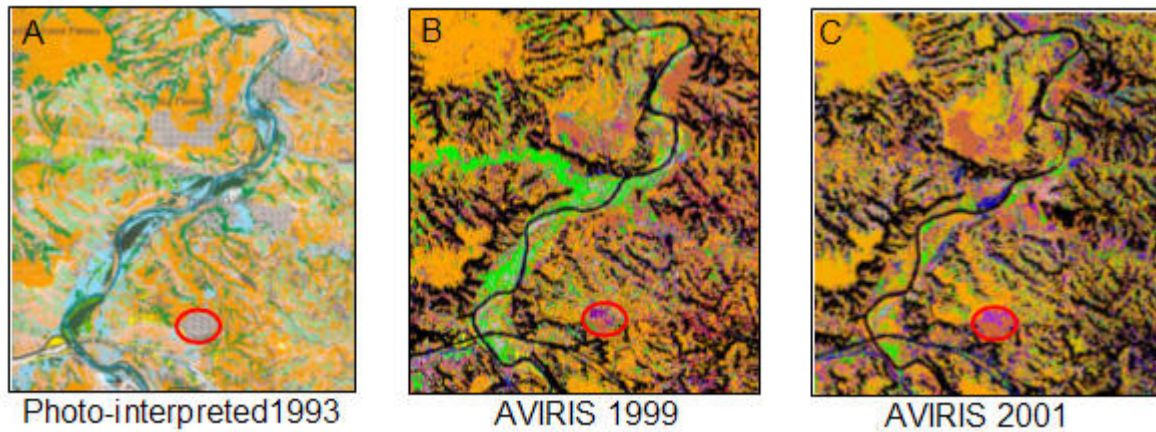
Figure 11. AVIRIS and photo-interpreted maps, showing advance and decline in leafy spurge (light green) between 1993 and 2001. Greater species/assemblage separation seen with AVIRIS maps (i.e., see red circled area that mapped as a single vegetation assemblage on 1993 map, two distinct vegetation classes in 1999 and 2001 AVIRIS maps. Black in the AVIRIS maps indicates non-vegetated landcover that was masked.

4. ACCURACY

Map accuracies were evaluated with a random point-based confusion matrix that is routinely used to validate multi-spectral classifications (Congalton and Green, 1998). Low overall accuracies were indicated: 39% for 1999, and 47% for 2001. User's accuracy values were high, however, (100% in 1999 and 86% in 2001) indicating that relatively little vegetation was erroneously classified as leafy spurge. The low producer's accuracy (26% for 1999 and 18% for 2001), however, suggests that a significant fraction of the leafy spurge was omitted from the map. High omission error was expected, because the accuracy assessments were run on the binary map of leafy spurge as the dominant component of a pixel only. Updated accuracies using the combined leafy spurge dominant and subordinate maps are in progress, however, the type and scale of the validation data (centroids of 3 m x 5 m plots) that were used as reference data in the error matrices was not appropriate for validating 17-m data. In addition, because leafy spurge often occurs in small or fragmented patches, the accuracy results were particularly sensitive to registration shifts. Overlay of field-defined vegetation polygons over the raster classifications suggests that the maps are likely better that the error matrices suggest (Figure 12). A visual comparison of the
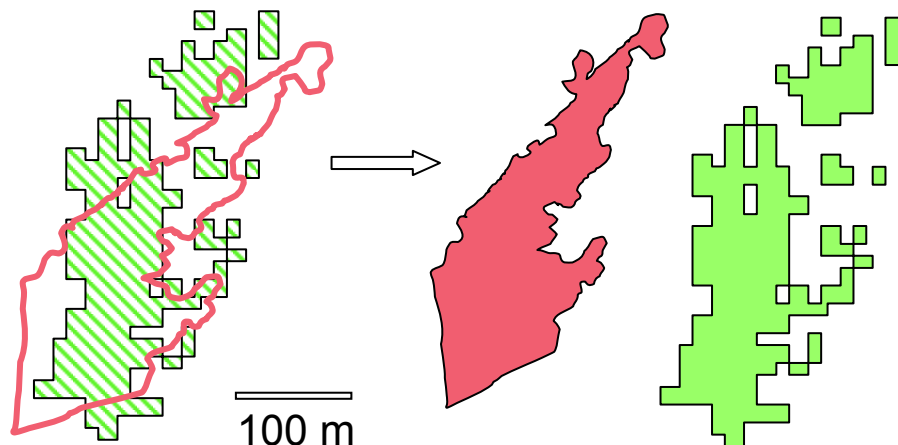

Figure 12. Field polygon (red) versus classified (green); size and shape correspond, location appears rotated between field location and imagery.

polygon delineated in the field to the area classified as leafy spurge suggests that the refined mapping method used here works well, but also suggests that registration problems persist between the image and reference data (that registration between image and reference data is problematic); for example, the overlay suggests a rotation between the raster and vector locations, which would result in lower accuracy values if the polygon were used as ground truth in an error matrix.

5. CHANGE MAPS

In spite of registration issues, the binary maps from 1999 and 2001 were successfully used to produce a map of the regional change in distribution of leafy spurge between these two years (Figure 13). In the western region, where bio-control efforts had been concentrated, the dominant blue indicates success of the treatments and reduction in leafy spurge. In the northeast, spotty red patches suggest expansion of leafy spurge in this region. Based on this information, land managers are planning to focus control efforts in this area that was formerly believed to be un-infested. The circled area in Figure 13 is dominated by areas of either no change or expansion of leafy spurge, and was originally believed to be erroneously classified, as this area was considered un-infested as well. A field check indicated heavy infestation with large continuous dense monocultures of leafy spurge, and the area was subsequently targeted for aerial spraying. The change map indicates approximately a 40% decrease in leafy spurge within THRO and the surrounding grasslands and range over the two-year period. Per-pixel change in fractional abundance could not be accurately determined. More precise registration between multi-temporal images will be required in order to complete temporal, pixel-to-pixel analyses, including a comparative study of the effectiveness of different controls that have been applied.
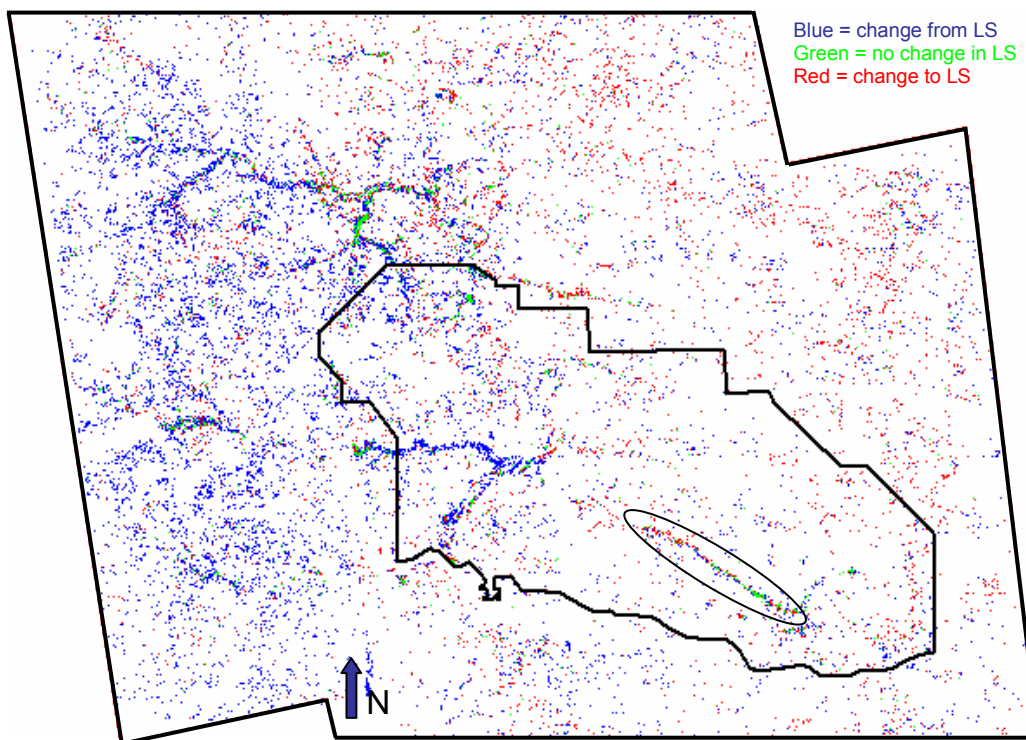

Figure 13. Change in leafy spurge (as the dominant component of a pixel) between 1999 and 2001. Blue indicates leafy spurge in 1999, absent in 2001 (reduction); green indicates leafy spurge both years (no change); red indicates leafy spurge absent in 1999, present in 2001 (expansion).

6. SUMMARY

Initial test maps of leafy spurge varied depending on the method that was used to produce them, indicating that the appropriate methods and algorithms should be selected cautiously. For detailed, accurate mapping of leafy spurge the following steps were critical: a cross-track illumination correction; thorough band editing; and endmembers derived from the image, after NDVI-masking to isolate vegetation. The MTMF algorithm performed well, and the associated infeasibility images allowed the classification to be fine-tuned.

The mapping method was then modified in order to decrease the interactive processing that was required and to increase the consistency of maps, both spatially and temporally. The critical modifications included: 1) separate extraction of general and vegetation libraries from unmasked and masked images, using a 2-step endmember collection with a modified selection strategy used to isolate classes; 2) selecting all possible endmembers from the imagery without restricting the selection to a theoretical maximum number; 3) detailed editing of endmember spectra and the final spectral libraries; 4) MNF retransformation of a single spectral library prior to mapping each flightline; 5) mapping with the MTMF algorithm using a hybrid approach with all possible endmembers as input rather than a single target endmember; 6) using a post-classification rule classifier to establish the MF threshold automatically and eliminate interactive, subjective decisions on MF threshold used for mapping; 7) applying a +1 sigma above the mean score from the infeasibility image to standardize the infeasible threshold selection for refinement of classification.

The modifications outlined above were used to capitalize on the advantages of the MTMF and linear SMA algorithms, while minimizing the drawbacks of each method. The resulting hybrid, modified MTMF method retains the advantages of both methods; for example with MTMF there is no restriction on number of endmembers, it is not necessary to simultaneously solve for all endmembers fractions, and additional infeasibility images are produced that allow maps to be refined. With linear SMA, theoretically all endmembers are derived and fractional abundances of all classes are calculated to produce a fully classified map without requiring decisions on thresholds. The modified method, however, addresses drawbacks of each algorithm and improves specifically on the MTMF application and results.

Because a full suite of all possible endmembers was extracted and used for mapping, and the number of endmembers is not restricted to a theoretical maximum with the MTMF, endmembers for subtly different classes can be collected for allow more successful species mapping. Theoretically, no classes were omitted, therefore a target endmember would not be inadvertently omitted. No *a priori* identification of the specific endmember target was required as is the case with the standard MTMF application using a single endmember. This is advantageous as it can be difficult to select the "most" correct image-derived endmembers before mapping is completed. This also eliminates another interactive decision at this stage of the processing. By using image-derived endmembers, classes are not restricted to those that could be characterized by ground-based spectral measurements.

When all MF scores "compete" for class assignment with the rule classifier, the threshold will automatically adjust as needed on a pixel-by-pixel basis. The best score class from all possible classes is simultaneously assigned, rather than requiring that each target class be individually mapped.

Sub-pixel abundance measurements are retained in the MF score images for each class. The target map can be extracted from the full classification and then coded by fractional abundance, and secondary maps of fractional abundance can also be produced for pixels in which a target is not dominant, but still a significant fraction of a pixel.

In addition to individual maps of specific targets, complete area-wide vegetation maps of the dominant material in each pixel can be produced rapidly and automatically, with greater detail than obtained with standard photo-interpreted vegetation mapping programs. The modified MTMF provides a potentially very useful method for more rapid, automated production of vegetation maps (over the standard manual interpretation of aerial photographs).

Because the spectral library was extracted from a single flightline, but transformed with the appropriate MNF statistics, results are more standardized and comparable between flightlines over a large

area. Spatial and temporal consistency of maps will be improved, and because all class coding is consistent, it allows easier comparisons, mosaicing, and analyses between flightlines.

By eliminating the need to decide on mapping thresholds or target endmembers, the modified MTMF is less interactive, and interpretive input and possible bias by the image analyst is minimized because the thresholds are determined automatically, using standardized criteria and methods.   Arbitrary decisions with respect to threshold placement are minimized, and images can be processed with less expertise. Complex technology and processing are more "user friendly", a bonus for monitoring and management applications. By standardizing thresholds, multi-temporal maps will be more comparable, as the thresholds are applied using consistent criteria over time.

Because interactive, manual adjustments are not necessary, the required validation data could potentially be minimized. In addition, the scene-wide threshold variability that results from the graphic threshold selection from isolated blocks of the full image is eliminated. Temporal monitoring is facilitated because results will be more comparable from one date to another. By increasing standardization and consistency of individual maps, change maps produced from them will more accurately represent real landcover changes, rather than apparent change that is actually an artifact of processing differences. By automating, processing is facilitated. A more standardized protocol can be developed, that can be applied more quickly and potentially with less training. Because the processing uses software and algorithms that are commercially available, no unique (in-house) programs or modifications of programs/software were required.

With this modified method, maps were as good as or better than any produced using interactive adjustments, and they were completed more rapidly. By explicitly selecting and defining a procedure, hyperspectral processing will be facilitated, and may lead to increased use by land managers as well as increase the chances of successful temporal and spatial monitoring of leafy spurge and other materials.

7. REFERENCES

Adams, J. B., M. O. Smith, and A. R. Gillespie, 1993, Imaging spectroscopy: Interpretation based on spectral mixture analysis, C.M. Pieters and P.A.J. Englert (Eds.), *Remote geochemical analysis: elemental and mineralogical composition*), New York: Cambridge Univ. Press, pp. 145–166.

Anderson, G.L., J.H. Evert, D.E. Escobar, N.R. Spencer, and R.J. Andrascik,1996, Mapping leafy spurge (*Euphorbia esula*) infestations using aerial photography and geographic information systems, *Geocarto International*, 11:81–89.

Anderson, G.L., E.S. Delfosse, N.R. Spencer, C.W. Prosser and R.D. Richard, 2003, Lessons in developing successful invasive weed control programs, *Journal of Range Management*, 56: 2–12.

Bangsund, D. A., J. R. Baltezore, J. A. Leitch, and F. L. Leistritz, 1993, Economic impact of leafy spurge on wildland in Montana, South Dakota, and Wyoming, *NDSU Agricultural Economics Report No.304*, North Dakota Agricultural Experiment Station, North Dakota State University, Fargo, North Dakota.

Beck, G. K., 1996, Leafy spurge, *Colorado State University Cooperative Extension No. 3*, 107, Natural Resources Series. http://www.colostate.edu/ds/

Boardman, J. W., 1998, Leveraging the high dimensionality of AVIRIS data for improved sub-pixel target unmixing and rejection of false positives: mixture tuned matched filtering, *Summaries of the seventh JPL Airborne Geoscience Workshop,* JPL Publication 97-1, Jet Propulsion Laboratory, Pasadena, California, pp. 55–56.

Callihan, R. H., J. P. McCaffrey, and V. J. Parker-Clark, 1990, Leafy spurge: biology and management. *The Service, December 1990, (Series no. 877)* 5p. Cooperative Extension System, Agricultural Experiment Station, University of Idaho, Moscow, Idaho.

Clark, R. N., A. J. Gallagher, and G. A., Swayze, 1990, Material absorption band depth mapping of imaging spectrometer data using the complete band shape least squares algorithm simultaneously fit to multiple spectral features from multiple materials, *Proceedings of the Third Airborne Visible/Infrared Imaging Spectrometer (AVIRIS) Workshop*, JPL Publication 90-54, Jet Propulsion Laboratory, Pasadena, California, pp. 176–186.

Congalton, R. and K. Green, 1998, *Assessing the Accuracy of Remotely Sensed Data: Principles and Practices,* CRC/Lewis Press, Boca Raton, Florida.

CSES, 2000, *Hyperspectral Imaging and Data Analysis*, Center for the Study of Earth from Space Short Course, June12-16, 2000, University of Colorado, p. 501.

DiPietro, D., S. Ustin, and E. Underwood, 2002, Mapping the invasive plant *Arundo donax* and associated riparian vegetation using AVIRIS, *Proceedings of the 11th JPL Airborne Earth Science Workshop,* Publication 03-4, Jet Propulsion Laboratory, Pasadena, California, pp. 65–74.

Dudek, K. B., 2005, Analysis and refinement of multi-temporal imaging spectroscopy methods for improving monitoring and management of *Euphorbia esula* L. (leafy spurge) in Theodore Roosevelt National Park, Ph.D. dissertation in progress, Colorado State University.

Dunn, P.H., 1979, The distribution of leafy spurge (*Euphorbia esula*) and other weedy *Euphorbia* spp. in the United States, *Weed Science* 27(5):509–515.

Dunn, P.H., 1985, Origins of leafy spurge in North America, *Leafy Spurge, Monograph series of the Weed Science Society of America*, Alan K. Watson, ed., 1985, Chapter 2 (3):7–13.

ENVI User's Guide, 2003, ENVI Version 4.0, September 2003 Edition, Research Systems, Inc.

Galitz, D., 1994, The biology of leafy spurge, *Proceedings: Leafy Spurge Strategic Planning Workshop*, Dickinson, North Dakota, March 29–30, 1994, pp. 57–62.

Geomatica 9 OrthoEngine User Guide, 2003, PCI Geomatics Enterprises, Inc., Richmond Hill, Ontario, Canada, p. 56-57.

Green, A. A., M. Berman, P. Switzer, and M. D. Craig, 1988, A transformation for ordering multispectral data in terms of image quality with implications for noise removal, *IEEE Transactions on Geoscience and Remote Sensing*, 26(1):65–74.

Kennedy, R. E., W. B. Cohen, and G. Takao, 1997, Empirical methods to compensate for a view-angle-dependent brightness gradient in AVIRIS imagery, *Remote Sensing of Environment* 62, 277–291.

Kokaly, R. F., R. Root, and K. Brown, 2001, Mapping the distribution of the invasive species leafy spurge (Euphorbia esula) in Theodore Roosevelt National Park using field measurements of vegetation spectra and CASI imaging spectroscopy data, *Third International Conference on Geospatial Information in Agriculture and Forestry*, Denver, Colorado. 5–7 November, 2001.

Kruse, F. A., A. B. Lefkoff, J. B. Boardman, K. B. Heidebrecht,, A. T. Shapiro, P. J. Barloon, and A. F. H. Goetz, 1993, The Spectral Image Processing System (SIPS) - Interactive Visualization and Analysis of Imaging Spectrometer Data, *Remote Sensing of Environment*, Special issue on AVIRIS, v. 44, pp. 145–163.

Lajeunesse, S., R. Sheley, R. Lym, D. Cooksey, C. Duncan, J. Lacey, N. Rees, and M. Ferrell, 1997, Leafy spurge: biology, ecology, and management, *EB-134, July 1997, Montana State University Extension Service*, 25 p.

Leitch, J. A., L. Leistritz, and D. A. Bangsund, 1994, Economic effect of leafy spurge in the upper Great Plains: Methods, models, and results, *Agricultural Economics Report No. 316*, March 1994. Department of Agricultural Economics, Agricultural Experiment Station, North Dakota State University, Fargo, North Dakota.

Lillesand, T. M. and R. W. Kiefer, 2000, *Remote Sensing and Image Interpretation*, John Wiley & Sons, Inc., New York.

O'Neill, M., S.L. Ustin, S. Hager, R. Root, 2000, Mapping the distribution of leafy spurge at Theodore Roosevelt National Park using AVIRIS, *Proceedings of the 9th Jet Propulsion Laboratory (JPL) Airborne Earth Science Workshop*, JPL Publication 00-18, Jet Propulsion Laboratory, Pasadena, California, pp. 339–347.

Parker-Williams, A. and E. R. Hunt, 2002, Estimation of leafy spurge cover from hyperspectral imagery using mixture tuned matched filtering, *Remote Sensing of Environment* 82, 448–456.

Root, R., S. Ustin, P. Zarco-Tejada, C. Pinilla, R.Kokaly, G. Anderson, K. Brown, K. Dudek, S. Hager, and E. Holroyd, 2002, Comparison of AVIRIS and EO-1 Hyperion for classification and mapping of invasive leafy spurge in Theodore Roosevelt National Park, *Proceedings of the 11th Jet Propulsion Laboratory (JPL) Airborne Earth Science Workshop*, JPL Publication 03-4, Jet Propulsion Laboratory, Pasadena, California, pp. 297–305.

Wallace, N. M., J. A. Leitch, and F. L. Leistritz, 1992, Economic impact of leafy spurge on North Dakota wildland, *NDSU Agricultural Economics Report No. 281*, 23 p. North Dakota Agricultural Experiment Station, North Dakota State University, Fargo, North Dakota.

High- and Low-Altitude AVIRIS Observations of Nocturnal Lighting

Christopher D. Elvidge[1] and Robert O. Green [2]

1. Introduction

Since the electric light was first commercialized in 1879 by Thomas Edison, utilization of exterior lighting of streets and buildings has expanded to become the normal practice in virtually every part of the world. Today the typical commercial center is bathed in continuous lighting, and pockets of nocturnal illumination (e.g., street and house lights) extend to the very edges of human settlements. Elvidge et al. (1997) developed methods to locate and define the spatial extent of nocturnal lighting across large land areas using low-light imaging data from the Defense Meteorological Satellite Program (DMSP) Operational Linescan System (OLS). This sensor has a unique capability to detect low levels of visible - near infrared radiance at night (Figure 1). The primary function of the DMSP-OLS is to provide global imagery of cloud cover. At night the observed visible - near infrared (VNIR) radiance is intensified, for the purpose of cloud detection using moonlight. In addition to moonlit clouds, the light intensification makes it possible to detect VNIR emissions emanating from the earth's surface, from cities, towns, industrial sites, gas flares, and ephemeral events such as fires. In the latter part of this decade NOAA, NASA and DoD plan to fly a new sensor (Visible Infrared Imaging Radiometer Suite – VIIRS) which will continue the record of low-light imaging earth observations, with improved spatial and radiometric properties over the OLS.
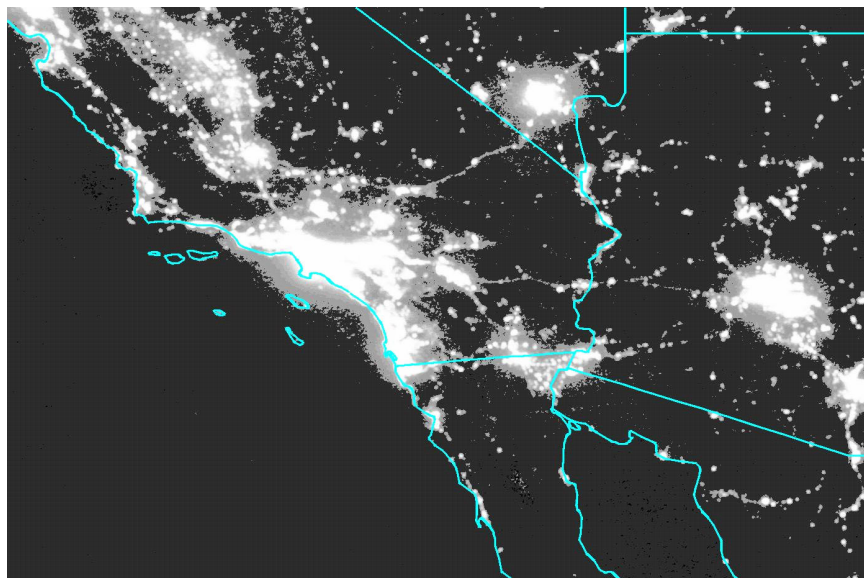

Figure 1. Cloud-free annual composite of DMSP nighttime lights of the Southern California region from 2003. Contrast enhanced to show all detected lighting.

[1] NOAA National Geophysical Data Center (chris.elvidge@noaa.gov)
[2] Jet Propulsion Laboratory, California Institute of Technology (rog@jpl.nasa.gov)

The spatial linkage between nocturnal lighting and the locations of concentrated human activity has lead to a series of applications for the DMSP nighttime lights data, including (1) spatially explicit estimates population numbers (Sutton *et al*., 2003), (2) heat island effects on meteorological records (Owen *et al*., 1998), (3) urban sprawl impacts on agriculture (Imhoff *et al*., 1997), (4) greenhouse gas emissions (Saxon *et al*., 1997), (5) terrestrial carbon dynamics (Milesi *et al.,* 2003), spatial distribution and density of man made impervious surfaces (Elvidge *et al*., 2004) and mapping spatial and temporal variations in squid fishing effort (Maxwell *et al*., 2004).

As part of our effort to further explore the remote sensing of nocturnal lighting, requests were made for a nighttime AVIRIS data acquisition over urban centers. There were five primary reasons for exploring the hyperspectral remote sensing of nocturnal lighting:

1. Primary types of outdoor lighting emit distinctive sets of narrow line emissions, which may be amenable to hyperspectral remote sensing (Elvidge and Jansen, 1999).
2. Distingishing lighting types may be useful for a variety of applications, such as analyzing the biological impacts of lighting (reference) or modeling the spatial distribution of economic activity.
3. Detection of specific emission lines could be used in the validating wavelength calibration of hyperspectral remote sensing data (Chrien, 1999).
4. It may be possible to calibrate or validate DMSP nighttime lights data using hyperspectral data.
5. It may be possible to simulate future planned or hypothetical sensor data of nocturnal lighting using AVIRIS data.

The requests for nighttime data resulted in the collection of low-altitude nighttime AVIRIS data over Las Vegas, Nevada, in 1998 and a high-altitude flight over Los Angeles in 2003. This paper describes our initial findings from an examination of these unique AVIRIS data sets.

2. Spectral Character of Nocturnal Lighting

Mercury and sodium vapor lamps are the primary type of lighting for streets, roads, parking lots and commercial / industrial facilities in many parts of the world. Mercury vapor lamps have a white or blue-white appearance produced via a large number of narrow line emissions (see Figure 2). High pressure sodium lamps produce an amber light, and have fewer emission lines than the mercury lamps. In areas near optical telescope facilities, low-pressure sodium lamps can be found, with even fewer emission lines. Many private homes and motorized vehicles have incandescent lamps, which have a strong blackbody emission character, with the bulk of the radiant emission in the infrared. Gas flares may exhibit emissions patterns that are indicative of the combination of gases being combusted.

Figure 2. Ground-based spectra of several types of outdoor lighting and a propane flame.
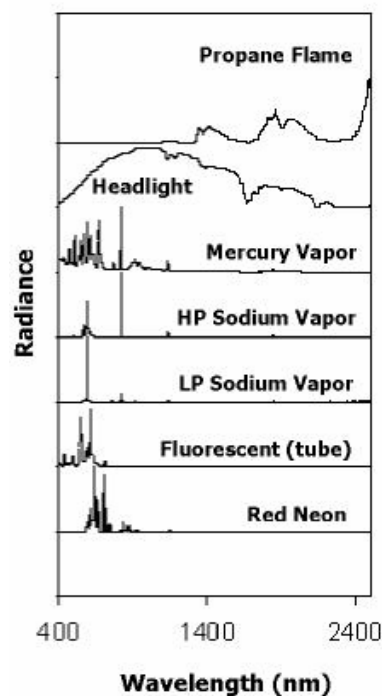
3. AVIRIS Data Acquisitions

Las Vegas, Nevada is internationally recognized as the most colorfully and brightly lit of cities (Figure 3). The Las Vegas lighting, along with its proximity to the primary AVIRIS staging area, dry air, and low cloud cover make it ideal for studying the hyperspectral remote sensing of nocturnal lighting. Low-altitude AVIRIS data were acquired over the central area of Las Vegas, Nevada at approximately 6:35 pm the night of October 4, 1998. AVIRIS was flown on a NOAA Twin Otter aircraft, acquiring data at an altitude of 12,500 ft above sea level (ASL), resulting in data with approximately 3-meter spatial resolution. The AVIRIS data that we analyzed had been radiometrically corrected, but had not been geometrically corrected. Two

Figure 3. Oblique aerial photograph of the Las Vegas Strip at night.

papers in the 1999 AVIRIS proceedings (Chrien, 1999 and Elvidge and Jansen, 1999) were based on the 1998 nighttime AVIRIS collect over Las Vegas.

Los Angeles is one of the largest cities in the world and has lighting that is typical of most cities in the developed world (Figure 4). High-altitude AVIRIS data were acquired over Los Angeles, California, at approximately 8:10 pm the night of September 22, 2003. AVIRIS was flown on NASA's ER-2, acquiring data at an altitude of 65,000 (+/-) feet ASL, yielding data with 20-meter spatial resolution. Two flight lines were acquired, a north–south line over central Los Angeles and an east–west line over San Gorgonio Pass, east of Los Angeles. DMSP visible and thermal band imagery acquired about 30 minutes later indicate that both areas were largely clear of cloud cover (Figure 5) and that lights were present in Los Angeles. As with the Las Vegas
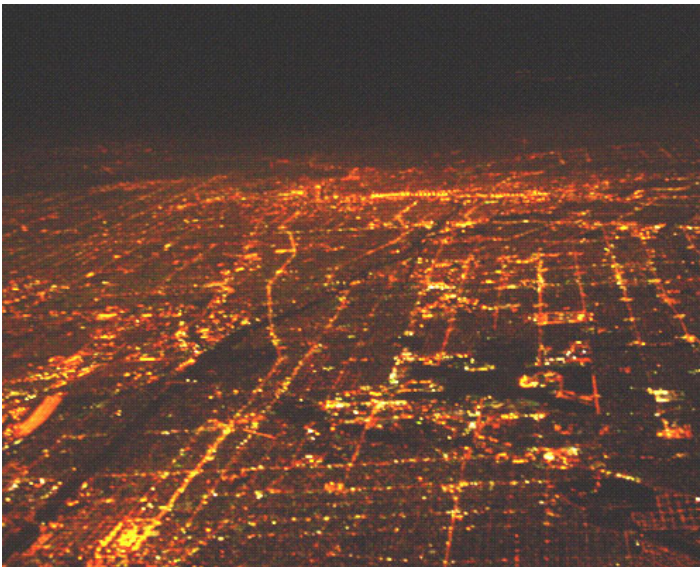
Figure 4. Oblique aerial photograph of nocturnal lighting in Los Angeles, California.
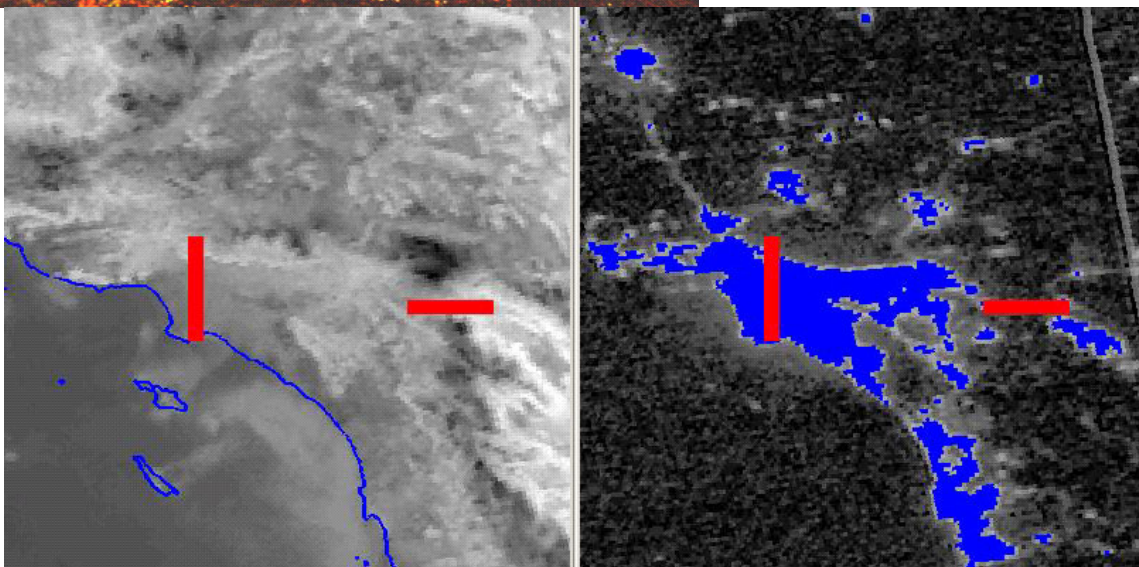
Figure 5. Thermal (left) and visible (right) band DMSP-OLS imagery from Satellite F-14 acquired at 03:43 GMT on September 22, 2003. The AVIRIS flight lines are shown in red. The areas where bright light saturated the OLS sensor are shown in blue.

data, the Los Angeles data were radiometrically corrected, but had not been geometrically corrected.

4. Results from Las Vegas AVIRIS data

Nocturnal lighting was detected in AVIRIS data collected over the Las Vegas Strip. Figure 6 shows the total radiance obtained by summing all the AVIRIS channels in the flight line. Note that most of the flight line lighting levels were below the detection limits of AVIRIS (in 1998). The aggregate spectrum of the flight line (Figure 7) shows a set of emission lines consistent with features found in mercury and sodium vapor lamp spectra.

Figure 8 shows a sampling of the spectra found in the Las Vegas data. Note that most of the spectra contain narrow emission lines, characteristic of vapor lamps, which emit light based on the excitation of electrons in specific elements. The lights observed at Las Vegas exhibit mercury and sodium emission features, plus a number of other more exotic elements associated with specialty lighting. The spectrum in the lower right hand corner shows a blackbody curve and is probably an incandescent light source.

Color composite images of the 1998 Las Vegas data revealed a series of landmark casinos and associated parking lots (Figure 9). It is possible to discern different types of lighting based on brightness differences in three spectral channels.
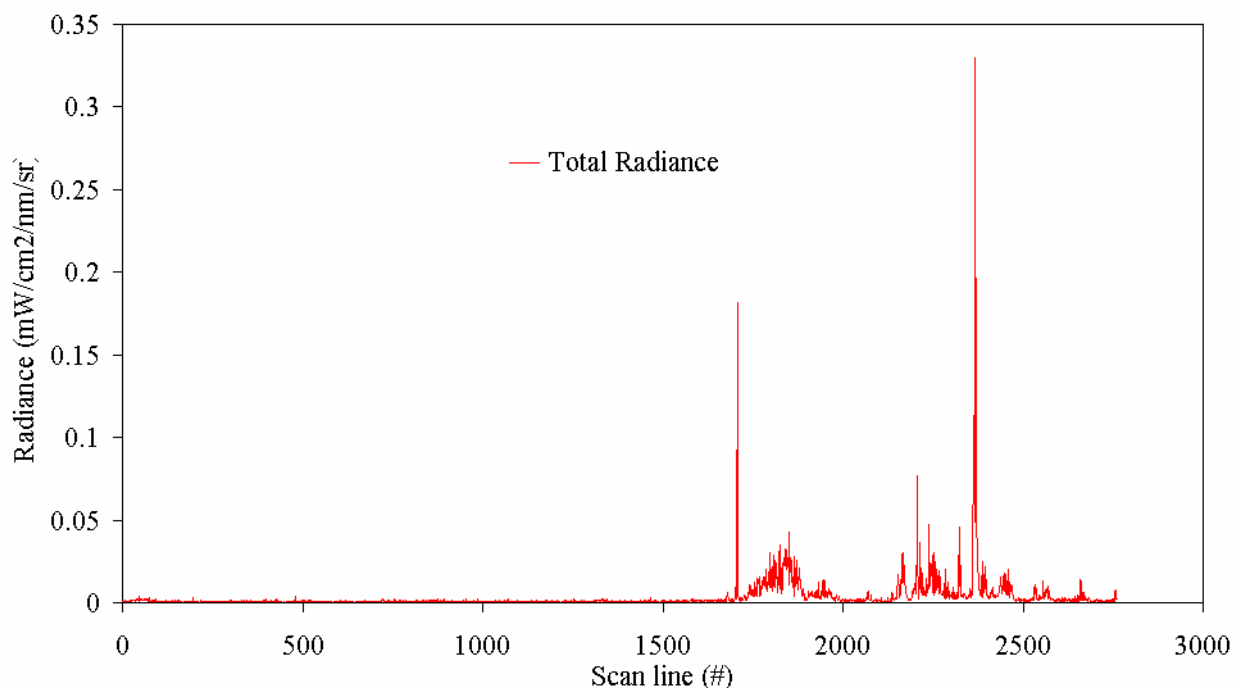
Figure 6. Total radiance observed by AVIRIS versus scanline from the 1998 low-altitude collection over Las Vegas, Nevada.
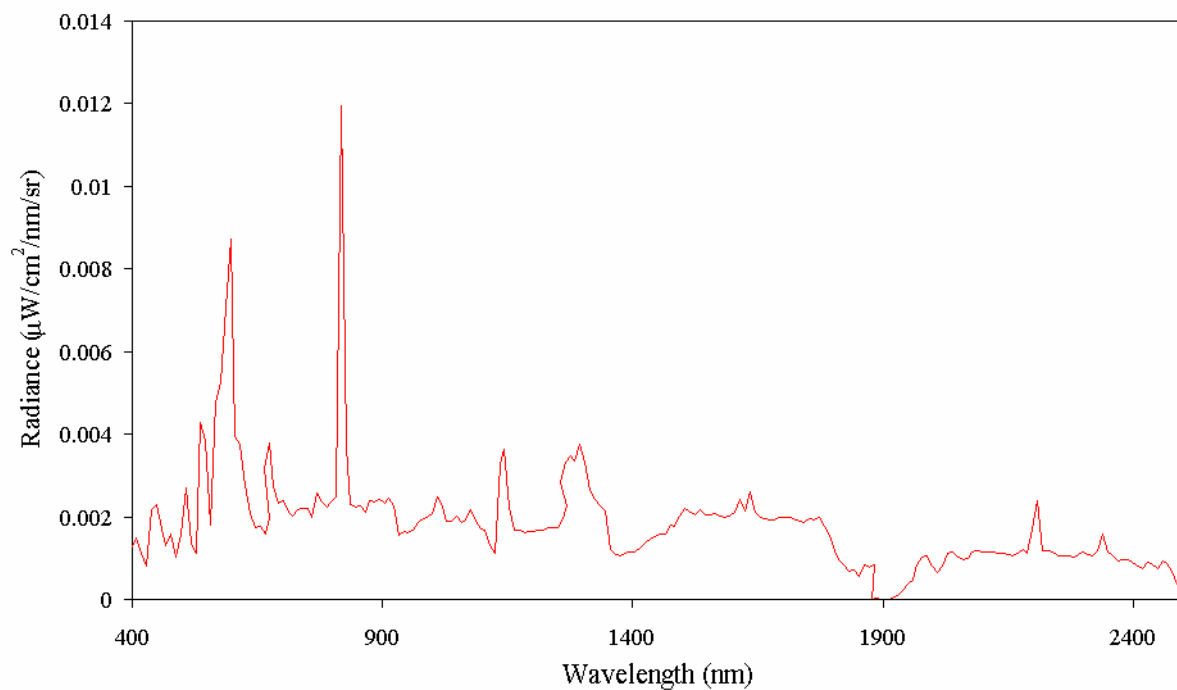
Figure 7. Aggregate spectral radiance observed by AVIRIS from the 1998 low-altitude collection over Las Vegas, Nevada.

Figure 8. Radiance spectra for a sampling of pixels exhibiting nocturnal lighting from the 1998 low-altitude AVIRIS collection over Las Vegas, Nevada.
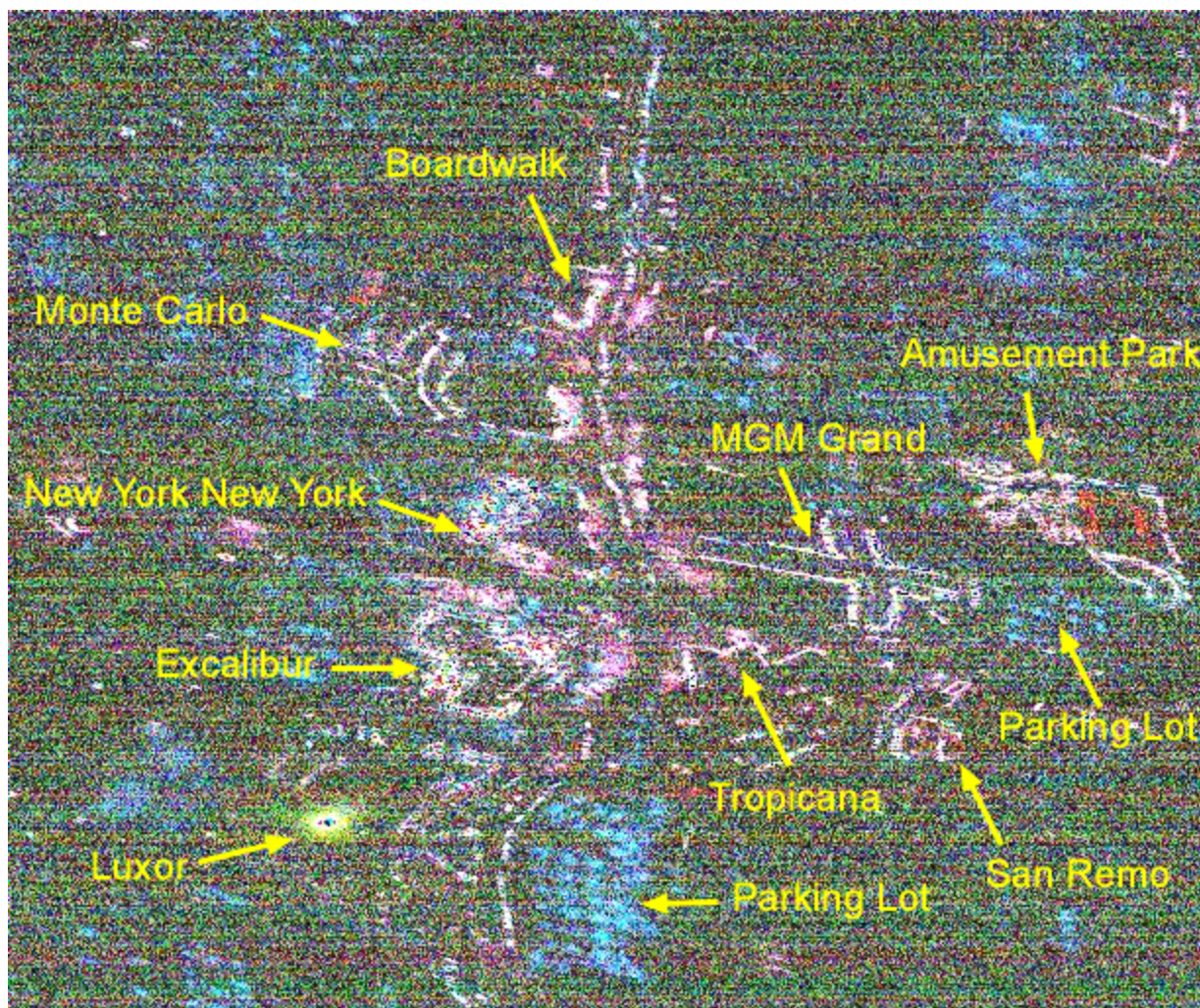
Figure 9. AVIRIS image color composite formed with bands 69, 50, and 83 as red, green, and blue respectively. Major landmarks are labeled in yellow.

5. Results from Los Angeles AVIRIS data

Very few areas in Los Angeles were bright enough to be detected using AVIRIS flown at high altitude in 2003. Unlike the aggregate spectrum of the Las Vegas flight line (see Figure 7), the aggregate spectrum of the Los Angeles flight line (Figure 10) exhibited none of the emission lines that characterize most outdoor lighting. The only feature of note from the aggregate spectrum is the slight downturn in radiance at the longest wavelengths (2300 to 2500 nm). This turns out to be an artifact induced by a previously unknown blackbody emission from the shutter used to block light transmission into the AVIRIS during the dark current measurement. The small number of pixels with detected emissions (Figure 11) appear to be heavily lit automobile dealerships, gravel quarries, and gas flares in oil refineries.
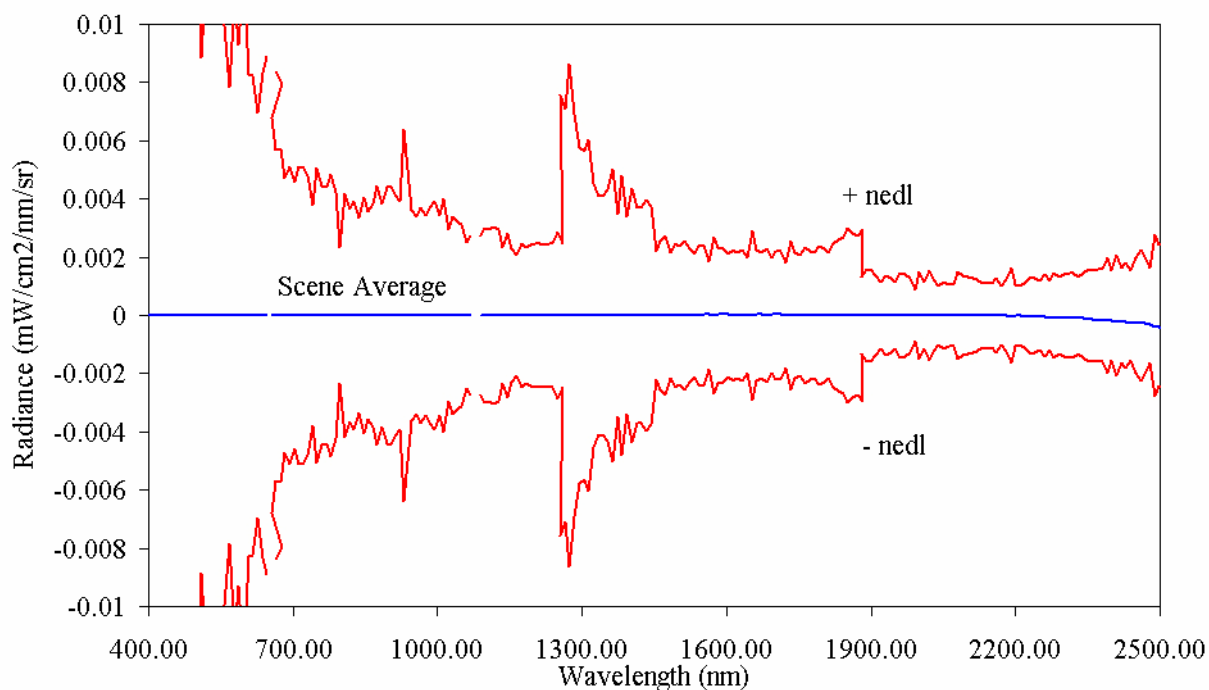
Figure 10. Aggregate spectral radiance observed by AVIRIS from the 2003 high-altitude nighttime collection over Los Angeles, California. (nedl = noise equivalent delta radiance)

6. Conclusion

Investigation with both high- and low-altitude AVIRIS data collected at night over urban centers indicates that the sensor is capable of detecting bright lights pointed up towards sky and minor gas flares in SWIR. In Las Vegas, hotel and casino lighting is directed upwards to illuminate the sides of buildings. In the typical American city, very few areas (e.g., automobile dealerships) are bright enough for AVIRIS detection at night. Open flames, such as those present in many oil refineries, have high emission in the short wave infrared and can be readily detected with AVIRIS. The spectral signatures of AVIRIS-detected nocturnal lighting and gas flares appear to have sufficient detail to make the identification of lighting type or the composition of the burning gas(es) feasible. Overall, our assessment is that AVIRIS detection limits (as of 2003) were not low enough to detect the bright emission lines associated with general street and outdoor lighting.

Aggregation of the 2003 Los Angeles nighttime AVIRIS data shows that the dark-current correction works well. We discovered a previously unknown blackbody emission coming from the shutter used to collect dark current data for spectrometer D.

As hyperspectral remote sensing technologies improve, the detection and mapping of nocturnal lighting features can be expected to advance. High-latitude nighttime AVIRIS imagery of Los Angeles was collected in 2004, affording another opportunity to examine these issues following a round of major upgrades to the AVIRIS sensor.
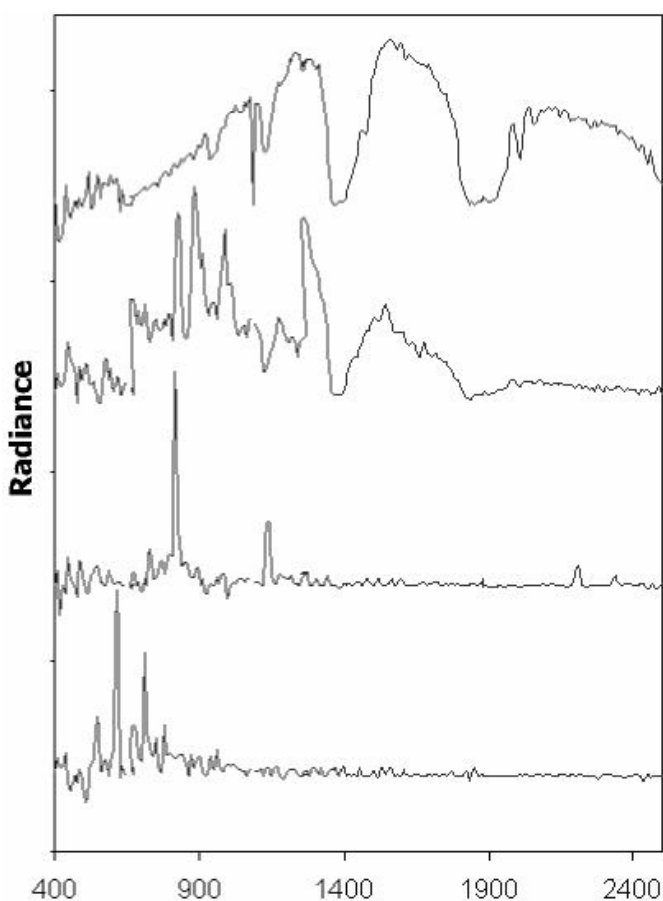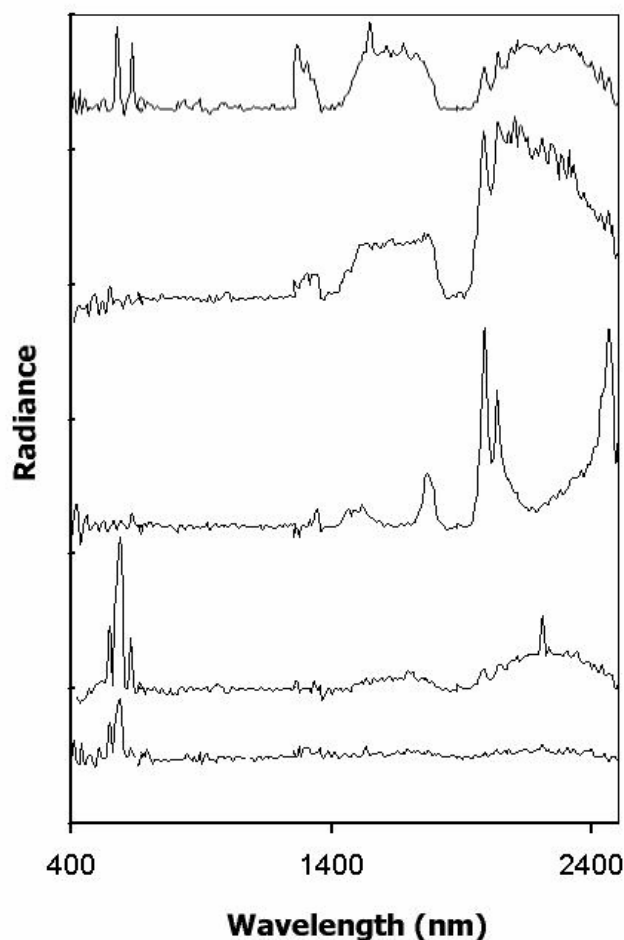
**Figure 11. Radiance spectra for a sampling of pixels exhibiting nocturnal lighting from the 2003 high-altitude nighttime collection over Los Angeles, California. The upper three spectra came from gas flares in oil refinery areas.**

7. Acknowledgments

8. References

Chrien, T.G., "Using Nighttgime Lights to Validate the Spectral Calibration of Imaging Spectrometers, *Summaries of the Eighth JPL Airborne Earth Science Workshop*, JPL Publication 99-17, Jet Propulsion Laboratory, Pasadena, California, 1999.

Elvidge, C. D., C. Milesi, J. B. Dietz, B. T. Tuttle, P. C. Sutton, R. Nemani, and J. E. Vogelmann, 2004, "U.S. Constructed Area Approaches the Size of Ohio, Eos," *Trans. AGU*, 85, (24), 233.

Elvidge, C. D., K. E. Baugh, E. A. Kihn, H. W. Kroehl, and E. R. Davis, E.R, 1997, "Mapping of city lights using DMSP Operational Linescan System data," *Photogrammetric Engineering and Remote Sensing*, v. 63, p. 727–734.

Elvidge, C. D., and W. T. Jansen, 1999, "AVIRIS Observations of Nocturnal Lighting, *Summaries of the Eighth JPL Airborne Earth Science Workshop*, JPL Publication 99-17, Jet Propulsion Laboratory, Pasadena, California, 1999.

Imhoff, M. L., W. T. Lawrence, C. Elvidge, T. Paul, E. Levine, M. Prevalsky, and V. Brown, 1997, "Using nighttime DMSP/OLS images of city lights to estimate the impact of urban land use on soil resources in the U.S," *Remote Sensing of Environment*, v .59, p. 105–117.

Maxwell, M. R., A. Henry, C. D. Elvidge, J. Safran, V. R. Hobson, I. Nelson, B. T. Tuttle, J. B. Dietz, and J. R. Hunter, 2004, "Fishery dynamics of the California market squid (*Loligo opalescens*), as measured by satellite remote sensing," *Fisheries Bulletin*, v. 102, p. 661–670.

Milesi, C., C. Elvidge, R. Nemani, and S. Running, 2003, "Assessing the impact of urban land development on net primary productivity in the southeastern United States," *Remote Sensing of Environment*, 86:401–410

Owen, T. W., K. P. Gallo, C. D. Elvidge, and K. E. Baugh, 1998, "Using DMSP-OLS light frequency data to categorize urban environments associated with U.S. climate observing stations," *International Journal of Remote Sensing*, v. 19, no. 17, p. 3451–3456.

Saxon, E. C., T. Parris, and C. D. Elvidge, 1997, "Satellite Surveillance of National CO_2 Emissions from Fossil Fuels," Harvard Institute for International Development (Harvard University), Development Discussion Paper No. 608.

Sutton, P., T. Obremski, and C. Elvidge, 2003, "Building and Evaluating Models to Estimate Ambient Population Density," *Photogrammetric Engineering and Remote Sensing*, v. 69-5, p. 545–552.

BAND-MOMENT COMPRESSION OF AVIRIS HYPERSPECTRAL DATA AND ITS USE IN THE DETECTION OF CROP STRESS

L. Estep [1]

1.0 Introduction

The USDA Shelton, NE, ARS Variable Rate (VRAT) Nitrogen Application site represents a well-documented corn growing quarter section. The field has four replicates of five plots, which vary in nitrogen treatments from 0-kg/ha to 200-kg/ha, in 50-kg/ha increments. The N-treatment plots are set out in a randomized, complete block design. Typically, the VRAT is planted in a ridge-till corn, monoculture and is watered by a linear irrigation system that is on a three-day period. Since water stress can increase reflectance from corn leaves in both the visible and NIR portions of the spectrum (Wooley, 1971), it is important that the field be adequately watered so that only nutrient related stress will predominate.

Figure 1 below shows an airborne image of the VRAT field with a north arrow superimposed. The N-treatment plots are set off along the central alleyway that runs from east to west and has a central pivot irrigator at its center.
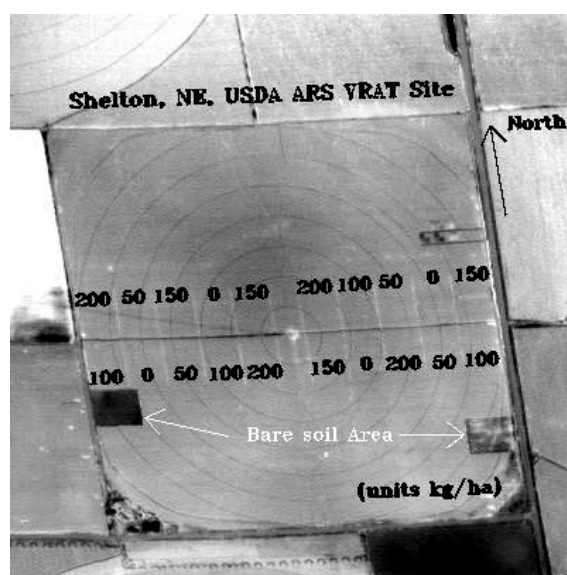
Figure 1. USDA ARS VRAT field

AVIRIS flew over the VRAT field on July 22, 1999. The AVIRIS image cube consisted of 3-m GSD pixels at 224 spectral bands per pixel. Several flight lines were collected and returned to JPL for processing. The data received from JPL was radiometrically calibrated. This data was, then, atmospherically corrected via the use of ATREM (Gao et al., 1992). The relative reflectance imagery produced by ATREM was then scaled to correspond more closely to actual in-field acquired reflectance using an empirical line function (ELF) procedure. These spectral reflectance readings, which were used for the ELF scaling, were collected over the treatment plots and bare field regions shown in Figure 1. The radiometer readings over the treatment plots were obtained with a high-lift unit that allowed the data

---

[1] Senior Staff Scientist, Science Systems Applications Incorporated, Stennis Space Center, Mississippi. lestep@cox.net

collector to position himself directly over the center of the crop plot, at some distance into the plot. The corners and center of each treatment plot were surveyed-in by a DGPS unit.

2.0 Earlier Associated Work

Using AVIRIS image data from the MAC Europe 1991 campaign, Clevers (1999) determined that the 224 bands of spectral information over agricultural sites could be compressed significantly by performing a principal component analysis (PCA) on the data. Clevers (1999) determined that 3 factors explained 96.8% of the total variance in the data set. The first factor was comprised of a broad spectral band in the NIR region that ranges from about 730 nm to 1350 nm. The second factor was composed of two distinct spectral regions. The first is in the visible (VIS) region from about 500 nm to 700 nm and the second region in the SWIR that runs from 1500 nm onwards. The third factor is associated with a few bands about the red-edge region—or around 717 nm. Thenkabail et al. (2000) has recommended a set of hyperspectral bands for agricultural studies. The total spectral range of the twelve bands described run from about 495 nm to 1025 nm. For each of the twelve band sets, a description of associated physical mechanisms that are involved for each specific spectral range is included.

In comparing Clevers (1999) and Thenkabail et al. (2000) work, their spectral bandsets, as might be expected, overlap. The bands one through four, recommended by Thenkabail, describe the *greenpeak* region. The bands five through eight cover the *red-edge* region. Therefore, Clevers' second factor involves the first eight bands suggested by Thenkabail. Similarly, Clevers' first factor involves the final four band sets recommended by Thenkabail. These final four band sets are associated with the heightened *NIR* 'plateau' reflectance past the red-edge rise (Thenkabail's bands 9 and 10) and with *water sensitive* bands (Thenkabail's bands 11 and 12). The *SWIR* region, which Thenkabail et al. (2000) does not consider, is found to be significant in Clevers' analysis. Interestingly, Kokaly (2000) has shown that leaf nitrogen concentration is assessable, due to an absorption-broadening feature in the SWIR. Apparently, this is associated with plant protein amide bonds. Furthermore, the SWIR region is known to provide some sensitivity to certain soil characteristics—including soil moisture.

In this study, the band sets alluded to above—namely, the green peak, red-edge, the water sensitive bands, the NIR region, and the SWIR of Clevers (1999) are used. Furthermore, the entire Clevers' band set and the less expansive band set of Thenkabail et al. (2000) are included. Table 1 provides a summary of these band set spectral ranges.

<center>Table 1. Band sets used in present study</center>

BAND SET NAMES	BAND SET SPECTRAL RANGES (NM)
Greenpeak band	0.49 - 0.57
Red-edge band	0.66 - 0.72
NIR band	0.81 - 0.925
Water Sensitive band	0.98 - 1.00
SWIR band	1500 - 2250
Clevers Total Band Set	117 bands (500 - 2250 nm)
Thenkabail et al. (2000)	12 bands (490 - 1025 nm)

A spectral or band-moments approach to hyperspectral image coding has been reported upon in the literature (Rundquist and Di, 1989; Staenz, 1996). The eight band-moments defined by the authors include mean, standard deviation, median, skewness, kurtosis, band-skewness, band-kurtosis, and band concentrated moment. The use of band-moments to characterize spectral imagery represents a form of lossy compression in the spectral domain. The spectral compression efficiency can be defined as the simple ratio of the number of input sensor bands to the number of output bands provided by the compression algorithm. For an AVIRIS cube, a spectral compression efficiency of 224 to 8 or 28 to 1—is achieved.

Foundationally, Papoulis (1965) has shown that if the spectral reflectance is finitely non-zero and at least piecewise continuous, then statistical moments of any order exist and are unique. Hence, the band-moments associated with a set of spectral reflectances uniquely characterize that spectral data set, and conversely (Rundquist and Di, 1989). Additionally, Rundquist and Di (1989) found that the use of band-moment compression reduced sensor noise and, in their study, improved image quality.

3.0 Objectives and Approach

The objectives of this research were to assess the value of band-moment compression of hyperspectral data for the detection of crop stress. In particular, is the compressed imagery able to detect crop stress effectively when compared to the non-compressed imagery from which it was derived? Estep and Davis (2001) have shown that for the crop and site studied, AVIRIS data is capable of mapping crop stress.

The analytical steps taken in this study will now be summarized. Given a specific band set (see Table 1), AVIRIS imagery of the VRAT was used to extract region-of-interest (ROI) data from the different N-treatment plots. These extracted data were compiled and employed to compute eight band-moments, which compressed the input band set. Compressed and non-compressed forms of the spectral band sets listed in Table 1 were used to compute the spectral class distances for the different N-treatment plots (the plots taken as classes).

The Euclidean and Bhattacharyya spectral distance metrics were used to determine whether the compressed band-moment bands provided comparable separation of the VRAT N-treatment plot classes when compared to the original non-compressed band sets. The spectral band sets of Table 1 were ranked in order of those providing the greatest relative N-treatment plot distances, considering only the band-moment band sets.

The ranking outcome based upon the relative spectral distances (magnitudes) between the N-treatment plots for the band-moment band sets of Table 1 are as follows: 1) red-edge, 2) SWIR, 3) greenpeak, 4) NIR, and 5) water sensitive bands of Thenkabail. If the compressed forms of the complete bandsets suggested by Clevers (1999) and Thenkabail et al. (2000) were considered independently, then the spectral distance rankings would place them first and second, respectively, with the other band sets following as listed. The eight moments associated with these band sets were then plotted as box and whisker plots to determine which band moments appeared to show the greater sensitivity, or variation, as a function of N-treatment. The band-moments that showed greatest sensitivity, in order, were the third central moment, the first moment (ordinary moment), and the eighth moment (band concentrated moment), either singly or in combination. These results agree with the findings of Staenz (1996).

Statistical moments that prove more sensitive than others, for a given Table 1 band set can be used as single band images, in transformations, or in band ratio forms to produce imagery for the detection crop stress. Band ratios that might be used to parallel ratios commonly used for plant stress detection might include the following: 1) RVI (Jordan, 1969), 2) NDVI (Rouse, 1973), 3) Gitelson-Merzlyak (1996), 4) and Schepers et al. (1996). In the present study, the Gitelson- Merzlyak (1996) and NDVI (Rouse et al., 1973) band ratios are used as templates to compute band-moment equivalent vegetation indices. A comparison is made between original AVIRIS hyperspectral band ratio imagery and the associated, band-moment ratio imagery. Statistical testing using ANOVA methods and follow-on Dunnett multiple comparison tests are used to determine whether the band-moment data set retains a separation of the N-treatment plots from the controls, when compared to the original uncompressed, hyperspectral band ratio imagery. Supervised classification methods are exercised upon both the original AVIRIS band sets of Table 1 and their associated band-moment band sets independently. A figure-of-merit (FOM) comparison is made on the resulting classification images to assay the effects on crop stress detection by the lossy band-moment compression method.

4.0 Discussion of Results

Given the abovementioned moment sensitivity, especially those of the third central moment, images that are the result of this computation are interesting in themselves. Figure 2 exhibits the third central moment of the mean for the greenpeak spectral band set (see Table 1). The third central moment is relatable to the skewness of a distribution, since skewness can be defined as the third central moment of the mean normalized to the cube of the standard deviation. Since Figure 2 is computed pixel-by-pixel over the scene, it provides an approximate measure of the relative departure from a symmetrical distribution for the spectral brightness values that compose each pixel. The greater the departure from symmetry, the darker the pixel becomes.

It is interesting to note that the untreated VRAT plots (marked '0' in the figure) exhibit the highest departure compared to the other plots present. In fact, it would appear that, in general, crop stress could be associated with heightened asymmetry in the spectral distributions of the pixels that image a stressed crop region.

Figure 2. Third central moment greenpeak band set image of VRAT field

As seen, Figure 2 shows considerable detail over the VRAT field. The darker tones indicate crop stress. Broadly speaking, there are two sorts of stress registered by the image. The first is the nutrient stress in the different N-treatment plots. The darker tones within certain of these plots indicate the presence of stress. The fact that some darker tones are showing up in some of the 100-kg/ha plots suggests that pre-visual nutrient stress detection might be possible with this single band-moment image.

The second source of stress is water stress indicated by a dark-toned arc-shaped band at the north-central periphery (top and central portion) of the field. This area was deliberately water stressed by shutting off the central pivot irrigation as it passes over this section of the field. The presence of this water-stressed region was created to aid in attempting to separate nutrient stress from water stress in the crop. Figure 3 shows the VRAT field in the eighth moment image (band concentrated mean) for the water sensitive band set of Thenkabail et al. (2000).
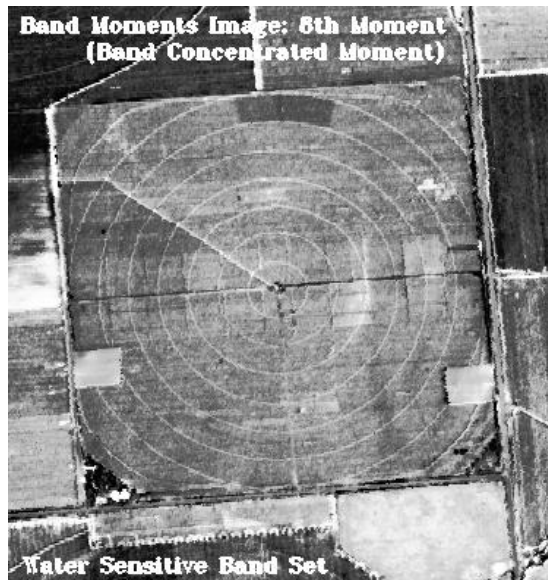
Figure 3. Eighth moment of water sensitive band set

The clarity with which only the water stressed region is displayed as a dark toned area, while the nutrient stressed areas associated with the N-treatment plots are comparatively muted, or displayed as brighter areas, suggests a possible methodology for separating these two types of crop stress.

4.1 Band-moments Transformed or Used in Combination as Vegetation Indices

Different statistical moments, for the different spectral band sets in Table 1, could be used in combination. That is, different transformations or ratio formulations could be employed using the band-moments band set of the compressed spectral image data. For example, a principal component analysis (PCA) could be run on the eight band-moment band set. Since the PCA analysis stacks the output imagery according to the amount of variance embedded in each image, with the image with greatest variance at the top of the output set, then the initial image highlights those spectral features that provide the most variation in the scene. The next PCA image down in the output set is non-correlated with the first image, and will highlight features that provide the next most variation in the scene—and so forth. Embedded noise in the original imagery due to sensor and environmental sources increasingly appears as one proceeds through the stack of output PCA for an image, since noise itself provides a source of variation. Moreover, the noise present often tends to be Gaussian with a mean near zero. The use of band-moment compression techniques serves to reduce the effects of noise, since the process is generally one of summation. Thus, when a band-moment band set is used as input to a PCA routine, the band output tends to show little or no effect from noise. Rather, the images move through a graded sequence of highlighting those image features that exhibit greater or lesser variation within the scene. Figure 4 displays an image that represents the third PCA band for an input greenpeak eight-band, compressed data set.

It is interesting that the image does not appear to show water stress effects. The stress exhibited is that due to the light toned, nutrient stress differences in the field. This image, then, represents a separation of nutrient stress from water stress effects.

An example of a possible implementation of ratios is that of the third central moments of the greenpeak and red-edge bands. This ratio emulates, to some extent, the ratio of bands suggested by Gitelson and Merzlyak (1996). Figure 5 displays the band-moment band set result of the Gitelson and Merzlyak ratio.
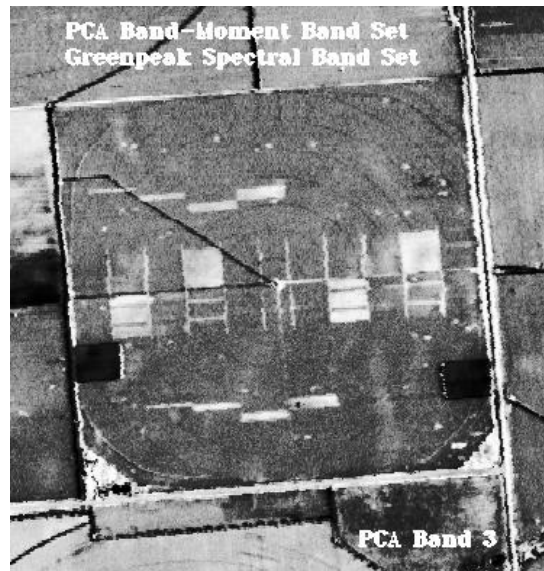
Figure 4. PCA band 3 of greenpeak band-moment band set

Figure 5. Third central moments of red-edge to greenpeak ratio image

As seen, Figure 5 provides considerable detail over the VRAT field. Certainly, the untreated N-treatment plots are clearly depicted. The gray tone scale provided within the image indicates a relative stress measure. Furthermore, the sensitivity to water stress, as shown by the deliberately un-watered region at the north periphery of the VRAT field is seen. Interestingly, the water-stressed area is a brighter region compared to the nutrient-stressed plot areas. In general, the band-moment ratio image appears to be rather sensitive to soil background conditions. This is evidenced by the detail shown in both in the VRAT field and the fields surrounding it.

In order to assess whether the band-moment band set provides relatively reliable crop stress detection, a Gitelson-Merzlyak ratio image was computed using uncompressed AVIRIS hyperspectral bands (image not shown). In order to provide a quantitative, head-to-head, evaluation of these two

Gitelson-Merzlyak images and their ability to separate the untreated, 50-, 100-, and 150-kg/ha plots from the controls (200-kg/ha), an ANOVA (Haber, A. and R. Runyon, 1977) was run on plot data extracted from these images. The data was extracted using ROI selections for each plot type and then compiling the result. In both cases, the ANOVA results allowed for the rejection of the null hypothesis at the $p < 0.0001$ levels.

The follow-on Dunnett multiple comparisons test (Siegel, 1956) determined that the Gitelson and Merzlyak algorithm could separate the 0-, 50-, and 100-kg/ha plots from the controls. Hence, statistically, pre-visual crop stress was detected.

The Dunnett multiple comparisons for the band-moment ratio image demonstrated that all the plots could be distinguished from the controls—including the 150-kg/ha plots. Thus, surprisingly, Figure 5 provides enhanced capability at statistically discerning the different N-treatment plots from the in-field controls.

A normalized difference approach, such as that used by an NDVI algorithm, could also be implemented with selected band-moments. The NDVI algorithm aids in the removal of additive noise sources—provided the wavelength regions associated with the band-moment in question have similar noise magnitudes. For example, if the eighth moments of the water sensitive bands and the Clevers' SWIR region bands are input to an NDVI ratio, Figure 6 is the result.

Figure 6. Eighth moments of water sensitive and SWIR band sets ratio image

The image details crop stress but does not distinguish between nutrient stress and water stress. Note that since the central pivot is on a three-day period and moves counter-clockwise in the image, the area immediately in front of the movement of the irrigator shows signs of water stress, since it has been two days since it received water. Also, variability in soil moisture retention appears to be indicated in the image for areas more recently irrigated. Although the NDVI algorithm (Rouse, 1973) endeavors to subtract out additive noise in the image data, ratio approaches, such as the RVI (Jordan, 1969), attempt to divide out multiplicative noise. Semenov and Yefremenko (1999) have suggested a form that allows for both additive and multiplicative noise removals. The form they provide is given as the following:

$$SALVI = \{(b1 - b2)(b2 - b3)\}/ \max \{b1 - b2)^2, (b2 - b3)^2\} , \qquad (1)$$

where b1, b2, and b3 are user selected wavelengths. ''SALVI' is an acronym, which stands for 'Semenov ALgorithm Vegetation Index.' The expression, provided by Equation (1), is the form of a second moment

of the brightness differences in the respective channels and resembles the computation of a cross-correlation coefficient for the respective bands. As can be seen, the expression will attempt to remove multiplicative and additive noises from the selected channels, provided the relevant noise sources are approximately the same in all three channels. Equation (1) was exercised with three band-moments as input bands. The band-moments employed were the third central moments of the red-edge, greenpeak, and water sensitive bands. For comparison, a similar computation using three analogous AVIRIS hyperspectral bands for the greenpeak, red-edge, and water sensitive region was generated. The SALVI image result yielded virtually the same appearance as in shown in Figure 5—with some slight differences. The SALVI image showed the water stressed area as more clearly defined. Also, the bare-field areas on the west and east side of the VRAT field were shown containing, apparently, some vegetation. As it happens, for the 22 July AVIRIS over flight, some weed cover did, in fact, tarnish some portions of these bare field regions. The comparable AVIRIS, original band SALVI type image does not show this.

Using ANOVA methods and follow up multiple comparison tests, it can be shown that both the compressed and uncompressed SALVI images can differentiate the untreated, 50-, and 100-kg/ha plots from the controls at approximately the same level of statistically accuracy. Thus, the use of three band moments in place of three analogous AVIRIS bands did not impact stress detection capability.

4.2 Supervised Classification Techniques and Class Discrimination

Using supervised classification techniques on both the band-moment band sets and the original band sets from which they were derived (see Table 1), an attempt was made to separate the different N-treatment plots, or classes, from one another. Staenz (1996) used supervised classification techniques (maximum likelihood and logistic classifiers) on a band-moment band set to separate different field crops. His classification results using compressed image data were only slightly less than with the original image data.

Figure 7 shows the result of applying the Spectral Angle Mapper (SAM) algorithm to the original Clevers' 117-band image. As can be seen, the image displays an apparent, varying fertilization application over the VRAT field. The SAM application to Clevers' compressed band-moment bandset image appeared virtually identical to Figure 7.
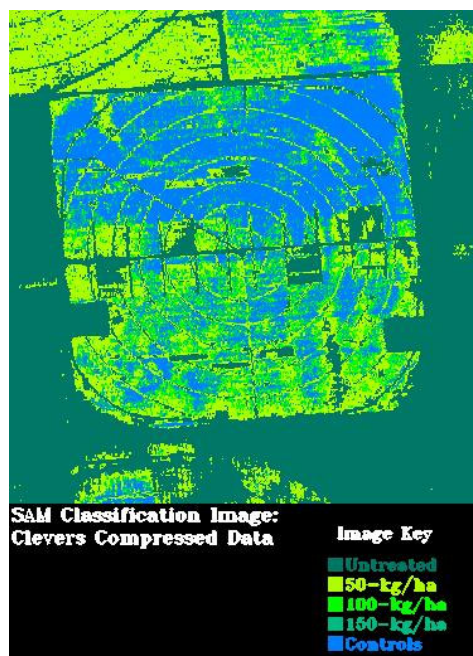
Figure 7. SAM classification image of Clevers' band set

To show this quantitatively, averages and standard deviations of image data for the classified N-treatment plots were taken from both classification images. These mean and standard deviation values were scaled to an effective mean fertilizer application for each plot of the respective images. The mean deviation was computed and is displayed on the plot. This provides an overall FOM on the relative quality of the classification accuracy.

Figure 8 provides plots of these results.
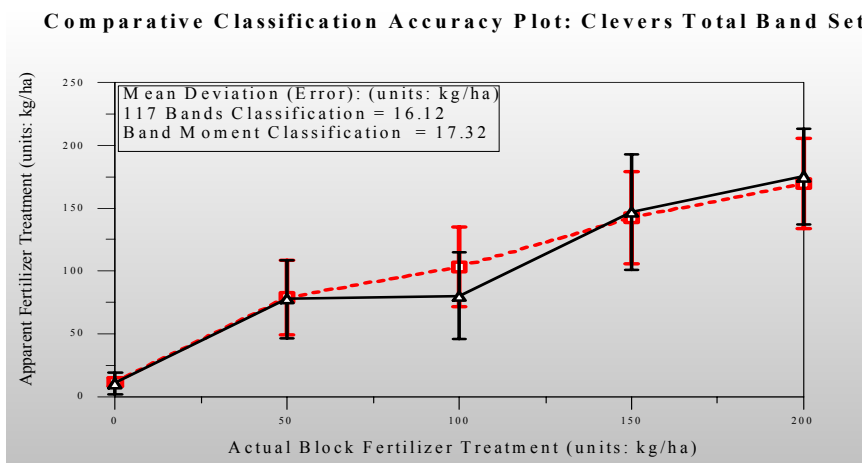
Figure 8. FOMs for Clevers' total band set and associated band-moment band set

As shown, the band-moment classification image, in terms of an apparent fertilizer application (shown as the solid line), compares favorably to the classification image that represents Clevers' total band set. The one principal offset is the 100-kg/ha plot value.

5.0 Summary and Conclusions

An AVIRIS image cube was subjected to compression using a band-moment methodology. Eight bands comprised the compressed band set. These bands represent statistical moments, which numerically summarize a given spectral band set. The compressed and uncompressed band sets of Table 1 were tested in various ways to determine how the band-moment compression method impacted the ability to detect crop stress over a test field. Since the band-moment compression procedure represents a lossy compression method, it was expected that some degradation of crop stress detection could occur.

The band-moment results derived from the compression process were analyzed in various ways. These band-moments were used as single band images for crop stress analysis—and used in transformation, such as PCA, and in ratio combinations to form novel vegetation indices. The compressed band set was used as input to a standard SAM classification routine, which generated a satisfactory classification image, when compared to a similar classification image using the entire 117 bands of the original hyperspectral data set.

In general, band-moment compression and analysis provides at least as good, or somewhat less, capability for detecting crop stress than does the original band set from which it was derived. The trade-off comes in increased noise immunity, decreased storage requirements, and increased speed of processing—especially when dealing with multiple hyperspectral image cubes over extensive areas.

6.0 Acknowledgements

portions of these data. The NASA Earth Science Applications Directorate at the John C. Stennis Space Center, Mississippi, supported this work.

7.0 References

Clevers, J., 1999, "The use of imaging spectrometry for agricultural applications," ISPRS Journal of Photogrammetry and Remote Sensing, 54: 299-304.

Estep, L. and B. Davis, 2001, "Nutrient Stress Detection in Corn, Using Neural Networks and AVIRIS Hyperspectral Imagery," AVIRIS Workshop Proceedings, JPL, Pasadena, California.

Gao, B.C., K.B. Heidebrecht, and A.F.H. Goetz, 1992, Atmospheric Removal Program (ATREM) User's Guide, version 1.1, Center for the Study of Earth from Space document, University of Colorado, 24 p.

Gitelson, A. and M. Merzlyak, 1996, "Signature analysis of leaf reflectance spectra: algorithm development for remote sensing of chlorophyll," J. Plant. Phys., 148: 494-500.

Jordan, C., 1969, "Derivation of leaf area index from quality of light on the forest floor," Ecology, 50: 663-666.

Kokaly, R., 2000, "Investigating a physical basis for spectroscopic estimates of leaf nitrogen concentration," http://speclab.cr.usgs.gov/PAPERS/nitrogen/nitrogen_rse.html.

Papoulis, A., 1965, Probability, Random Variables, and Stochastic Processes, New York: McGraw-Hill.

Rouse, J., 1973, Monitoring the vernal advancement and retrogradation of natural vegetation. NASA Report, Greenbelt, Maryland.

Rundquist, D. and L. Di, 1989, "Band moment analysis of imaging spectrometer data," Photogrammetric Engineering and Remote Sensing, 55: 203-208.

Schepers, J., T. Blackmer, W. Wilhelm, and M. Resende, 1996, "Transmittance and reflectance measurements of corn leaves from plants with different nitrogen and water supply," J. Plant Phys., 148: 523-529.

Semenov, A. and V. Yefremenko, 1999, "Algorithms for processing multispectral images with certain invariant properties," Mapping Sciences and Remote Sensing, 36: 125-132.

Siegel, S., 1956, Non-parametric Statistics. New York, McGraw-Hill

Staenz, K., 1996, "Classification of a hyperspectral agricultural data set using band moments for reduction of the spectral dimensionality," Canadian Journal Rem. Sens., 22: 248-257.

Thenkabail, P., R. Smith, and E. De Pauw, 2000, "Hyperspectral vegetation indices and their relationships with agricultural crop characteristics," Rem. Sens. Env., 71: 158-182.

Wooley, J., 1971, "Reflectance and transmittance of light by leaves," J. Plant Phys., 47: 656-662.

OCEANOGRAPHIC STUDIES USING AVIRIS IN MONTEREY BAY, CALIFORNIA

Andrew M. Fischer,[1] John P. Ryan,[1] Erich V. Rienecker,[1] Patrick McEnaney,[1]
Laurence C. Breaker,[2] Nicholas A. Welschmeyer[2]

1. Introduction

The coastal waters of Monterey Bay (Figure 1) are dynamic and complex. Ocean processes at multiple temporal and spatial scales influence the distribution and abundance of phytoplankton and marine life. These processes range from the large-scale influences of the California Current, to mesoscale eddies and filaments and small-scale frontal dynamics. Human activities on land (agriculture, urban development and waste treatment) can also influence the ecology of Monterey Bay. Estuarine and riverine plumes can carry land-based sources of pollutants and nutrients into coastal waters. Several of these processes occur at scales greater than that covered by in situ measurements, and often cannot be resolved by techniques of satellite remote sensing, which cover large areas at relatively coarse resolution (~1 km). Therefore, it is critical to use new techniques, at appropriate scales, to fill these gaps in observations. Ultimately, multidisciplinary studies requiring sampling across these scales are needed in order to understand how these processes influence the ecology of Monterey Bay.

Recent acquisitions by the Airborne Visible Infrared Imaging Spectrometer (AVIRIS) over Monterey Bay have begun to close these gaps in observations. AVIRIS, coupled with in situ measurements and multidisciplinary, multi-sensor analyses, have revealed small-scale ocean processes and phenomena important to understanding bay ecology. These processes relate to red tide development and estuarine plumes.
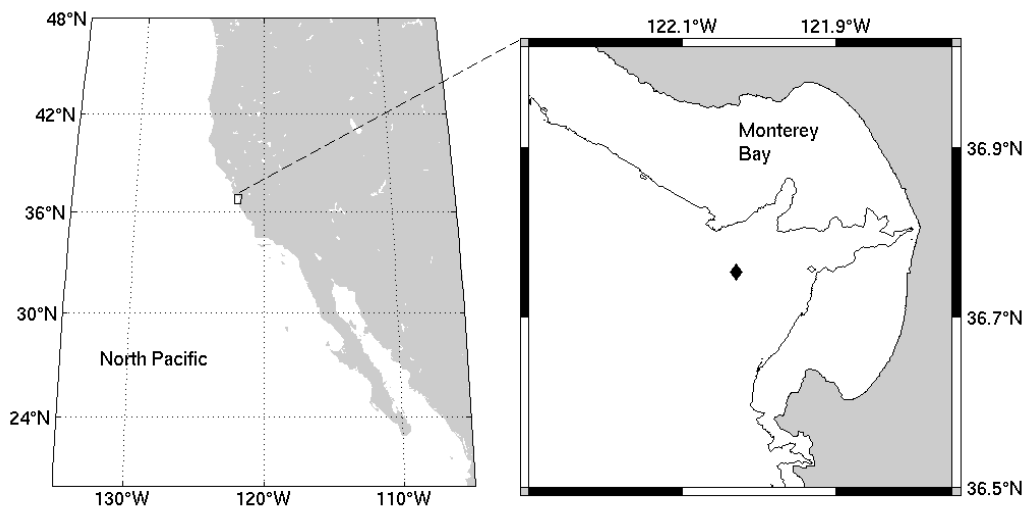

Figure 1: Monterey Bay, located on the central coast of California, is known for its productive marine waters and diverse marine life. The time-series oceanographic research station (M1) is located in the center of the Bay (diamond).

[1] Monterey Bay Aquarium Research Institute, Moss Landing, California (afischer@mbari.org)
[2] Moss Landing Marine Laboratories, Moss Landing, California

1.1 Red tide

Red tide blooms in coastal ocean environments have substantial economic consequences primarily through introduction of toxins into the food web and generation of hypoxic or anoxic conditions during bloom decay (Shimizu, 1989; Horner et al., 1997; Smayda, 2000; Hoagland et al., 2002). These blooms are termed red tides because their dense accumulations of microscopic algae cause ruddy discoloration of near surface waters. Red tides that have deleterious consequences are termed harmful algal blooms (HABs). Because of their substantial impacts, red tides and HABs are important phenomena to detect and predict, and their complexity necessitates observing and modeling systems that integrate diverse scales and methods of sensing. Here we report progress on a red tide study employing AVIRIS as a key observational asset within an observing system array that included satellites, aircraft, ships, mooring and microscope. With this array we closely observed genesis and evolution of a red tide in Monterey Bay to reveal complex processes forcing the genesis and evolution of the event.

1.2 Elkhorn Slough plume

The Elkhorn Slough is a significant year round link between land use activities and the coastal waters of Monterey Bay. Agricultural runoff, collected in the slough during periods of precipitation, can be carried, by means of tidal exchange, into Monterey Bay. Tidal scouring of the banks and bed of the slough, can resuspend pollutants that have accumulated in sediments over the past several decades. Increased flux of nutrients and pollutants into the Bay can influence water quality, increase the prevalence of harmful algal blooms and marine diseases, and have consequences for nearshore ecology.

This exchange is of particular concern because its physical configuration has been drastically altered by human intervention. In 1946, the Army Corps of Engineers changed the morphology of Elkhorn Slough by cutting through the dune barrier separating the slough from Monterey Bay. Since then, the slough has been transformed from a sluggish backwater to a shallow, tidally forced embayment. Maximum tidal currents in the main channel of the slough have increased from approximately 1.5 knots in 1971 to 3.0 knots today, and the tidal prism, the volume of water that is exchanged between the slough and the bay over a tidal cycle, has increased by 43 percent during the last decade.[3] As the tidal currents and tidal prism continue to increase, and the surrounding watershed is subject to growing population pressures and land use change, there is a need to understand the physical extent and the biological impacts of the plume of water entering the bay from the slough.

Recent measurements have revealed components of the physical and biological exchange between the Elkhorn slough and Monterey Bay. Here we have combined in situ measurements with AVIRIS hyperspectral imagery to begin to understand the constituents of the slough plume, their transport and fate.

---

[3] Breaker et al., In preparation

2. Methods
2.1 Red Tide
2.1.1 AVIRIS

AVIRIS was flown on the high altitude ER-2 platform over Monterey Bay on October 7, 2002. The bay and adjacent waters were imaged in 51 minutes with four swaths, each 11 km wide and overlapping by ~1 km. Flight line orientation was optimized relative to local sun angle during the acquisition period. These data were atmospherically corrected using Tafkaa atmospheric correction software (Montes, 2004; Gao et al., 2000). Aerosol model parameters (tau 550 and relative humidity) for the Tafkaa input files were derived from **Sea**-viewing **Wi**de **F**ield-of-view **S**ensor (SeaWiFS) ancillary products. The SeaWiFS satellite collected data over Monterey Bay within 26 minutes of AVIRIS flight time. Chlorophyll concentrations were computed using the same algorithm that is used for SeaWiFS satellite imagery (O'Reilly et al., 1998).

2.2 Elkhorn Slough plume
2.2.1 AVIRIS

AVIRIS imagery from the high-altitude ER-2 platform was collected over Monterey Bay on October 13, 2000 and October 7, 2002. A discharge plume was observed exiting the mouth of the Elkhorn slough (Figure 2a & 2b). This tidal discharge interacts with alongshore currents and subsurface topography, to create a complex region of frontal zones (Figure 2c). Observation of this plume within the AVIRIS imagery, highlighted a phenomenon of estuarine/oceanic exchange that has until now been overlooked by researchers in Monterey Bay.
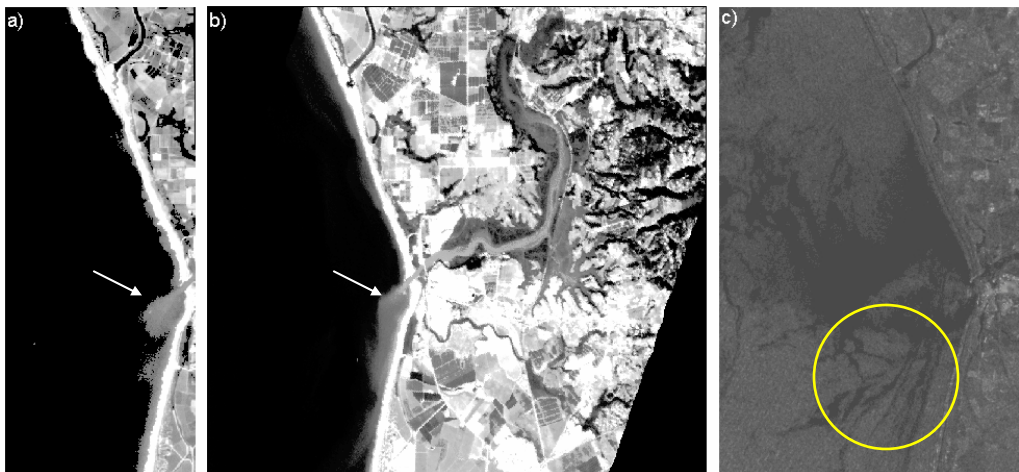
Figure 2: a) An enhanced gray-scale image, derived from hyperspectral imagery collected by the Airborne Visible/Infrared Imaging Spectrometer (AVIRIS) on October 13, 2000, reveals a discharge plume exiting the mouth of the slough. b) AVIRIS captured this same feature during an overflight on October 7, 2002. c) Multiple narrow frontal zones (within yellow circle) are evident in imagery captured by synthetic aperture radar, revealing complex interactions between the slough plume and canyon upwelling.

The AVIRIS observations launched a series of in situ measurement efforts described below. Further analysis of AVIRIS imagery was conducted to begin to understand this exchange. AVIRIS imagery was atmospherically corrected as in 2.1.1. The appropriate flight

lines from the AVIRIS mission were subset to encompass the slough and the surrounding nearshore waters of Monterey Bay. The methods employed by Kruse et al. (1997), were then used to classify the nearshore water types of the slough, plume and coastal ocean. This preliminary procedure was carried out in order understand spectral differences in potential water types classes and aid in understanding the fate of the plume class and interaction of slough/plume with the oceanic classes. The procedure consists of 4 steps. First is the application of a "minimum noise fraction" (MNF) transform to the atmospherically corrected image. This procedure is used to reduce the number of spectral dimensions to be analyzed. The MNF transform orders the data according to the signal-to-noise ratio and reduced redundancy by selecting out bands, which contain the most information (Green et al., 1988). Second, is the application of the pixel purity index (PPI) algorithm, to determine pure endmember spectra. Finally, the spectral angle mapper (SAM) classification procedure, using image derived endmembers, produced reasonable classes distinguishing, slough, plume and oceanic waters.

2.2.2 In situ Observations

The plume exiting the slough was characterized by in situ observations on several occasions from the R/V Zephyr. These measurements were not concurrent with the AVIRIS overflight, but were collected in subsequent field operations. A continuous underway-mapping system collected sea surface parameters of temperature, salinity, color dissolved organic matter (CDOM) and chlorophyll fluorescence, transmission (a proxy for turbidity), and nitrate. Water samples and CTD profiles were collected at six successive sampling stations with increasing distance seaward of the slough. Water samples were analyzed for chlorophyll and carotenoids, naturally occurring plant pigments, and fatty acid content. Data were collected at the lowest stage of the ebb tide, when the extent of the plume is most prominent.

3. Results
3.1 Red Tide

At the time of this writing we are preparing to submit this red tide study for review by *Science*. To avoid potential copyright concerns we present here only a brief summary to highlight the key contribution made by AVIRIS in this multidisciplinary study. Satellite ocean color observations, mooring observations, and *in situ* surveys of Monterey Bay illustrated dramatic short-term changes in the physical and biological environment preceding a red tide. Specifically, the bay was flushed by an intrusion of offshore waters, after which a red tide bloom rapidly formed throughout most of the bay. Between the ~1 km x 1 km pixel of the satellite and the periodic synoptic maps of the ocean interior by towed undulating vehicle, the very high resolution synoptic remote sensing by AVIRIS contributed a key finding about the creation of highly concentrated red tide patches by physical processes. In this aspect of the study, we combined surface chlorophyll concentrations estimated from AVIRIS with same-day imaging of the bay by synthetic aperture radar (SAR). This combination of physical and bio-optical remote sensing, a first in coastal ocean studies, revealed the alignment of the most highly concentrated red tide patches in convergence zones created by internal waves.

3.2 Elkhorn Slough plume

Several sea surface parameters were collected by the underway-mapping system (Figure 3) revealing complex interaction between plume waters and upwelled water from the Monterey Bay submarine canyon. The slough water, identified by salinity, was primarily in two narrow bands following the canyon shelf break. A high nutrient (nitrate) signal, coincident with warm temperature and low salinity, was associated with the plume only very close to the source (within ~50 m). Seaward of this there was also a high nitrate signal aligned with a cold, salty anomaly. This supports a source from subsurface ocean (vertical mixing or upwelling). Although the slough plume had lower mean transmission (higher turbidity) than the offshore surface oceanic water, the maximum in turbidity was not in the slough plume. Instead it was in the upwelled canyon head-waters, identified by salinity and temperature.
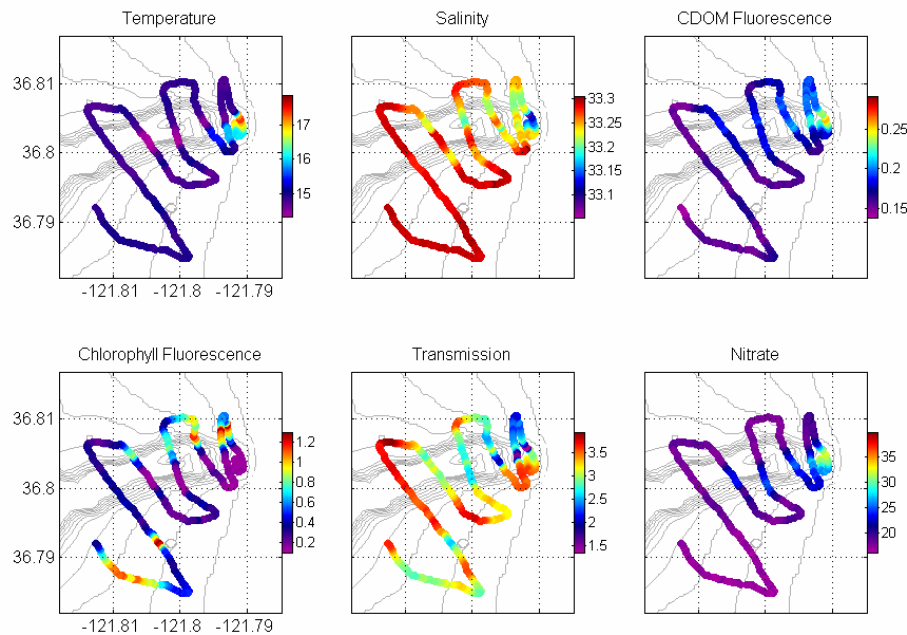
Figure 3: Underway-mapping results show complex interactions between plume and oceanic waters, influenced by upwelled waters at the head of the Monterey submarine canyon. The underway results are plotted over canyon bathymetric contours (light gray).

The plume's physical characteristics, depicted through ship-based profiles, show a wedge of warmer less saline water exiting the slough at maximum ebb tide, producing a sharp salinity gradient (halocline) where slough waters meet oceanic waters (Figure 4a). The resulting density gradient (pycnocline) enhances stratification, isolates plume waters from oceanic waters below, suppresses vertical mixing, and makes conditions potentially favorable for phytoplankton growth and harmful algal blooms.
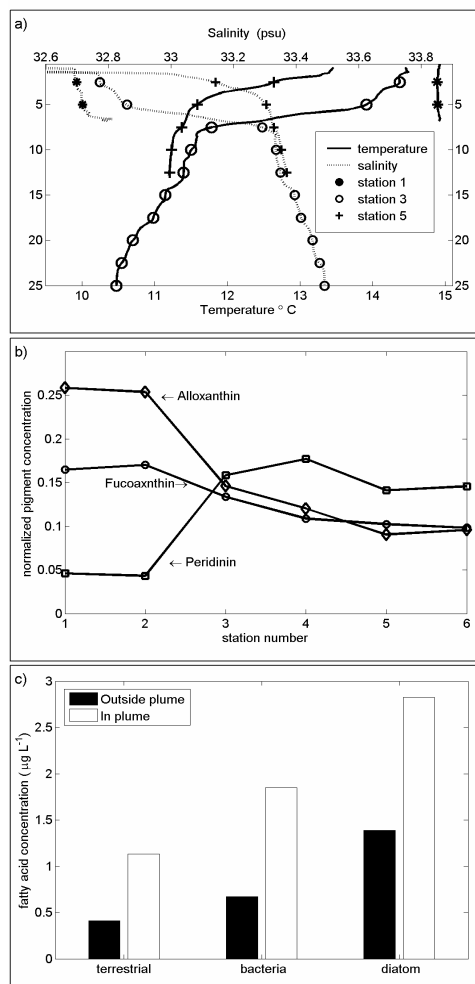
Figure 4: a) Temperature and salinity profiles of the plume show a low-salinity cool mass of water exiting the slough on low tide. The dotted lines are salinity and the solid lines are temperature. The solid circles indicate measurements taken inside the harbor entrance (station 1), the open circle just outside mouth of the harbor (station 3) and, and plus symbol indicates a sample taken at the 70-meter isobath (station 5). b) Fucoxanthin, alloxanthin and peridinin pigment concentrations retrieved from water samples. c) Fatty acid concentrations of terrestrial matter, bacteria and diatoms averaged among the 6 stations (white bar) and compared with and a control sample of oceanic water (dark bar).

Water samples, collected in successive sampling stations with increasing distance seaward of the slough, reveal distinct assemblages of phytoplankton between plume and bay waters. Analyses of these samples show high concentrations of alloxanthin, a carotenoid found in the phytoplankton group *Cryptophyta*, dominating the inland waters of Elkhorn slough (Figure 4b). Further from shore, alloxanthin concentrations diminish and concentrations of peridinin, a pigment indicative of the phytoplankton group *Dinoflagellata*, increase. It is possible that a plume of inland slough water, on a low enough tide, can introduce rich concentrations of cryptophytes into the bay influencing food web dynamics and biogeochemical transformation rates.

The water samples were examined further using fatty acid biomarker analysis. Examination of specific fatty acids and different lipid classes will provide a better understanding of sources of input to plume waters. The results show that plume water carries indicators of terrestrial material, bacteria and diatoms. Fatty acid concentrations of each of these markers were more abundant than those sampled from a control sample taken from nearby oceanic waters (Figure 4c). The presence of terrestrial biomarkers indicates the transport of "foreign" or land-based materials into Monterey Bay.

The SAM classification results produced reasonable classes separating slough, plume and ocean waters (Figure 5a), confirming the presence of a plume of spectrally distinct water (as in the visible image) exiting the slough and entering Monterey Bay. The plume becomes entertained in the alongshore current and proceeds south along the shoreline. The mean spectra of the classes differ in magnitude throughout the spectrum (Figure 5b). The overall increase in brightness in the slough and plume spectra is most likely due to suspended solids and the resultant increase in scattering.

Suspended sediment concentrations derived from the AVIRIS imagery (Binding et al., 2003), show elevated sediment in plume surface waters, with the highest
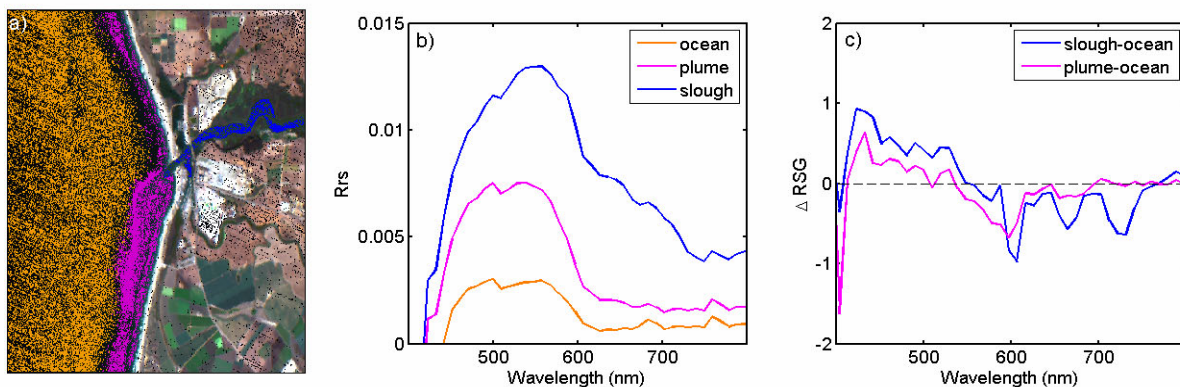
Figure 5: a) Spectral Angle Mapper classes for ocean (orange), plume (magenta) and slough (blue), b) class mean spectra, c) the first derivative of slough and plume classes referenced against the first derivative of the ocean class.

concentrations within the slough and at its mouth (Figure 6). Sediment loads vary between image dates, with ranges between 1 and 900 mg L^{-1} on October 13, 2000 and between 3-400 mg L^{-1} on October 7, 2002. This variability may be based on the rainfall, the stage and height of the tide and the degree of land use activity. The striking feature of these two images is that the suspended sediments quickly settle out of surface waters. The sediment particle size, sources and transport of eroded material from the banks and bottom of the slough should be examined further. Validation of the sediment algorithm results and field verification of sediment particle size distribution are currently being conducted.
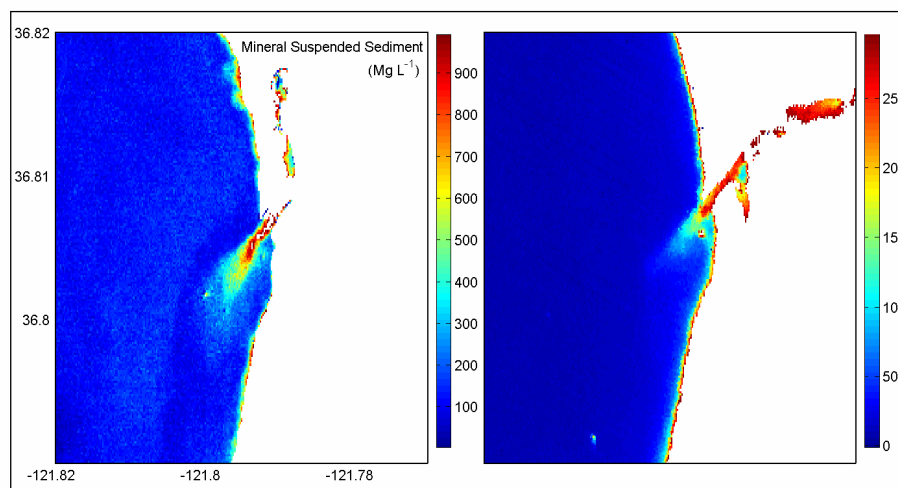
Figure 6: Mineral suspended sediments derived from the 2000 (left) and 2002 (right) AVIRIS captures of the slough plume.

Variations in magnitude and shape of the water type class spectra from the SAM classification results provide a useful framework for future algorithm development in plume studies. Mean raw spectra show subtle changes in slough spectral shape between 600 and 750 nm indicating subtle changes in variations of reflectance from plume and ocean spectra (Figure 5b). There is also a peak at approximately 645 nm in the slough spectra. To understand differences in spectral shape and further distinguish spectral differences between classes, first

107

order derivative spectra were generated after mean-filter smoothing (filter size = 3 points). First derivatives of slough and plume spectra, referenced against oceanic spectra, share subtle variations in spectra at approximately 600 nm (Figure 5c).   However, differences in reflectance between in the referenced slough and plume spectral derivatives appear at 660 and 730 nm. A spectral feature evident in the slough class has diminished once they have become a plume in the coastal ocean. Further examination to understand this variation in class spectra is currently being conducted.

4. Summary

AVIRIS imagery collected from the high altitude ER-2 platform has revealed small-scale processes in Monterey Bay, which play an important role in coastal ecology. The high-resolution AVIRIS imagery revealed convergence zones, created by internal-wave activity, which can concentrate potentially harmful red-tide organisms. The imagery also observed a coastal estuarine plume, which is potentially influencing the bay by introducing sediments, unique microbes and terrestrial matter. This sediment-laden plume creates complex interactions with upwelled waters from the head of the Monterey submarine canyon. Analyses of phytoplankton pigments show that cryptophytes, which dominate the inland waters of the slough, can be introduced into the Bay on spring tides, influencing ecology throughout the bay. Further analysis of fatty acid concentrations confirms the transport of terrestrial matter and bacteria into the bay. Heightened levels, or blooms of diatoms in the plume, may be a result of elevated levels of nutrients transported from the surrounding agricultural fields. Mean class spectra from the SAM classification procedure shows variability in spectra between slough, plume and bay waters. Spectral differences at 660 and 730 nm might form the basis for algorithm development to track slough or plume constituents throughout the bay via remote sensing. Finally, an application of sediment algorithms shows the rapid settling out of mineral suspended sediments in the plume.

5. Future Work

Dynamic ocean and estuarine processes in Monterey Bay present extremely difficult challenges in oceanographic sampling. Processes interacting at multiple spatial and temporal scales create a highly dynamic target, which can be difficult to resolve. AVIRIS overflights from 2000 and 2002 have bridged gaps in these scales and have been extremely valuable in identifying small-scale processes in Monterey Bay. We will continue multidisciplinary studies with AVIRIS imagery, combining in situ and multi-sensor analyses to sample across multiple temporal and spatial scales. Red tide development was observed during the most recent (2004) AVIRIS acquisition. This imagery will be critical for examining the development of this red tide event. Further spectral analysis of water class spectra will form the basis of algorithm development to derive inherent optical properties. Testing is now underway to validate and extract suspended sediment concentrations and color dissolved organic matter (CDOM). Particle–size spectrum analyses are being conducted to determine size, source and transport of sediments from the slough into the coastal ocean. AVIRIS will continue to provide us with a greater understanding of the influence of oceanographic and estuarine phenomena on the ecology of Monterey Bay.

6. References

Binding, C.E., D.G Bowers, E.G. Mithcelson-Jacob, 2003, "An algorithm for the retrieval of suspended sediment concentrations in the Irish Sea from SeaWiFS ocean colour satellite imagery." International Journal of Remote Sensing, vol. 24, no. 19, pp. 3791–3806.

Green, AA M. Berman, B. Switzer, M.D. Criag, 1998, "A transformation for ordering multispectral data in terms of image quality with implications for noise removal." IEEE Transactions on Geoscience and Remote Sensing, vol. 26, no. 1, pp. 65–74.

Hoagland, P., D. M. Anderson, Y. Kaoru, A. W. White, 2002, "The economic effects of harmful algal blooms in the United States: Estimates, assessment issues, and information needs *Estuaries*, vol. 25, no. 4B, pp. 819.

Horner, R.A., D. L. Garrison, F. G. Plumley, 1997, "Harmful algal blooms and red tide problems on the U.S west coast." *Limnology and Oceanography,* vol. 42, pp. 1076.

Gao, B.C., Montes, M. J., Ahmad, Z. & Davis, C. O., 2000, "Atmospheric correction algorithm for hyperspectral remote sensing of ocean color from space." *Applied Optics,* vol. 39, pp. 887.

Kruse, F.A., L.L. Richardson, V.G. Ambrosia, 1997, "Techniques for geological analysis of hyperspectral data applied to near-shore hyperspectral ocean data." Foruth International Conference on Remote Sensing for marine and Coastal Environments, Orlando, Florida, 17–19 March.

Montes, M.J., Geo, B.G & Davis, C.O., 2004, "NRL Atmospheric Correction Algorithms for Oceans: Tafkaa User's Guide." NRL/MR/7230-04-8760.

O'Reilly, J. E. et al., 1998, "Ocean color chlorophyll algorithms for SeaWiFS." *Journal of Geophysical Research,* vol*. C* 103, pp. 24937.

Shimizu, Y., in *Red Tides Biology, Environmental Science, and Toxicology: Proceedings 1st International Symposium on Red Tides,* T. Okaichi, D. M. Anderson, T. Nemoto, Eds. (Elsevier, New York, 1989), pp. 17–22.

Smayda ,T. J., 2000, "Ecological features of harmful algal blooms in coastal upwelling ecosystems." *South African Journal of Marine Science*, vol. 22, pp. 219.

A Parallel Processing Algorithm for Remote Sensing Classification

J. Anthony Gualtieri
Code 606.3 and Global Sciences and Technology
NASA/GSFC Greenbelt, Maryland 20771
gualt@backserv.gsfc.nasa.gov

1   Introduction

A current thread in parallel computation is the use of cluster computers created by networking a few to thousands of commodity general-purpose workstation-level commuters using the Linux operating system. For example on the Medusa cluster at NASA/GSFC, this provides for super computing performance, 130 Gflops (Linpack Benchmark) at moderate cost, $370K. However, to be useful for scientific computing in the area of Earth science, issues of ease of programming, access to existing scientific libraries, and portability of existing code need to be considered. In this paper, I address these issues in the context of tools for rendering earth science remote sensing data into useful products. In particular, I focus on a problem that can be decomposed into a set of independent tasks, which on a serial computer would be performed sequentially, but with a cluster computer can be performed in parallel, giving an obvious speedup. To make the ideas concrete, I consider the problem of classifying hyperspectral imagery where some ground truth is available to train the classifier. In particular I will use the Support Vector Machine (SVM) [1] approach as applied to hyperspectral imagery [16].

The approach will be to introduce notions about parallel computation and then to restrict the development to the SVM problem. Pseudocode (an outline of the computation) will be described and then details specific to the implementation will be given. Then timing results will be reported to show what speedups are possible using parallel computation. The paper will close with a discussion of the results.

2   Supervised Classification of Hyperspectral Data

I will address the problem of supervised classification of hyperspectral images working only in the spectral domain. Because the data is *high dimensional*, in that there are hundreds of channels of spectral information per pixel comprising a spectra and represented as a vector of values, algorithms that use all of the channels can be computationally expensive. The traditional approach to handling this is to perform a pre-processing dimension reduction step, but this removes valuable information. Here we will use an algorithm that uses all the channels.

For supervised classification, the problem separates into a training phase and a testing phase. For the training phase we are given exemplars with class labels, in this case the spectra associated to the ground truth pixels in the scene. These are used to train the classifier. In the testing phase the trained classifier is then applied to pixels not yet classified and not used in the training phase.

---

[1] The term "machine" in Support Vector Machine is only a name and does not imply a hardware device.

2.1 Simplifying Classification with Many Classes

2.1.1 Training

Given we have an algorithm to classify a pair of classes, how do we build classification algorithms that can handle multiple classes? Let K be the number of classes, where $K \approx 10\ldots 20$ and more, and where each class contains varying numbers of training vectors (spectra in the case of hyperspectral imagery). A successful strategy to cope with large numbers of classes is to decompose the problem into a number of simpler classification problems that each deal with only *pairs* of classes. One such method is to train over all possible pairs of classes, $K(K-1)/2$, in number, and then use some voting scheme in the testing phase of the classification. Call this the K choose 2 method. An alternative approach is to train K pair classifiers, each of the form 1 versus $K-1$ and then in the testing phase compare results from the K classifiers to render a classification. Call this the 1 vs. $K-1$ method. The second method involves a heavy burden on training the K such classifiers, one for each class, because there will be many training spectra from the $K-1$ classes that are lumped together for training. The SVM training algorithm has computational complexity $O(m^2)$, where m is the number of training vectors in the pair of classes. Computational complexity here means how the time to complete the computation on a single processor scales in terms of the number of units of data, m, to be processed — in this case the number of training spectra. Thus, if time to completion is given by $t = Am^2 + Bm + C$, where t is time to completion, and A, B, C are constants, then $t \sim O(m^2)$. To obtain an estimate of the complexities of the two methods, assume each training class is the same size, $\frac{m}{2}$. Then the time complexity for the two approaches is given in Table 1. In the left column is the K choose 2 approach and in the right column is the 1 vs. $K-1$ approach. The second row indicates where these results come from.

Table 1: Time complexity on a single processor for performing SVM training for a classifier of K classes each containing $m/2$ exemplars.

K choose 2	1 vs. $K-1$
$O(K^2 m^2) \sim$	$O(K^3 m^2) \sim$
$K(K-1)/2 * O(m^2)$	$K * O(((K-1)\frac{m}{2} + \frac{m}{2})^2)$

There is a time complexity advantage to using the K *choose* 2 method. We adopt this approach in the what follows. In addition, there is some evidence that the K *choose* 2 method is more accurate than the 1 vs. $K-1$ method [17]. For the K choose 2 method, simple parallelism can be readily obtained by putting each pair-training computation on a different processor on the cluster machine. If there are more pairs than processors, then they are stacked onto processors and solved sequentially. Note we will not parallelize the basic pair-training algorithm as this would require having detailed knowledge of the SVM training algorithm optimization method, though see [28], for results from such an approach for training a pair classifier with very large numbers of training vectors.

2.1.2 Testing

Once we have trained the $K(K-1)/2$ pair classifiers, we obtain the classification in the testing phase by applying all the pair classifiers to each spectra (one per pixel) to be classified, and for each pair noting which of the two classes is found for that pixel. Then all $K(K-1)/2$ results per pixel (think of votes) are placed into one of K bins and the bin with the largest number of votes is declared the class for that pixel. For ties in the number of votes, either a random selection is made or some refinement using a numerical measure from the pair classifier is used. Thus, if we define $V_{\mathbf{r}} \in [1, \ldots, K]$ as the classification label for the pixel at position $\mathbf{r}$, then the winning class label at pixel $\mathbf{r}$ is given by

$$V_{\mathbf{r}} = \arg \max_k \sum_{i,j \; i<j} \delta_{k, v_{\mathbf{r}}(i,j)}, \tag{1}$$

where for pair classifier i, j,

$$v_{\mathbf{r}}(i,j) = \left\{ \begin{array}{ll} i & \text{if class } i \text{ wins over class } j \\ j & \text{if class } j \text{ wins over class } i \end{array} \right. ,$$

and

$$\delta_{m,n} = \left\{ \begin{array}{ll} 1 & \text{if } m = n \\ 0 & \text{if } m \neq n \end{array} \right.$$

is the Kronecker delta function.

Here parallelism can be used in several ways. We can use a single processor testing code for all $K(K-1)/2$ pairs, and segment the imagery into tiles that cover the whole scene, and process the tiles each on a different processor. Or we may use a single processor code that implements the testing phase for each of the $K(K-1)/2$ pair classifiers applied to the whole image on a single processor, and follow this with a voting scheme to obtain the final classification. The voting scheme part could be run on a single processor as it is likely to be very fast, or if need be, applied on different processors in a tiling of the image.

2.2 The Support Vector Machine Algorithm

The basic algorithm used in this paper to perform supervised classification of hyperspectral remote sensing data is the SVM coupled with the Kernel Method [25]. Previous work using the SVM algorithm together with the Kernel Method derives from the machine-learning community, with methods pioneered by Vapnick, and extended by Boser, Guyon, and Vapnick [2], and Cortes and Vapnick [6]. In particular the SVM approach yields good performance on *high-dimensional* data such as hyperspectral imagery, and does not suffer from the *curse of dimensionality* [1], which limits the effectiveness of conventional classifiers due to the Hughes effect [18]. This because the SVM classifier depends on only a small subset of the training vectors, called the support vectors, which define the classifier as used in the testing phase.

Application of SVM to hyperspectral data was first demonstrated by Gualtieri and co-workers in [16] [15] [14]. I direct the reader to those references for details of the SVM formulation and application to several hyperspectral data sets, including Indian Pines 1992 of image size 145 × 145 with 200 bands and 16 classes [2] [22], and Salinas 1998 with image size 512 × 215 with 224 and 16 classes [3] [21]. In the reported work above, all implementations were performed on a single workstation class processor and used T. Joachim's open source SVM^{light} package [19] [20]. The most computationally expensive task within the SVM training requires quadratic optimization, for which A. Smolla's open source PR_LOQO was used [26]. More recent work [29] [23] [4] [3]. has provided further validation of SVM's utility for hyperspectral classification.

3 Parallel Implementation for Supervised Learning by Porting Serial Code

We take as given a serial code for performing SVM training and testing for classification of hyperspectral data. Here we introduce more of the details of the parallel computation and demonstrate how the serial code can be adapted to parallel computation.

---

[2] A 145 × 145 pixel and 220 band subset in BIL format of radiance data that has been scaled and offset to digital numbers, DN, from radiance, rad in units $W/(cm^2 * nm * sr)$ according to DN = 500 * rad + 1000 as 2bit signed integers. It is available at ftp://ftp.ecn.purdue.edu/biehl/MultiSpec/92AV3C. Ground truth is also available at ftp://ftp.ecn.purdue.edu/pub/biehl/PC_MultiSpec/ThyFiles.zip. The full data set is called Indian Pines 1 f920612t01p02_r02 as listed in the AVIRIS JPL repository (http://aviris.jpl.nasa.gov/ql/list92.html). The flight line is Lat_Start: 40:36:39 Long_Start: -87:02:21 Lat_End: 40:10:17 Long_End: -87:02:21 Start_Time:19:42:43GMT End_Time:19:46:2GMT. See also http://dynamo.ecn.purdue.edu/~biehl/MultiSpec/aviris_documentation.html

[3] AVIRIS Hyperpsectral Radiance Data from f981009t01r_07. The full flight line is 961 samples by 3479 lines consisting of 224 bands of BIP calibrated radiance data that is scaled to lie in [0,10000] as 2bit signed integers. We have studied part of scene 3. The full flight line is called f981006t01p01_r07 as listed in the AVIRIS JPL repository. The flight line is [Lat_Start: +36-15.0 Long_Start: -121-13.5 Lat_End: +36-21.0 Long_End: -121-13.5 Start_Time: 1945:30GMT End_Time: 1950:15GMT.

3.1 Programming Model, Hardware, Message-Passing Interface

For parallel programming, currently the most popular model is Multiple Instruction Multiple Data (MIMD). Here each of the processors can perform different instructions on different data, and there is no synchronization of the processor clocks. Because of the lack of explicit synchronization, any interprocessor communication must be explicitly initialized and and then tested for completion at the sending and the receiving processors, if subsequent processing is to remain synchronized. This overhead of testing for completion is assumed to be the responsibility of the programmer, and is part of what makes this programming model difficult to use.

Such MIMD machines may or may not have a shared memory system among all the processors, but the most typical use a collection of nodes each consisting of a symmetric multiprocessor (SMP) with a shared memory and shared disk. Typically each SMP node may comprise two to four single processors. Here shared memory is only at the nodes. In the sequel we will take the basic unit of computation as the processor. The differences in communication within a node and between nodes will not be considered, which is reasonable given the particular problems we solve. This particular hardware configuration is called a Beowulf cluster and can consist of a few to hundreds of nodes [27].

The software used here to coordinate the processors is the Message Passing Interface (MPI) [10] [8] [13]. MPI extends the C and C++ languages (or Fortran) with a set of subroutines that implement communication and data movement among unsynchronized processors, and provides for methods to test for synchronization. With careful layout of data and communications, the multiple processors can divide up a computation efficiently, although there is a heavy load on the programmer to craft the code. The actual code used in any particular parallel problem is heavily problem dependent.

3.2 Pleasingly Parallel Problems

If we can decompose the serial code into a series of tasks with minimal communication between the tasks, namely at the beginning and ending of the tasks, then the porting of the serial code fits under the rubric of *pleasingly parallel.* [4] As an example, consider problems involving imagery where the spatial coordinates do not enter explicitly into the computation. A decomposition can result from dividing the image into tiles on which the same computation is to be performed. A very simple example would be normalizing an image by dividing by a given constant value. In a serial machine code, a loop over all N pixels is run, and each pixel is normalized one after the other, taking $O(N)$ time. In a parallel setting, if we had as many processors as pixels, then each processor would perform one division operation taking $O(1)$ time. For comparison, a less trivial task would be to find a normalization factor by adding values from each pixel and dividing by the number of pixels. On a parallel machine, explicit communication between nodes would be required as part of the task. In fact, this can be accomplished in $O(log_2 N)$. See Appendix A.

The SVM training and testing problem we address here can be thought of as having a simple decomposition into independent parts that can be processed, with communication occurring only at the start and finish of each task.

3.3 Organizing the Problem

Let us now consider how to organize a cluster computer for a pleasingly parallel problem with n_p number of processors and n_t number of independent tasks. Call the set of tasks the task list. We wish to find an approach that keeps all the processors busy as much of the time as possible. If the size of the task list is $n_t \leq n_p$, then put one task on each processor and wait until the last task completes.

If $n_t > n_p$, a naive solution would be to first put an equal number of tasks, $\lfloor n_t/n_p \rfloor$, [5] on each processor

---

[4]This is also referred to as *embarrassingly parallel* in that, in principle the decomposition of the problem is trivial.

[5]$\lfloor x \rfloor$ is the floor function, defined as the nearest integer to x that is smaller than or equal to x.

and let them run sequentially on each processor until complete. If there are remaining tasks, $n_{rem} = n_t - \lfloor n_t/n_p \rfloor \neq 0$, then put these last tasks on any of n_{rem} processors. However, this will be efficient only if all tasks take the same amount of time. This solution is like the queuing problem in a bank where a large number of people enter at one time and each go to a teller in a separate queue. If no more people enter and once in a line you cannot shift, then roughly the lines start out at the same length. However, as transaction duration for each person varies, some people will have longer waits than others while eventually some tellers will have no customers. For SVM, the training times will be different because of different numbers of training vectors in the classes to be trained on.

At this point, note that it has not been said where the original complete task list lives, or how the task list is divided up and communicated among the processors. This is taken care of by designating a particular processor of the cluster as the *boss processor*, whose job is to manage the apportioning of the task list and the communication of tasks to the remaining processors, which are called the *worker processors*. Then with the boss processor able to monitor the status of each worker processor, the boss processor can, first using a list of tasks waiting to be done, send one each to all the worker processors and thereafter wait for workers to be done and then send the next task in the list to that worker processor. In this way, all the worker processors are always busy. We have implemented this approach in prototype program called **boss_workers** and subsequently mapped the learning phase and the testing phase of the supervised classification onto it. However, there still remain issues concerning the sending and receiving of communications from the boss to the worker, and from the worker to the boss. We address this below.

3.4 Aspects of Communication in MPI

Here we give an overview of how to handle the asynchronous communication between processors in the MPI language for this particular application. Communications consists of two parts, sending and receiving. To describe this process we use a metaphor based on the postal system and described in Table 2. Here buffer is

Table 2: Postal system analogy to MPI send and receive statements.

Postal System	MPI
sender writes letter	sender loads buffer
sender posts letter and waits for notice of receipt	sender executes MPI_Send on buffer
recipient waits for mail to be received	receiver executes MPI_Receive on buffer
recipient reads letter	receiver unloads buffer

a piece of memory available to the sending and receiving processor. Note that MPI_Send and MPI_Receive do not "simply post the letter" or check for "receipt of a letter", and then continue to do other things. These MPI statements are called blocking send and receives, and they cause the processor to wait for completion before continuing to the next statement in the code. This may have a problematic side effect as illustrated in Table 3, showing deadlocking involving executing MPI_Send and MPI_Receive on processors i and j. The

Table 3: Deadlocking in MPI.

processor i	processor j
MPI_Send(j)	MPI_Send(i)
MPI_Recv(j)	MPI_Recv(i)

problem is that it is possible, depending on buffer size, for neither MPI_Send(i) or MPI_Send(j) to complete because each MPI_Send awaits the execution of the MPI_Recv on the other processor, which cannot be reached.

To handle this problem and to make MPI code *safe*, [6] meaning here that deadlocking cannot occur, MPI provides a second kind of Send and Recv called *non-blocking* designated MPI_ISend and MPI_IRecv. These statements post the send and receive messages, but do not wait for completion. Now to know if the messages are completed, another class of MPI statements called MPI_Wait is needed.

3.5   Boss_workers algorithm in MPI

Now we can can give an abstract version of the `boss_workers` algorithm written in pseudocode. In programming in MPI the approach is to write a *single* code that will be running simultaneously on the boss and the worker processors. Thus, we can have sections of identical code running on all the processors, albeit not synchronized, or we can can have sections that are specific to one or more processors. The overall code makes this distinction by using a function in MPI that returns the number of the processor it is running on. By testing on this number in an *if* or *case* statement, we can designate in the single MPI code, sections that will run only on designated processors. In the `boss_workers` code, one processor, numbered 0, is the boss, and $1 \ldots n_{worker}$ are the workers. Communication issues here only involve the boss communicating with a worker. No worker-to-worker communication occurs.

We present below a simplified code for the `boss_workers` algorithm. The framework for this code is described for the case of each task taking the same computational effort (same time to execute) in the book and on the web site of Peter Pacheco [24], with particular applicaton to matrix vector multiplication. However, for the classification problem, the worker tasks require different computational effort, and also require a generalization. This has been provided by William Gropp in the example of the use of the MPI command `MPI_Waitsome`, [12]. Beside the communications, the computational parts are:

`make_task_list`, where the `boss` generates the tasks.

`boss_make_task`, where the `boss` takes a particular task and creates data for a `worker`.

`worker_work` takes the input data sent by the `boss`, and the `worker` creates an output that is returned to the `boss`.

`consume`, where the `boss` takes the output from the `worker` and completes processing on that output.

In application to the training phase the `worker_work` would be replaced by a module that performs SVM supervised learning, which for training takes as input the pair of two sets of exemplar or training vectors and outputs a file describing the appropriate classifier in terms of the support vectors it finds. For the testing phase, the input is the set of classifiers found in the training phase, and the hyperspectral cube of unclassified data. The output is the classified image. In the following pseudocode, scalar variable declarations are not explicitly included while arrays `a, b` with `n, m` elements, respectively, are explicitly declared with `allocate( a[0:n-1]), b[0:m-1], ...)`.

---

[6]The problem of *safety* and a related concept *fairness* can be resolved in a variety of ways. See [11].

```
boss_workers( n_tasks, n_procs ) {

    my_id  = MPI_Comm_rank;      % get my own processor number
    n_workers = n_proc - 1;      % don't count boss
    boss = 0;                    % boss is always labeled 0
    i_task_bs = 0;               % running index of boss task ( 0 based )
    i_task_wk = 0;               % running index of worker tasks (0 based) labels
                                 % task, but not always  worker doing task

    if ( my_id == boss ) {              % in this part is the code that runs on the boss
        allocate( buff_bs_snd  [0:n_task_chunk-1],    % buffers for boss
                  buff_bs_snd  [0:n_task_chunk-1],
                  indices_bs_rec[0:n_task_chunk-1],
                   status_bs_rec[0:n_task_chunk-1],
                  indices_bs_rec[0:n_task_chunk-1]  );
        make_task_list( n_tasks, task_list );
        n_tasks_chunk = minimum( n_tasks, n_workers );   % max tasks running at once
        n_tasks_to_do = n_tasks;
        i_done        = 0;                       % 0 based count of completed tasks

        for (i=0;i< n_tasks_chunk;  i++) {                        % full execution
            boss_make_task( i_task_bs, n_tasks, task_list,  buff_bs_snd[i] ); % of loop sends
            MPI_Send(  buff_bs_snd[i], i+1,  i_task_bs+1 );       % out one chunk of
            MPI_Irecv( buff_bs_rec[i], i+1  );                    % tasks and posts
            i_task_bs = i_task_bs + 1;                           % recv's
        }
        while (n_tasks_to_do > 0 ){
            MPI_Waitsome( n_tasks_chunk,  n_done, indices_bs_rec, senders_array );
            for (j=0; j<n_done; j++ ) {
                k = indices_bs_rec[j];         % k is index of the buff which received the send
                sender  = senders_array[j]
                consume( buff_bs_rec[k] );
                i_done        = i_done + 1;   % total completed tasks
                n_tasks_to_do = n_tasks_to_do + 1;
                if ( i_task_bs <= n_tasks - 1 ) { % if tasks are left send a new task to
                                                  % processor that finished and post a receive
                    boss_make_task( i_task_bs, n_tasks, task_list,   buff_bs_snd[k] );
                    MPI_Send(   buff_bs_snd[k],  sender, i_task_bs+1 );
                    MPI_Irecv(  buff_bs_rec[k],  sender, request_bs_rec[k]  );
                    i_task_bs  = i_task_bs + 1;
                }
            }
        }
        for (i=0; i< n_workers; i++) {
            MPI_Send(0, 0, i+1, DIETAG );  % all done, send DIETAG is a defined constant
        }                                  % to status_wk_rec on worker to notify worker
    }                                      % to shut down
    else{  while (1) {
            allocate( status_wk_rec[0], buff_wk_rec[0], buff_wk_snd[0] );
            MPI_Recv( buff_wk_rec[0], boss,  status_wk_rec );
            i_task_wk = status_wk_rec;  %
            if ( i_task_wk == DIETAG) {
                break;
            }
            worker_work( buff_wk_rec[0],  buff_wk_snd[0] );
            MPI_Send(  buff_wk_snd[0], boss, i_task_wk );
        }
    }
}
```

4 Data Input and Output

A secondary issue is how data is to be passed to and from boss and workers. We can either have the boss read all the data and then explicitly pass the data to the workers at the time it is needed or we can make all the data available to the workers who then read the parts they need, based on names of data passed to them by the boss. Because the data set can be large, there are questions of how to best distribute the data to optimize overall computational time.

We elected to have all the input and output be processed by the workers, and have only labels describing the files to be input and output, passed by the boss to the workers. This finesses the passing of large data files between the boss and the workers, and places that burden on the file system of the cluster. For the benchmark computations of SVM training and testing, each node has its own copy of all required input files and writes only to its local disk.

It is possible to have all files shared by workers and boss by using Network File System (NFS), where the operating system passes copies of the needed file to the nodes as they need them. This effectively shares the same file system on all processors, and preliminary results for the SVM problem show similar performance. Note that the total size of the input data and output data in the training phase is 1.6 MB and 6.8 MB, respectively, and for the testing phase 23.6 MB and 2.5 MB, respectively. Given input/output (IO) speeds on the hardware used here, the time for IO of the data used here is small compared to processing times. However, for larger problems, the IO time costs may become significant, and different approaches may be needed for higher performance.

4.1 Details of the MPI Subroutines Used

The explanation of the MPI functions and a definition used in the pseudo code are:

MPI_Send(buff_bs_snd[i], i+1, i_task_bs+1)   This posts the data from the boss buff_bs_snd[i] into the communication channel to processor i+1 with message tag i_task_bs+1 . Only when the buffer is received and emptied does it complete (blocking send).

MPI_Irecv(buff_bs_rec[i], i+1)   This accepts the data into buff_bs_rec[i] on the boss processor from the worker processor i+1 and continues without waiting for completion (nonblocking receive).

MPI_Waitsome(n_tasks_chunk, n_done, indices_bs_rec, senders_array)   Waits for multiple communications to complete on the boss from n_tasks_chunk different workers. The quantity indices_bs_rec is an array of size n_tasks_chunk that contains the index identifying the receiving buffers among all the buffers buff_bs_rec[ ] corresponding to the members of the array senders_array of size n_tasks_chunk, which contains the identities of the n_tasks_chunk senders.

MPI_Recv(buff_wk_rec[0], boss, status_wk_rec)   Blocking receive that accepts the data into the buffer buff_bs_rec[0] from the boss processor with resulting status written to the structure status_wk_rec.

DIETAG is a defined constant to signify work is completed.

In this implementation the buffers passed between boss and workers, buff_bs_snd, buff_bs_rec, buff_wk_snd, and buff_wk_rec, are very small structures containing labels describing files to be read by the workers, and timing information to be returned.

4.2 Implementation Details

In this code development for SVM, we opted to use a library of open source routines in C called LIBSVM, written by Chih-Chung Chang and Chih-Jen Lin [5]. In addition to a series of routines for input and output,

they have created a library of core subroutines and a set of data structures that we use in our parallel code. To handle hyperspectral data we have written our own IO routines as well as routines to convert from a hyperspectral cube to the data structure they use. These routines are then embedded into the `boss_workers` code.

In vanilla MPI only the single data type, vector, can be defined for the buffers that pass data to and from the boss to the workers, however, it is extremely useful to be able to pass structures or other more complex data types in the buffers. One can use various MPI routines to do this, but a utility called AutoMap [7] automates this and is used in this implementation.

5 Timing and Speedup

To examine the performance of the parallelization of SVM code as implemented in the `boss_workers` algorithm, first we demonstrate the scaling of the speedup (ratio of single code execution time over parallel code execution time) for the `boss_workers` code on a very simple task. Here the work done on each worker processor is to make it sleep for a fixed length of time. Then as a benchmark of a real problem, we apply training and testing of the SVM to the well-studied hyperspectral data set, Indian Pines 1992 [22], of size $[n_l, n_s, n_b] = [145, 145, 200]$ with $K = 16$ classes. In what follows, all times reported are wall clock time, overall elapsed time, rather than actual computation time as performed by the processor. The times reported are based on the nodes in use having only one user. It is possible to have time sharing of parallel jobs, but this is not the case here.

5.1 Simple Validation

Let the work done on each worker processor be to sleep for a fixed length of time, say 5 s. We expect that if the number of processors matches the number of tasks, then total computing time will remain the same independent of the number of tasks. Table 4 shows the total time taken (wall-clock) assuming no other jobs running. Except for the jump of 1 s for $n_p = 1 + 100$, the results are consistent with the notions above. The slight increase in time is presumably due to the boss performing the overhead of managing the workers.

Table 4: Time to completion (s) and speedup for the fixed length computation of sleep 5 s versus number of processors.

$n_{proc} = 1 + n_{work}$	1+1	1+2	1+3	1+4	1+5	1+10	1+20	1+30
time (s)	5.04	5.16	5.17	5.18	5.21	5.22	5.30	5.44
speedup	1.00	0.98	0.97	0.97	0.97	0.97	0.95	0.93

$n_{proc} = 1 + n_{work}$	1+40	1+50	1+60	1+70	1+80	1+90	1+100	1+110
time (s)	5.59	5.73	5.96	5.96	6.77	6.96	7.59	6.51
speedup	0.90	0.88	0.85	0.85	0.74	0.72	0.66	0.77

5.2 SVM Training on Indian Pines 1992

For this data set there are 16 classes giving $16 * 15/2 = 120$ pairs. The number of training vectors in the 16 classes is given in Table 5. It is clear that the pair involving classes 2 and 11 will take more training time than any of the other pairs, and it this pair that is the cause of the limiting behavior in the speedup as seen below. Table 6 shows timing results with varying numbers of processors applied to training 120 pair classifiers.

119

Table 5: Training class sizes for the 16 classes in the Indian Pines 1992 data set. These sizes represent 20% of the available ground truth.

class label	1	2	3	4	5	6	7	8
# train vec.	10	286	166	46	99	149	5	97

class label	9	10	11	12	13	14	15	16
# train vec.	4	193	493	122	42	258	76	19

Table 6: Time to completion (s) and speedup of the training phase for the Indian Pines 92 full data set versus number of processors.

$n_{proc} = 1 + n_{work}$	1+ 1	1+ 2	1+ 3	1+ 4	1+ 5	1+ 10	1+ 20	1+ 30	1+ 40	1+ 50
time (s)	31.8	17.2	13.3	10.8	9.7	8.8	9.0	9.1	9.3	9.2
speedup	1.0	1.9	2.4	2.9	3.3	3.6	3.5	3.5	3.4	3.5

$n_{proc} = 1 + n_{work}$	1+ 60	1+ 70	1+ 80	1+ 80	1+ 90	1+ 90	1+100	1+110	1+120	
time (s)	9.5	9.2	9.2	9.5	9.3	9.4	8.7	9.8	9.9	
speedup	3.3	3.4	3.5	3.4	3.4	3.4	3.6	3.3	3.2	

Here there is the expected result that the speedup improves and then levels out or saturates, (reaches a constant value) around 1+10 processors and then trends slightly down. The trend down for a larger number of processors possibly reflects the communications between the boss processor and the workers occurring in a shorter interval leading to more contention for bandwidth in the network that connects the processors to each other. The small variations up and down for 1+10 and more processors in the speedup are not understood.

The reason that the speedup saturates is because the processor times are not the same. When there is one task that takes substantially longer than any other task, then several faster tasks can be completed before the longest task. Thus, while one processor is tied up with longest task, there will be a given number of processors, fewer than the number of tasks, where cumulatively all the shorter tasks will be completed in the same time as the longest task. Adding more processors than this number will not increase speedup as the time limitation will be the time of the longest task.

5.3 SVM Testing on Indian Pines 1992

For testing, we split the computation into a part that applies each of the 120 classifiers built in the training phase above to the whole data cube, and a part that aggregates these results to get the final classification result. The first part results in 120 arrays, each the size of the image, and where each element is the winning label of one of the two classes from each particular classifier. The aggregation part combines these 120 arrays in a voting scheme according to Eq. 1 on page 2. This second step can be computed quickly, less than 1 s for the 120 145 × 145 array to be processed, so there is no need to parallelize this step here. In Table 7 are given the results of applying all 120 pair classifiers to the data cube without the aggregation step for varying numbers of worker processors.

Here speedup saturates at around 1+30 processors. The reason for saturation is the same as that for the training phase, a nonuniform distribution of processing times over the tasks. Again the relation of the time for the slowest pair to complete versus the other times to completion determines some number of processors

Table 7: Time to completion (s) and speedup for computation of testing phase (without final voting) for Indian Pines 92 full data versus number of processors.

$n_{proc} = 1 + n_{work}$	1 + 1	1 + 2	1 + 3	1 + 4	1 + 5	1 + 10	1 + 20	1 + 30	1 + 40
time (s)	237.5	120.7	91.3	76.2	67.3	45.8	37.0	32.9	33.6
speedup	1.0	2.0	2.6	3.1	3.5	5.2	6.4	7.2	7.1

$n_{proc} = 1 + n_{work}$ y	1 + 50	1 + 60	1 + 70	1 + 80	1 + 90	1 +100	1 +110	1 +120	
time (s)	35.3	33.6	33.0	31.8	34.6	34.1	33.5	33.7	
speedup	6.7	7.1	7.2	7.5	6.9	7.0	7.1	7.0	

where saturation occurs. This slowest pair determines the fastest time for completion for all tasks that can be accomplished on a cluster of processors with more than the saturation point number of processors.

6   Discussion

In this paper aspects of parallel computation implemented on a Beowulf cluster as applied to the supervised classification of hyperspectral imagery are examined. Because this type of classification is computationally expensive, scaling as $O(m^2 K^2)$, where K is the number of classes and m is the number of training vectors per class, the application of parallel techniques is justified. The structure of this problem avails itself of simple parallelization because both the training and the application of the trained classifier to the unclassified imagery, the testing phase, can be decomposed into $K(K-1)/2$ simpler tasks involving only pairs of classes. The problem then is to pass these multiple smaller tasks to the processors of the cluster machine so as to keep all the processors busy. A simple algorithm called the boss_workers algorithm implements this. One processor, the boss, creates a list of tasks and then passes the tasks to the worker processors and awaits their completion at which point a remaining task is sent to the available worker. Implementation of this algorithm in the standard language for cluster computing, MPI with C (or Fortran), must deal with the lack of explicit synchronization among the processors. In particular the various task usually complete in differing lengths of time. MPI handles this using a set of routines to send, receive, and test for completion of communication.

A measure of the effectiveness of parallelization is the speedup. Speedup, S, is defined as the ratio of time to completion on a single processor to time to completion on multiple processors. For pleasingly parallel problems where n_t tasks are all decoupled, and where the time to completion is each task is the same, then

$$S = \frac{n_t}{\lceil \frac{n_t}{n_w} \rceil},$$

and [7]

$$S = n_t \text{ if } n_w \geq n_t.$$

This shows that speedup saturates at n_t when $n_w \geq n_t$ if all processes take the same length of time. If there are different times of computation, then lower speedups occur, saturating at fewer numbers of processors. The results obtained above show speedups for supervised classification of hyperspectral imagery for the small problem studied here to be of the order of 3.5 for the training phase and around 7 for the testing phase, much less than the optimal value of 120, obtained only if all the tasks take the same time to complete. The reason for the saturation is due to a non-uniform distribution of times among the tasks. The reason for the training having a lower speedup than the testing phase is because it has a more non-uniform distribution of

---

[7] $\lceil x \rceil$ is the ceiling function, defined as the nearest integer to x which is larger than or equal to x.

processing times than for testing. If the processing times are ordered from longest to slowest, then roughly the distribution is more non-uniform if the differences in processing times for tasks are greater. Recall that if all the processing times are equal, the speedup saturates only when $n_{tasks} = n_{workers}$. The distribution of task times in descending order for the first thirteen for the training phase, in s, is

$$7.50 \quad 5.79 \quad 3.32 \quad 1.86 \quad 1.85 \quad 1.49 \quad 0.84 \quad 0.74 \quad 0.62 \quad 0.58 \quad 0.58 \quad 0.48 \quad 0.38$$

while for the testing phase, in s, it is

$$31.2 \quad 29.5 \quad 20.7 \quad 15.5 \quad 14.7 \quad 9.9 \quad 8.0 \quad 7.0 \quad 6.9 \quad 6.3 \quad 5.8 \quad 5.6 \quad 4.9.$$

The steeper drop in processing times for the training phase than testing phase causes a more rapid saturation of speedup at a lower value. Note that the time for longest task for the training phase is 7.5 s which is close to the saturated time of 9 s, while for the testing phase the time of the longest task is 31 s which is close to the saturated time of 33 s The task times are only for the worker performing the task without the overhead of the boss_worker code creating the tasks and managing them.

In conclusion, though the programming burden of using MPI can be substantial, because all the details of the multiple processor synchronization and communication are the responsibility of the programmer, the low cost and ready availability of cluster hardware suggests that for typical hyperspectral scene sizes of the order 1000×10000 with numbers of classes of multiples of 10 can be managed. Of note is that it is currently possible to build very inexpensive low-power clusters [8] [9] that could be made portable.

Because results so far for supervised SVM classification can detect subtle class differences, the approach discussed here provides a means to push the use of SVM techniques to much larger scenes and number of classes than are currently performed for hyperspectral imagery. It remains for future work to see how far this approach can more fully exploit the large amount of information contained in hyperspectral imagery with reasonable times for computation.

Acknowledgments

Appendix A Simple example of parallel computation

In time step 1 and in parallel let processor p_1 perform the addition of a_1, a_2, p_2 perform the addition of a_3, a_4, ... $p_{N/2}$ perform the addition of a_{N-1}, a_N. In time step 2, let p_1 add the the result from step 1 to the result from $p2$ in step 1, p_2 add the the result from step 1 to the result from $p3$ in step 1, ... $p_{N/4}$ add the result from step 1 to the result from $p_{N/2}$. Continuing like this eventually leads to the last single addition between p_1 and p_2 at time step $O(log_2 N)$. Note that we spend a fixed time at each step to pass values between processors, which itself occurs $O(log_2 N)$ times.

---

[8]Proteus cluster with 14 nodes, (mini ITX boards), power consumption 170 W, peak demand 438 W. Controlling nodes have 256 MB RAM, gigabit ethernet, and a 40 GB hard drive. The NFS server node is similarly equipped. Computational nodes have 256 MB RAM. Peak performance 5.2 GFLP and 10,400 MIPS with 13 computational nodes. Cost $\approx$ $3000.

References

[1] R. E. Bellman. *Adaptive Control Processes: A Guided Tour.* Princeton University Press, Princeton, New Jersey, U.S.A., 1961.

[2] B. E. Boser, I. M. Guyon, and V. N. Vapnik. A training algorithm for optimal margin classifiers. In *Fifth Annual Workshop on Computational Learning Theory*, pages 144–152. ACM, June 1992.

[3] L. Bruzzone and F. Melgani. Classification of hyperspectral images with support vector machines: multiclass strategies. In *Proceedings of SPIE*, 2004.

[4] G. Camps-Valls, L. Gómez-Choval, J. Calpe-Maravilla, E. Soria-Olivas, J. D. Martín-Guerrero, and J. Moreno. *Support Vector Machines for Crop Classification Using Hyperspectral Data*, pages 134 – 141. Springer-Verlag, Heidelberg, October 2003.

[5] Chih-Chung Chang and Chih-Jen Lin. Libsvm – a library for support vector machines. The demo is available from `http://www.csie.ntu.edu.tw/~cjlin/libsvm/`.

[6] C. Cortes and V. N. Vapnik. Support vector networks. *Machine Learning*, 20:1–25, 1995.

[7] J. E. Devaney, M. Michel, J. Peeters, and E. Baland. Automap: A software tool for the automatic creation of mpi data structures from user code. Technical report, NIST, April 1997. `http://www.itl.nist.gov/div895/savg/parallel/`.

[8] Ian Foster. *Designing and Building Parallel Programs.* Addison-Wesley, 1995.

[9] Glen Gardner, 2004. `http://members.verizon.net/~vze24qhw/`.

[10] W. Gropp. *Tutorial on MPI: The Message Passing Interface.* Argonne National Lab., Argonne, Illinois. Available at `http://www-unix.mcs.anl.gov/mpi/tutorial/gropp/talk.html\#Node0`.

[11] W. Gropp. *Tutorial on MPI: The Message Passing Interface.* Argonne National Lab., Argonne, Illinois. See node 87 to node 93 in `http://www-unix.mcs.anl.gov/mpi/tutorial/gropp/talk.html\#Node0`.

[12] W. Gropp and E. Lusk. *Exercises for the MPI Tutorial.* Argonne National Lab., Argonne, Illinois. Available at `http://www-unix.mcs.anl.gov/mpi/tutorial/mpiexmpl/src/fairness/Cwaitsom%e/solution/.html`.

[13] W. Gropp, E. Lusk, and A. Skjellum. *Using MPI: Portable Parallel Programming with the Message Passing Interface.* MIT Press, 1996.

[14] J. A. Gualtieri and S. Chettri. Support vector machines for classification of hyperspectral data. In *International Geoscience and Remote Sensing Symposium.* IEEE, 2000.

[15] J. A. Gualtieri, S. R. Chettri, R. F. Cromp, and L. F. Johnson. Support vector machine classifiers as applied to aviris data. In R. Green, editor, *Summaries of the Eighth JPL Airborne Earth Science Workshop:JPL Publication 99-17*, pages 217–227. Jet Propulsion Laboratory, California Institute of Technology, Pasadena, California, Feb 1999. Available at `http://aviris.jpl.nasa.gov/docs/workshops/99\_docs/toc.htm`.

[16] J. A. Gualtieri and R. F. Cromp. Support vector machines for hyperspectral remote sensing classification. In R. J. Merisko, editor, *27th AIPR Workshop, Advances in Computer Assisted Recognition, Proceedings of the SPIE, Vol. 3584*, pages 221–232. SPIE, 1998.

[17] C.W. Hsu and C. J. Lin. A comparison of methods for multi-class support vector machines. *IEEE Trans. on Neural Networks*, 13(2):415–425, 2002.

[18] G. F. Hughes. On the mean accuracy of statistical pattern recognizers. *IEEE Transactions on Information Theory*, 14(1):55–63, 1968.

[19] T. Joachims. Making large-scale SVM learning practical. In B. Schölkopf, C. Burges, and A. Smola, editors, *Advances in Kernel Methods - Support Vector Learning.* MIT Press, 1998. Available at `http://www-ai.cs.uni-dortmund.de/DOKUMENTE/Joachims_98b.ps.gz`.

[20] T. Joachims, 2001. The SVM^{light} package is written in GCC and distributed for free for scientific use from `http://ais.gmd.de/~thorsten/svm_light/` It can use one of several quadratic optimizers. For our application we used the A. Smola's PR_LOQO package [26].

[21] L. F. Johnson. Aviris hyperpsectral radiance data from: f981009t01r_07, 1998. `ftp://makalu.jpl.nasa.gov/pub/98qlook/1998_lowalt\_index.html`.

[22] D. Landgrebe. Indian pines aviris hyperpsectral radiance data: 92av3c, 1992. Available at `ftp://ftp.ecn.purdue.edu/biehl/MultiSpec/92AV3C`. `ftp://ftp.ecn.purdue.edu/pub/biehl/PC_MultiSpec/ThyFiles.zip`. `http://aviris.jpl.nasa.gov/ql/list92.html`. `http://dynamo.ecn.purdue.edu/~biehl/MultiSpec/aviris_documentation.html%`.

123

[23] M. Lennon, G. Mercier, and L. Hubert-Moy. Classification of hyperspectral images with nonlinear filtering and support vector machines. In *International Geoscience and Remote Sensing Symposium*, 2002.

[24] Peter S. Pacheco. *Parallel Programming with MPI*. Morgan Kaufmann, 1996. `http://nexus.cs.usfca.edu/mpi/`.

[25] B. Schölkopf, C. Burges, and A. Smola, editors. *Advances in Kernel Methods*. MIT Press, 1998.

[26] A. Smola, 2001. The PR_LOQO quadratic optimization package is distributed for research purposes by A. Smola at `http://www.kernel-machines.org/code/prloqo.tar.gz`.

[27] T. Sterling, D. Savarese, D. J. Becker, J. E. Dorband, U. A. Ranawake, and C. V. Packer. BEOWULF: A parallel workstation for scientific computation. In *Proceedings of the 24th International Conference on Parallel Processing*, volume I, Architecture, pages I:11–14, Boca Raton, Florida, August 1995. CRC Press.

[28] G. Zanghirati and L. Zanni. A parallel solver for large quadratic programs in training support vector machines. *Parallel Computation*, 29(4):535–551, 2003.

[29] Junping Zhang, Ye Zhang, and Tingxian Zhou. Classification of hyperspectral data using support vector machine. In *Proceedings 2001 International Conference on Image Processing*, volume 1, pages 882–885, October 2001.

ON THE VALUE OF HYPERSPECTRAL REMOTE SENSING IN MAPPING URBAN LAND COVER

Martin Herold and Dar Roberts
Department of Geography, University of California, Santa Barbara
Santa Barbara, California 93106
martin@geog.ucsb.edu

Introduction

Urban environments represent one of the most challenging areas for remote sensing analysis due to high spatial and spectral diversity of surface materials (Ben Dor et al., 2001, Roessner et al., 2001). Typical urban surface types include a wide range of roofs, roads, sidewalks and parking lots of variable age, quality and composition. Further complicating the urban landscape are bare soil, vegetation, and other landscaping elements, creating a spectral diversity that far exceeds natural environments. Given this general complexity, this study investigates the value of hyperspectral remote sensing data in accurate mapping of urban land cover. The investigations include the assessment of a comprehensive urban spectral library to describe issues of spectral characteristics and spectral separability of urban materials and land cover types. Mapping applications are presented from high-resolution AVIRIS data, simulated multispectral sensor configurations and LIDAR covering the Santa Barbara urban region. The analyses focus on different spatial and spectral sensor configurations and their affects on the mapping accuracy The next section will give a summary of the findings and conclusions. For more detailed information the reader is referred to the references at the end of the paper.

Summary of results

The investigations concerned with urban spectrometry provided a systematic and quantitative view of the spectral complexity and unique spectral characteristics of urban environments. Urban materials such as roofing materials, pavement types, soil and water surfaces, and vegetated areas, represent a large variety of surface compositions that are reflected in characteristic spectral properties. The analysis of spectral separability of urban materials and land cover types using the B-distance provided a detailed assessment of how specific urban land cover types separate based on their material properties. Some categories are not spectrally distinct over the spectral range between 350 nm and 2400 nm and have expected limitations in their accurate mapping from remote sensing datasets. Examples include: a) bare soil targets versus concrete roads, b) asphalt roads versus composite shingle, tar and gray tile roofs, c) gray tile roofs versus composite shingle and tar roofs, and d) asphalt roads versus parking lots. With the exception of concrete roads, these surface types mainly represent low reflectance targets with no significant broad absorption features. Road surfaces showed the largest variance in their spectral material separability and were especially confused with specific non-transportation cover types (Herold et al., 2004).

The evaluation of most suitable spectral bands again reflects the spectral diversity of urban environments. A set of fourteen optimal bands was derived for mapping the urban environment from the ground spectral library and the AVIRIS spectral library (Figure 1, Herold et al., 2003). The spectral location of the bands emphasizes the important features that characterize most urban targets, such as increasing reflectance towards longer wavelength, and the distinct small-scale spectral variation in the visible and short-wave infrared representing specific absorption features due to the material composition. A comparison of the bands most suitable for separating urban targets with the spectral configuration of common multispectral remote sensing systems showed that the unique urban spectral characteristics are not resolved in those sensors due to the location of the bands and their broadband character (Herold et al., 2003, Roberts and Herold, 2004).
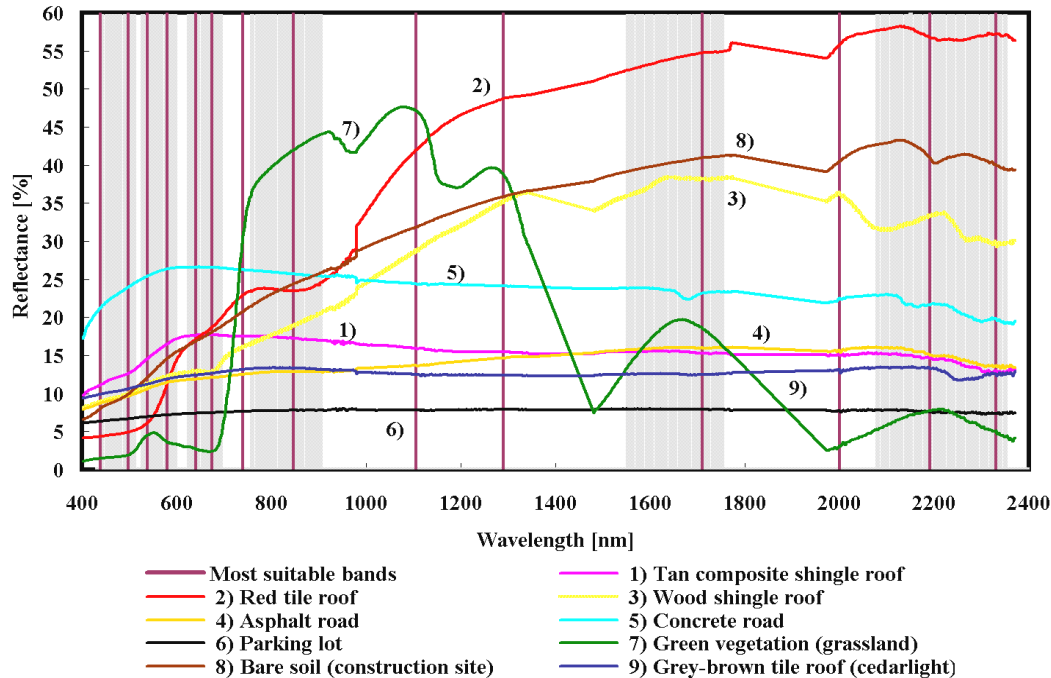
Figure 1: Most suitable spectral bands for urban mapping derived from the ASD spectral library and the AVIRIS data compared to spectral signatures of several urban land cover types and the spectral coverage of LANDSAT TM satellite sensor (gray in the background).

The majority of the fourteen most suitable spectral AVIRIS bands are located outside or near the edge of the spectral coverage of common broadband multispectral satellite systems such as IKONOS and LANDSAT TM. Expected spectral limitations of these systems were confirmed by the AVIRIS classification results. The difference between overall classification accuracy of urban classes was nearly 30% between IKONOS and AVIRIS, and ~13% between LANDSAT and AVIRIS, with distinct differences for individual classes. However, the AVIRIS land cover classification of twenty-six different urban land cover classes illustrated general limitations in mapping the urban environment even using hyperspectral optical remote sensing data. This again reflects the very similar spectral characteristics of certain land cover types indicated in the spectral separability analyses. Due to high spectral within-class variability resulting from roof geometry, condition, and age, their separability and classification accuracy was low, reaching only 66.6% for the twenty-two urban categories (Herold et al., 2003, Roberts and Herold, 2004). Nevertheless, for specific important land cover types such as wood shingle roofs, this investigation produced a very detailed level of classification with high accuracy. It should be noted that this image classification applied a simple pixel-based Maximum Likelihood classification algorithm on a purely spectral basis

The use of three-dimensional information provided by LIDAR data can significantly improve the mapping of urban land cover. In particular for classification of buildings/roofs and roads, LIDAR seems to be very important since both classes have distinct three-dimensional characteristics (Figure 2). In fact, the combination of IKONOS and LIDAR data produced more accurate results than using only spectral data from AVIRIS. AVIRIS, on the other hand, performed better for other classes like vegetation and bare soil. The combination of AVIRIS and LIDAR provided the best land cover classification performance with over 90 % overall accuracy for 6 classes.

The land cover classification results showed a strong dependence on the spatial resolution. The map accuracy significantly decreased between 4 and 16 m spatial resolution. At coarser resolutions the spectral signals from individual urban land cover features (mainly buildings, roads, and green vegetation) increasingly merge into mixed pixels. The individual classification accuracies for the categories steadily

decreased, i.e. green vegetation gets increasingly overmapped due its distinct spectral characteristic, whereas built areas tends to be underestimated (Herold and Roberts, 2004).
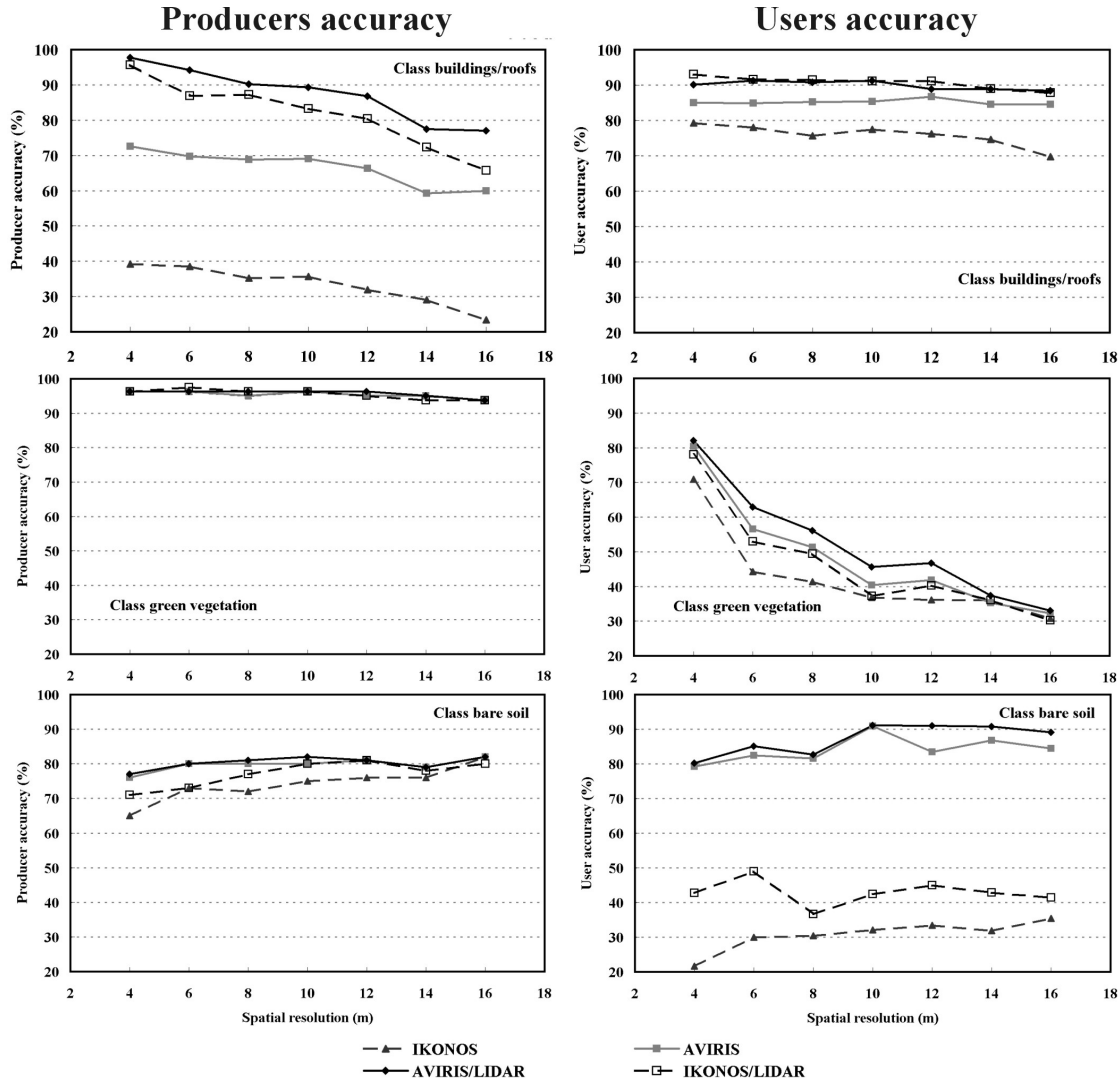

Figure 2: Producer and user accuracies in four land cover classes for different sensor configurations (IKONOS, LIDAR, AVIRIS) and degraded spatial resolutions.

In terms of spatial-spectral tradeoffs, the variations in map accuracy with spatial resolution (4–16 m) were smaller than those for changing spectral information (IKONOS, AVIRIS, LIDAR, Figure 3). This suggests that it would be proper to pick a low spatial resolution AVIRIS dataset over a high-spatial resolution IKONOS dataset, at least from a pixel-based spectral mapping perspective. Moreover, the decrease in overall accuracy from 4 to 16 m for the AVIRIS data was only a difference of seven percent. For the combination of IKONOS/LIDAR this change was nearly 20 %. At 16 m spatial resolution the classification performance of IKONOS/LIDAR drops below the AVIRIS accuracy. Hence, AVIRIS data analyses are less sensitive to changes in spatial resolutions. Although the trends certainly vary for individual land cover classes, IKONOS and LIDAR classification data strongly depend on the accurate representation of individual urban land cover features and should only be used at fine spatial resolutions. If only coarse spatial resolution data are available hyperspectral datasets should be preferred for urban land cover mapping (Herold, 2004).
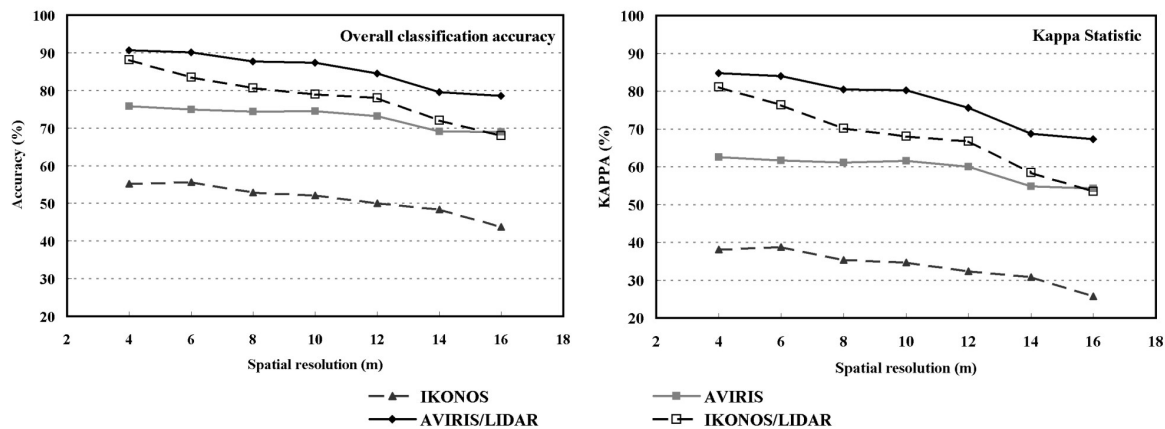
Figure 3: Overall accuracies and KAPPA coefficient for different sensor configurations and varying spatial resolution.

References

Ben-Dor, E., Levin, N. and H. Saaroni 2001. A spectral based recognition of the urban environment using the visible and near-infrared spectral region (0.4-1.1 m). A case study over Tel-Aviv, *International Journal of Remote Sensing*, 22, 11, 2193–2218.

Herold, M., Gardner, M., and Roberts, D. A. 2003. Spectral Resolution Requirements for Mapping Urban Areas, *IEEE Transactions on Geoscience and Remote Sensing*, 41, 9, pp. 1907–1919.

Herold, M. 2004. Remote sensing and spatial metrics for mapping and modeling of urban structures and growth dynamics, PhD dissertation, Department of Geography, University of California Santa Barbara.

Herold, M., Roberts, D., Gardner, M., and P. Dennison 2004. Spectrometry for urban area remote sensing–Development and analysis of a spectral library from 350 to 2400 nm, *Remote Sensing of Environment*, in press.

Herold, M. and D. A. Roberts 2004. The spectral dimension in urban remote sensing. in Juergens, C. and T. Rashed (eds.) *Remote Sensing of Urban and Suburban Areas*, Kluwer, in press.

Roberts, D. A. and M. Herold 2004. Imaging spectrometry of urban materials. in King, P.and G. Swayze, (eds.), *Molecules to Planets: Infrared Spectroscopy in Geochemistry, Exploration Geochemistry and Remote Sensing* (Mineral Association of Canada), in press.

Roessner, S., Segl, K., Heiden, U. and H. Kaufmann 2001. Automated differentiation of urban surfaces based on airborne hyperspectral imagery, *IEEE Transactions on Geoscience and Remote Sensing*, 39, 7, 1525–1532.

ROAD CONDITION MAPPING WITH HYPERSPECTRAL REMOTE SENSING

Martin Herold,[1] Dar Roberts,[1] Omar Smadi,[2] and Val Noronha[1]

[1]Department of Geography, University of California, Santa Barbara
Santa Barbara, California 93106
martin@geog.ucsb.edu
[2]Center for Transportation Research and Education, Iowa State University at Ames

1. Introduction

The quality standards for transportation infrastructure have evolved considerably over the last three decades. The data accuracy requirements to support road management have decreased from tens of meters to a few decimeters with annual update rates. Roads are prioritized for maintenance and treatment as a result of pavement inspections. The cost of frequent, comprehensive inspection is high, and many jurisdictions limit their surveys to major roads, while minor roads are surveyed in 3-year cycles. For this purpose, a number of survey technologies have been applied to road condition mapping. The common practice today is extensive field observations by experts who characterize the Pavement Condition Index (PCI), based on established physical parameters such as cracking, rutting, raveling, etc. Other technologies are evolving such us the application of Pavement Management Systems (PMS); typically coupled with GPS/GIS technology and semi-automated in-situ pavement health surveys facilitated by vans. They capture exhaustive photographic and video logs of pavement quality (and at the same time asset inventory), while recording road geometry with GPS and Distance Measuring Instruments. This produces a detailed and georeferenced condition report, with PCI ratings for every ~10 m of road. Nevertheless, this remains an expensive and troublesome survey, while cost and safety considerations require that it be done at regular intervals.

Recent advances in hyperspectral remote sensing technology have shown capabilities to derive physical and chemical material properties on a very detailed level (Clark, 1999). Consequently one would raise the questions: Can we map road surface conditions with hyperspectral remote sensing to support current practice in transportation infrastructure management? Previous studies on pavement condition mapping with remote sensing are rare. Early studies in the 1970s dealt with the visual interpretation of physical surface distresses (e.g., cracks, see Figure 1). The results showed that distresses are distinguishable but only in very large-scale aerial photographs. Currently emerging technologies in this context are observations from Unmanned Airborne Vehicles (UAV). Although mapping efforts are only marginally developed, they have potential to support transportation infrastructure surveys (Brecher et al., 2004). Figure 2 shows an example for UAV based observations for road pavement assessment. UAV based sensors are another new and economic source of remotely sensed information that could support road maintenance efforts and have to be considered in the exploration of hyperspectral imaging.

Figure 1: Pavement surface defects mapped from aerial photographs on different scales (Stoeckeler, 1970)

The potential of hyperspectral remote sensing is mentioned on several occasions (Usher and Truax, 2001; Gomez, 2002). However, this potential has only recently been explored by the National Center for Remote Sensing in Transportation (NCRST) at UC Santa Barbara (Brecher et al., 2003; Noronha et al., 2002; Herold et al., 2003). An experiment in Santa Barbara and Goleta, CA was conducted
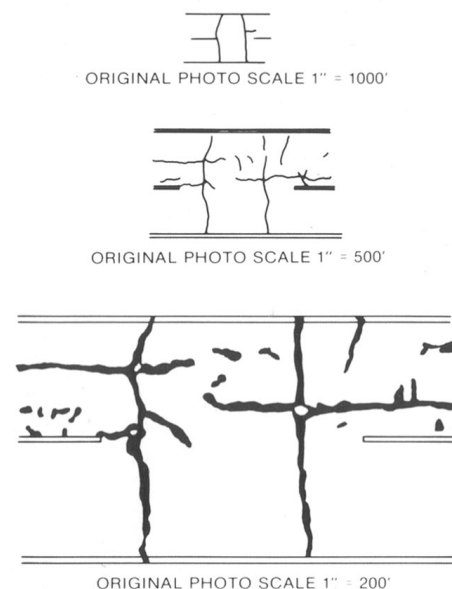
Figure 2: UAV-based observation for visual interpretations of road distresses over Gilroy, California.
(©MLB http://www.spyplanes.com/)

to explore the hyperspectral capabilities in mapping road conditions. The investigated roads were surveyed with "common practice" techniques by Roadware's ARAN survey vehicle and inspected by qualified pavement experts from Iowa State University, and California firms associated with CALTRANS. The Santa Barbara County PMS provided additional spatial information about road conditions. A comprehensive spectral library of road surfaces and distress was acquired using an ASD hand held spectrometer to study generic spectral characteristics of road conditions. The roads were sensed by NASA-JPL's low altitude AVIRIS and by the HyperSpecTIR sub-meter hyperspectral sensor of Spectir Inc. Based on this comprehensive database, we investigated the spectral properties of road surface distresses and compared different of survey methods. The ultimate goal was to explore relationships between remotely sensed parameters (i.e., spectral reflectance) and road condition parameters such as PCI. This relationship needs to be established if remote sensing is to support pavement health surveys.

2. Data and Methods

2.1 Study area

The study focused on several roads in the Goleta urban area, located 170 kilometers northwest of Los Angeles in the foothills of the California Coast Range. Figure 3 shows the study area north of Interstate 101. The main roads of interest are Fairview Avenue and Cathedral Oaks and in particular near the intersection of both which is shown in the upper middle part of the AVIRIS image (Figure 3). Both roads have four lanes, two in each traffic direction, and represent major urban roads. The SB County PCI values for these roads show that the roads reflect a large variety of conditions (Figure 3). The eastern part of Cathedral Oaks has a PCI of nearly 100. This road was resurfaced just before the study started. Fairview and the western part of Cathedral Oaks have fair/poor conditions with PCI values on the order of 40-60. Fairview pavement is in particular poor conditions. The central divider of Fairview was the boundary between two traffic management zones. Every rehabilitation effort had to funded and coordinated by to different institutions. This resulted in delays and failure of necessary maintenance and continued deterioration of the road surface is apparent today.

2.2 Road condition data

Road distress surveys are required as part of the planning and design of pavement rehabilitation projects. They provide information on the various distress types, their location, severity and extent (Miller and Bellinger, 2003). Traditionally, these surveys are based on extensive field observations by trained experts. They evaluate the pavement condition in-situ considering a variety of distress types and aggregate the information into a Pavement Condition Index (PCI, Figure 4). The PCI is a single road
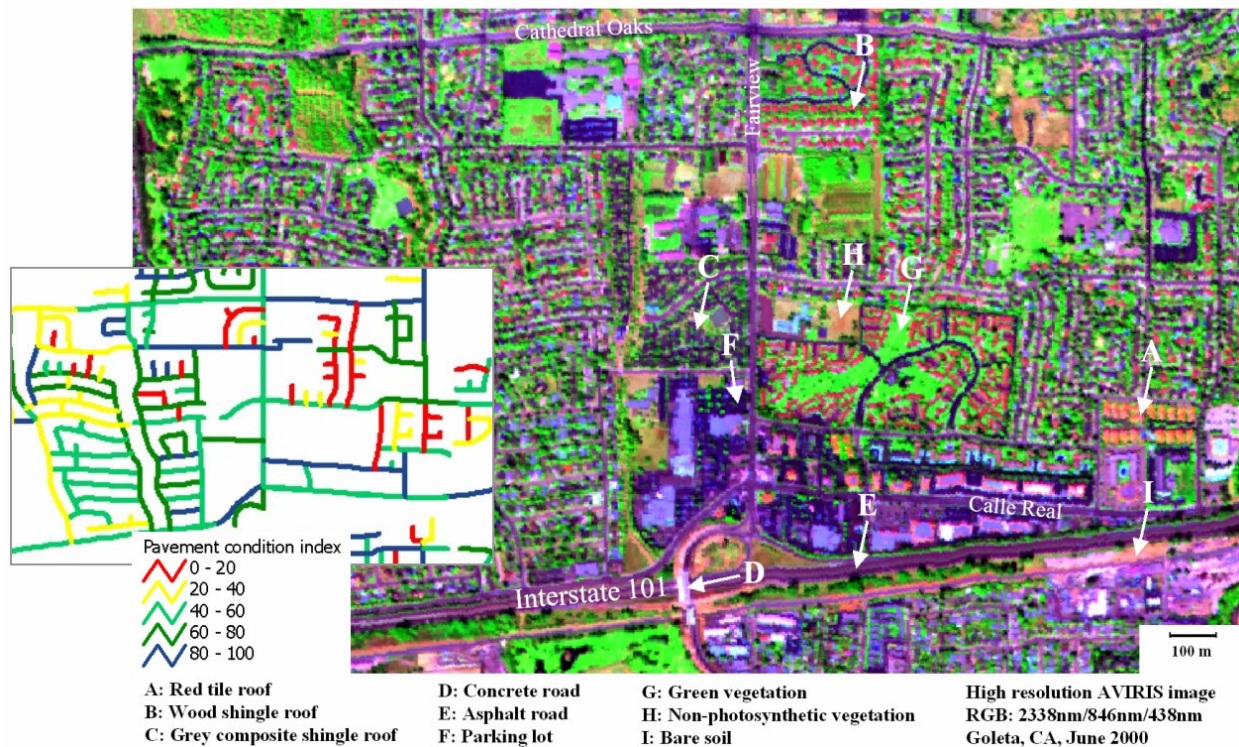
Figure 3: AVIRIS image of the Fairview/Cathedral Oaks study area shown with the distribution of the PCI from the Santa Barbara County database.

performance indicator with a scale usually between 0 and 100. In this study two expert groups surveyed the roads in June and July 2003 (Fairview and Cathedral Oaks). A qualified pavement expert led the first group from the Center for Transportation Research and Education from the Iowa State University at Ames. The second expert group included representatives from California firms associated with CALTRANS: Independent Seals, Western Paving and Vulcan Paving. The experts were asked to categorize the road condition in five categories (excellent, good, fair, poor and very poor) and suggest a road management action (do nothing, maintenance, minor rehabilitation, major rehabilitation, and replacement).

The second source of road information was provided the Santa Barbara (SB) County road database. Since 2001 the County has been using the MicroPaver Pavement Management System (PMS). This PMS is a decision making tool for cost effective maintenance and repair alternatives for all roads within the County. MicroPaver helps to evaluate present and future pavement conditions, deterioration rates, work history and budget scenarios. The PMS is linked to ArcView GIS and a digital road database that was available for this
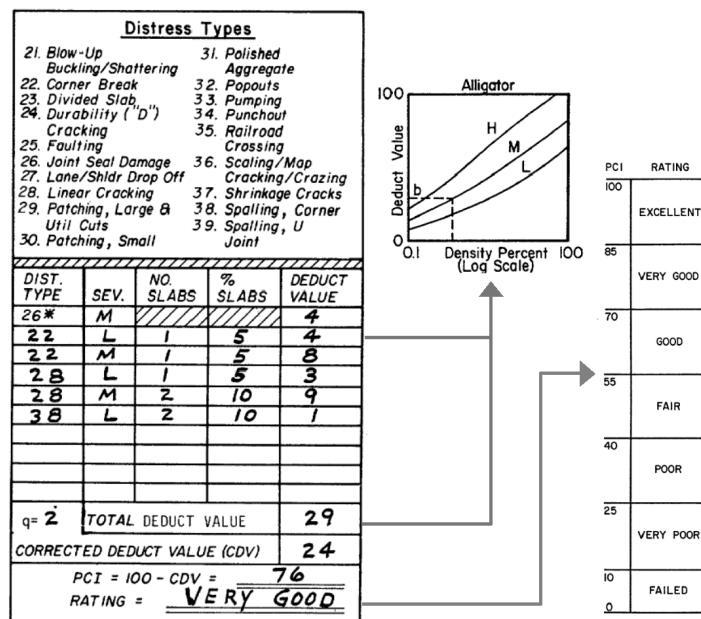

Figure 4: Road condition survey sheet outlined by the U.S. Army Corps of Engineers (1982).

131

study. Figure 3 shows a subset of this database. The PCI is reported for relatively large road segments and does not discriminate between different lanes. The "County PCI" was provided for January 2002. In February 2002 the city of Goleta was incorporated and the responsibility of road management went to the new city administration, which did not maintain and update the GIS database.

The third survey technique provided very detailed information about road distresses. The observations were performed in December 2002 with the Automatic Road Analyzer (ARAN) of the Roadware cooperation (www.roadware.com). ARAN is mounted on a specially modified vehicle that houses an extensive set of computers and sensors including: lasers, inertial measurement units, accelerometers, ultrasonic transducers, digital cameras and other advanced technology subsystems (Figure 5). GPS on the vehicle and at a base station ensures accurate locational data. The survey provides geocoded road distresses information of over 30 individual parameters aggregated for 10 m road or lane segments. For further analysis the original data were aggregated to 50 m road segments and the individual road distress measures were merged to a PCI and Structure index. Similar to the ones for field surveys, the "Roadware PCI" categorizes the majority of distresses in a rating based on 0 to 100 scale with 100 being the best condition. The PCI calculations are based on deduct values (Figure 4) that come from the actual Roadware observations (see also Figure 4). The structure index works in a similar manner. The only difference is it only considers distresses that are related to the structure, e.g., only alligator, block, and transverse cracking.

All road condition information was integrated into a GIS database. The Roadware data and the Expert evaluations use similar road segments (~ 50 m length) and consider the direction of four lane roads. The County PCI represents much larger road segments on the order of several hundred meters to one kilometer. Furthermore there is a difference in time of acquisition, the County data represent the conditions in January 2002, the Roadware data December 2002 and the experts visited in June/July 2003. However, there was no road construction or maintenance within the period of data acquisition that affected the validity of this study.

Figure 5: The Roadware pavement health survey with the ARAN survey vehicle, GPS base station, the video/road distress log and the resulting GIS database.

2.3 Spectral library

Spectral libraries contain pure spectral samples of surfaces, including a wide range of materials over a continuous wavelength range with high spectral detail, and additional information and documentation about surface characteristics and the quality of the spectra (i.e., metadata). In May 2001 and February 2004 two ground spectra acquisition campaigns were conducted in the study area. Ground spectra were acquired with an Analytical Spectral Devices (ASD) Full Range (FR) spectrometer (Analytical Spectral Devices, Boulder, CO, USA). The FR spectrometer samples a spectral range of 350-2400 nm. The instrument uses three detectors spanning the visible and near infrared (VNIR) and shortwave infrared (SWIR1 and SWIR2), with a spectral sampling interval of 1.4 nm for the VNIR detector and 2.0 nm for the SWIR detectors. FR field spectrometer data are widely used and considered to provide high quality spectral measurements. All targets were documented and integrated into a spectral library (Figure 6). The spectra library contains various types of roads (asphalt, concrete, gravel) and different distresses of asphalt road surfaces.
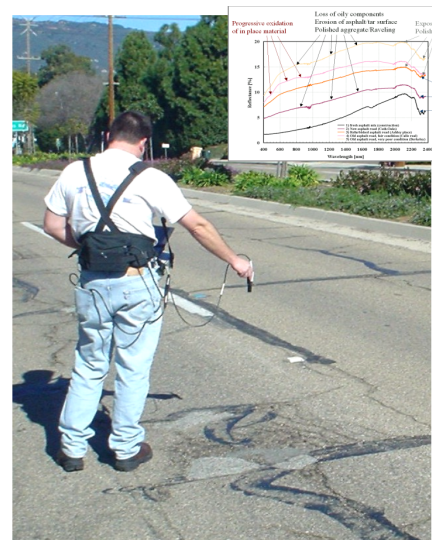

Figure 6: Acquisition of spectral samples of road surface distresses.

2.4 Remote sensing data

Two hyperspectral datasets were acquired in the study area. The AVIRIS sensor flew on June 9th, 2000. The data were acquired at a spatial resolution of approximately 4 meters. The AVIRIS sensor acquires 224 individual bands with a nominal bandwidth of 8-11 nm, covering a spectral range from 370 to 2510 nm (Green et al., 1998). The Jet Propulsion Laboratory (JPL) and the University of California, Santa Barbara (UCSB) preprocessed the data for motion compensation and reduction of geometric distortions due to topography. The data were processed to apparent surface reflectance using modified Modtran radiative transfer code and further adjusted using a ground reflectance target from the spectral library (Green et al., 1993). In general, the spatial and spectral quality of the AVIRIS data were excellent (see Figure 3).

As second set of hyperspectral remote sensing observations was provided from the Spectir Inc. located in Goleta, CA (www.spectir.com). The company developed a new sensor "HyperSpecTIR" (HST) with 227 bands over a range of 450-2450 nm. The main advantage of this HST is the high spatial resolution. Due to an onboard, integrated stabilization system the flight altitude can be very low with a GIFOV of about 0.5 m. This is quite an advantage over AVIRIS for detailed mapping of road conditions (Figure 7). One tradeoff is the narrow swath of only 40 m. Several roads were missed during the acquisition campaign and the study was limited to specific parts of the test area. Despite its spatial advantages, the spectral calibration of the data was insufficient and only the bands from 450 nm to about 900 nm covered by the first spectrometer sensor could be used for the analysis. The Spectir data were experimental from the HST I sensor. The recently completed HST II and III sensors, along with improved

Figure 7: Comparison of spatial detail provided by the AVIRIS and HyperSpecTIR sensor.

spectral calibration will hopefully enhance the spectral quality of future datasets.

The analysis of the remote sensing only considers the actual visible road surfaces. All other land cover types were excluded by using an accurate road outline available in digital format. Vegetation and shadows obscuring the road surface were excluded in HST data where they were clearly visible. The remote sensing investigations applied specific reflectance ratios that are discussed later. The local variance in the 3x3 neighborhood of these ratios was also calculated and included in the analysis.

2.5 Statistical analysis

Statistical analyses were performed to compare the remote sensing signal and the road condition information. The PCI and reflectance are both quantitative measurements and bivariate ordinary least square regressions were applied to explore the correlation between the variables. The PCI values (from Roadware and the County) are reported as averages over road segments. The statistical comparison used the average of the remote sensing signal over the same road area to allow a one to one comparison. This segment-based relationship was then used to convert the remote sensing data to PCI values on the pixel level.

A comparison between the quantitative remote sensing signal and the categorical road ratings of the experts requires a different statistical method: Analysis of Variance (ANOVA). The key statistic in ANOVA is the F-test of difference of category means, testing if the means of the category formed by values of the independent variable (remote sensing signal) are different enough not to have occurred by chance. In other words, ANOVA describes if the remote sensing signal is statistically different for the various categories of road conditions.

3. Comparison of road surveys

All three road survey techniques (expert visit, Roadware, County PMS) applied in this study can be considered part of the "common practice" in pavement management. Although the individual surveys have slight differences in time of acquisition and spatial unit (extend of road segments), the data can be compared to explore similarities and differences among them (Figure 8). Diagram A and B compare the County PCI to the Roadware PCI and structure index. There is a good linear relationship between both PCI measures. One large County road segment contains several smaller Roadware segments and the variability in the Roadware PCI emphasizes the road condition variability within the larger County segments. The relationship between County PCI and Roadware structure index is non-linear (Diagram B). This is expected since the structure index only contains the structural damages. Early pavement degradation usually does not result in severe structural damages and the structure index remains high. The structure index better describes distresses for roads in poorer conditions with significant structural damages, i.e., there is quite some variability in lower structure index values with the County PCI staying fairly constant. Diagrams C and B in Figure 8 relate the expert opinions to the Roadware data. Both show good relationships. The Roadware PCI clearly reflects the difference between a very good road ("do nothing") and the roads that need rehabilitation or replacement. A similar distribution is shown in Diagram D. Although the overall relationships between the different survey techniques is obvious, there is a fair amount of variability and disagreement in particular for roads in poorer conditions. Consequently, the "common practice" techniques are not completely congruent and reliable. Every decision based on these will require some kind of compromise especially for approaching expensive rehabilitation or replacement projects.

4. Spectral characteristics of road conditions

The spectral signal from different types of road materials such as concrete and asphalt are different and hyperspectral sensing can easily distinguish between them (Herold et al., 2004). This study focuses on the variability within asphalt road surfaces i.e., the spectral effects of aging and deterioration of asphalt pavement (Figure 9).
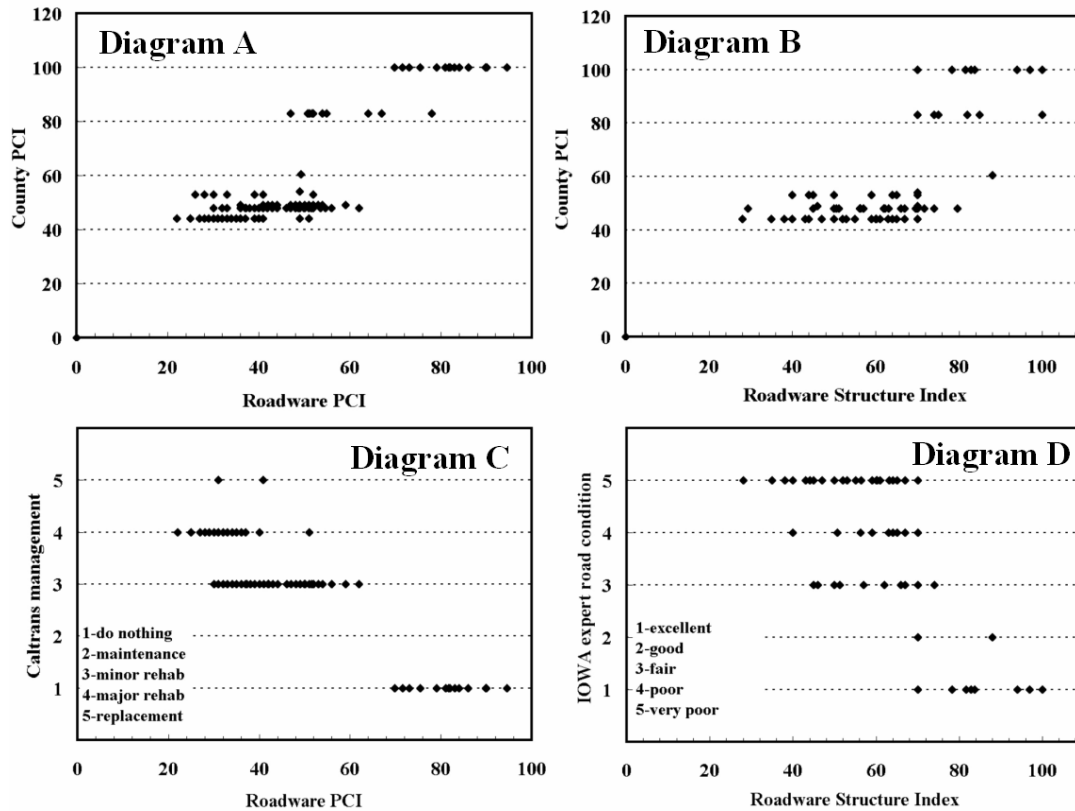
Figure 8: Comparison of road condition survey data (Note: The y-axes of diagrams C and D are categories.)

The natural aging of asphalt is caused by reaction with atmospheric oxygen, photochemical reactions with solar radiation, and the influence of heat, and results in three major processes (Bell, 1989): the loss of oily components by volatility or absorption, changes of composition by oxidation, and molecular structuring that influences the viscosity of the asphalt mix (steric hardening). The loss of oily components is relatively short-term; the other two are more long-term processes. The results of these processes are represented in the spectra. New asphalt surfaces have the lowest reflectance with a linear increase in reflectance towards 2100 nm. The surface is nearly completely covered with asphalt mix (spectrum 1). Hydrocarbon absorptions are evident at ~1750 nm and above 2100 nm with a significant doublet at 2310 and 2350 nm (Cloutis, 1989). As the pavement ages and its condition deteriorates, reflectance increases in all parts of the spectrum. The asphalt mix seal starts eroding exposing the rocky components of the pavement (spectrum 2). This process continues until the rocky components dominate the asphalt surface. With the erosion of the asphalt mix the road surface is less viscous and more prone to structural damages like cracking. This decreases asphalt mix absorptions resulting in a significant increase in object brightness. This difference is highest in the NIR and SWIR with more than 10% reflectance. The spectral shape in NIR and SWIR changes from slightly concave for new asphalt to more concave for older surfaces. The oxidation process and exposing of rocky components is clearly shown by the appearance of iron-oxide absorption features at 520, 670 and 870 nm in spectra 2 and 3. The hydrocarbon features are only distinct for new asphalt surfaces and vanish with age and poorer surface conditions. Furthermore there is significant change in slope in the transition from hydrocarbon to mineral absorption. For older roads the slope increases between 2100-2200 nm and decreases between 2250-2300 nm.

Spectral characteristics of specific road damages are presented in Figure 10. The spectra show that cracks and old crack seals produce decreasing brightness. For new crack sealing, this effect is more dominant and results in near constant low reflectance similar to the ones found for parking lot surfaces (Herold et al., 2004). Some older cracks contain green vegetation, which again has a strong impact on the spectral response exposing typical spectral features from chlorophyll, water content and lingo-cellulose.
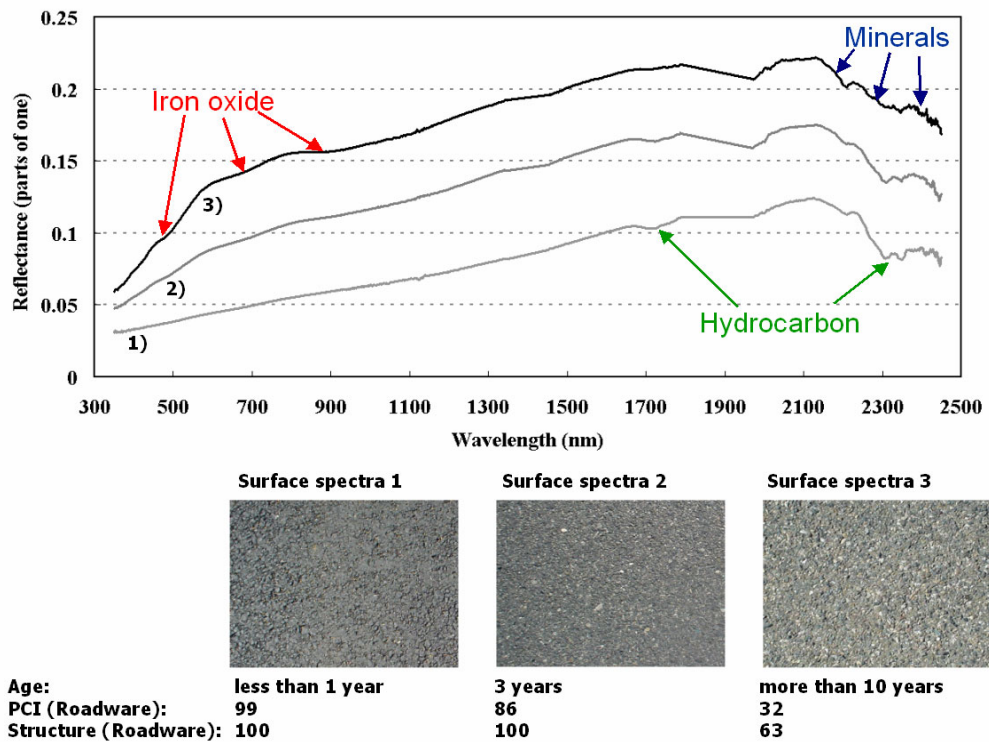
135

Figure 9: Spectral effects of asphalt aging and deterioration from the ASD ground spectral measurements (the major water vapor absorption bands are interpolated).
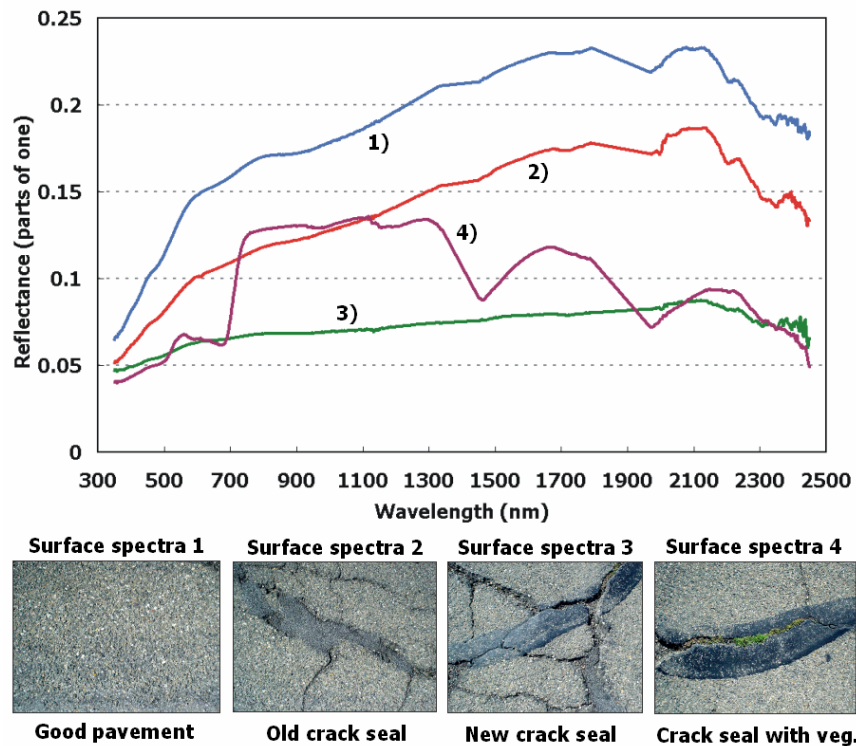

Figure 10: Spectral effects of different structural road damages from the ASD ground spectral measurements (the major water vapor absorption bands are interpolated).

5. AVIRIS data analysis

Spectral analyses of road surfaces suggest several features that have utility for spectral identification of road aging and deterioration. The coarse spatial resolution of the AVIRIS data and the spectral quality of the HST data, however, only allowed for the use of very general spectral features, i.e., small absorption features were excluded from the hyperspectral data analysis. The investigations were based on two image ratios (Figure 11).

These ratios emphasize the increasing brightness and the change towards more concave spectral shape in the VIS for older roads. The first ratio (VIS2) represents the reflectance difference between 830 nm and 490 nm. This ratio is low for new asphalt surfaces and increases with age and level of deterioration, partially caused by the iron oxide absorptions. The SWIR ratio reflects the spectral contrast between ~2120 nm and ~2340 nm, which decreases for older asphalt surfaces (Figure 9 and 11). The AVIRIS based image ratios were compared to the County PCI values (Figure 12). The graphs show a large amount of variation in the ratios versus the PCI values. There is some indication of the expected decrease in image ratios for higher PCI values. The variability of the ratios seems to increase for roads with lower PCI. However, the relationship is very weak (R-squared values in the order of 0.1-0.2) and it can be

1) fresh asphalt mix (construction)
2) New asphalt road (Cath.Oaks)
3) Refurbished asphalt road (Ashley place)
4) Old asphalt road, fair condition (Calle real)
5) Old asphalt road, very poor condition (Berkeley)

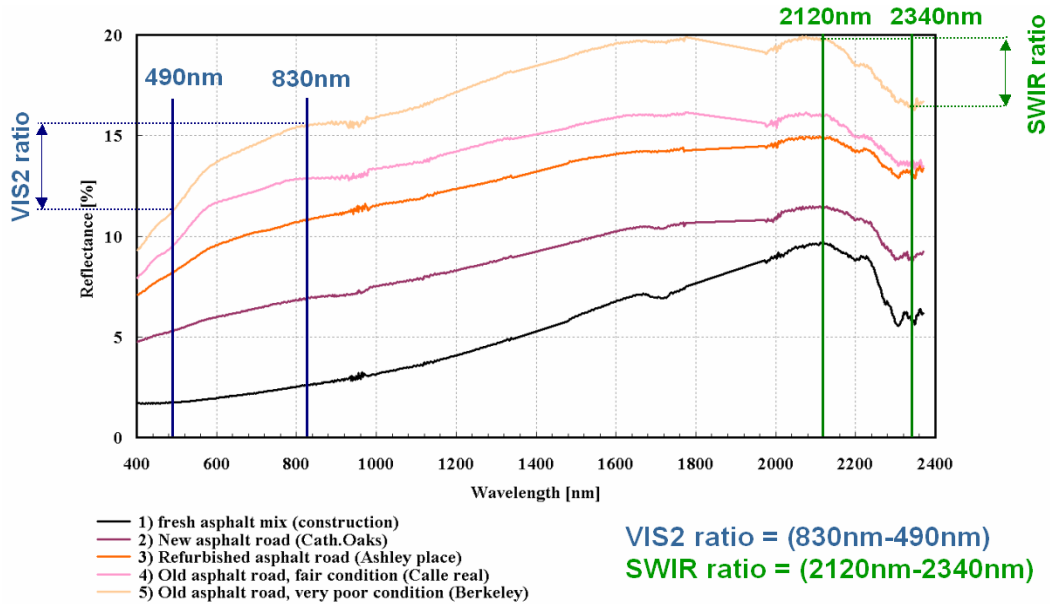VIS2 ratio = (830nm-490nm)
SWIR ratio = (2120nm-2340nm)

Figure 11: Two image ratios used for the hyperspectral data analysis shown with ASD ground spectra of different asphalt road surfaces.
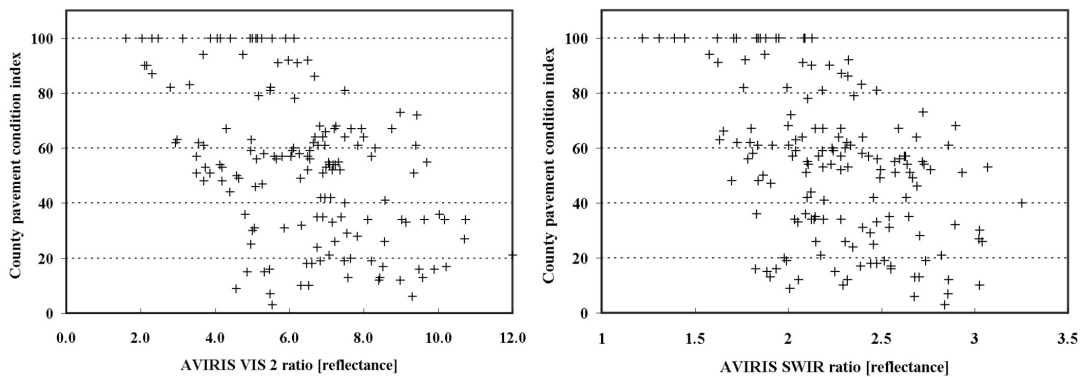

Figure 12: Comparison of two AVIRIS-based image ratios versus the County PCI.

concluded that AVIRIS data did not allow for mapping of road conditions in this study. This limitation can be related to the spatial resolution. Figure 7 emphasizes the spatial detail provided by the AVIRIS sensors. Pure road surface pixels are rare and surrounding land cover types (vegetation, gravel, buildings etc.) affect the spectral signal and add significant variability and uncertainty to analysis of road conditions (Figure 12).

6. Hyperspectir data analysis

The HST analysis only focused on the VIS2 ratio since the spectral quality of the data limited the investigations on the VIS-NIR region. The spatial resolution was very beneficial since road surface features and distresses are represented in the HST data (Figure 13). The spatial distribution of the VIS2 ratio showed expected general road surface pattern. Roads with recently paved surfaces (upper left part of Figure 13, east Cathedral Oaks) show low ratio values on the order of 2-4 % reflectance difference (dark green and blue) between 830 and 490 nm. The highlighted part of west Cathedral Oaks presents the transition between a newer split-seal refurbished road (green-yellow) and an older part with several sealed transverse cracks (yellow-orange). The southern part of Fairview shows an area with severe alligator and block cracking. The crack patterns are visible in the VIS2 distribution with lower ratio values (see Figure 10). This adds spatial variance to the ratio values and appears for roads with structural damages.

The HST VIS2 values show a significant correlation with the Roadware PCI values (Figure 14, Diagram A). For roads in good condition the relationship is very distinct. The variability increases for high ratio/low PCI values, hence to spectral signal of the roads get more complex and the relationship is not as obvious. Diagram B shows the spatial variance in the VIS2 ratio versus the Roadware structure index. This relationship represents the fact that structural road damages add complexity to the spectral signal. There is, however, significant variability for very high PCI values. They are false positives, basically other features that add variability to the spectral signal and do not represent road damages such as shadows from light poles, cars etc.

The statistical relationships in Figure 14 are strong enough to convert the remote sensing signal (VIS2 ratio, VIS2 ratio variance) to road condition parameters (PCI, structure index). The spatial distributions
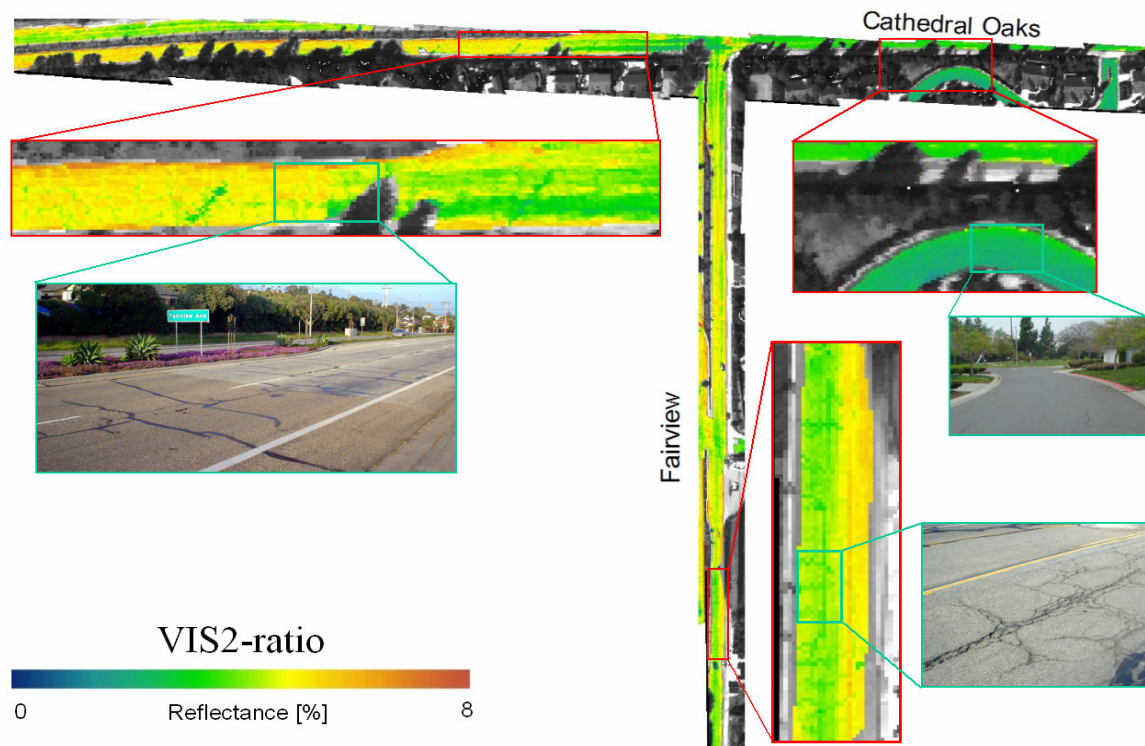

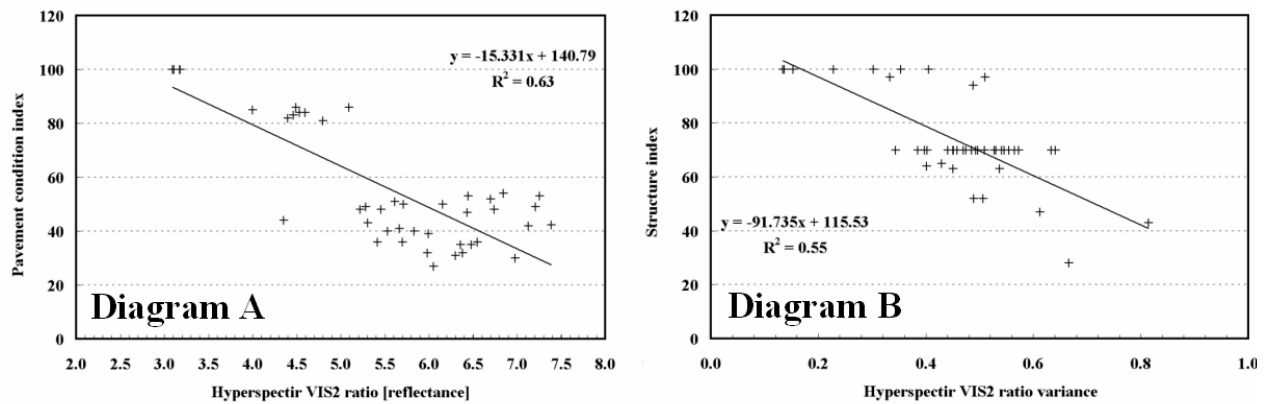Figure 13: Spatial distribution of the VIS2 ratio derived from the HST data.

Figure 14: Comparison between HST VIS2 ration and Roadware PCI and structure index.

are shown in Figure 15. The PCI patterns highlight recently paved roads with high values (see Figure 13). Road surfaces in poorer condition show lower PCI values and higher variability. Specific cracking patterns are revealed in the highlighted area of Fairview. The structure index was derived from the local VIS2 ratio variance. The spatial distribution emphasizes local pattern of road surface variability caused by structural damages. In the areas of newly paved roads in the upper left on the bottom map, there are some small high-variance features near the edges of the roads that are not road distresses representing false positives. Cracking patterns and other distresses are reflected in the other highlighted areas on Fairview and west Cathedral Oaks which show high variance.

Figures 14 and 15 show the relationship between the remote sensing signal and descriptive parameters of road condition. However, the remaining question is to what extent can remote sensing signals be translated into specific management suggestions. An analysis of variance (ANOVA) was applied to show if the remote sensing signal is statistically different for the various categories of management. The ANOVA results relating the VIS2 ratio values to four categories of possible CALTRANS management actions are shown in Table 1.

Table 1: ANOVA results of HST VIS2 ratio versus CALTRANS management suggestion.

```
Category          Value(%)      Std.Error      Difference
Do nothing          3.13          0.44
Maintenance         5.73          0.16                2.60
Minor Rehab         6.18          0.51                0.45
Major Rehab         6.05          0.36               -0.13

Multiple R-Squared: 0.46
F-statistic: 11.24
```

The R-squared of 46 % and the F-statistic of 11.24 indicates that there is a significant relationship between both variables. The ANOVA was performed beginning with the first management category: "do nothing". This category has an average HST ratio value of 3.13. Compared to this category the management suggestion "maintenance" is significantly different indicated by the mean value of 5.73. The statistical difference between both categories is 2.6 % reflectance in the VIS2 ratio. Basically this is the expected VIS2 ratio difference between a road that requires no work and a road that requires maintenance. The difference between the categories "maintenance" versus "minor rehab" versus "major rehab" are 0.45 and 0.13 respectively. They are in the range of the standard error and suggest that there is no significant difference between these categories or the difference is far too small to be accurately represented in the remote sensing data.
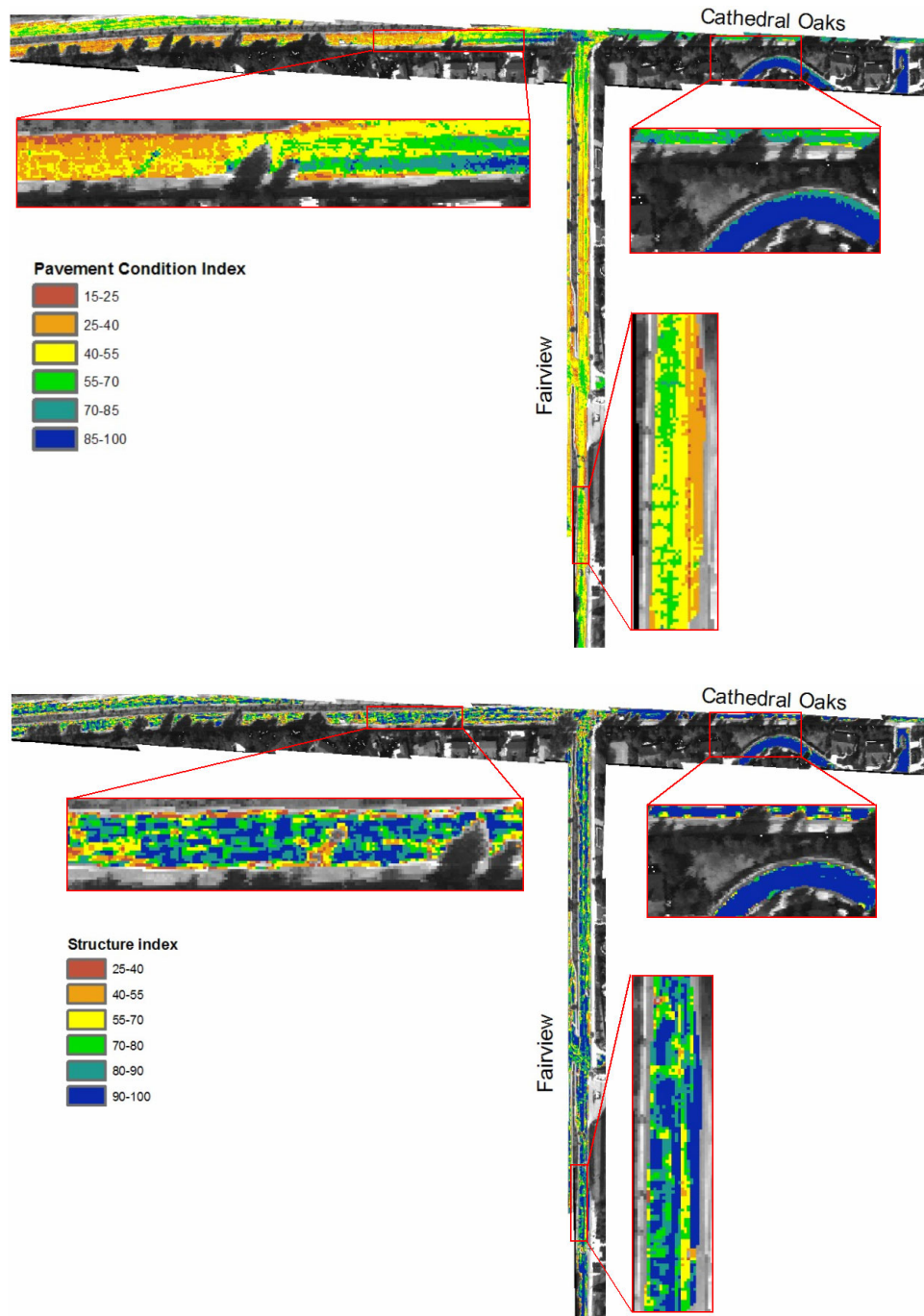
139

Figure 15: Spatial distribution of PCI and structure index derived from HST data.

The ANOVA results again emphasize an observation that was found for several analyses during this study. Obviously, both the "common practice" methods and the remote sensing analysis are effective in identifying roads in good and very good condition. The variance and uncertainty in the data significantly increases for road surfaces in poor condition. Only the expert in-situ observations can be considered a reliable differentiation between roads that need i.e., rehabilitation versus replacement. The broader issue in this context is that pavement health estimation of low quality road surfaces is a complex science and art. There are about 40 different physical pavement properties listed in the international pavement condition rating manual (ASTM D6433, 2003). Some of these refer to visual characteristics, while others address subsurface conditions (e.g., depths of cracks and small distinct scale variations within cracks) that

all surface sensors (Vehicle observations or remote sensing) are not able to acquire and it is doubtful that this detailed level of information can ever be acquired with these methods.

7. Conclusions

This study combined field spectrometry, in-situ road surveys and hyperspectral remote sensing to explore the potential in mapping road conditions from remote sensing. The aging and degradation of road surfaces are represented by distinct spectral characteristics. This study used image ratios and the spatial variance measures to relate the remote sensing signal to pavement condition indices. Image ratios showed the best correlation with the PCI, and variance correlated with an index describing structural road damages (e.g., cracks). Essential for the mapping of road deterioration are the spatial sensor resolutions. The GIFOV should be at least on the order of 0.5 m for detailed road condition observations. The mapping results are most accurate for roads in good conditions. Older roads are more complex and their condition evaluation is more uncertain, in both remote sensing data vehicle-based in-situ observations.

There are some limitations to this study. The investigation only focused on a small study area and on asphalt road surfaces. There were some problems with the spectral calibration of the high resolution HyperSpecTIR data. With better-calibrated data it should be possible to explore other hyperspectral mapping techniques including the short-wave infrared and small absorption features that were identified in the spectral library analysis. In summary, road condition mapping from hyperspectral remote sensing has some potential. It is not likely that remote sensing will take the part of an expert field inspector, but it can offer insights into surface conditions and other aspects that the inspector cannot evaluate except with laborious and destructive testing and field surveys can be limited and optimized. However, this is the first time this issues was presented in this context and further studies are needed to refine to analysis and develop a mapping strategy based on existing technology and in comparison to sensor developments (UAV-based).

Acknowledgement

References

ASTM D6433-03, 2003. Standard Practice for Roads and Parking Lots Pavement Condition Index Surveys, ASTM International-Active Standard 2003, ASTM website: http://www.astm.org (accessed March 2004).

Brecher, A., Noronha, V., and M. Herold, 2004. UAV2003: A roadmap for deploying unmanned aerial vehicle (UAVs) in transportation, Findings of Specialist Workshop in Santa Barbara, California, December 2003, URL: http://www.ncgia.ucsb.edu/ncrst/meetings/uav2003/ncgia.html (accessed April 2004)

Bell, C. A., 1989. Summary Report on the Aging of Asphalt-Aggregate Systems, Strategic Highway Research Program (SHRP) Publications SHRP-A-305, 100 p., URL: http://gulliver.trb.org/publications/shrp/SHRP-A-305.pdf (accessed March 2004).

Clark, R.N., 1999. Spectroscopy of Rocks and Minerals and Principles of Spectroscopy, In: A.N. Rencz (ed.). *Manual of Remote Sensing*, Chapter 1, John Wiley and Sons, New York, pp. 3–58.

Cloutis A. E., 1989. Spectral Reflectance Properties of Hydrocarbons: Remote-Sensing Implications, *Science*, 4914, 165–168.

Gomez, R. B., 2002. Hyperspectral imaging: a useful technology for transportation analysis, *Opt. Eng.*, 41, 9, 2137-2143.

Green, R. O., Conel, J. E., and D. A. Roberts, 1993. Estimation of Aerosol Optical Depth, Pressure Elevation, Water Vapor and Calculation of Apparent Surface Reflectance from Radiance Measured by the Airborne Visible-Infrared Imaging Spectrometer (AVIRIS) using MODTRAN2, *Proceedings of SPIE Conference* no. 1937, Imaging Spectrometry of the Terrestrial Environment, pp. 2–5.

Green, R. O., Eastwood, M. L., Sarture, C. M., Chrien, T. G. et al., 1998. Imaging spectroscopy and the Airborne Visible Infrared Imaging Spectrometer (AVIRIS), *Remote Sensing of Environment*, 65, 3, 227–248.

Herold, M., Gardner, M., Noronha, V., and Roberts, D., 2003. Spectrometry and Hyperspectral Remote Sensing of Urban Road Infrastructure, *Online Journal of Space Communications*, 3, URL: http://satjournal.tcom.ohiou.edu/issue03/applications.html (accessed March 2004).

Herold, M., Roberts, D., Gardner, M., and P. Dennison, 2004. Spectrometry for urban area remote sensing–Development and analysis of a spectral library from 350 to 2400 nm, *Remote Sensing of Environment*, in press.

Noronha, V., Herold. M., Gardner, M. and Roberts, D. A. 2002. Spectrometry and Hyperspectral Remote Sensing for Road Centerline Extraction and Evaluation of Pavement Condition, Proceedings of the Pecora Conference, Denver, Colorado, November 2002.

Miller, J. S. and W. Y. Bellinger, 2003. Distress Identification Manual for the Long-Term Pavement Performance Program (Fourth Revised Edition), Federal Highway Administration Report: FHWA-RD-03-031, URL: http://www.tfhrc.gov/pavement/ltpp/reports/03031/03031.pdf (accessed March 2004).

Stoeckeler, E. G., 1970. Use of aerial color photography for pavement evaluation studies. Highway Research Record 319:40–57.

U.S. Army Corps of Engineers, 1982. Technical manual on pavement maintenance and management, TM 5-623, URL: http://www.usace.army.mil/publications/armytm/ (accessed March 2004).

Usher, J. and D. Truax, 2001. Exploration of Remote Sensing Applicability within Transportation. Remote Sensing Technologies Center final projects report, URL: http://www.rstc.msstate.edu/publications/99-01/rstcofr01-005b.pdf (accessed March 2004).

COMPARISON OF AVIRIS AND MULTISPECTRAL REMOTE SENSING FOR DETECTION OF LEAFY SPURGE

E. Raymond Hunt, Jr.[1] and Amy E. Parker Williams[2]

1.0 Introduction

Leafy spurge (*Euphorbia esula* L.) is a noxious perennial weed that infests approximately 2 million hectares of land in North America and causes severe economic impacts (Anderson et al. 2003). Biologically-based integrated pest management is practical for the control of leafy spurge (Anderson et al. 2003). What is now required is methodology to locate and monitor existing plant populations of leafy spurge as part of the integrated pest management.

Remote sensing has been successfully used to locate and monitor leafy spurge distribution because the unique coloration of the flower bracts (Everitt et al. 1995; Anderson et al. 1996; Ustin et al. 2004). Parker Williams and Hunt (2002) showed that the hyperspectral technique, Mixture Tuned Matched Filtering (Boardman 1998), accurately estimated the amount of leafy spurge cover. Furthermore, Parker Williams and Hunt (2004) showed that classification of leafy spurge presence/absence was 95% accurate. As shown in Figure 1, it is the reflectance from the flower bracts in the yellow-green region of the spectrum, due to an approximately 1:1 chlorophyll-carotenoid ratio, that allows the flowering shoots of leafy spurge to be distinguished from co-occurring species with hyperspectral imagery (Hunt et al. 2004). In northeastern Wyoming, determination of the presence or absence of leafy spurge, while flowering, was 95.2 % accurate with hyperspectral imagery (Parker Williams and Hunt, in press). However, the non-flowering shoots of leafy spurge have a similar reflectance spectrum as other vegetation (Parker Williams and Hunt 2004).

Hyperspectral imagery would be ideal to map the distribution and abundance of leafy spurge, except the area covered is small, the data are not routinely available at the period of peak flowering. Two multispectral sensors on satellite platforms are the Enhanced Thematic Mapper Plus (ETM+) onboard the Landsat 7 satellite and the Système Pour d'Observation de la Terre (SPOT) 4 sensor/satellite (Fig. 1). Landsat ETM+ has bands in the visible (400–700 nm), near-infrared (700–1100 nm), and shortwave-infrared wavelengths (1100–2500 nm) with a pixel size of 900 m^2 (Fig. 1). Landsat ETM+ also has bands in the thermal
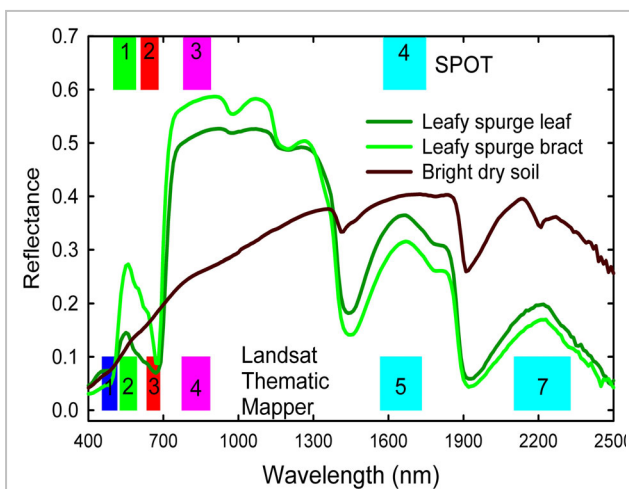

Figure 1. Spectrum of dry soil, leafy spurge leaves, and flower bracts. Shown along the top and bottom are the wavelength intervals of Landsat Thematic Mapper and SPOT 4 sensors.

[1] USDA Agricultural Research Service, Hydrology and Remote Sensing Laboratory, Beltsville, Maryland 20705, erhunt@hydrolab.arsusda.gov
[2] University of Wyoming, Department of Botany, Laramie, Wyoming 82071

infrared (band 6), and a panchromatic (band 8). SPOT 4 has four bands with a pixel size of 400 m² (Fig. 1). The advantages of multispectral imagery are that these data are routinely available, and there are extensive software packages for handling the data, and expertise with the data are widely available. With the green and red bands, the distinctive yellow-green color of the flower bracts should be detectable, hence the objectives of this study are to compare the ability of Landsat 7 ETM+ and SPOT 4 to AVIRIS for the detection of leafy spurge.

## 2.0 Methods

2.1 Study Area

The area for this study was the TEAM Leafy Spurge site near Devils Tower National Monument in Crook County, Wyoming, USA (Parker Williams and Hunt, 2002, 2004). The site was between 44.4 to 44.6° North latitude and 104.6 to 104.9° West longitude. Elevations range from 1219 m along the Bell-Fourche River to 1584 m at the Missouri Buttes. The vegetation in the study area is a mosaic of conifer woodlands, northern mixed-grass prairie, and riparian zones with deciduous shrubs and trees. Leafy spurge is well established throughout the study area.

The period of flowering in 1999 began in late June and lasted until mid July. All of the ground data collection occurred during this period (Parker Williams and Hunt, 2002, 2004). Two sets of plots were established in the study area using a 1991 Landsat 5 Thematic Mapper image to cover adequately the different vegetation types. The first set were circular plots (46 m diameter) used for determining cover of flowering leafy spurge (Parker Williams and Hunt, 2002). The second set were rectangular plots (50 m by 50 m) used for classification accuracy (Parker Williams and Hunt, 2004). Because all plots in the first set had some leafy spurge, we combined these plots with the second set to increase the number of points for accuracy assessment (Fig. 2).

2.2 Image Analysis and Vegetation Indices

A Landsat 7 ETM+ image (path 35 row 29) acquired on July 8, 1999 was obtained from the United States Geological Survey EROS Data Center. The study area was on the extreme eastern boundary of the ETM+ image. A SPOT 4 image centered on Devils Tower was acquired on July 11, 2000, a year after data collection (Fig. 2). The Landsat 7 ETM+ image was georegistered to the SPOT image. The residual mean square error (RMSE) of the Landsat image to the SPOT image was 22 m.

The Airborne Visible Infrared Imaging Spectrometer (AVIRIS) was

Figure 2. SPOT image with plots.

144
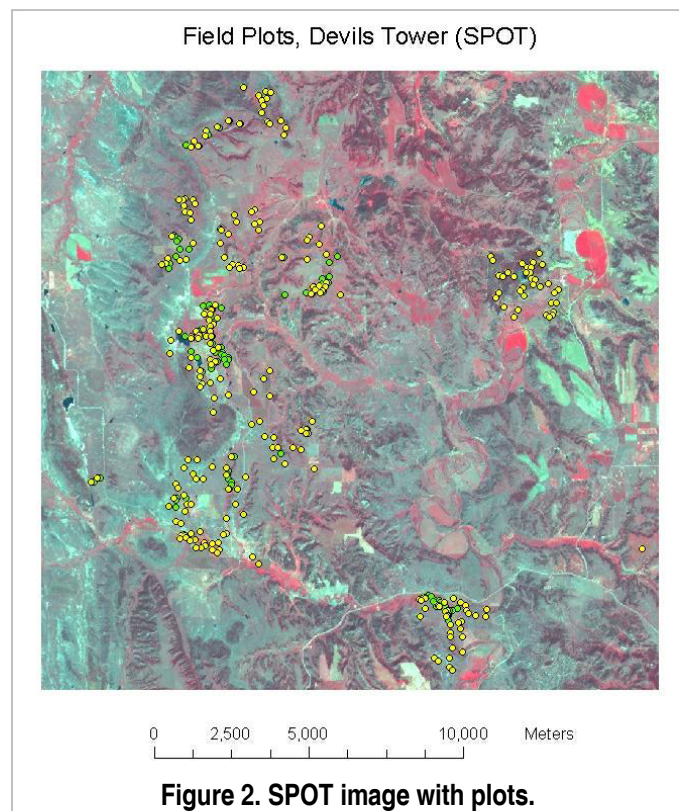
flown at high altitude over the study site on July 6, 1999 (Parker Williams and Hunt 2002). The AVIRIS data were atmospherically corrected using the ATREM 3.1 program (Gao et al. 1999). The atmospherically-corrected reflectances were smoothed using the spectral reflectances of a large talus field at the base of Devils Tower, which was measured using an ASD Fieldspec UV/VNIR spectroradiometer (Analytical Spectral Devices, Inc. Boulder, Colo.). The image files did not have a geometric lookup table, therefore the three AVIRIS flight lines (11 scenes total) were georegistered to the SPOT image. The RMSE between the AVIRIS and SPOT images was 26 m.

Originally a SPOT image was acquired on July 9, 1999, but the selected gains were set too low, hence band 3 (near-infrared) was saturated over vegetation for much of the image. About one-third of the plots with leafy spurge were used for release sites of *Aphthonia* species flea beetles in 1999 (Parker Williams, 2001), and the flea beetles may have reduced the amount of cover of flowering leafy spurge somewhat for the SPOT 4 image.

Bands 1 through 4 of the Landsat ETM+ image and bands 1 through 3 of the SPOT 4 image (Fig. 1) were atmospherically corrected using an empirical line approach using the average reflectance spectrum of the talus field and a dark pixel subtraction. The shortwave-infrared bands were atmospherically corrected using the talus-field reflectances from the AVIRIS image.

A standard technique with multispectral imagery is the use of vegetation indices. Based on the spectral differences of leafy spurge leaves and flower bracts, several indices were tested with the AVIRIS, ETM+ and SPOT 4 data. The first index was the Normalized Difference Vegetation Index (NDVI):

$$NDVI = (NIR - Red)/(NIR + Red) \tag{1}$$

where NIR was AVIRIS band 54 (855 nm), ETM+ band 4 or SPOT 4 band 3, and Red was AVIRIS band 31 (665 nm), ETM+ band 3 or SPOT 4 band 2 (Fig. 1). The second index was the Green Normalized Difference Vegetation Index (GNDVI):

$$GNDVI = (NIR - Green)/(NIR + Green) \tag{2}$$

where Green was AVIRIS band 20 (556 nm), ETM+ band 2 or SPOT 4 band 1 and the NIR band was defined in Equation 1. The third index was the Green:Red reflectance ratio (G:R):

$$G:R = Green/Red \tag{3}$$

where the green and red bands were defined in Equations 2 and 1, respectively.

Various methods of classification were tried on the AVIRIS, ETM+, and SPOT images. Supervised methods used large fields of leafy spurge near Devils Tower National Monument for a flowering leafy spurge signature, vegetation pixels with no spurge were selected based on the ground data. Other land cover classes (rocks, soils, crops, forest, water, roads, etc.) were added as needed. The spectral signature for flowering leafy spurge for the Spectral Angle Mapper

(SAM) method was obtained from the same fields as the supervised classification. One-sample Z-tests were used to test if the kappa-hat statistic were significantly different from zero and two-sample Z-tests were used to test if two classifications were significantly different (Congalton and Green 1999).

2.3 Canopy Reflectance Modeling

The Scattering by Arbitrarily Inclined Leaves (SAIL) model was designed to predict canopy reflectance for various leaf area indices (LAI) and measured leaf reflectances and transmittances (Verhoef, 1984). A graphical user interface for the Microsoft Windows operating system was programmed in Visual Basic and is available from the corresponding author.

The soil, leaf and flower bract reflectance spectra (Fig. 1) were used as inputs to the SAIL model. Grass and forb reflectance and transmittance spectra were obtained from measurements on *Poa pratenesis* L. (Kentucky bluegrass) and *Taxiarium officialis* L. (dandilions), respectively made with an ASD FieldSpec Pro FR spectroradiometer and LICOR LI-1800-12 integrating sphere (Lincoln, Nebraska). Leafy-spurge flowers and leaves, and forb leaves, were assumed to have a typical planophile (horizontal) leaf distribution, and grass leaves were assumed to have a typical erectophile (vertical) leaf distribution. The SAIL model was run for various combinations of leaf area index (LAI), forb cover, grass cover, leaf cover of leafy spurge, and flower cover of leafy spurge. Leaves of forbs, grass, and leafy spurge were placed in a lower canopy layer, and flowers of leafy spurge (when present) were placed in the top canopy layer.

3.0 Results and Discussion

3.1 Vegetation Indices

All of the vegetation indices were significantly, but not strongly, correlated ($P < 0.05$) with the measured cover of flowering leafy spurge for the prairie cover type. The slopes of vegetation indices versus spurge cover were not significantly different from zero for the woodland cover type (data not shown). The G:R reflectance ratio was the best correlated index for the AVIRIS image ($R^2 = 0.23$, Fig. 3), the ETM+ image ($R^2 = 0.24$, Fig. 4), and the SPOT 4 image ($R^2 = 0.26$, Fig. 5). The R^2 were 0.12, 0.16, and 0.19 for NDVI and spurge cover for the AVIRIS, ETM+, and SPOT 4 images, respectively (data not shown). Finally for the GNDVI, the R^2 were 0.05, 0.12, and 0.19, respectively. We tried other band combinations using AVIRIS data, particularly using band 25 (606 nm) and we did not find a better index than G:R for detecting flowering leafy spurge.
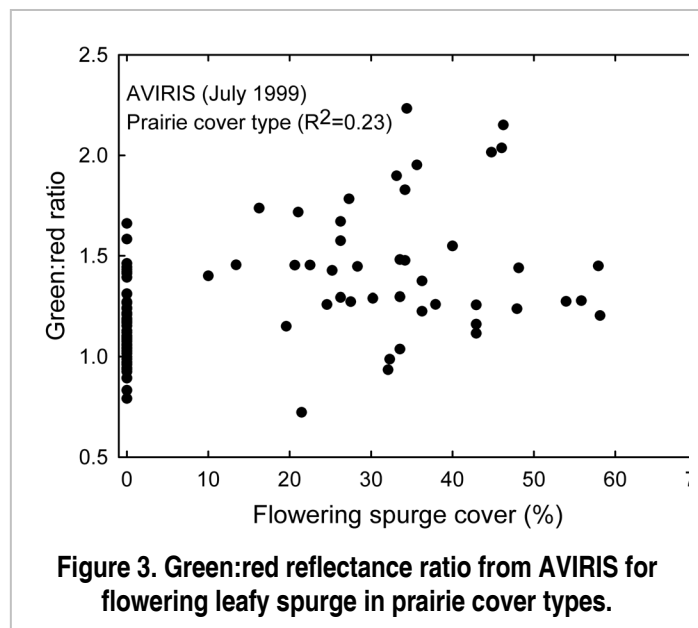

Figure 3. Green:red reflectance ratio from AVIRIS for flowering leafy spurge in prairie cover types.

146

3.2. Canopy Reflectance Modeling

The SAIL model was used in exploration to determine if another vegetation index to detect flowering leafy spurge was possible. As LAI increases, the spectral reflectance in the near-infrared increases, the spectral reflectance in the red decreases, and the spectral reflectance in the green remains about equal to the spectral reflectance of the soil (Fig. 6). At constant LAI, spectral reflectances in the near-infrared increase with increased cover of leafy-spurge leaves in grass because of the difference between the planophile leafy-spurge and the erectophile grasses (data not shown). At constant LAI, spectral reflectances also increase in the green with increased cover of leafy-spurge leaves and flowers in grass (Fig. 7). The relationship of G:R with increased cover of leafy-spurge flowers generally increased at low LAI for mixtures of leafy spurge in both forbs and grasses (Fig. 8, 9). However, the change in G:R with increased LAI was much more than the change in G:R associated with increased cover of leafy-spurge flowers. From the SAIL model results, there was not a better index than G:R for detecting flowering leafy spurge, but this index performed poorly when LAI was variable.

Figure 4. Green:red reflectance ratio from SPOT 4 for flowering leafy spurge in prairie cover types

Figure 5. Green:red reflectance ratio from Landsat 7 Enhanced Thematic Mapper Plus (ETM+) for flowering leafy spurge in prairie cover types.

3.3 Classification

The best method of supervised classification was minimum distance (Table 1). The classifications for Landsat ETM+, SPOT 4, and AVIRIS were all significantly better than chance ($P < 0.05$), and there were no significant differences among the three types of imagery in detecting flowering leafy spurge (Table 1). On the other hand, SAM classification using the Landsat ETM+ and SPOT 4 images were not better than chance, whereas the AVIRIS image did have a significantly better detection rate of flowering leafy spurge (Table 2). The threshold angle for a match with SAM was reduced from 0.1 radians (the default value) to 0.05 radians, because use of the larger threshold would have included most of the non-forest, vegetated pixels as leafy spurge present.
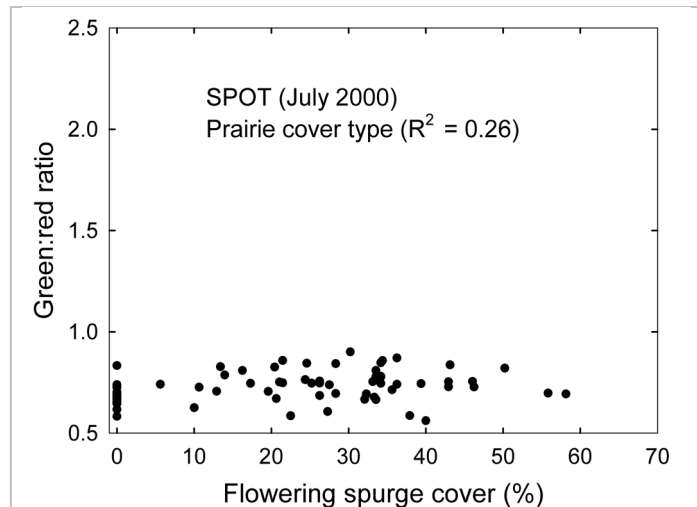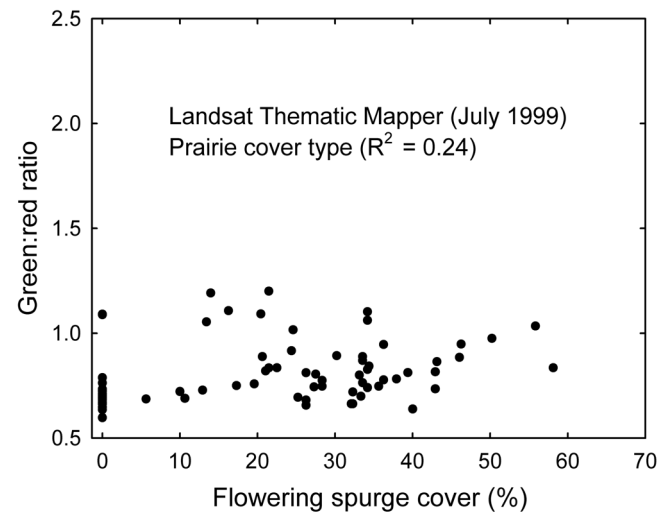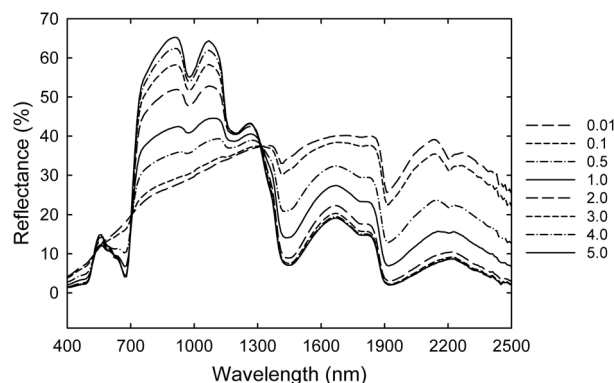
Figure 6. Canopy spectral reflectance from the SAIL model at various leaf area index (LAI) for a mixture of 50% grass, 25% leafy-spurge leaves, and 25% leafy-spurge flowers.
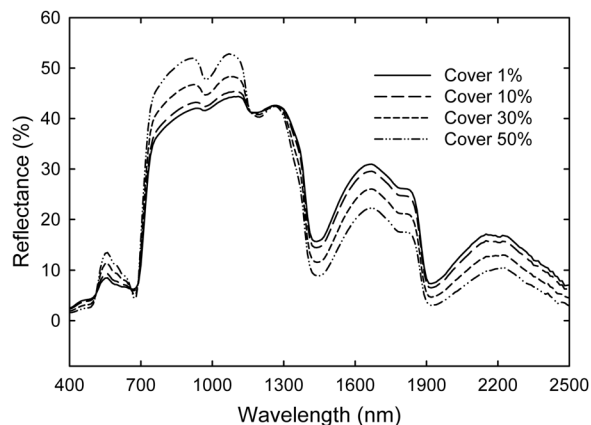

Figure 7. Canopy spectral reflectance from the SAIL model at various total cover of leafy-spurge flowers and leaves in grass. Total LAI was 1 m²/m² and leafy-spurge leaf cover was set equal to flower cover, so 50% total cover is 25% flowers and 25% leaves.
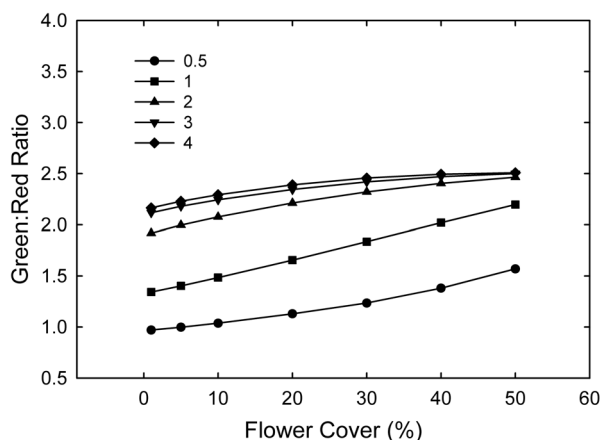

Figure 8. Green:red reflectance ratio from the SAIL model at various LAI and leafy-spurge cover in forbs.
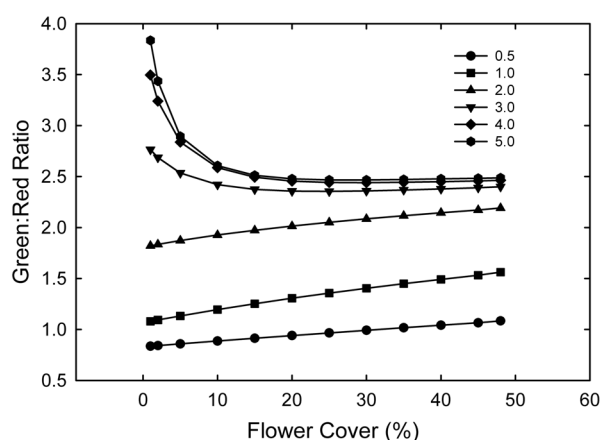

Figure 9. Green:red reflectance ratio from the SAIL model at various LAI and leafy-spurge cover in grass.

These results are not nearly as good as reported before with mixture-tuned matched filtering (Parker Williams and Hunt 2002, 2004). One reason may be due the geometric correction of the AVIRIS imagery (Peleg and Anderson 2002). Parker Williams (2001) located each plot using digital orthophotos, and did not georegister the images. We performed a standard hyperspectral data reduction and a mixture-tuned matched filtering analysis for the AVIRIS mosaic and found the overall accuracy was 75% (data not shown), similar to the results with SAM (Table 2).

4.0 Conclusions

These results show there is little predictive power using vegetation indices to estimate the amount of leafy spurge, even with AVIRIS, when there are variations of LAI across the landscape. Furthermore, we did not find a "best band" that would optimize performance of multispectral sensors, even though flowering leafy spurge has bright, distinctive yellow-green

bracts. Supervised classification techniques did not perform well, even with a large number of bands available to separate different classes of vegetation. Thus, applying multispectral techniques to hyperspectral imagery did not increase the ability of remote sensing to detect leafy spurge. We show here that hyperspectral techniques making use of the entire reflectance spectrum (the Spectral Angle Mapper), work far better with hyperspectal data for detection of flowering leafy spurge compared to multispectral data. Underwood et al. (2003) also showed that hyperspectral techniques applied to AVIRIS data worked well for detection of two other non-native plants, iceplant (*Carpobrotus edulis*) and jubata grass (*Cortaderia jubata*). Therefore, hyperspectral analyses are required to bring out the power of hyperspectral data for remote sensing.

Table 1. Presence/absence of leafy spurge using Minimum Distance Supervised Classification.

Sensor		Ground Data		
		Present	Absent	Accuracy
Landsat 7 ETM+	Present	54	30	
	Absent	60	102	63 % *
SPOT 4	Present	68	35	
	Absent	46	97	67 % *
AVIRIS	Present	63	27	
	Absent	51	105	68 % *

* Significant at $P < 0.05$

Table 2. Classification of presence/absence of leafy spurge using the Spectral Angle Mapper with threshold of 0.05 radians.

Sensor		Ground Data		
		Present	Absent	Accuracy
Landsat 7 ETM+	Present	8	8	
	Absent	106	124	54 %
SPOT 4	Present	22	32	
	Absent	92	100	50 %
AVIRIS	Present	83	33	
	Absent	31	99	74 % *

* Significant at $P < 0.05$

5.0 References

Anderson, G. L., E. S. Delfosse, N. R. Spencer, C. W. Prosser, and R. D. Richard, 2003, "Lessons in Developing Successful Invasive Weed Control Programs," *J. Range Manage.*, vol. 56, pp. 2-12.

Boardman, J. W., 1998, "Leveraging the high dimensionality of AVIRIS data for improved sub-pixel target unmixing and rejection of false positives: mixture tuned matched filtering," *Summaries of the Seventh JPL Airborne Geoscience Workshop*, JPL Publication 97-1, Jet Propulsion Laboratory, California Institute of Technology, Pasadena, California, pp. 55-56.

Congalton, R. G. and K. Green, 1999, *Assessing the Accuracy of Remotely Sensed Data: Principles and Practices*, Lewis Publishers, Boca Raton, Florida.

Everitt, J. H., G. L. Anderson, D. E. Escobar, M. R. Davis, N. R. Spencer, and R. J. Andrascik, 1995, "Use of Remote Sensing for Detecting and Mapping Leafy Spurge (*Euphorbia esula*)," *Weed Technol.*, vol. 9, pp. 599-609.

Gao, B.-C., K.B. Heidebrecht, and A.F.H. Goetz, 1999, *Atmosphere REMoval Program (ATREM) User's Guide, Version 3.1.* Center for the Study of Earth from Space (CSES), Cooperative Institute for Research in Environmental Sciences (CIRES), University of Colorado, Boulder, Colorado.

Hunt, E. R., Jr., J. E. McMurtrey, III, A. E. Parker Williams, and L. A. Corp, 2004, "Spectral Characteristics of Leafy Spurge (Euphorbia Esula) Leaves and Flower Bracts," *Weed Sci.*, vol. 52, pp. 492-497.

Parker Williams, A. E., 2001, *Biological control and hyperspectral remote sensing of leafy spurge (Euphorbia esula L), an exotic plant species in North America.* PhD Dissertation, Department of Botany, University of Wyoming, Laramie, Wyoming.

Parker Williams, A. and E. R. Hunt, Jr, 2002, "Estimation of Leafy Spurge Cover from Hyperspectral Imagery Using Mixture Tuned Matched Filtering," *Remote Sens. Environ.*, vol. 82, pp. 446-456.

Parker Williams, A. E. and E. R. Hunt, Jr., 2004, "Accuracy Assessment for Detection of Leafy Spurge with Hyperspectral Imagery," *J. Range Manage.*, vol. 57, pp. 106-112.

Peleg, K., and G. L. Anderson, 2002, FFT regression and cross-noise reduction for comparing images in remote sensing. *Int. J. Remote Sens.*, vol. 23, pp. 2097-2124.

Underwood, E., S. Ustin, and D. Dipietro, 2003, "Mapping nonnative plants using hyperspectral imagery," *Remote Sens. Environ.*, vol. 86, pp. 150-161.

Ustin, S. L., D. A. Roberts, J. A. Gamon, G. P. Asner, and R. O. Green, 2004, "Using imaging spectroscopy to study ecosystem processes and properties," *Bioscience*, vol. 54, pp. 523-534.

Verhoef, W., 1984, "Light Scattering by Leaf Layers with Application to Canopy Reflectance Modeling: the SAIL Model," *Remote Sens. Environ.*, vol. 16, pp. 125-141.

Combination of Imaging Spectrometer Data and High-Resolution LIDAR Data by 3-D Radiative Transfer Modeling

Benjamin Koetz,[a] Felix Morsdorf,[a] Mathias Kneubuehler,[a] Michael Schaepman,[b] Erich Meier,[a] Klaus Itten,[a] and Britta Allgoewer[c]

1 Introduction

Coniferous forests represent canopies with a high heterogeneity in the horizontal and as well in the vertical dimension. Consequently the interaction of incident radiation is dominated by the complex 3-D canopy structure and architecture. Radiative transfer approaches based on coupled leaf and canopy radiative transfer models (RTM) still allow the simulation of the multi-directional canopy reflectance as a function of leaf optical properties, canopy structure and viewing geometry as well as the retrieval of biophysical and biochemical canopy variables.

High-resolution imaging spectrometry supported by light detection and ranging (LIDAR) data and the complex 3-D radiative transfer model FLIGHT (North, 1996) are employed to assess the influence of canopy heterogeneity and structure on canopy reflection. Exhaustive ground measurements of biochemical and biophysical parameters combined with the geometry of single trees derived from LIDAR data provide the possibility of a realistic scene parameterization of a boreal forest in Switzerland.

2 Data

This study is based on an extensive field campaign during summer 2002 in the Eastern Ofenpass valley, which is part of the Swiss National Park (SNP) (Kötz et al., 2004). The Ofenpass represents an inner-alpine valley at an average altitude of about 1900 m above [mean] sea level (a.s.l) with annual precipitation of 900-1100 mm. The south-facing Ofenpass forests, the location of the field measurement, are largely dominated by mountain pine (*Pinus montana ssp. arborea*) and some stone pine *(Pinus cembra L.)* a second tree specie that is of interest for natural succession (Zoller, 1992; Zoller, 1995; Lauber and Wagner, 1996). These forest stands can be classified as woodland associations of *Erico-Pinetum mugo* (Zoller, 1995). Unique ground-based characterization of the canopy structure, biochemistry and optical properties of the canopy elements were conducted using various instruments, ranging from non-destructive spectroradiometric measurements to dry biomass estimation of needles.

The field data have been collected on four core test sites each subdivided into 9 plots spaced in a grid of 10 meters. The core test sites were selected following a stratified sampling scheme to cover different canopy densities within a stand of *Pinus montana ssp. arborea* (Fig.1). They were set up according to the elementary sampling units of the VALidation of Land European Remote-sensing Instruments (VALERI) scheme (Baret et al., submitted). For the presented study we selected two test sites (LWF1 and STA1) representing different canopy densities.

[a] Remote Sensing Laboratories (RSL), Dept. of Geography, University of Zurich, Winterthurerstrasse 190, CH-8057 Zurich, Switzerland, Email: bkoetz@geo.unizh.ch

[b] Centre for Geo-Information, Wageningen University and Research Centre, Droevendaalsesteeg 3, NL-6708 PB Wageningen, The Netherlands

[c] Geographic Information Systems, Dept. of Geography, University of Zurich, Winterthurerstrasse 190, CH-8057 Zurich, Switzerland
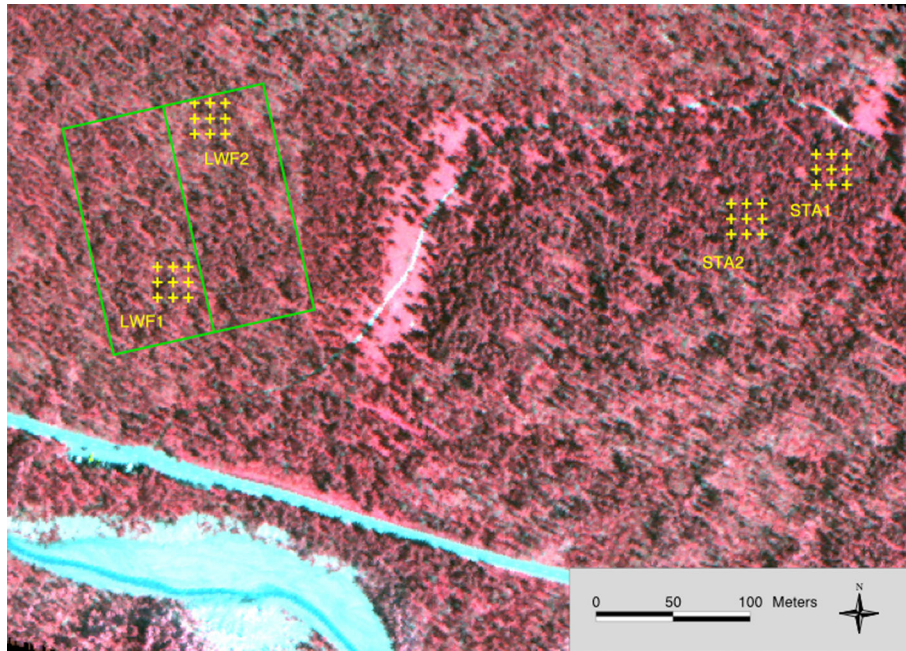
Figure 1: Airborne imaging spectrometer data over the four core test sites (yellow crosses indicate the sampling points). The image composite represents geocoded and atmospherically corrected data of the spectrometer ROSIS in spatial resolution of one meter resolving the heterogeneity of the observed forest. The Long-term Forest Ecosystem Research site of WSL where forest stand characteristics are acquired is indicated by the green rectangle.

Canopy structure was described using two different methods, well known in the literature (Smolander and Stenberg, 1996; Chen et al., 1997) and adapted to heterogeneous canopies. Measurements were carried out using two canopy analyzer LAI2000 (LICOR, 1992) and hemispherical photographs to provide canopy structure variables (EYE-CAN, 2003) separately for the crown and understory layer. The LAI2000 was used to estimate two canopy variables: the effective LAI (leaf area index) and the gap fraction. The clumping effects at the shoot and crown level, typical for coniferous foliage, were corrected following an approach proposed by (Chen et al., 1997). Hemispherical photographs taken parallel with the LAI2000 measurements allowed the separation of the canopy into its constituent foliage and wood fractions, i.e., needles, trunk and branches (Jonckheere et al., 2003; Weiss et al., 2003).

Standard wet-laboratory procedures were used for determination of foliage water, chlorophyll content and dry matter. The samples were collected from the upper part of the tree crowns, each consisting of one branch carrying newly developed and old needles.

The spectral properties of several canopy components including the reflectance of the understory, woody parts and the foliage were measured in the field with the ASD field spectroradiometer (Analytical Spectral Devices, 1997). Field spectra were collected during the overflight in nadir measurement configuration, 1.5 m above the ground and within 2 hours of solar noon under clear sky conditions. All spectra were converted to absolute reflectance by reference measurements over a Spectralon panel with known spectral properties.

2.1 Imaging spectrometer data

The imaging spectrometer data were acquired on the 14th of August 2002 parallel to the ground measurements with the Digital Imaging Airborne Spectrometer (DAIS) 7915 (Chang et al., 1993). The local illumination and observation conditions were summarized by a solar zenith

angle of 45.3° deg, a solar azimuth angle of 122.9° deg, and the flight heading of 293° deg. The DAIS 7915 Kennedy scanner covered a spectral range from the visible to the thermal infrared (VIS/near infrared (NIR): 0.5–1.1 μm, short-wavelength infrared (SWIR) 1: 1.6-1.8 μm, SWIR2: 2-2.5 μm, mid infrared (MIR): 3-5 μm, thermal infrared (TIR): 8.7-13 μm) with 79 bands. The airborne campaign was organized to cover the Ofenpass valley providing imaging spectrometer data in a spatial resolution of five meters. The images were geo-atmospherically processed with the software modules PARGE and ATCOR4 to obtain geocoded top-of-canopy reflectance (Richter and Schläpfer, 2002; Schläpfer and Richter, 2002; Schläpfer et al., 2003).

2.2 LIDAR data

In October 2002, an airborne LIDAR survey of the test site in the Swiss National Park was also carried out to derive structural forest parameters. The sensor used was the FALCON, a push-broom laser altimeter operated by the TopoSys company. During this campaign the system provided both first and last reflection of the laser signal on the ground (first/last pulse) in a point density of more than 30 points per m^2 with a footprint size of about 30 cm in diameter. The segmentation of the single LIDAR returns into tree crowns allowed for the retrieval of the geometric properties of single trees, such as tree position, height, crown radius and crown length (Morsdorf et al., 2004).

3   RTM parameterization: explicit scene representation

The 3-D radiative transfer model FLIGHT (North, 1996) coupled to the leaf model PROSPECT (Jacquemoud et al., 1996) was employed to simulate multi-directional and hyperspectral canopy reflectance. The PROSPECT model, which provided the foliage optical properties as a function of the biochemistry, characterized the radiative transfer at the foliage level. The PROSPECT leaf model was chosen due to its small number of parameters and its wide validation, including the application to coniferous foliage (Kuusk and Nilson, 2000; Zarco-Tejada et al., 2004). FLIGHT is a three-dimensional ray-tracing model using Monte Carlo techniques for the radiative transfer within crown boundaries and deterministic ray tracing between the crowns and other canopy components. The canopy structure is represented by geometric primitives defined by the crown shape and size, tree height, tree position and distribution. The geometric representation of FLIGHT deals explicitly with crown overlapping, mutual shading and multiple scattering between crowns.

For the average scene representation the radiative transfer was parameterized at the foliage and canopy level by the average field data of the two core test sites describing the biochemical and biophysical properties of the canopy (Table 1). Certain parameters also applied for the explicit scene representation, such as the foliage parameter and the LAI.

The explicit scene representation was based on the ability of FLIGHT to represent the complex scene of a heterogeneous forest by taking into account the geometry of single trees composing the scene. The relevant information on the tree position, height and crown geometry was provided by the LIDAR data set (cf., Fig. 2a). The reconstruction of the observed forest scene based on the LIDAR-derived tree geometry allowed consequently to consider the actual canopy structure (e.g., fcover) as well as the detailed heterogeneity of the canopy within the radiative transfer. Important processes as for example shadowing of the background, mutual crown shadowing and multiple scattering between crowns could be explicitly described (Gerard and North, 1997).

Table 1: Field observations of canopy variables including relative measurement errors relevant for the canopy parameterization of the RTMs PROSPECT and FLIGHT. The spectral properties of the woody parts and understory were characterized by spectroradiometric field measurements.

	unit	LWF1	STA1
Foliage parameters (PROSPECT)			
Water content	g/cm^2	0.047 (7.5%)	0.042 (7.5%)
Dry matter	g/cm^2	0.038 (7.5%)	0.035 (7.5%)
Chlorophyll content	µg/cm^2	61.8 (1.54%)	62.8 (1.54%)
Mesophyll structure	unitless	3.78 (22%)	
Canopy structure (overstory)			
LAI	Unitless	2.18 (13%)	3.99 (17%)
Fractional cover	%	0.55 (13%)	0.79 (17%)
Wood fraction	%	0.3	0.4
Crown shape		Cone	
FLIGHT (average scene representation)			
Tree height	m	11.93 ± 2.9	
Tree distribution		Poisson distribution	
Crown radius	m	1.765	
Crown base	m	7	
Trunk diameter	m	0.179 (at ground)	
Leaf angle distribution		Spherical	

4   Results

Canopy reflectance has been extracted from the imaging spectrometry data over the area (30 x 30 m^2) of the two selected test sites LWF1 and STA1 and has been averaged to represent the complete scene of the respective site. Subsequently canopy reflectances for the two sites have been simulated by the coupled RTM taking into account an average scene as well as an explicit scene representation. The comparison of simulated and measured canopy reflectance revealed a reasonable performance of the radiative transfer model for both scene representations confirming the appropriate choice of the RTM relative to the complexity of canopy structure. The explicit scene representation still improved significantly the accuracy and uncertainty of simulated canopy reflectance relative to the average scene representation (cf., Fig. 2b). In the case of the LWF1 site, the mean simulated reflectance didn't deviate significantly between the average and explicit scene representation. Nevertheless the explicit scene representation showed a reduced uncertainty associated with the simulated reflectance, which probably is due to the direct assessment of the fractional cover based on the LIDAR-derived tree geometry and distribution. Over the denser stand, STA1, the imaging spectrometer measured rather low canopy reflectance, which was only reproduced by the explicit scene representation. Processes like mutual crown shadowing, being more dominant for denser canopies, could have been here more accurately represented within the explicit scene.

The presented study demonstrated on two selected cases the potential of the combination of high-resolution imaging spectrometry and LIDAR data for an improved parameterization of the radiative transfer within a coniferous forest. The combined use of the two data sources over 3D-RTM also provided a strategy to resolve explicitly the heterogeneity of a coniferous forest scene, which will lead in future to more reliable and robust RTM retrieval algorithms.
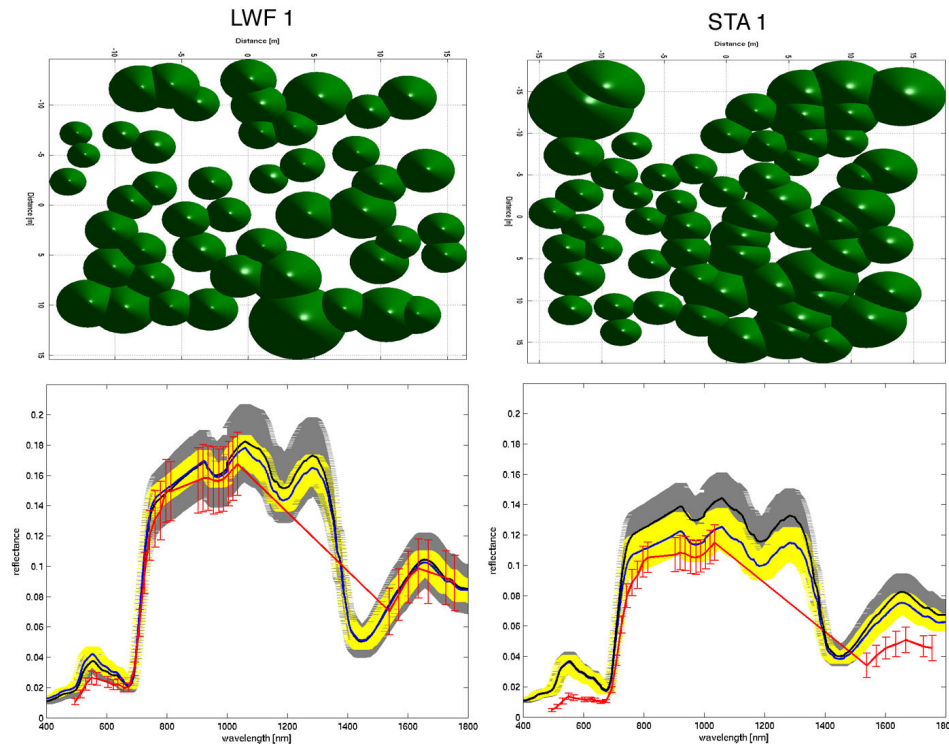
Figure 2: a) Nadir view of the explicit geometric representation of the scenes LWF1 and STA1
b) Mean canopy reflectance and associated uncertainties of the scenes LWF1 and STA1 (DAIS: red, average scene: black/grey, explicit scene: blue/yellow)

5 References

Analytical Spectral Devices, I. (1997). *FieldSpec, User's Guide*. Boulder, Colorado, Analytical Spectral Devices, Inc., 81.

Baret, F., Weiss, M., Garrigue, S., Allard, D., Guinot, J. P., Leroy, M., Jeanjean, H., Bohbot, H., Bosseno, R., Dedieu, G., Di Bella, C., Espana, M., Gond, V., Gu, X. F., Guyon, D., Lelong, C., Mougin, E., Nilson, T., Veroustraete, F. and Vintilla, R. (submitted), VALERI: a network of sites and a methodology for the validation of medium spatial resolution land satellite products. *Remote Sensing of Environment*.

Chang, S.-H., Westfield, M. J., Lehmann, F., Oertel, D. and Richter, R. (1993), 79-Channel Airborne Imaging Spectrometer. *Im. Spec. of the Terr. Env., SPIE,* 1937, 164–172.

Chen, J. M., Rich, P. M., Gower, S. T., Norman, J. M. and Plummer, S. (1997), Leaf area index of boreal forests: Theory, techniques, and measurements. *Journal of Geophysical Research-Atmospheres,* 102(D24), 29429–29443.

EYE-CAN (2003). EYE-CAN 1.0: A software to process hemispherical images for vegetation biophysical characteristic estimation. Ramonville, NOVELTIS, INRA,

Gerard, F. F. and North, P. R. J. (1997), Analyzing the effect of structural variability and canopy gaps on forest BRDF using a geometric-optical model. *Remote Sensing of Environment,* 62(1), 46–62.

Jacquemoud, S., Ustin, S. L., Verdebout, J., Schmuck, G., Andreoli, G. and Hosgood, B. (1996), Estimating leaf biochemistry using the PROSPECT leaf optical properties model. *Remote Sensing of Environment,* 56(3), 194–202.

Jonckheere, I., Fleck, S., Nackaerts, K., Muys, B., Coppin, P., Weiss, M. and Baret, F. (2003), Review of methods for in situ leaf area index determination: Part I. Theories, sensors and hemispherical photography. *Agricultural and Forest Meteorology,* in press.

Kötz, B., Schaepman, M., Morsdorf, F., Bowyer, P., Itten, K. and Allgöwer, B. (2004), Radiative Transfer Modeling within a Heterogeneous Canopy for Estimation of Forest Fire Fuel Properties. *Remote Sensing of Environment,* in press.

Kuusk, A. and Nilson, T. (2000), A directional multispectral forest reflectance model. *Remote Sensing of Environment,* 72(2), 244–252.

Lauber, K. and Wagner, G. (1996). *Flora Helvetica. Flora der Schweiz*. Bern, Stuttgard, Wien, Paul Haupt Verlag, pp. 1613.

LICOR (1992). *LAI-2000 Plant Canopy Analyzer – Operating Manual*. Lincoln, Nebraska, LI-COR, Inc.,

Morsdorf, F., Meier, E., Kötz, B., Itten, K. and Allgöwer, B. (2004), LIDAR based geometric reconstruction of broreal type forest stands at single tree level for forest and wildland fire management. *Remote Sensing of Environment,* in press.

North, P. R. J. (1996), Three-dimensional forest light interaction model using a Monte Carlo method. *Ieee Transactions on Geoscience and Remote Sensing,* 34(4), 946–956.

Richter, R. and Schläpfer, D. (2002), Geo-atmospheric processing of airborne imaging spectrometry data. Part 2: atmospheric/topographic correction. *International Journal of Remote Sensing,* 23(13), 2631–2649.

Schläpfer, D., Koetz, B. and Gruber, S. (2003). The influence of DEM characteristics on preprocessing of DAIS/ROSIS data in high altitude alpine terrain. *3rd EARSEL Workshop on Imaging Spectroscopy*, Oberpfaffenhofen,

Schläpfer, D. and Richter, R. (2002), Geo-atmospheric processing of airborne imaging spectrometry data. Part 1: parametric orthorectification. *International Journal of Remote Sensing,* 23(13), 2609–2630.

Smolander, H. and Stenberg, P. (1996), Response of LAI-2000 estimates to changes in plant surface area index in a Scots pine stand. *Tree Physiology,* 16(3), 345–349.

Weiss, M., Baret, F., Smith, G. J., Jonckheere, I. and Coppin, P. (2003), Review of methods for in situ leaf area index (LAI) determination Part II: Estimation of LAI, errors and sampling. *Agricultural and Forest Meteorology,* in press.

Zarco-Tejada, P. J., Miller, J. R., Harron, J., Hu, B., Noland, T. L., Goel, N., Mohammed, G. H. and Sampson, P. H. (2004), Needle chlorophyll content estimation through model inversion using hyperspectral data from boreal conifer forest canopies. *Remote Sensing of Environment,* 89(2), 189–199.

Zoller, H. (1992). Vegetationskarte des Schweizerischen Nationalparks und seiner Umgebung. Bern, Hallwag AG.

Zoller, H. (1995). *Vegetationskarte des Schweizerischen Nationalparks. Erläuterungen*. National Park Forschnung, pp. 108.

An Improved Data Structure for AVIRIS-Type Imaging Spectrometer Measurements

Pablo J. Martínez, Daniel Hermosel, *Robert O. Green, Javier Plaza, Rosa M. Pérez

Computer Science Dept. University of Extremadura (Spain)

*Jet Propulsion Laboratory, California Institute of Technology, Pasadena, California 91109

1. Introduction

Imaging spectrometers, such as the Airborne Visible/Infrared Imaging spectrometer (AVIRIS), measure spectra in the region from 400 to 2500 nm at nominally 10-nm sampling. This gives approximately 200 continuous spectral channels of data for every spatial element measured. These spectroscopic measurements are used to determine the composition and infer processes of the Earth system through spectroscopy analysis. Spectroscopic analysis is based on the physics, chemistry, and biology revealed through the interaction of energy with matter recorded in each measured spectrum.

AVIRIS measures spectra sequentially of the radiance incident at the aperture of the instrument. These measurements are stored as a 224-dimensional spectral vector Ll. This vector holds the radiance (L) for each of the 224 wavelengths (l) measured. Traditionally these spectra are arranged as a bidimensional array of spectra Lx,y, l. Figure 1 shows a portrayal of this traditional storage architecture for the AVIRIS image of Moffett Field, California.
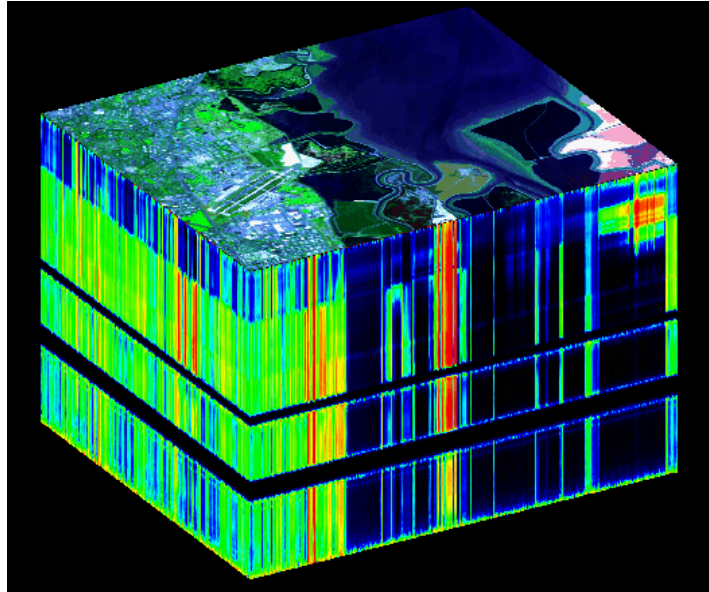

Figure 1: Traditional image cube where every spatial element x,y of the scene has a vector, Lx,yl, that is the radiance for the l spectral channel and the x,y spatial element.

However, this traditional format of data structure has not been designed optimally for AVIRIS-type imaging spectrometer images where each spectrum is measured sequentially with some variation in pointing from aircraft motion. Rather the data structure heritage is from image framing cameras where all

the image pixels are obtained simultaneously. For example, from a metric camera carefully modeled and with thousands of spatial points and few spectral bands. This traditional data structure format imposes an unnecessary burden on point sequential data instruments such as AVIRIS.

2. AVIRIS-Type Imaging Spectrometer Measurement

AVIRIS uses a cross-track scanners to measured spectra across the field-of-view and aircraft motion to build up the along track image. Each spectrum is measured sequentially across the scan. This imposes a cylindrical coordinate system to the spatial location of each measured spectrum. To acquire data with nominally uniform cross-track to cross-track scan, the AVIRIS scan mirror rotates backwards quickly before beginning the next forward scan of image collection. No ground image data is collected during the back scan. Based solely on the scanner, AVIRIS collects data in a cylindrical coordinate system across a 33 degree field-of-view. Figure 2 gives a depiction of the cross-track scan approach used by whiskbroom instruments such as AVIRIS.
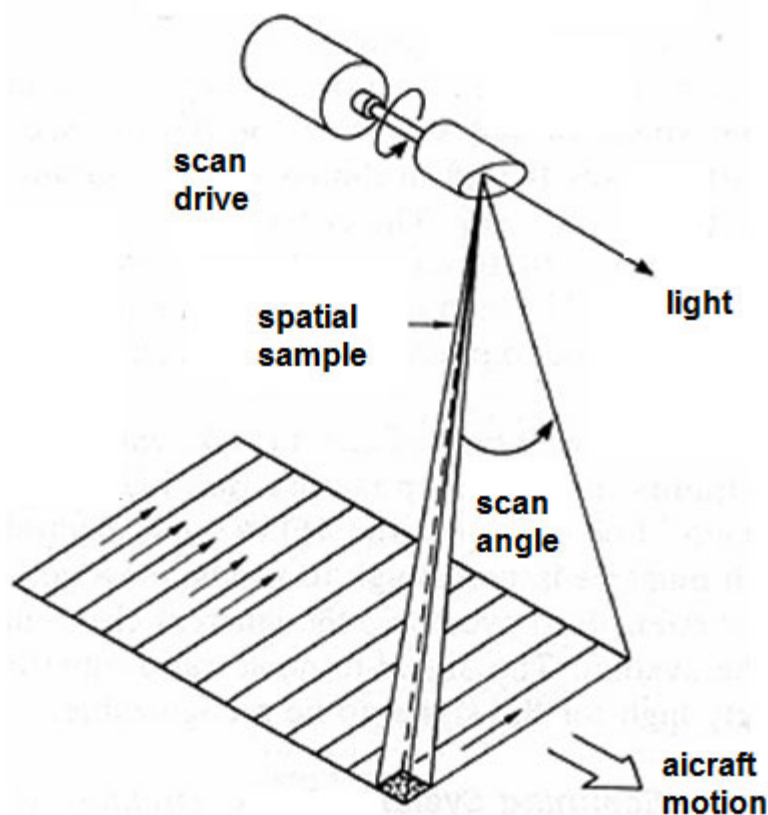

Figure 2. Nominal spatial sample acquisition for a whiskbroom scanner instrument. For AVIRIS each spatial sample records a 224-channel spectrum.

The simple cylindrical coordinate system provide by the scan mirror and scan drive is complicated when combined with the effects of aircraft motion a turbulent atmosphere. The aircraft platform for AVIRIS and any airborne instrument impart translations in the x,y,z directions and angular motions in the roll, pitch and yaw sense. Figure 3 shows the translation and rotational effects imposed upon AVIRIS from the aircraft motion.
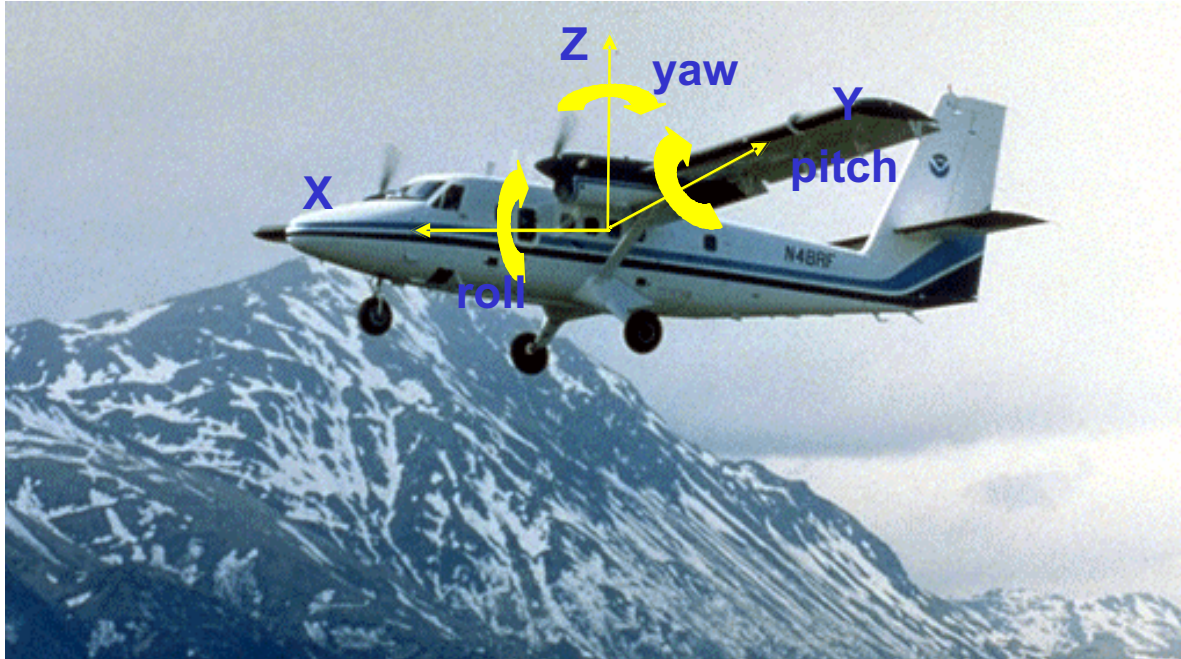
Figure 3. Image of AVIRIS in the Twin Otter aircraft platform with representation of translation and angular motion imparted to the AVIRIS measured spectral data.

The combination of the whiskbroom scan mirror approach in conjunction with an aircraft acquisition platform assures that the AVIRIS measurements are not acquired as a simple three dimensional array of x,y,l arrays. For this reason the AVIRIS instrument includes a GPS/INS (Global Positioning System/Inertial Navigation System) to record both the instrument position and pointing throughout the period of data acquisition. These position and pointing measurement allow the AVIRIS measurements to be forced into an approximation of the traditional simple three-dimensional array data storage and display structure. The measurements also allow contemplation of a new more efficient data storage structure for AVIRIS-type imaging spectrometer measurements.

3. Traditional AVIRIS Georectification and Data Distribution Format Approach

Using the knowledge of the cylindrical motion of the AVIRIS scan mirror and the knowledge of AVIRIS position and pointing from the GPS/INS, the measured location of each AVIRIS spectrum may be predicted. The projected spatial size of each area sampled (Ground-Instantaneous-Field-of-View, GIFOV) may also be calculated based on the distance between AVIRIS and the surface for each spatial sample. The GIFOV varies as a function of panoramic scan angle, terrain elevation, and aircraft motion. Figure 4 show the panoramic scan angle type growth of the GIFOV as larger scan angles. This effect is not large for AVIRIS with a scan angle of ±16.5 degrees. For AVIRIS a 4-m sample dimension at nadir is 4.17 m at the maximum scan angle.
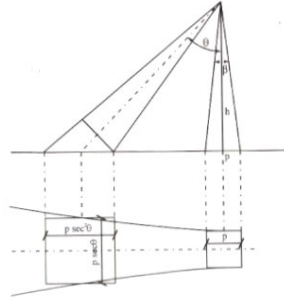
Figure 4. Panoramic growth for spatial GIFOV as a function of increasing scan angle.

Because of these motion and angular effects AVIRIS data must be geo-rectified to place them in a regular coordinate system that allows knowledge of the location of each spectrum measured. Figure 5 shows and AVIRIS image for a small town near Rogers Dry Lake, California before and after geo-rectification.
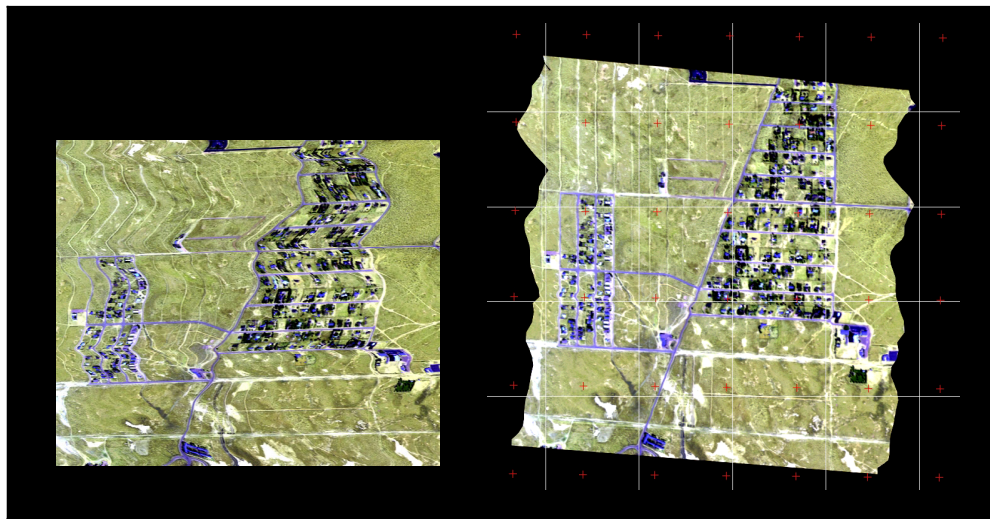

Figure 5. AVIRIS data before and after geo-rectification.

AVIRIS geo-rectification is accomplished by using the AVIRIS scan mirror knowledge in conjunction with the GPS/INS knowledge to predict the location and size or each GIFOV on the surface. In this process the UTM location of each measured spectrum is calculated and stored in the Input Geometry (IGM) file.

To generate a geo-rectified AVIRIS image a nearest neighbor sampling algorithm is used to place the nearest measured AVIRIS spectrum into the UTM coordinate system of geo-rectified product. In this process a Geometric Lookup Table (GLT) file is created. This file shows the source spectrum for each location in the geo-rectified image in terms of the line and sample location from the original measured data. If the spectrum in the geo-rectified product is directly measured the sign of the data in the GLT file is positive. If the spectrum is a nearest neighbor, then the sign is negative.

Currently AVIRIS geo-rectified data are delivered with each spectrum placed in the geo-rectified image based upon the GLT file. This has the important advantage of providing a data set that is easily compatible with the wide range of current imaging analysis systems. This choice was made to keep the barriers to analysis or imaging spectroscopy as low as possible for the widest number of people.

160

There are several notable disadvantages to this choice for distribution of AVIRIS data. In the process of nearest neighbor infilling of the geo-rectified product some spectra are replicated and some spectra are not reported. Replicated spectra occur when AVIRIS has undersampled the surface due to rapid aircraft motion. Failure to report some spectra occurs when AVIRIS has measured the same location on the surface two or more times due to turbulent motion of the aircraft. In addition, in the process of creation the georectified produce in the traditional Lx,y,l preservation of the edges of the measurements in the geo-rectified product requires insertion of many zero value spectra. The net result of the current geo-rectification process is inflation of the size of the data set. This can be a severe effect in cases where the AVIRIS aircraft motion was excessively fast and turbulent.

In addition, accurate comparison of unmixing results obtained from different spectral images is a difficult task by the inaccuracies in the position of the centers and foot-print sizes of each pair of pixels. .

In order to assure the geocorrected data are real you must test the GLT file for each pixel and in some turbulent flights several points can be selected for the same geographical position. (Fig Boardman JPLWS 2004).

These consequence of the choice to deliver AVIRIS geo-rectified data in the traditional Lx,y,l format cause us to consider alternate approaches to the representation of AVIRIS data in distribution and analysis.

4. A New Approach to AVIRIS Data Representation

In considering a new approach, we asked these questions:

1. Can the spectral measurements format and the image format impose the structure of the AVIRIS hyperspectral data?

2. Can the visualization task impose the hyperspectral data structure?

3. Can a hyperspectral image be considered like a regular sampled scene?

4. Why not use a data structure related to the sensor acquisition task?

5. Why use spatial discrete coordinates when the real scene coordinates are continuous?

6. Why use images in the preliminary computing phases if you need to lose spatial information?

5. Our Proposed Solution: Sparse Matrix

In order to preserve this acquisition scheme we propose a "data measurement register (DMR)" as the data structure. For each sensor measurement we use a register with the following fields:

1. Latitude

2. Longitude

3. Altitude

4. Roll

5. Pitch

6. Yaw or Heading

7. Time

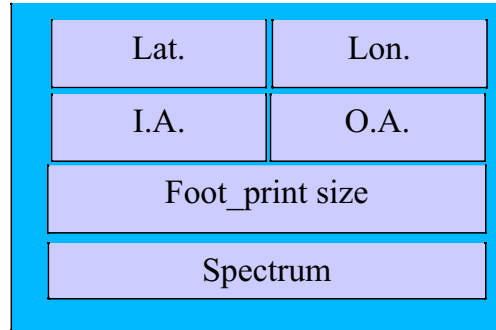8. Spectrum Lx,y compressed in an appropriate lossless manner.

Figure 6. Data measurement register.

Using this data measurement register you may store an image as a file of DMR. The main disadvantage of this kind of structure is the loss of the location principle for the spatial image information (neighbor pixels on the image can be stored separately in the file and memory).
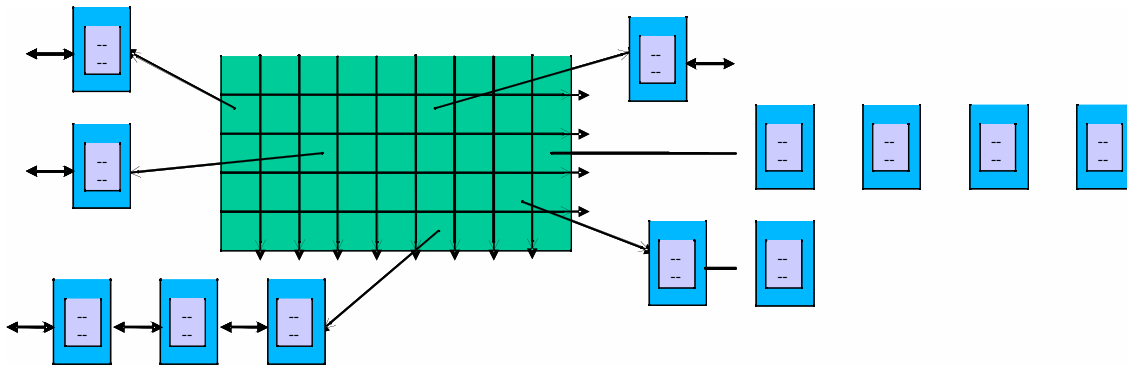

Figure 7. Sparse matrix illustration.

In order to avoid these problems we propose a new data structure for AVIRIS spectral images that we term a Sparse Matrix. In a Sparse Matrix DMR data are linked to a regular spatial grid. The size of this grid can be obtained from the spatial information itself (using the real spatial sampling information) or from the size of the map you need as the final result of your remote sensing task. In each cell of the matrix there is a pointer to a dynamic set of vector of the structure. Some of then could be null.

6. Sparse Matrix Advantages

1. A Sparse Matrix does not miss any sensor acquired information (no re-sampling is applied).

2. The data processing subject is the sensor measurement.

3. The continuous ground coordinates (Latitude – Longitude) are preserved.

4. Data (for unmixing, classification, etc.) are independent from the visualization task.

5. Only in the last steps of the data management interpolation or resampling is applied.

7. Conclusions

A new more rigorous treatment of the spatial sampling of AVIRIS image data is an important next step in imaging spectroscopy analysis as the GIFOV and sub-GIFOV scale.

Future multi-angular and unmixing research and applications will likely require comparison of two or more imaging spectrometer data sets on a spatial element by spatial element basis.

New, more appropriate data structures will enable this new advanced research.

Sparse Matrix facilitates comparison between image pixels in a quantitative way, by using accurate comparison techniques as producer and consumer accuracy (Congalton).

Sparse Matrix facilitates comparison between different sensor data, including ground truth data obtained by field spectrometers.

Sparse Matrix can help the breakup of the AVIRIS processing program into a series of simple object-oriented program modules.

Sparse Matrix will improve the parallel computation of hyperspectral datasets.

New algorithms will be designed for this kind of data.

8. Bibliography

Plaza, A., Martinez, P., Perez, R., and Plaza, J.
A quantitative and comparative analysis of endmember extraction algorithms from hyperspectral data.
IEEE Transactions on Geoscience and Remote Sensing, Vol. 42, pp. 650–663, 2004.

Plaza, A., Martinez, P., Perez, R., and Plaza, J.
Spatial/spectral endmember extraction by multidimensional morphological operations.
IEEE Transactions on Geoscience and Remote Sensing, Vol. 40, pp. 2025–2041, 2002.

Brun, A., Fisher, C., Dittman, C., and Rither, R.
Quality Assessment, Atmospheric and geometric correction of airborne hyperspectral Hymap data.
Proceedings of the EARSEL Workshop on Imaging Spectroscopy, Herrsching, 2003.

Boardman, J. W.
Precision Geocoding of low altitude AVIRIS data: lessons learned in 1998
Proceedings of the JPL Eighth AVIRIS Workshop, JPL Publication 99-17, Jet Propulsion Laboratory, Pasadena, California, 1999.

9. Acknowledgment

AVIRIS ARTIFACTS APPEARING IN LOW-LIGHT IMAGERY

Marcos J. Montes[1]

1. Introduction

AVIRIS is an excellent instrument for hyperspectral remote sensing. Its high levels of spectral resolution and energy resolution allow the detection of otherwise undetectable natural features. The high quality of the data also allows us to find artifacts in the image due to imperfections in the optics or the electronics. Researchers who work in low light (perhaps a better phrase is "low surface reflectance") environments have an opportunity to find these artifacts because the process of atmospheric correction removes most – or all – of the signal. This document lists artifacts that I have noticed when processing AVIRIS data, measured mostly over the oceans or coastal areas. When possible, I list the years the artifacts are present, and their causes. Some of the items listed below are available in previously published proceedings and they are included here because of their effects on low-light imagery.

This paper should not be interpreted in any way as saying that researchers should not use AVIRIS data. Indeed, AVIRIS is the best hyperspectral sensor for many applications. Depending on what kind of data you have, and what you do with the data, these artifacts may indeed have absolutely no effect; on the other hand, they may have a large effect on other data sets or with certain processing methods.

AVIRIS spectral and radiance calibration data is presented by the AVIRIS team both at the AVIRIS meetings, and in the various proceedings of those meetings. Note that most of the field calibration events use high-reflectance targets: several playas in California and Argentina were used for this purpose. The series of papers documenting in-flight calibration experiments includes (but is not limited to) Green and Pavri (2003, 2002, 2001, 2000), Green et al. (1999, 1998a, 1996, 1995, 1993, 1992, 1990) and Conel (1988).

Other sensors also have known artifacts, and many of these artifacts are easily visible in their published imagery. Some artifacts are corrected in post-processing, and may not appear in published imagery. Typical artifacts present in imagery from the Portable Hyperspectral Imager for Low-Light Spectroscopy (PHILLS) sensor (and how they are dealt with) are presented in Leathers et al. (2002) and Snyder et al. (2004). Many of the artifacts affecting Hyperion data are presented in several papers in the TGARS *Special Issue on the Earth Observing (EO-1) Mission* (TGARS 2003; Pearlman et al. 2003; Bindschadler et al. 2003; Green et al. 2003; Goetz et al. 2003; Datt et al. 2003; Goodenough et al. 2003). In many ways, most of the AVIRIS artifacts listed below are subtle and not obvious to the eye.

In the following sections, I will frequently mention the effect of the artifacts on atmospheric correction as applied to water (oceanic) scenes. This specifically refers to atmospheric correction methods over the ocean by assuming that there is no (or extremely little) water leaving radiance in the near infrared (NIR) and/or short-wave infrared (SWIR) due to the extremely high absorption of light by water in that spectral range. The assumption is typical for atmospheric correction algorithms used with data obtained from many multi-spectral and hyperspectral sensors; see, for example Gao et al. (2000). The large contrast between the water and the land in the NIR and SWIR bands makes it easier to see the effects of many of these artifacts. Because of this, examples of typical coastal areas are presented for many of these artifacts showing the effects to data in the NIR/SWIR bands in scenes with both water and land in the imaged area.

Finally, all of the examples below are either from calibrated data (L_{obs}) or from apparent reflectance [$\rho^{*}_{obs}=\pi L_{obs}/(\mu_0 E_0)$, where ρ^{*}_{obs} is the apparent reflectance, L_{obs} is the observed radiance, and $\mu_0 E_0$ is the product of the cosine of the solar zenith angle and the solar irradiance at the top of the atmosphere] data prior to the 2004 flight season. None of the data used in the examples in the following sections has been atmospherically corrected.

---

[1] Naval Research Laboratory, Code 7232, Washington, DC 20375; Marcos.Montes@NRL.Navy.mil

2. Central blue stripe—scattered light artifact in the center of the swatch

This artifact is present in the AVIRIS ER-2 data. This manifests itself as a faint stripe running down the middle of the image, as shown in Figure 1. It is visibly present in approximately bands 7–28, and is roughly confined to cross-track samples 302–309 (for image cubes with 614 cross-track samples). It is visible in some of the online quick-look imagery, especially over the ocean. Since the ER-2 has a closed cabin, AVIRIS must observe through the ER-2 hatch window. Observation through this window causes the stripe, which is not present in the Twin-Otter data (R. O. Green, 2002; private communication). This feature is present in data since at least 1995, and is in current data. The fractional brightening in these bands is small, and the feature is obvious principally because of its spatial characteristics. The brightening due to the changing geometry of the swells in Fig. 1 is usually much larger, but with much different spectral and spatial characteristics. As the blue stripe appears only in the blue-green bands, it does not cause errors in determining the atmospheric correction parameters. Because atmospheric correction subtracts a large portion of the uniform blue signal across the image, this feature tends to appear with greater contrast after atmospheric correction.

3. Slew

The slew effect is mentioned in the *.readme files that come with the AVIRIS data set. Slew is described as a slight shift in the IFOV when moving from regions of very different brightness. When the detectors move from a bright to a dark area, the next few pixels brighten measurably, as shown in Figs. 2 and 3. The number of pixels affected by slew appears to be a function of the spectrometer, and perhaps band number, as seen in Fig. 3. A typical non-georectified AVIRIS scan line has already been reversed about the center (i.e., swapping pixels 1 and 614, 2 and 613, etc.) before being sent to the user: in the data space, the scanner goes from the right side of the image to the left side[2], but facing forward in the plane, the scanner images from the left to the right. The effect is most noticeable when scanning from bright coasts to darker water, as shown in Fig. 2. Slew, in other words, presents a method of determining the scan direction in some scenes.

The top image in Figure 2 is portion of the data set f010731t01p03_r02, and the bottom is portion of the data set f010731t01p03_r03. These runs were flown in opposite directions [see Table 1 in Montes et al. (2003) for the flight directions], and in these non-georectified images, the right half of f010731t01p03_r02 overlaps with the right half of f010731t01p03_r03 (note, however, that the images in Fig. 2 are sub-images, showing only the rightmost ~350 pixels, i.e., the overlapping area, of each set). The left side of the coasts in each image shows a brightening. The common features in the right side of each image show a brightening that is always to the left of the land, which is geographically the opposite shore in each image. The effects of slew are evident when ratioing (top image in Fig. 3) or differenceing data from adjacent bands that have different slew characteristics, and in cross-track profiles when going from bright to dark areas (bottom plot in Fig. 3).

The effect on atmospheric correction algorithms includes incorrect selections for aerosol model and/or aerosol optical depth for pixels that are a few pixels down scan from the land, which would lead to incorrect water leaving radiances throughout the visible, and therefore incorrect derived products. However, if the pixels affected by slew are not used to derive aerosol parameters, then there is probably little effect on reflectance or products since this effect is again most noticeable in regions of high contrast: going from land that is bright in the NIR/SWIR to water that is dark in the NIR/SWIR. This effect is different from the atmospheric adjacency effect (see, for example, Reinersman and Carder 1995), which also may need to be correctly dealt with in any atmospheric correction scheme. Slew is more limited in spatial scale than the adjacency effect; care should be taken when removing adjacency effect, especially if slew is ignored.
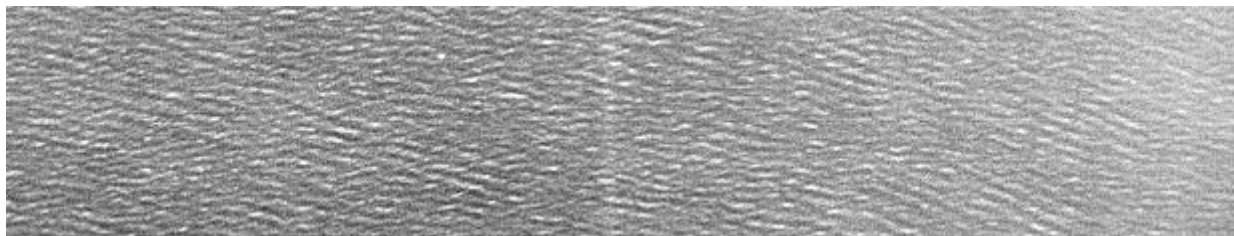

Figure 1. A central blue stripe. This grayscale image is from a section of band 15 of f010731t01p03_r04.

---

[2] See the "Data Facility" portion of the AVIRIS web page.

Figure 2. Examples of slew. Both the top and the bottom images are the rightmost ~350 samples of non-georectified 1.24 μm band apparent reflectance images processed from AVIRIS collected on 2001 July 31. In these images, a simple land mask (black areas) has been applied for all pixels with NDVI>0.0. The flight direction in each image is from the top of the page to the bottom, and the scan direction is from the right to the left. The flight lines were flown in opposite directions, and portions of the images presented here clearly overlap. One consequence of slew is the brightening of darker pixels in the scan direction when going from a bright (the masked land) to a dark area (the water, here grey). Five landmarks present in each image are labeled A, B, C, D, and E. It is clear that the observed brightening is in the scan direction and *not* an inherent feature of observed land and water.
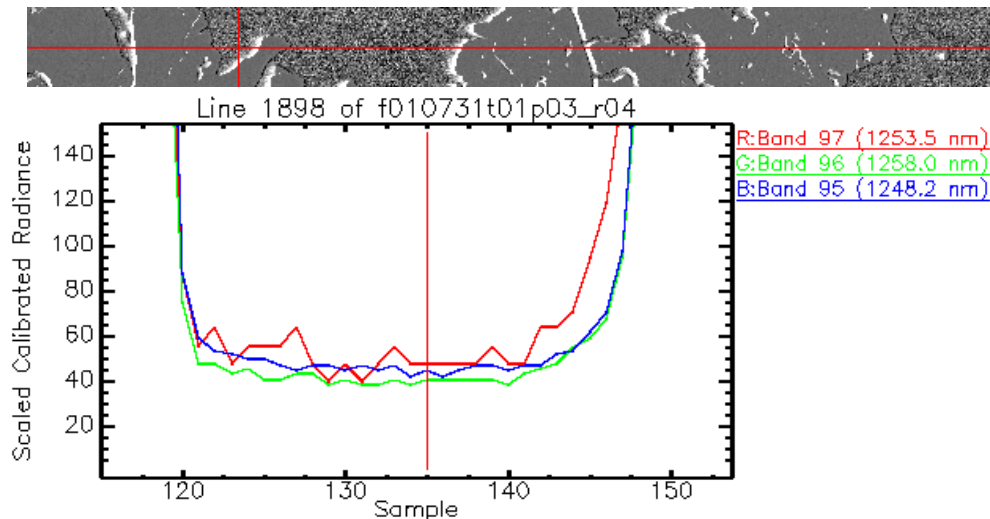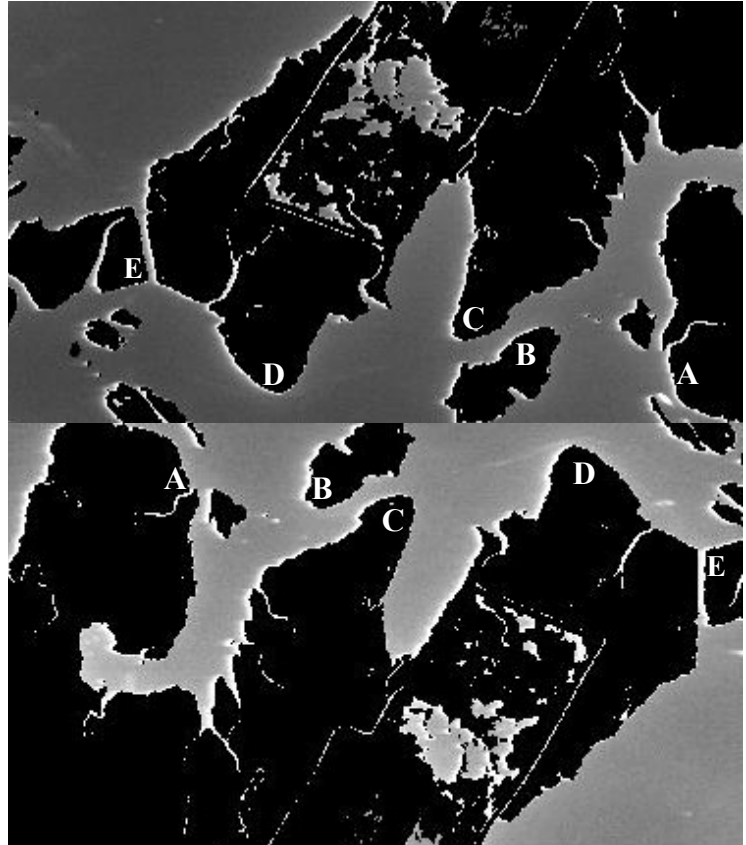

Figure 3. At the top is a gray-scale image of the ratio of band 97 divided by band 96 from a part of the calibrated radiance data from the AVIRIS set f010731t01p03_r04. The ratio increases to > 1.5 (white) going from land (flat grey, μ=1.20, σ=0.07) to water (speckled grey, μ=1.15, σ=0.17). The bottom figure is an x-profile of *radiance* from a portion of the horizontal red line in the upper image. The vertical red line in the lower plot is at the same location as the vertical red line in the upper image. Band 97 takes a longer time to transition from the brighter values on the land to the lower values in the water than either band 95 or 96. All rise at more similar rates when scanning from the darker water to the brighter land. Note that band 97 is on the C spectrometer, while bands 95 and 96 are on the B spectrometer, and that $\lambda_{95} < \lambda_{97} < \lambda_{96}$. The scan direction is from right to left.
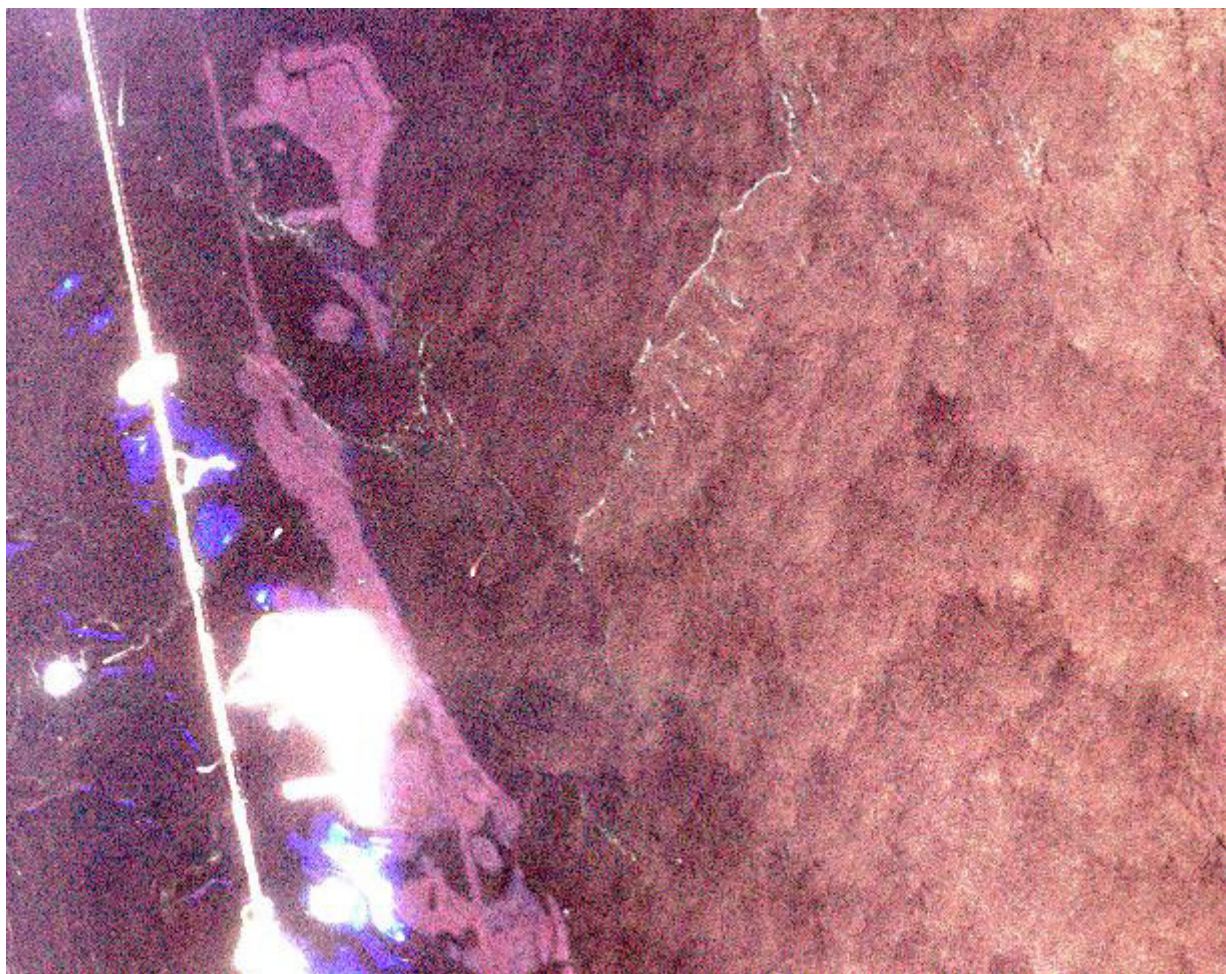
Figure 4. An example of ghosting. This is a portion of f960323t01p02_r10a from the Florida Keys. The flight direction was from the top of this image to the bottom. This 3-color image is from bands 93, 72, and 54, regions of the spectrum where there is strong water absorption. The blue areas are very shallow areas where there is still noticeable signal from the bottom at 867 nm (band 54). The ghosts are obvious, and only appears in 1996 data.

4. Ghost images in 1996 flight year data

The 1996 AVIRIS data has "ghost images" that are most noticeable in areas with both dark backgrounds and bright objects in the field of view, as shown in Fig. 4. This is most easily seen in the NIR/SWIR near water, although it should be present at all wavelengths. In the combination of NIR/SWIR bands used in Fig. 4, the land is saturated and appears white. The ghosts have the same shape and are much dimmer than their source on the land, but clearly of similar magnitude to the signal over the water. The ghosts were due to a window that was used to keep the foreoptics clean. The window, however, introduced some extra reflections and caused the ghosts. This was reported at the 1997 workshop, and was mitigated in 1997, at which time the window was replaced with a door. This door is open only when data is collected. No written record of this ghost exists in the 1998 proceedings (R. O. Green, 2002, private communication). In the NIR, the ghost is usually noticeably brighter than the surrounding water. Using pixels with the ghost images to determine aerosol model and optical depth by assuming the signal is due to only atmosphere and specular reflection causes the wrong aerosol optical depth and/or aerosol model to be selected. Approximately 0.5% of the radiance of the source of the ghost will appear at the location of the ghost. The ghost image appears ~290 pixels (along track) before the actual feature is seen in the data. The number of pixels varies somewhat since ~290 lines are covered in about 24 seconds of time, and the ER-2's orientation may change a fair bit in ~24 seconds. Changes in pitch will affect the displacement in the along-track direction, changes in roll will affect the displacement in the cross-track direction, and changes in heading will affect both; velocity and acceleration variations will also affect the position of the ghost relative to the source. BRDF effects may also play a role in the brightness of the ghost since the source of the ghost is ~13° in front of the image.

5. Band 77

This very noisy band is mentioned in the *.readme files beginning in 2000. This is more problematic over dark images [such as water which absorbs quite strongly at this wavelength (~1.06 µm) and therefore has low signal] than over bright ones. This band needs to be avoided when performing atmospheric correction; unfortunately, this band is in a portion of the spectrum that is relatively free from atmospheric absorption, so it may be used by various atmospheric correction algorithms. Because of this, it is best to delete this band or otherwise to ensure that algorithms do not use this band. Some spectral effects are present in Figs. 1 and 2 of Green et al. (2001). Noise characteristics of this band are easily seen when calculating statistics for a "region of interest" in dark regions of the image.

6. Band 30

Green and Pavri (2001) mentioned the fact that band 30 was excessively noisy in 2000 flight year data. For relatively dark data from an AVIRIS flight in 2001 over a uniform area of Great Bay, New Jersey, the standard deviation in band 30 is about twice that of neighboring bands, and the noise has a visible spatial structure in band 30 images. This band is at about 655 nm, so it is near a rather useful region of the spectrum for ocean studies. It is well worth the time to display this band separately before deciding whether to use data from this band in other data products. The noise is of less consequence for images that are bright in this spectral region.

7. A/B spectrometer overlap region

The A & B spectrometers overlap over a fairly wide spectral range. For the 2001 data, the last three bands of the A spectrometer are very close in wavelength to the first three bands of the B spectrometer. The overlap provides a region to check the cross-calibration between the spectrometers. In order to analyze this effect for a coastal image, scatter plots were generated from the calibrated, non-geocorrected AVIRIS data file f010731t01p03r04_sc04.v1-.img. These scatter plots may be found in Fig. 6. For the oceanic pixels, band 34 is ~ 4.5% brighter than band 31 and band 35 is ~ 7% brighter than band 32. Using the AVIRIS spectral calibration, the wavelength difference is $\lambda_{34} - \lambda_{31}$ = –0.17 nm with very similar FWHM; $\lambda_{35} - \lambda_{32}$ = –2.1 nm, but $FWHM_{32}/FWHM_{35}$ = 0.75. Band 30 is a bit more problematic to analyze because of the obvious spatially structured noise (see §6, above). For ocean and bay pixels, the tendency is for band 30 to be about 6% brighter than band 33, but this is not the case for the brighter land pixels (the bright orange blob in the top plot of Fig. 6). When subtracting ~50% of the signal for atmospheric correction (which is a conservative estimate over water at these wavelengths), the differences become 10% or more. Because of this, it becomes necessary to remove some of the bands in the overlap region so spectra look reasonable. The choice of which bands to keep depends on knowing which bands are better behaved in the sensor, and may also be aided by the availability of field measurements. The characteristics of this overlap region will change, as the AVIRIS instrument is serviced and modified yearly.

8. Adjustment of the spectral calibration

The AVIRIS spectral calibration is determined in the laboratory, under laboratory conditions. As with the radiance calibrations, the best spectral calibration is one that is determined with the sensor in its operating environment. Most spectrometers will require some sort of correction to their laboratory spectral calibration: this effect also occurs in Hyperspectral Digital Imagery Collection Experiment (HYDICE), PHILLS, and HYPERION data. I refer the reader to Gao et al. (2004) and the references therein for a detailed discussion. A summary of the discussion involving AVIRIS is that the correction needed for the spectral calibration changes from year to year: this is not surprising since a lot of work is performed on the AVIRIS instrument between flight seasons. However, the offsets do not appear to change much within a single flight season.

9. Cross-track hatch AR-coating transmittance variation

While attempting to analyze cross-track spectral calibration effects such as smile (e.g., Gao et al. 2002; Gao et al. 2004), we came across a previously unreported AVIRIS artifact. This artifact is probably due to an anti-reflection coating on the ER-2 hatch window (R. O. Green, 2002, private communication). The magnitude appears to be both a function of wavelength as well as cross-track sample number. This effect has been observed in data from 1995, and 2000-2002; it probably exists in all data from the ER-2, but we have not had a chance to examine data from each year. To observe this effect, average a whole non-georectified AVIRIS calibrated radiance cube [224 bands x 614 samples x 512 (or more) lines] down to a single line (224 bands x 614 samples x 1 line). Divide this by the average spectrum of a sample near the central line, avoiding any samples affected by the "blue-stripe" of §2. What is left is the ratio of observed spectra. The solar spectrum and the detector response have been divided out. The remaining quantity is the ratio of the atmospheric and surface reflectance folded together with any cross-track response of the
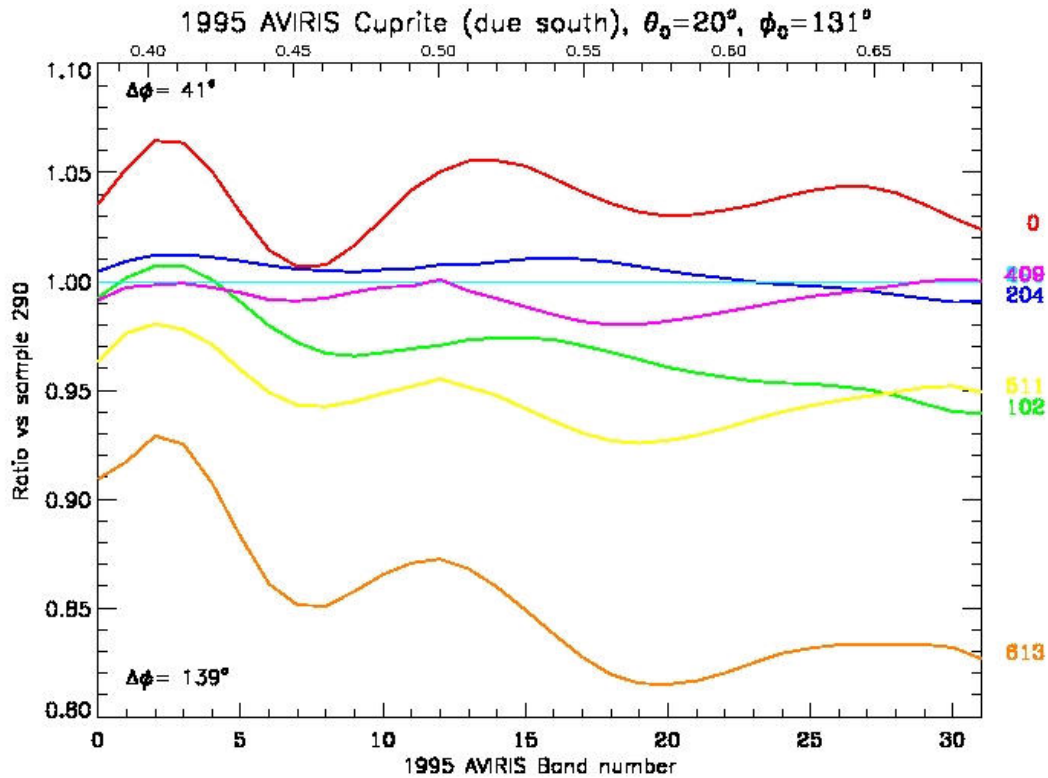
Figure 5, showing an example of the cross-track hatch AR-coating transmittance variation, as derived from a 1995 Cuprite data set. The bottom x-axis is band number, and the top x-axis is the approximate wavelength. The colored curves are associated with the colored labels to the right. The labels are the cross-track sample number, with numbering beginning at 0 as the leftmost pixel in a standard AVIRIS calibrated radiance data set.

complete windows-optics-sensor system. The results, shown in Fig. 5, are a sinusoidal modulation of the first several bands of the A-spectrometer, with a peak-to-peak magnitude of perhaps 5% at the samples furthest from the center. The features are not present in data from the B-spectrometer. These features have been observed over both land and water, in data from many flight seasons.

The effects for atmospheric correction are uncertain, as yet. These bands are not used to determine atmospheric correction parameters over water, and so the effect should be most apparent in products derived from bands in the A spectrometer. This wavelength and sample dependent artifact is a systematic error that can probably be corrected in post-processing. AVIRIS calibration data from a reasonably uniform area (such as the Ivanpah Playa) that spans the field of view will be useful in fully characterizing this effect, as would other methods of removing the variable trends (in which we are not interested) that occur in Fig. 5, leaving only the sinusoidal effect.

10. Algorithmic challenges for low-light imagery

Images of dark areas present challenges other than instrument artifacts. For **any** instrument, atmospheric correction will be difficult if the mean (μ) in a particular band in a typical region of interest is less than about 3 times the standard deviation (σ). Spectral regions where this typically occurs are associated with strong atmospheric absorption bands and/or low instrument sensitivity. Over dark water targets in the NIR and SWIR the spectral width of the atmospheric absorption features where $\mu < 3\sigma$ increases quite a bit compared with much brighter targets over the land. Spectral regions with this property will not be corrected accurately, and deleting these spectral bands (or some other reasonable treatment) is justified for many low-light imagery scenes.

There are natural features in the data that present continuing challenges for atmospheric correction. Waves and swells are present in much open-ocean data, and are easily resolved at the 20 meter spatial scale of AVIRIS. The atmospheric adjacency effect (i.e., light reflected from the surface from outside the pixel then scattered in the atmosphere into the field of view of the pixel) and the topographic adjacency effect (i.e., the sky does not illuminate

a full 2π steradians of the field of view, and instead some of the light illuminating the pixel in question is directly reflected from trees, mountains, cliffs, buildings, etc.) present features that may be of similar in magnitude to the artifacts presented here. These effects are not due to the sensor. However, in order to correct for these effects in low-light environments, we also need to be able to correct for any instrumental effects in the data that are of similar magnitude.

11. Closing comments

The artifacts presented here are for AVIRIS data prior to the 2004 flight season. It may very well be the case that other artifacts exist, but are not covered here. Those presented here are merely the ones that were noticed in the analysis of AVIRIS data from coastal environments. Some of the artifacts mentioned here have been fixed (the "ghosts of 1996," presented in §4), or are being analyzed and fixed, either in hardware (so as not to affect future data) or in software (and the fixes may then be applicable to archival AVIRIS data). The most serious artifacts in terms of magnitude and pervasiveness in the data are those in §9 (cross-track hatch AR-coating transmittance variation), and, arguably, §3 (slew). Most of the others can be reasonably easily handled by the user by examining and either editing or excising the data (§5, §6, and §7). The spectral calibration (§8) is rectified by adjusting the central wavelength of the spectral bands so that solar and terrestrial absorption features present in the data match those in spectral line databases. As the engineers and scientists associated with the AVIRIS project continue to improve the instrument, one can expect a continuing characterization of the instrument and the mitigation of these and other artifacts.

Acknowledgment

References

Bindschadler, R., and H. Choi, "Characterizing and Correcting Hyperion Detectors Using Ice-Sheet Images," *IEEE Trans. On Geosci. Rem. Sens.*, 41(6), 1189–1194, 2003.

Conel, J. E., R. O. Green, R. E. Alley, C. J. Bruegge, V. Carrere, J. S. Margolis, G. Vane, T. G. Chrien, P. N. Slater, S. F. Biggar, P. M. Teillet, R. D. Jackson, and M. S. Moran, "In-Flight Radiometric Calibration of the Airborne Visible/Infrared Imaging Spectrometer (AVIRIS)," *SPIE,* Vol. 924, *Recent advances in sensors, radiometry and data processing for remote sensing*, 1988.

Datt, B., T. R. McVicar, T. G. Van Niel, D. L. B. Jupp, and J. S. Pearlman, "Preprocessing EO-1 Hyperion Hyperspectral Data to Support the Application of Agricultural Indices," *IEEE Trans. On Geosci. Rem. Sens.*, 41(6), 1246–1259, 2003.

Gao, B.-C., M. J. Montes, Z. Ahmad, and C. O. Davis, "Atmospheric correction algorithm for hyperspectral remote sensing of ocean color from space," *Applied Optics*, 39(6), 887–896, 2000.

Gao, B.-C., M. J. Montes, and C. O. Davis, "A Curve Fitting Technique to Improve Wavelength Calibrations of Imaging Spectrometer Data," in *Proceedings of the 11th JPL Airborne Earth Science Workshop*, JPL Pub. 03-4, Jet Propulsion Laboratory, Pasadena, California, pp. 99–105, 2002.

Gao, B.-C., M. J. Montes, and C. O. Davis, "Refinement of Wavelength Calibrations of Hyperspectral Imaging Data using a Spectrum-Matching Technique," *Remote Sens. of Env.*, 90(4), pp. 424–433, 2004.

Goetz, A. F. H., B. C. Kindel, M. Ferri, and Z. Qu, "HATCH: Results From Simulated Radiances, AVIRIS and Hyperion," *IEEE Trans. on Geosci. Rem. Sens.*, 41(6), 1215–122, 2003.

Goodenough, D. G., A. Dyk, K. O. Niemann, J. S. Pealman, H. Chen, T. Han, M. Murdoch, and C. West, "Preprocessing Hyperion and ALI for Forest Classification," *IEEE Trans. on Geosci. Rem. Sens.*, 41(6), 1321–1331, 2003.

Green, R. O., J. E. Conel, V. Carrere, C. J. Bruegge, J. S. Margolis, M. Rast, and G. Hoover, "In-flight Validation and Calibration of the Spectral and Radiometric Characteristics of the Airborne Visible/Infrared Imaging Spectrometer (AVIRIS)," *Proc. SPIE Conference on Aerospace Sensing, Imaging Spectroscopy of the Terrestrial Environment*, Orlando, Florida, April 16–20, 1990.

Green, R. O., J. E. Conel, C. J. Bruegge, J. S. Margolis, V. Carrere, G. Vane, and G. Hoover, "In-flight Calibration of the Spectral and Radiometric Characteristics of AVIRIS in 1991," *Summaries of the Third Annual JPL Airborne Geoscience Workshop*, JPL Publication 92-14, Vol. 1, pp. 1–4, Jet Propulsion Laboratory, Pasadena, California, 1992.

Green, R. O., J. E. Conel, M. Helminger, J. van den Bosch, C. Chovit, and T. Chrien, "Inflight Calibration of AVIRIS in 1992 and 1993," *Summaries of the Fourth Annual JPL Airborne Geoscience Workshop*, JPL Publication 93-26, Vol. 1, Jet Propulsion Laboratory, Pasadena, California, October 25, 1993.

Green, R. O., J. E. Conel, M. Helmlinger, J. van den Bosch, and P. Hajek, "In-Flight Radiometric Calibration of AVIRIS in 1994," *Proc. of the Fifth Annual JPL Airborne Earth Science Workshop*, JPL Publication 95-1, Jet Propulsion Laboratory, Pasadena, California, January 23–26, 1995.

Green, R. O., Conel, J. E., Margolis, C. Chovit, and J. Faust, "In-Flight Calibration and Validation of the Airborne Visible/Infrared Imaging Spectrometer (AVIRIS)," *Proc. Sixth Annual Airborne Earth Science Workshop*, JPL Pub. 96-4, Vol. 1, Jet Propulsion Laboratory, Pasadena, California, March 3–5, 1996.

Green R. O., B. Pavri, J. Faust, O. Williams, and C. Chovit, "Inflight Validation of AVIRIS Calibration in 1996 and 1997," *Proc. Seventh Airborne Earth Science Workshop*, JPL Pub. 97-21, Vol. 1, pp. 193–205, Jet Propulsion Laboratory, Pasadena, California, 1998a.

Green, R. O., M. L. Eastwood, and C. M. Sarture, "Imaging Spectroscopy and the Airborne Visible Infrared Imaging Spectrometer (AVIRIS)," *Remote Sens Environ* 65: (3) 227–248 SEP 1998b.

Green, R. O., B. Pavri, J. Faust, C. Chovit, and O. Williams, "AVIRIS In-Fight Radiometric Calibration Results for 1998," *Proc. Eighth Airborne Earth Science Workshop*, JPL Publication 99-17, Vol. 1, pp. 161–175, Jet Propulsion Laboratory, Pasadena, California, 1999.

Green, R. O., and B. Pavri, "AVIRIS Inflight Calibration Experiment, Measurements, Analyses and Results, Sensitivity Analysis and Intraflight Stablity," *Proc. Ninth Airborne Earth Science Workshop*, JPL Publication 00-18, pp. 207–222, Jet Propulsion Laboratory, Pasadena, California, 2000.

Green, R. O., T. Chrien, and C. Sarture, "Exploring a Black Body Source as an Absolute Radiometric Calibratoin Standard and Comparison with a NIST Traced Lamp Standard," in *Proceedings of the Tenth JPL Airborne Earth Science Workshop*, JPL Pub. 02-1, Jet Propulsion Laboratory, Pasadena, California, pp. 193–203, 2001.

Green, R. O., and B. Pavri, "AVIRIS Inflight Calibration Experiment Measurements, Analyses, and Results in 2000," in *Proceedings of the Tenth JPL Airborne Earth Science Workshop*, JPL Pub. 02-1, Jet Propulsion Laboratory, Pasadena, California, pp. 205–218, 2001.

Green, R. O., and B. Pavri, "AVIRIS Inflight Calibration Experiment Results for 2001," in *Proceedings of the 11th JPL Airborne Earth Science Workshop*, JPL Pub. 03-4, Jet Propulsion Laboratory, Pasadena, California, pp. 125–137, 2002.

Green, R. O., and B. Pavri, "Inflight Calibration Experiment Results for AVIRIS on May 6, 2002 at Rogers Dry Lake, California," *Proceedings of the 12th Airborne Earth Science Workshop,* JPL Pub. 04-6, Jet Propulsion Laboratory, Pasadena, California, pp. 109–120, 2003.

Green, R. O., B. E. Pavri, and T. G. Chrien, "On-Orbit Radiometric and Spectral Calibration Characteristics of EO-1 Hyperion Derived with an Underflight of AVIRIS and *In Situ* Measurements at Salar de Arizaro, Argentina," *IEEE Trans. On Geosci. Rem. Sens.*, 41(6), 1194–1203, 2003.

Leathers, R. A., T. V. Downes, W. A. Snyder, J. H. Bowles, C. O. Davis, M. E. Kappus, W. Chen, D. Korwan, M. J. Montes, W. J. Rhea, and M. E. Carney, "Ocean PHILLS Data Collection and Processing: May 2000 Deployment, Lee Stocking Island, Bahamas," NRL/FR/7212—02-10,010, 2002.

Montes, M. J., B.-C. Gao, C. O. Davis, and M. Moline, "Analysis of AVIRIS Data from Leo-15 Using Tafkaa Atmospheric Correction," *Proceedings of the 12th Airborne Earth Science Workshop,* JPL Pub. 04-6, Jet Propulsion Laboratory, Pasadena, California, pp. 212–218, 2003.

Pearlman, J. S., P. S. Barry, C. C. Segal, J. Shepanski, D. Beiso, and S. L. Carman, "Hyperion, a Space-Based Imaging Spectrometer," *IEEE Trans. on Geosci. Rem. Sens.*, 41(6), 1160–1173, 2003.

Reinersman, P. N., and K. L. Carder, "Monte Carlo simulation of the atmospheric point-spread function with an application to correction for the adjacency effect," *Appl. Opt.*, 34, 4453–4471, 1995.

Snyder, W. A., C. O. Davis, J. H. Bowles, B.-C. Gao, D. Gillis, D. Korwan, G. Lamela, M. Montes, and W. J. Rhea, "PHILLS-1 Hyperspectral Data Processing: 2001 LEO-15 Deployment," NRL/FR/7230—04-10,060, 2004.

(TGARS) *Special Issue on the Earth Observing (EO-1) Mission, IEEE Trans. on Geosci. Rem. Sens.,* 41(6), pp. 1147–1414, June 2003.
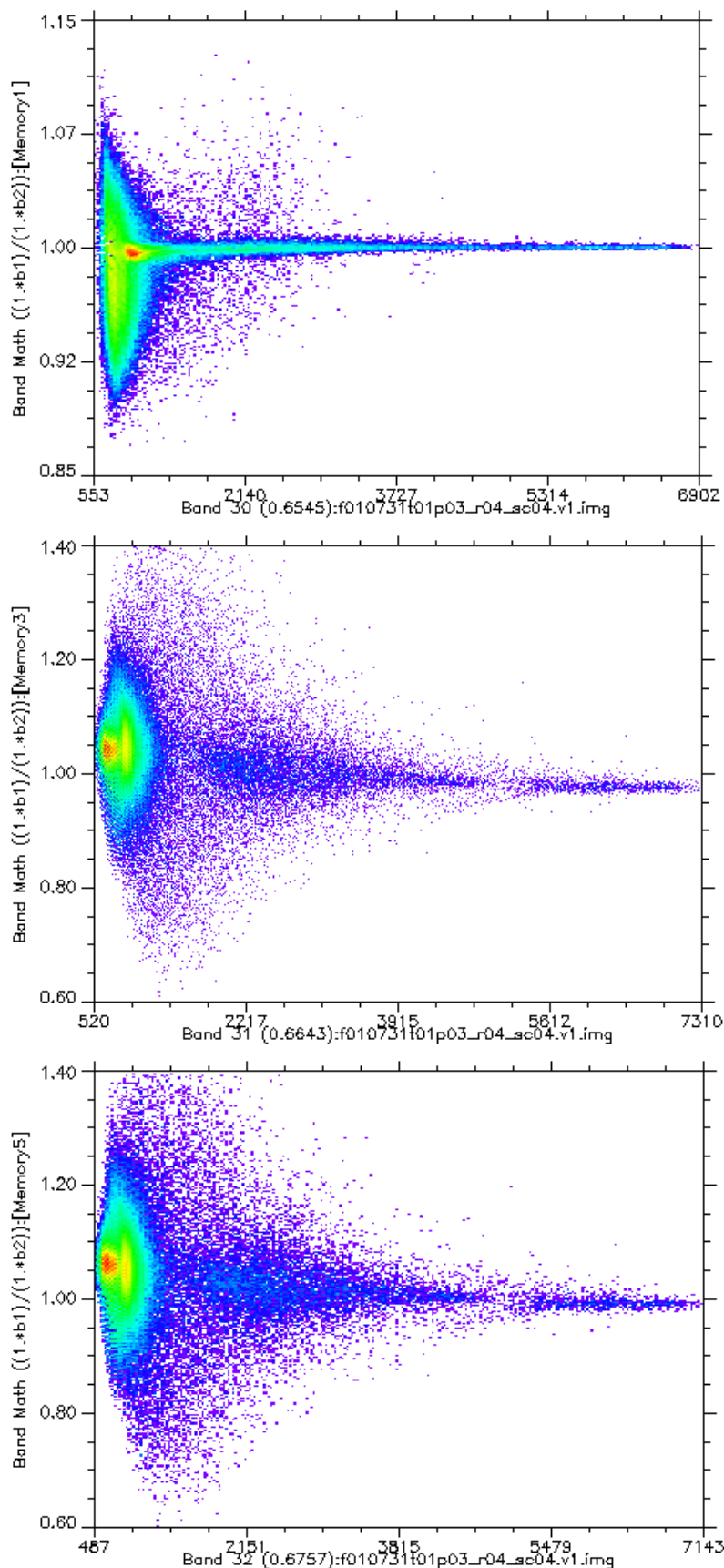
Figure 6. Scatter plots of near-overlapping bands from the A/B spectrometer region. Please note that the abcissa and ordinate have different scales on each of the three plots. The quantities plotted are: the ratio of band 33 to band 30 vs. band 30 (*top*); the ratio of band 34 to band 31 vs. band 31 (*middle*); and the ratio of band 35 to band 32 vs. band 32 (*bottom*). Colors indicate the density of points in each region, with red being the highest density and purple being the lowest density.

Pixels from the ocean and bay are in the leftmost yellow strip in the top, and in the bright red/orange blobs on the left in the middle and bottom scatter plots. In fact, the red/orange indicates that a very large majority of the pixels are in those neighborhoods.

Pixels from land areas make up the orange blob (top) and the yellow blobs (bottom and middle) somewhat to the right (i.e., higher values of the abcissa) of the pixels from the ocean or bay.

173

HYPERSPECTRAL REMOTE SENSING OF OCEAN COLOR:
A COMPARISON OF HYPERION WITH AVIRIS

Marcos J. Montes,[*] Bo-Cai Gao,[†] and Curtiss O. Davis[§]

1. Introduction

Remote sensing has the promise to be a useful tool for observing the processes that occur on many spatial and temporal scales in the coastal ocean. The fairly high spatial resolution (~2–30 m) of the current generation of hyperspectral imagers allows for much detailed study of these areas than can be performed with moderate-resolution multi-spectral sensors such as Sea-viewing Wide Field-of-View Sensor (SeaWiFS) and Moderate-Resolution Imaging Spectrometer (MODIS). The Hyperion sensor aboard the Earth Observing 1 Satellite (EO-1) serves as a testbed for hyperspectral imagers in space. We acquired Hyperion imagery of the region around the Looe Key on October 26, 2002. A portion of the Hyperion scene was also observed in 1996 with the Airborne Visible Infrared Imaging Spectrometer (AVIRIS). We address issues of atmospheric correction and calibration and compare R_{rs} values for the intersecting portions of the AVIRIS and the Hyperion imagery.

2. Atmospheric Correction

Over the past two decades, atmospheric correction algorithms for application to case 1 waters (i.e., clear, deep ocean waters) have been developed by Howard Gordon's research group at the University of Miami. The complexity of these algorithms has increased greatly with time; from the early single scattering algorithm used for Coastal Zone Color Scanner—CZCS (Gordon, 1978) to the present, more complete multiple scattering algorithm for SeaWiFS (Gordon and Wang, 1994). For the operational SeaWiFS algorithm, a simplified two-layer atmosphere system, i.e., aerosols being confined in the bottom boundary layer and atmospheric gaseous molecules being located in another layer above the aerosol layer, is assumed. An aerosol model and an aerosol optical depth are derived from channels located centered at 0.76 and 0.87 μm by assuming water-leaving radiances to be zero in that spectral range. A sophisticated lookup table procedure is used for the aerosol retrievals. The atmospheric path radiances in the visible are predicted based on the derived aerosol information. The difference between the measured radiances above the atmosphere-ocean system and the predicted path-radiance is the water-leaving radiance transmitted to the top of the atmosphere.

However, this approach does not work for some ocean environments, such as the shallow ocean environment in this study. Over a bright sand bottom, a turbid coastal environment, or a coccolithophore bloom the water-leaving radiances in the 0.66–0.87 μm range are typically not close to zero. In the former case, reflectance by bright ocean bottoms in optically shallow water causes much more water leaving radiance at these wavelengths than is measured in open oceans with similar water types. In the latter cases, this is due to scattering by suspended materials. Under these conditions, the channels in this spectral region have very limited use for the retrieval of information on atmospheric aerosols. The algorithms of Gordon (1997) and Fraser et al. (1997) derive aerosol information from channels in the 0.66–0.87 μm spectral range. These algorithms cannot be easily adapted for the retrieval of water-leaving radiances over coastal waters. In view of this situation, we have designed a different retrieving algorithm that can use channels in longer wavelengths, in addition to these channels, to derive aerosol information.

Since the liquid water absorption increases rapidly as a function of wavelength, one can assume that the water leaving radiance is zero at long enough wavelengths, even in turbid waters or over bright, shallow bottoms. In this case, one can use two or more of the atmospheric transmission window regions near 0.865, 1.04, 1.24, 1.64, and/or 2.25 μm in order to determine the aerosol type and optical depth. Our Tafkaa aerosol lookup tables include all of those wavelengths, in addition to several in the visible and near-infrared (VNIR) portion of the spectrum. The tables were calculated with Ahmad and Fraser's (1982) radiative transfer code that includes all orders of scattering, and components of polarization. The lower boundary condition is a rough ocean surface with capillary wave distribution as described by Cox and Munk (1954), as well as the effects of foam. The tables were calculated at 14 wavelengths and 3 wind speeds. There are 10 aerosol optical depths, 5 overall aerosol models, each of which has 5

---

[*] U.S. Naval Research Laboratory, Code 7232, Washington, DC 20375; Marcos.Montes@NRL.Navy.mil
[†] U.S. Naval Research Laboratory, Code 7232, Washington, DC 20375
[§] U.S. Naval Research Laboratory, Code 7203, Washington, DC 20375

size distributions (i.e., relative humidities). The geometrical grids have 9 solar zenith angles (θ_0), 17 view zenith angles (θ), and 17 relative azimuth angles ($\Delta\phi$). The calculations were output at 9 sensor altitudes, and all the calculations assume a surface at sea-level. A thorough description of our algorithm may be found in Gao et al. (2000), and modifications are described in Montes et al. (2003).

3. Hyperion and AVIRIS

Some of the principal differences affecting coastal ocean data obtained with Hyperion and AVIRIS are listed in Table 1. Because it is airborne, AVIRIS can obtain data along many different possible paths, and the paths can have variable lengths. The satellite path of EO-1 and the small cross-track field of view limit the scenes obtained with Hyperion to particularly long and narrow (~7 km) swaths along the satellite's track. However, the very wide full-field of view for AVIRIS scenes can lead to solar glint or to cross-track differential specular reflection effects in a large fraction of an oceanic scene unless the ER-2 flight line is nearly into or out of the sun. Hyperion's much narrower field of view makes it relatively easier to avoid solar glint, especially with its ability to point off-nadir. On the other hand, the low signal-to-noise ratio (SNR) and the noisy data in the short-wave infrared (SWIR) make it difficult to use the SWIR bands for atmospheric correction as described in §2.

Table 1. Comparison of Design Features

|	1996 AVIRIS	HYPERION
Sensor Design	Whisk broom, 4 spectrometers	Push broom, 2 spectrometers
Platform	Airborne ER-2 @ ~20km	EO-1 Satellite @ 705 km
Spectral Characteristics	224 bands, $\Delta\lambda$~10 nm, FWHM~10 nm, range: 0.375–2.50 µm	198 bands, $\Delta\lambda$ ~11 nm, FWHM ~11 nm; range: 0.43–2.4 µm
Typical GSD	~ 20 m from ER-2	~30 m from orbit
Full field of view	30° (~12 km at ER-2 altitude)	0.6° (~7 km from orbit)
SWIR Comments	Relatively high SNR	Relatively low SNR

4. Data and Processing

The AVIRIS and Hyperion data were obtained several years apart, with different orientation, in different seasons, and at different spatial scales. The AVIRIS data was obtained in a flight mostly along the Florida Keys, approximately from east to west. The Hyperion image, on the other hand, is mostly from north to south. While the solar zenith angles were fairly similar, the relative azimuth angles ($|\phi_0 - \phi|$) were quite different. For AVIRIS, ϕ changes at nadir assuming that the ER-2 is in level flight with no pitch or roll. In this case, ϕ takes on different values to the left and right of nadir, and typically $\phi_{left} = \alpha_h + 90°$ and $\phi_{right} = \alpha_h - 90°$ (where left and right refer to the plane in this case, and the view azimuth is measured from the surface to the sensor), so $\phi_{left} = 350°$ and $\phi_{right} = 170°$.

Table 2. Comparison of Data Collection Conditions

	AVIRIS	HYPERION	Comments
Data Set	f960323t01p02_r10a	EO1H0150432002299110KY	
Date (Gregorian / GMT)	1996 March 23	2002 October 26	Different Seasons
Time (24 hour GMT)	19:48	15:27	
Time (24 hour EST)	14:48	10:27	Afternoon vs. morning
Solar Zenith Angle θ_0	40°	45°	
Solar Azimuth Angle ϕ_0	240°	143°	Clockwise from N
View Zenith Angle θ	$0° < \theta < 15°$	27° (to the west of nadir)	Hyperion viewed off-nadir
View Azimuth Angle ϕ	See text	101°	Clockwise from N
Mean Heading α_h	260°	191°	Clockwise from N

Several features are easily recognizable in both images in Fig. 1, and the approximate borders of the region of overlapping data have been marked. The intersection of the images includes portions of No Name and Mayo Keys, Porpoise Key, a large part of Big Pine Key (the largest island in the imagery), all of Little Torch Key, Middle Torch Key, Ramrod Key, and portions of Big Torch and Summerland Keys. The pixels in the Hyperion image are markedly non-square due to the large view zenith angle of that data.

Figure 1. Images showing the approximate area of overlap between the AVIRIS and the Hyperion imagery. In this imagery, the eastern and western borders of the Hyperion image are the *solid* and *dashed* blue lines, respectively. Likewise, the southern and northern borders of the AVIRIS image are the *solid* and *dashed* red lines, respectively. The images are not to scale, and neither image has been geo-rectified. Due to the off-axis pointing of Hyperion, the cross-track ground sample distance (GSD) is ~ 34m, and its pixels are not square. Each image is a small portion of a much larger data set.

March 23, 1996   October 26, 2002
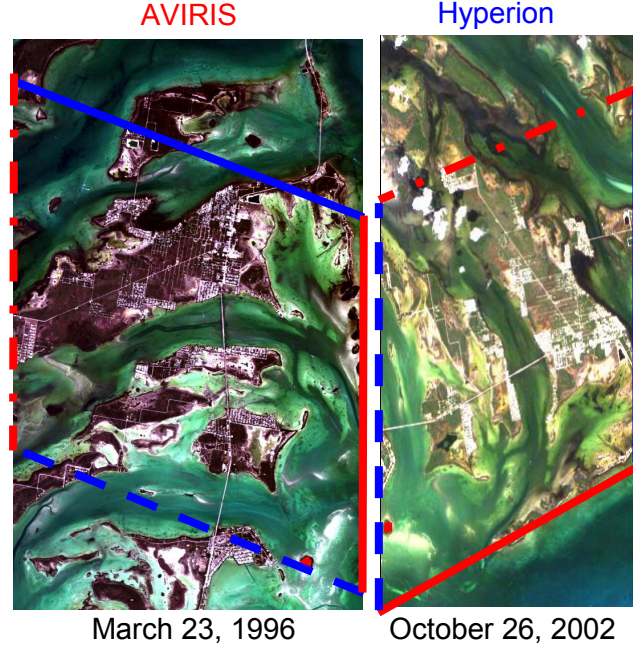
The AVIRIS data was processed using the standard Tafkaa processing chain. A land mask was created to mask the land in order to bring out the features in the water. Three, four, or five NIR/SWIR bands were used to determine the aerosol model using Tafkaa. Small effects arising from the cross-track viewing geometry and the changing along-track solar geometry were corrected for. While all areas were processed, we avoided analysis in areas with the "ghosts" that are present in the 1996 AVIRIS data (Montes, 2004) as these will give false aerosol retrievals.

The Hyperion processing was rather more involved as there are several artifacts that affect Hyperion data (Datt *et al.,* 2003; Goodenough *et al.,* 2003, Green *et al.,* 2003, and other articles in the TGARS *Special Issue on EO-1 Mission* 2003). We elected to use only the calibrated VNIR bands of the first spectrometer due to the low SNR in the SWIR spectrometer. It was necessary to apply a "flat-fielding" or "de-striping" process in order to remove (or reduce) along track striping in the imagery. We used our own custom written software implementing the process described in Kruse *et al*. (2003) in order to reduce the striping in the imagery. As we were using only the VNIR spectrometer, the only bands we could use in order to determine the aerosol parameters were the 0.750 μm and 0.865 μm bands. However, the presence of a bright, shallow bottom prevents us from using the 0.750 μm band for aerosol determination in large parts of the Hyperion image. Since we were not interested in correcting land or clouds, but we wanted to differentiate optically shallow water from much deeper water, we created a program to determine whether a pixel was land or water. All non-land, non-water pixels were called clouds. In general we can tolerate error in the land and cloud confusion since we were only concerned with water. A sub-class of shallow water pixels was determined from water pixels where $\rho^*_{obs}(0.79 \text{ μm})/\rho^*_{obs}(0.75 \text{ μm}) > t$, where $t=1.05$ is a threshold determined from the data, $\rho^*_{obs}=\pi L/(\mu_0 E_0)$, $\mu_0 = \cos(\theta_0)$, and E_0 is the solar irradiance above the atmosphere. Standard pixel-to-pixel Tafkaa processing was performed on the data using the 0.750 μm and 0.865 μm bands to determine the aerosol model and optical depth in the non-shallow area. In the shallow areas, aerosol models and optical depths from nearby areas were used.

5. Results

The comparison of these data sets is problematic since they were obtained at such different times, and since there is no contemporaneous ground truth data for either date in the area where these images overlap. The tidal states are uncertain, so relative submerged depths are not known. However, tide charts show typical ranges of tides to be of order 0.40 m, so this uncertainty is not too large. The aerosol was retrieved using Tafkaa assuming there was no water leaving radiance at 0.865, 1.04, 1.24, and 1.64 μm for the AVIRIS data, and the retrieved aerosol optical depth at 0.55 μm $\tau_{550} = 0.1$ for the 1996 AVIRIS data. For Hyperion, low SNR in the SWIR led to the use of only the 0.750 and 0.865 μm bands for the determination of the aerosol properties, and $\tau_{550} = 0.2$ was derived for the

Hyperion data. However, because of the different season, the different time of day, there may be different sediment loads, different phytoplankton populations, and so perhaps somewhat different inherent optical properties (absorption and scattering profiles) in the water. To top it off, the intersection of the imagery has no deep water pixels (pixels that are unaffected by the reflectance of the ocean bottom) which would be in many ways the best to compare. We are left with comparisons of various locations in the image where the bottom is visible. Some results are shown in Figs. 2 & 3. In both cases, we have achieved reasonable (remarkable?) matches for $\lambda > 0.6$ μm. Is this merely fortuitous? As stated earlier, the tidal state is not going to be a great effect because the tides are so small, and yet the increasing absorption of light by water for $\lambda > 0.6$ μm (and therefore high sensitivity to depth in this wavelength range) would seem to indicate that the depths and bottom albedo are nearly identical when viewed 6.5 years apart. In both cases we have truncated the Hyperion spectra at about 0.43 μm, but truncation of Hyperion spectra at ~0.45 μm is not uncommon for ocean researchers, and is justified based on the noisiness in the bands at about 0.43 and 0.44 μm (Jupp, 2002). The atmospherically corrected Hyperion spectra all appear to be somewhat low in the blue compared to the atmospherically corrected AVIRIS spectra; however, even the atmospherically corrected AVIRIS spectra appear to be somewhat low at $\lambda < 0.45$ μm. While these results are tantalizing, a more thorough comparison still needs to be performed. This will require geocorrecting each image, or warping one of the images to the other, as well as resampling to a common spatial scale.

6. Conclusions

We have shown that it is possible to derive very similar spectra over shallow coastal areas from different hyperspectral sensor flown on different platforms, in different seasons, with different solar and view geometry. The derived atmospheric correction parameters for the two images using Tafkaa also differ. While there may be some calibration issues in the blue with both AVIRIS and Hyperion, the derived results are generally acceptable. Remote sensing of oceans with narrow field of view hyperspectral imagers in sun-synchronous orbits with off-nadir pointing ability allows us to avoid regions of high specular reflection. Such a sensor with high SNR in the VNIR and SWIR would allow derivation of aerosol parameters using the longer wavelengths and would be an ideal instrument for environmental assessment of the global coastal ocean.
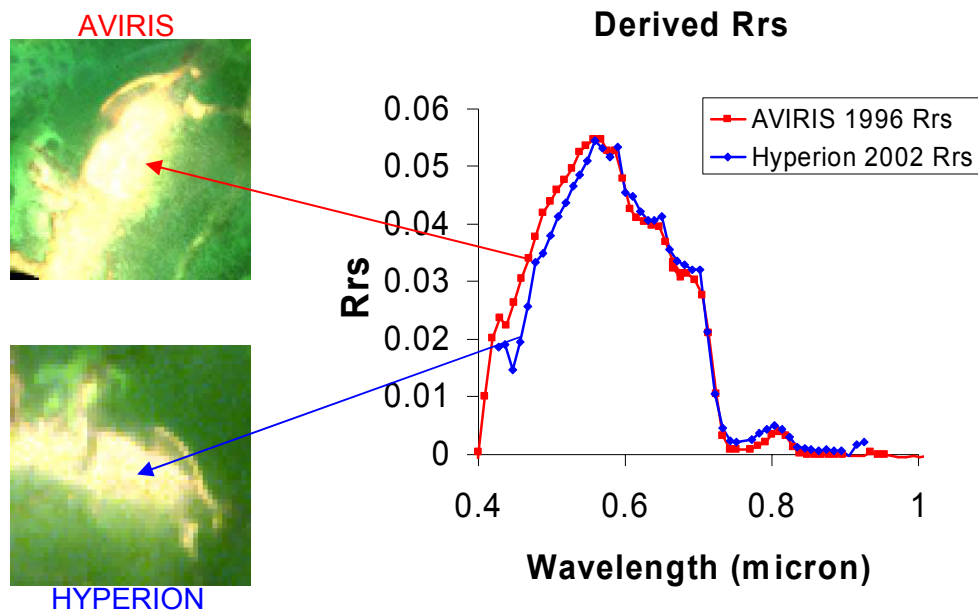

Figure 2. Spectra from a sandy region in the overlapping area; the images to the left are not georectified, but identification of identical features is obvious. The AVIRIS spectra are 3x3 pixel averages, and the Hyperion spectra are 2x2 pixel averages, in order to cover more similar spatial areas. The bump near 0.810 μm indicates a depth of < 2m.

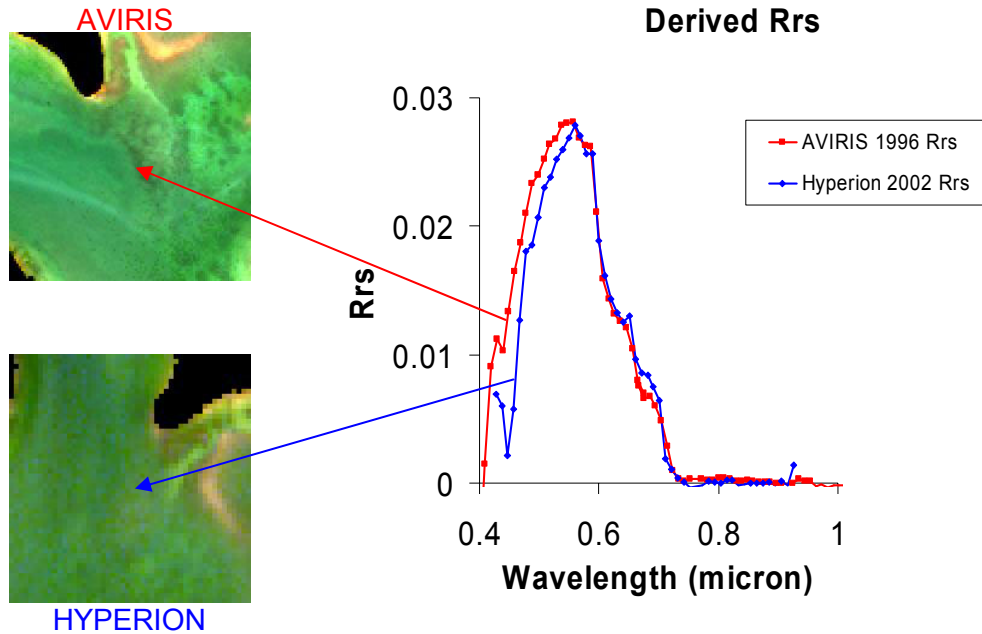Figure 3. Same as in Figure 2, but from a deeper location and a different bottom type.

References

Ahmad, Z. and R. S. Fraser, 1982, "An iterative radiative transfer code for ocean-atmosphere systems," *J. Atmos. Sci.*, 39, 656–665.

Cox, C., and W. Munk, 1954, "Statistics of the sea surface derived from sun glitter," *J. Mar. Res.*, 14, 63–78.

Datt, B., T. R. McVicar, T. G. Van Niel, D. L. B. Jupp, and J. S. Pearlman, 2003, "Preprocessing EO-1 Hyperion Hyperspectral Data to Support the Application of Agricultural Indices," *IEEE Trans. On Geosci. Rem. Sens.*, 41(6), 1246–1259.

Brando, V. E. and A. G. Dekker, 2003, "Satellite Hyperspectral Remote Sensing for Estimating Estuarine and Coastal Water Quality," *IEEE Trans. on Geosci. Rem. Sens.*, 41(6), 1378–1387.

Fraser, R. S., S. Matoo, E.-N. Yeh, and C. R. McClain, 1997, "Algorithm for atmospheric and glint corrections of satellite measurements," *J. Geophys. Res.*, 102, 17107–17118.

Gao, B.-C., M. J. Montes, Z. Ahmad, and C. O. Davis, 2000, "Atmospheric correction algorithm for hyperspectral remote sensing of ocean color from space," *Applied Optics*, 39(6), 887–896.

Goodenough, D. G., A. Dyk, K. O. Niemann, J. S. Pealman, H. Chen, T. Han, M. Murdoch, and C. West, 2003, "Preprocessing Hyperion and ALI for Forest Classification," *IEEE Trans. On Geosci. Rem. Sens.*, 41(6), 1321–1331.

Gordon, H. R., 1978, "Removal of atmospheric effects from satellite imagery of the oceans," *Appl. Opt.*, 17, 1631–1636.

Gordon, H. R., 1997, "Atmospheric correction of ocean color imagery in the Earth Observing System era," *J. Geophys. Res.*, 102, 17081–17106.

Gordon, H. R. and M. Wang, 1994, "Retrieval of water leaving radiance and aerosol optical thickness over the oceans with SeaWiFS: A preliminary algorithm," *Appl. Opt.*, 33, 443–452.

Green, R. O., B. E. Pavri, and T. G. Chrien, 2003, "On-Orbit Radiometric and Spectral Calibration Characteristics of EO-1 Hyperion Derived with an Underflight of AVIRIS and *In Situ* Measurements at Salar de Arizaro, Argentina," *IEEE Trans. On Geosci. Rem. Sens.*, 41(6), 1194–1203.

Jupp, D. L. B., 2002, "Discussion around Hyperion Data: Background notes for the Hyperion Data Users Workshop," CSIRO EOC, Canberra, Australia.

Kruse, F. A., J. W. Boardman, and J. F. Huntington, 2003, "Comparison of Airborne Hyperspectral Data and EO-1 Hyperion for Mineral Mapping," *IEEE Trans. on Geosci. Rem. Sens.*, 41(6), 1388–1400.

Montes, M. J., B.-C. Gao, and C. O. Davis, 2003, "Tafkaa atmospheric correction of hyperspectral data," in Proc. SPIE Vol. 5159 *Imaging Spectrometry IX*, S. S. Shen, P. E. Lewis, eds., (SPIE, Bellingham, Washington) pp. 188–197.

Montes, M. J., 2004, "AVIRIS Artifacts Appearing in Low-Light Imagery," *Proceedings of the 13th Airborne Earth Science Workshop,* this volume.

Special Issue on the Earth Observing (EO-1) Mission, IEEE Trans. On Geosci. Rem. Sens., 41(6), pp. 1147–1414, June 2003.

SPECTRAL CHARACTERIZATION OF CHANGES IN GRASSLAND UNDER CLIMATIC AND SOIL GRADIENTS IN KOHALA, HAWAII

Izaya Numata,[1] Dar Roberts,[1] Oliver Chadwick,[1] Yasha Hatzel[1]

1. INTRODUCTION

Kohala Mountain, in Northern Hawaii, provides an ecosystem characterized by a strong climatic gradient along the leeward side of the mountain. The climatic gradient extends from arid to humid conditions from the coast to the top of the mountain. Along this climatic gradient, soil biogeochemical processes operate differently. Chadwick et al. (2003) found that increasing rainfall with increasing elevation caused fundamental changes in soil physical and chemical properties. Vegetation, which is sensitive to water availability and soil characteristics for its development, should be a good indicator of climatic shifts that occur on Kohala Mountain.

Field-level hyperspectral data provide a rich data source to quantitatively and qualitatively characterize land surface features and can be used as a reference for airborne or satellite sensor data. Once water status of vegetation is estimated using hyperspectral data (Curran, 1989; Kumar et al., 2001), vegetation changes over Kohala Mountain can be well characterized by using remote sensing. We analyzed changes in grassland cover along Kohala Mountain, coupling grass field spectra with climate and soil data. The objectives of this study are 1) spectral characterization of grassland changes along climatic and soil gradients over Kohala Mountain, and 2) analysis of the relationships between environmental parameters (climate and soil) and field spectra.

2. STUDY SITE DESCRIPTION

Our study site is located on the leeward side of Kohala Mountain (20.4N, 155.4.30W). Eight transects were selected along the climatic gradient on the leeward side of Kohala Mountain (Figure 1). Elevations range between 186 m and 1138 m at the study site. Annual precipitation varies from 180 mm, at site B, to 1380 mm, at site J. There are basically four dominant vegetation species along the sample transects: Buffel grass (*Cenchrus cillaris*) and keawe tree (*Prosopis pallida*), mostly found in the dry areas, and kikuyu grass (*Pennisetum clandestinum*) and orchard grass (*Dactylis glomerata*) found from intermediate to higher elevation sites. Soils along the sampling transects were developed on the same parent material, Hawi lavaflow.

3. METHODS

There are three steps involved in this study: 1) calculation of climatic parameters, 2) soil sampling and spectral measurements in the field, and 3) data processing and analyses.

3.1 Calculation of climatic parameters

Monthly precipitation was calculated using a second-order polynomial developed by Chadwick et al. (2003). This equation was developed based on nearly 20 years of rainfall records measured at nine rainfall gauges in Kohala. Monthly potential evapotranspiration (PET) was interpolated from the PET map developed by Ekern and Chang (1985) and Shade (1995). Water

---

[1] Department of Geography, University of California, Santa Barbara (numata@geog.ucsb.edu)
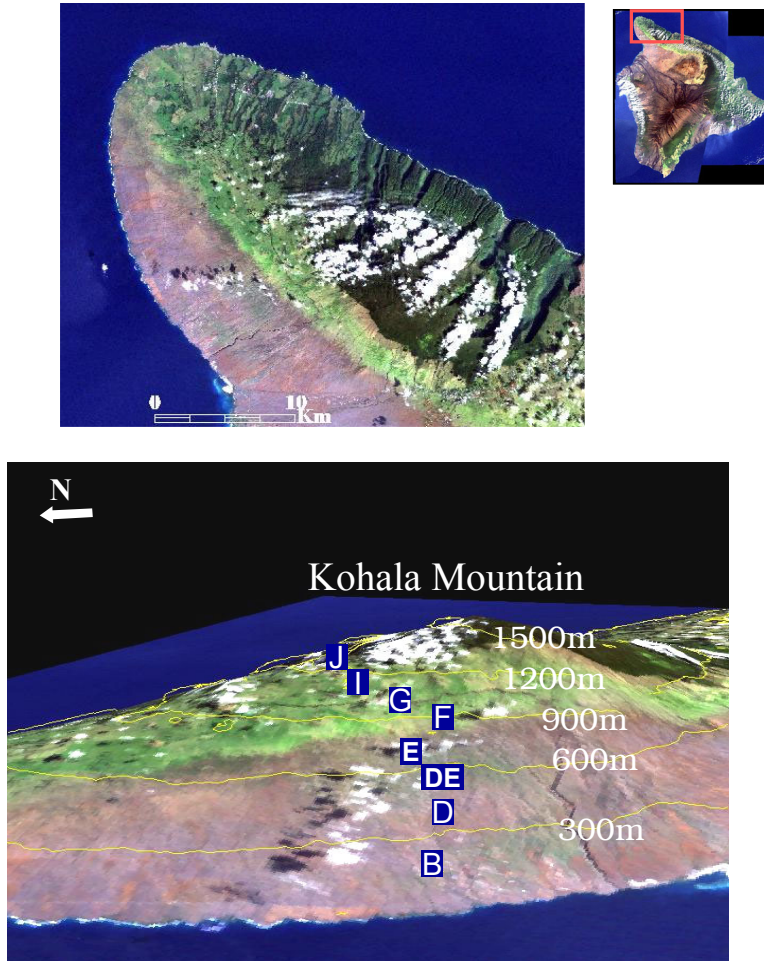
Figure 1. Overview of Kohala Mountain (above), Sample transects along the leeward side of Kohala Mountain

balance was calculated simply by subtracting Monthly PET from Monthly Precipitation. For more details, see Chadwick et al. (2003).

3.2 Soil sampling and spectral measurements in the field

The fieldwork was conducted from June 23 through July 2, 2002. We collected soil samples and field-spectra from each transect. Most transects were 50 m long, but for site F, which is a topographically rough land surface with variable vegetation types (mixed grass and shrub), we established a 100 m transect. An ASD full range spectrometer (350 to 2500 nm; Analytical Spectral Devices, Boulder, Colorado), borrowed from JPL/NASA, was used for field optical measurements over the transects. The ASD spectra were collected with a 22° field-of-view (FOV) at 2-m intervals along each transect at a 1m sensor height. All measurements were collected within 2 hours of local solar noon on clear-sky days. Five replicates were measured for each grass canopy. These spectra were standardized to spectralon (Labsphere, Inc, North Sutton, NH) measured at approximately 10-minute intervals, and converted into reflectance. Following each spectral measurement, grass canopy height and digital photographs of the grass canopy were measured. Soil classification for each study transect had already been accomplished by Chadwick et al. (2003). For this study, six soil samples were collected from 0 to 30 cm from each transect for physical and chemical analyses.

3.3 Data analyses

Two vegetation indices were calculated from the ASD reflectance spectra: the Normalized Difference Vegetation Index (NDVI) = [NIR-R]/[NIR+R] (Choudhury, 1987) and the Soil Adjusted Vegetation Index (SAVI) = 1.5*([NIR – R]/[NIR+R+0.5) (Huete, 1988). Linear spectral mixture analysis (Adams et al., 1993) was also performed to decompose the ASD spectra into four fractional components: non-photosynthetic vegetation (NPV), green vegetation (GV), soil, and shade. Additionally, root-mean-square (RMS) error was calculated for each measurement. Endmembers were selected by comparing our spectral library to the corresponding canopy digital photographs taken from the same field spectral measurement points.

Soil physical and chemical analyses were conducted in the laboratory. In this study, soil chemical data were not used. Soil physical properties used in this study were: Coarse fragment % and pore volume. More details regarding the laboratory analyses, see Chadwick et al. (2003).

4. RESULTS AND DISCUSSION

4.1 Water balance and grassland changes derived from hyperspectral data

Figure 2 shows water balances at different sites, obtained in February, April, June, and December. We divided the transects into three zones: dry, intermediate, and wet. In the dry zone (B, D, and DE), water balance is always negative from December to June, while the wet zone (I and J) shows positive water balance from December to April, and negative in June.

The spectral reflectances in Figure 3 are related to the land surface characteristics of each transect and changes in grassland over the climatic gradient. Low and flat reflectance spectra in the dry zone indicate the presence of bare soil and low vegetation coverage. Dry grass is well expressed by the ligno-cellulose absorptions in the short wave-infrared (2100 to 2300 nm). The intermediate zone shows the transition of spectral signatures from dry grass to green grass, with an increase of chlorophyll absorption in the visible region. In the wet zone spectra, the reflectances show the characteristics of green vegetation such as more pronounced chlorophyll absorption in the visible, a pronounced red-edge, and the water absorption features found at the 970 nm, 1200 nm and 1450 nm in the near infrared (Curran, 1989; Dawson et al., 1992; Peñuelas et al., 1993).
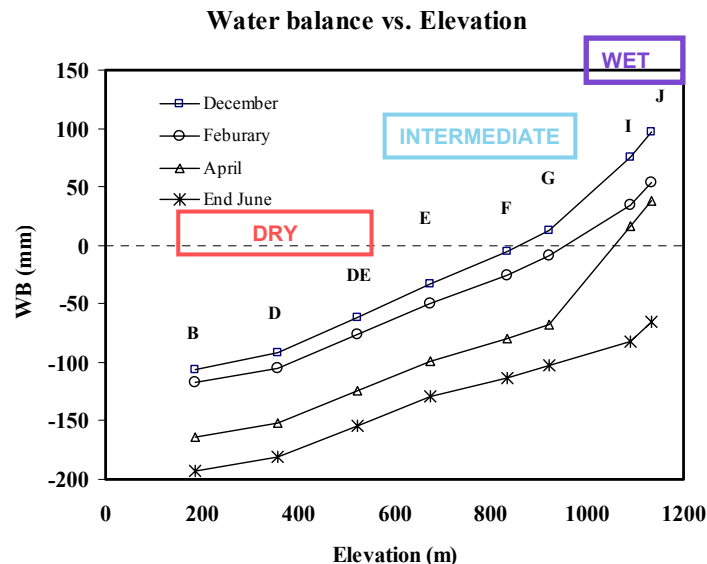

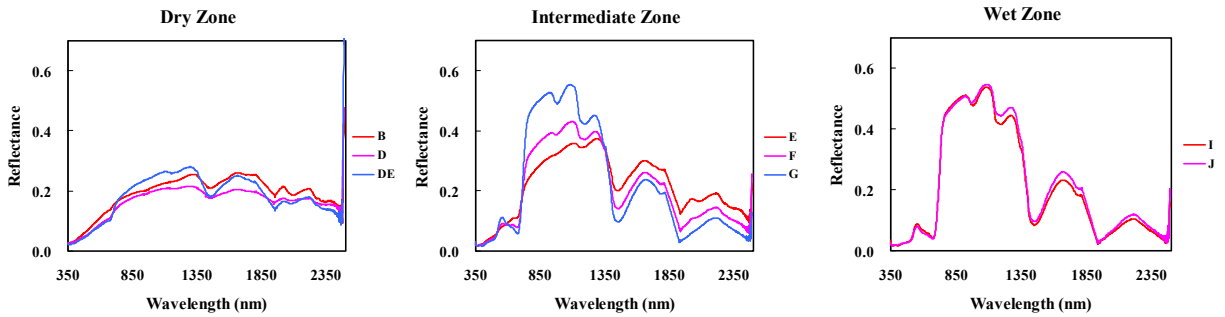Figure 2. Water balance along the sample transects in different months (December to end of June)

Figure 3. Mean reflectance measured in three climatic zones: a) dry, b) intermediate, and c) wet

Vegetation indices, NDVI and SAVI, plotted along the transects (Figure 4.a) provide a good insight into changes in grass as a function of water balance. These vegetation indices tend to saturate in the wet zone, between G and J. Transect F, which is the most heterogeneous, shows the largest variability expressed by standard deviation.

By analyzing the fractional cover changes (Figure 4.b), we are able to understand better changes in the land surface along the transects. The dry zone is strongly characterized by high
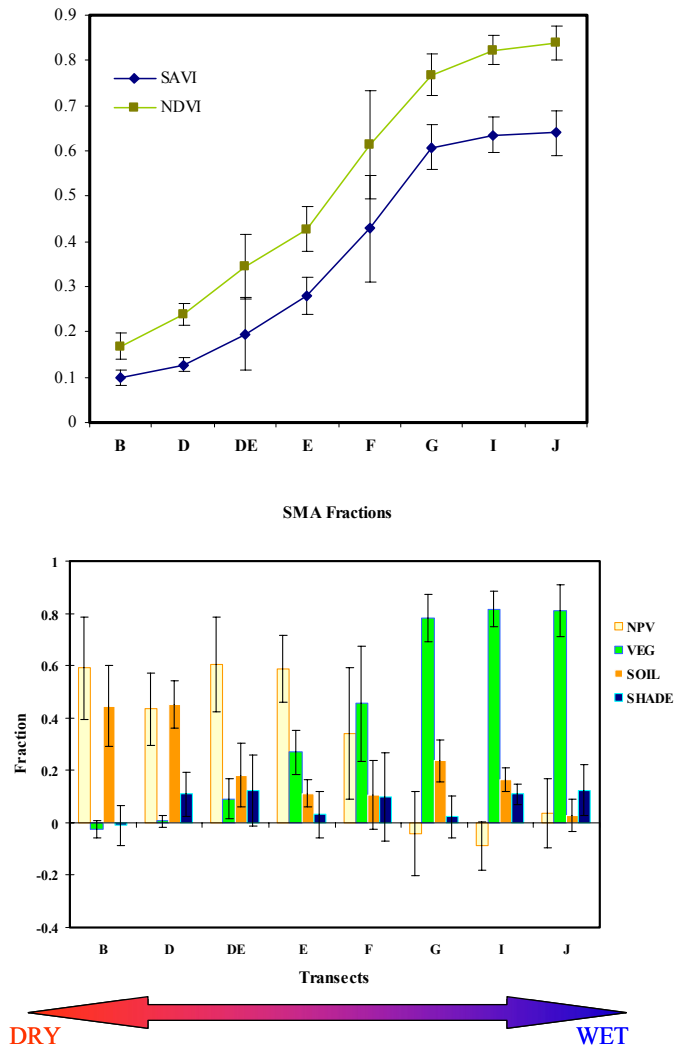
Figure 4. a) NDVI and SAVI along the sample transects; b) SMA fractions along the transects

184
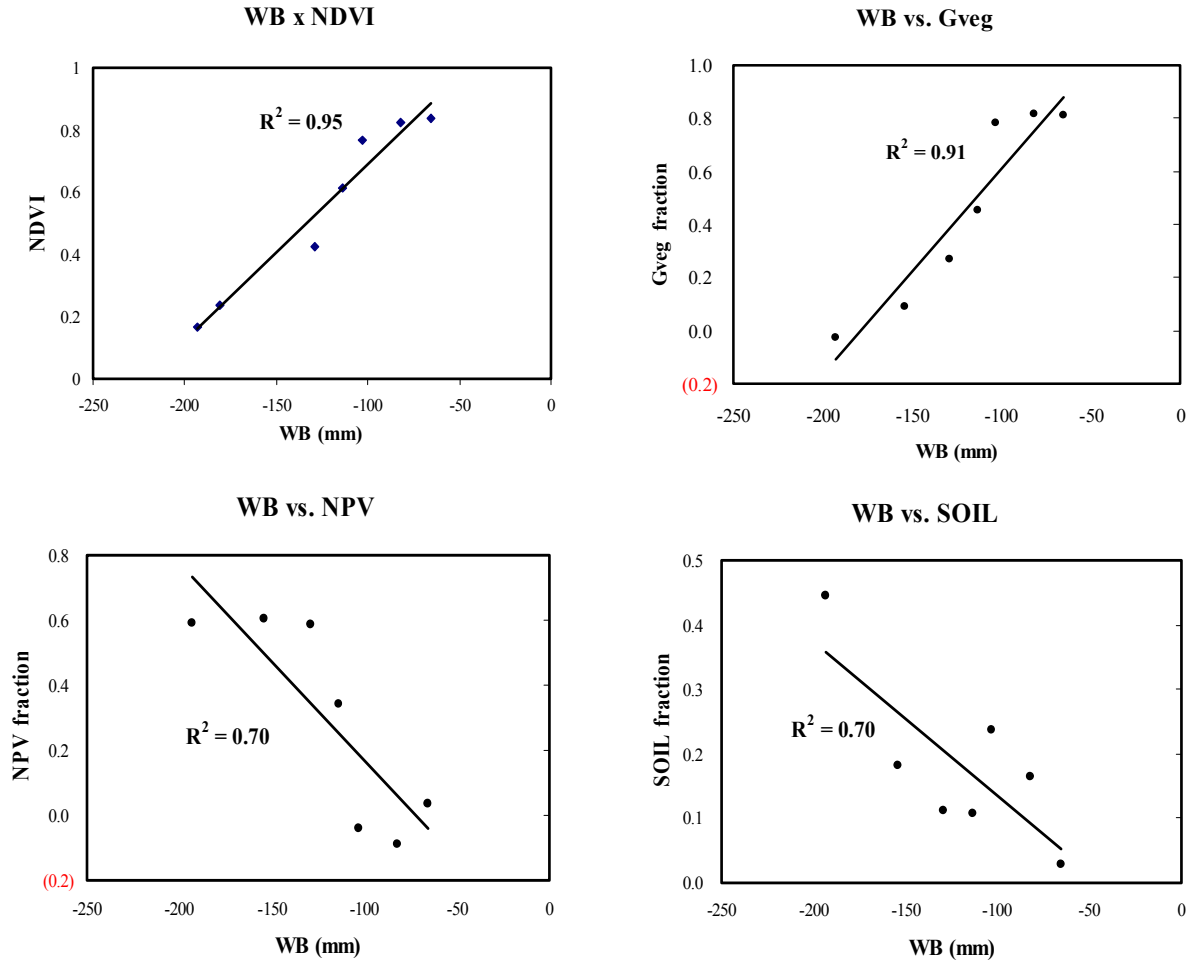
Figure 5. Correlation of WB with remotely sensed data

NPV and soil fractions, and low GV fraction, indicating sparse vegetation cover and high water stress on vegetation. NPV and soil fractions tend to decrease as water balance increases with elevation. GV fraction, on the other hand, shows an opposite trend, low in the dry zone and high in the wet zone. Note that in the transect F, the most heterogeneous site, a high variability is shown by a large variance as found in the vegetation indices previously.

In terms of relationships between climatic variation and vegetation changes derived from field spectra, NDVI and GV fractions showed a high positive linear correlation with water balance (R^2=0.95 and 0.91, for NDVI and GV, respectively), while soil and NPV are negatively correlated with water balance (Figure 5).

4.2 Soil physical properties and vegetation changes derived from hyperspectral data

With increasing rainfall along the climate gradient, there is a reduction in soil particle size and an increase in pore volume that enhances soil water holding capacity (Chadwick et al., 2003).

Coarse fragment % and pore volume formed the basis of the soil physical gradient and its impact on vegetation density and the vegetation indices. Coarse fragment % is the amount of soil fragments larger than 2mm contained in soil, while the pore volume refers to the total space or

185

pore formed among soil particles, where water in soil is stored in. Figure 6 shows a negative correlation between these two variables. Smaller soil particles and the consequent greater porosity, leads to greater water holding capacity when compared with those areas with high coarse fragment %. Therefore sites B, D, and DE, both receive little annual rain and store relatively small amounts of water. Meanwhile, the higher elevation sites such as I and J, receive high levels of annual rainfall and with their large pore volumes can store more moisture. These variables also show good relationships with remotely sensed data, GV and NPV (Figure 7, only GV fraction is shown in

Figure 6. Coarse fragment% and pore volume along the transects

the figures). Note that our spectra were collected in June-July, in the dry summer, in which water balance at the all sampling sites reaches negative, however we have just seem high vegetation signals from the wet zone (Figure 5). The grasses at sites I and J remain green even during the period of negative water balance because their elevated water holding capacity stores water for long periods.
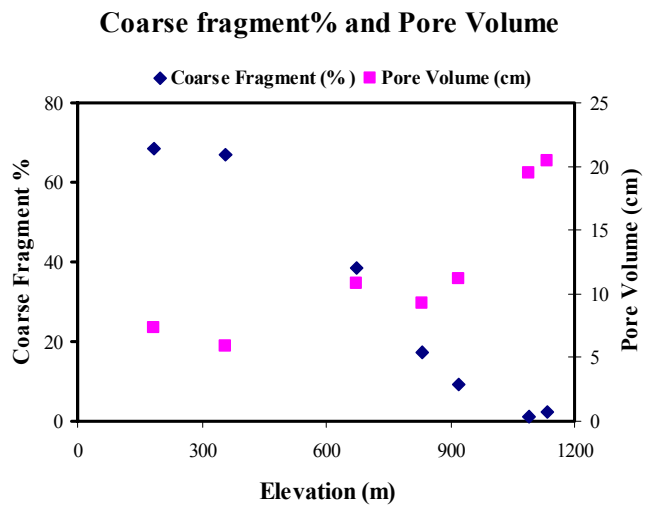
While water balance controls overall changes in vegetation along Kohala Mountain, the effects of soil physical properties on vegetation become more evident and more important in the dry summer when water balance is negative. Consequently, the combination of climate with soil properties is expected to be responsible for spatial and temporal changes in grassland in this region.
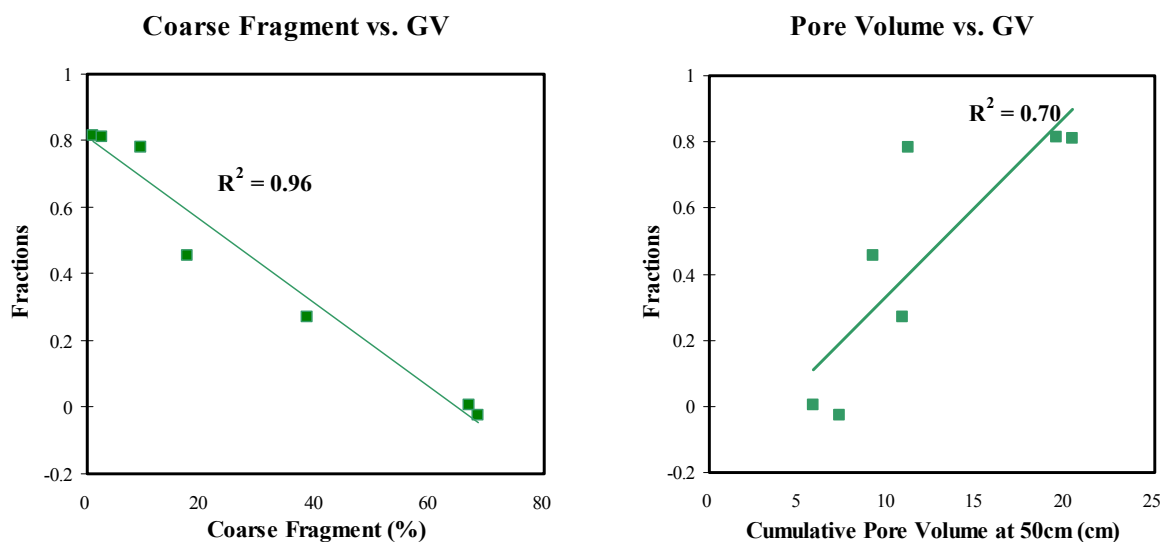

Figure 7. Correlation of GV with coarse fragment (left) and with pore volume (right)

5. CONCLUSIONS AND FUTURE RESEARCH

Kohala Mountain provides an ideal ecosystem to study interactions among climate, soil and vegetation. This study showed a simple application of hyperspectral data for characterizing the changes in grassland under climatic and soil gradients.

- ○ Water balance is the major source of changes in grassland along Kohala Mountain, showing high correlation with vegetation changes derived from field level hyperspectral data.
- ○ Soil physical properties related to water holding capacity also control the grass status on Kohala. However, the effects of soil physical properties are expected to become more evident and more important in the dry summer, when water balance reaches negative.
- ○ Field level spectra provided good indicators of vegetation changes and fractional cover changes gave good insight into land cover changes along the transects.

The high correlation of vegetation changes with climate and soil properties can lead us to characterization of continuous land-surface changes by using AVIRIS data. In addition, it is recommendable to extend this study to other seasons (seasonal analysis).

6. ACKNOWLEDGEMENTS

7. REFERENCES

Adams, J.B., Smith, M.O., Gillespie, A.R. 1993. "Imaging spectroscopy: interpretation based on spectral mixture analysis." In *Remote Remote Geochemical Analysis: Elemental and Mineralogical Composition*, Pieters, C.M., Englert, P. Eds., 7. Cambridge University Press, New York, pp. 145–166.

Chadwick, O. A., R. T. Gavenda, E. F. Kelly, K. Ziegler, C. G. Olson, W. C. Elliott, and D. M. Hendricks. 2003. "The impact of climate on the biogeochemical functioning of volcanic soils," *Chemical Geology*, **202**, 195–223.

Choudhury, B.J. 1987. "Relationships between vegetation indices, radiation absorption and net photosynthesis evaluated by a sensitivity analysis," *Remote Sensing of Environment*, **22**, 209–233.

Curran, P.J. 1989. "Remote Sensing of foliar chemistry," *Remote Sensing of Environment*, **35**, 69–76.

Dawson, F.M., Steven, M.D., Malthus, T.J., Clark, J.A. 1992. "High-spectral resolution data for determining leaf water content," *Inernational Journal of Remote Sensing*, **13**, 461–470.

Ekern, P.C., and Chang, J.H. 1985. Pan evaporation. Hawaii Department of Land and Natural Resources, No. R74. Honolulu, Hawai.

Huete, A.R. 1988. "A soil adjusted vegetation index (SAVI)," *International Journal of Remote Sensing*, **9**, 295–309.

Kumar, L., Schmid, K., Dury, S., Skidmore, A. 2001. "Imaging spectrometry and vegetation science." In *Imaging Spectrometry: Basic principles and prospective applications*, van der Meer, F.D., de Jong, S.M. Kluwer Academic Publishers, Netherlands, pp. 111–154.

Peñuelas, J., Fielella, I., Biel, C., Serrano, L., Savé, R. 1993. "The reflectance at the 950-970 nm region as an indicator of plant water status," *International Journal of Remote Sensing*, **14**, 1887–1905.

Shade, P.J., 1995. "Water budget for the Kohala area, Island of Hawaii," U.S. Geological Survey, Water-Resources Investigations Report 95-4114. Honolulu, Hawaii.

USING CART MODELING AND AVIRIS IMAGERY FOR ASSESSING RISK OF WEED INVASION AT VANDENBERG AIR FORCE BASE

Karen Olmstead,[1] Susan Ustin,[2] and Ted Ernst[3]

1. Introduction

Invasion by noxious weeds is a serious and rapidly accelerating ecological to the long-term environmental health of natural ecosystems. Current estimates indicate that in the U.S., weeds infest 70,000 hectares and cost more than $100 billion annually, causing severe economic losses and ecological degradation (Babbitt 1998; Pimentel et al. 2000).

One of the major problems faced by environmental managers is the difficulty in mapping the location of invasive weeds; traditional mapping methods using extensive ground surveys can be very costly and time-consuming. New remote sensing technologies, especially hyperspectral imagers, such as the Airborne Visible and Infrared Imaging Spectrometer (AVIRIS), may improve monitoring and mapping capability and improve early detection and management of invasive weeds. Our research addresses two broad objectives: 1) develop methods to inventory the spatial extent of established populations of noxious weeds; and 2) develop methods to estimate the likelihood of expansion in spatial distribution of invasive noxious weeds into additional habitat areas.

In a previous paper (Underwood et al. 2002), we presented our results for mapping iceplant and jubata grass at Vandenberg Air Force Base (VAFB) using classified AVIRIS images. In this paper we are presenting the preliminary results of our modeling efforts using the previously developed AVIRIS weed maps and classification and regression tree (CART) analyses to predict areas vulnerable to weed invasion.

2. Study Area

Vandenberg Air Force Base covers 98,400 acres (Fig. 1) in Santa Barbara County, and represents one of the last relatively undisturbed areas in coastal California (Keil and Holland 1998). The climate is
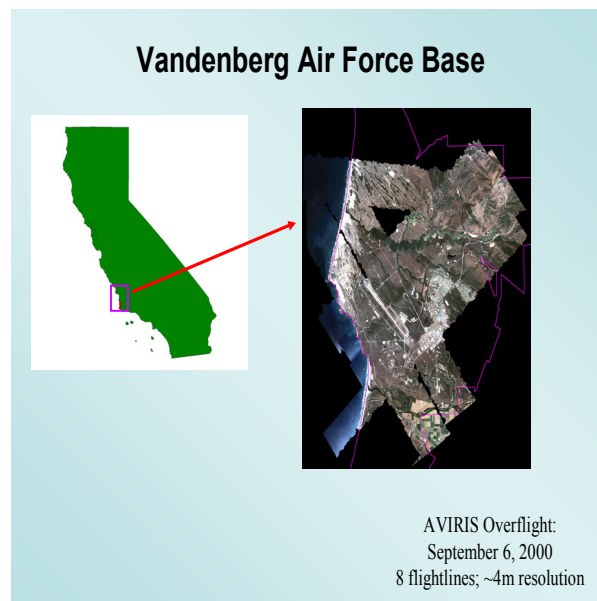

Vandenberg Air Force Base

AVIRIS Overflight:
September 6, 2000
8 flightlines; ~4m resolution

Figure 1. Map showing location of Vandenberg Air Force Base and area covered by AVIRIS overflight.

[1] Center for Spatial Technologies and Remote Sensing, University of California, Davis (ksolmstead@ucdavis.edu)
[2] Center for Spatial Technologies and Remote Sensing, University of California, Davis (slustin@ucdavis.edu)
[3] Dynamac Corp., Corvallis, Oregon (ernst@peak.org)

semiarid, but moderated by maritime influence and fog drip, and the landscape is typified by complex and varied topography, geology, and soils (The Nature Conservancy 1991).

The location of the base is in the ecological transition zone between northern and southern California, resulting in diverse environmental conditions and the presence of several unique and highly localized plant communities (Keil and Holland 1998) (Fig. 2). Since the military mission at VAFB requires extensive land space as a buffer for surrounding communities, much of the base remains relatively undisturbed (Coulombe and Cooper 1976). Despite this isolation, alien plant species have become established and invasive at VAFB, resulting in several communities dominated by introduced plants (Keil and Holland 1998).

Of particular concern, are *Carpobrotus edulis*, *C. chilensis*, and their hybrids (iceplant, also known as hottentot fig or sea fig, respectively) and *Cortaderia jubata* (jubatagrass, also known as purple pampas grass or Andean pampas grass) (Fig. 3). Both pose serious threats to two sensitive vegetation types, coastal dune scrub (hereafter, scrub) and maritime chaparral (hereafter, chaparral).
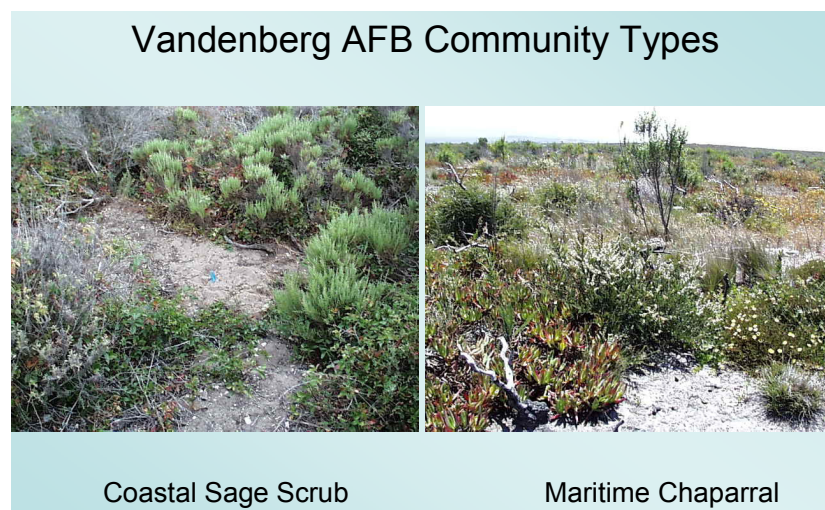

Figure 2. Two plant communities were studied: coastal sage scrub and maritime chaparral.
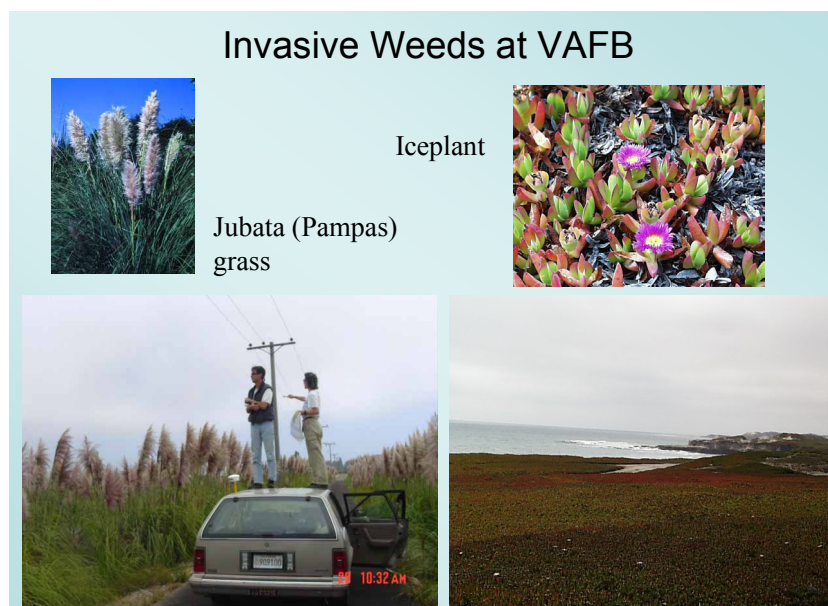

Figure 3. Jubata grass and iceplant are two invasive weed species threatening the coastal scrub and maritime chaparral communities.

3. Field Sampling and Analyses

We collected ecological data to 1) identify relationships between weed distributions to natural and anthropogenic disturbance at a small fine-grained scale, b) identify ecological conditions associated with target weeds and c) identify potential indicators or environmental correlates of target weed presence and abundance within specific natural communities.

Sampling was restricted to an area characterizing the range of invasion by the target weeds in scrub and chaparral communities from relatively intact native vegetation to large monocultures of iceplant or jubatagrass. Detailed species abundance data and rapidly assessed small-scale environmental/disturbance data were collected on the ground from 21 June to 26 July 2000. Sample sites were selected to represent the five community types: Scrub-Intact (n = 19), Scrub-Iceplant (n = 19), Chaparral-Intact (n = 19), Chaparral-Iceplant (n = 10), and Chaparral-Jubatagrass (n = 21).

In addition to the field data, we had access to the geographic information system (GIS) database maintained for VAFB. The GIS layers included hydrography, elevation, soil survey information, and fire history.

To characterize the vegetation, assess the relationships of communities and target species to environmental variables, and to identify potential fine-grain and landscape scale indicators for target species presence, we used an iterative multivariate approach integrating hierarchical clustering classification, nonmetric multidimensional scaling (NMS), multiple response permutation procedures (MRPP), Mantel tests, and classification and regression tree (CART) analysis using a common dissimilarity measure (Sorensen's distance) where appropriate (Urban et al. 2002). Plant community characteristics were described using classification procedures based on species cover data. The existence of associations between species composition, location, environmental variables and GIS variables were evaluated using Mantel tests. The first parameter space was composed of the site level environmental data collected on the ground at each site. The geographic parameter space was based on landscape scale information derived from GIS layers and included soils, hydrologic features, physiography, and fire history. The best suite of explanatory variables from the GIS subsets were aggregated into a final set for analyses.

Figures 4a and 4b are the NMS results for the chaparral and scrub communities. The numbering of NMS axes is arbitrary since axes scores are computed simultaneously. We present the pairs of axes that explain the greatest portion of the variation. Sites were ordinated on the basis of similar species composition. The position of the invasive species are coded on the ordination plot as: CORJUB= *Cortedaderia jubata*, CAREDU= *Carpobrotus edulis* and CARCHI= *Carpobrotus chilensis*. The radiating lines are vectors representing the direction and magnitude of the correlations of the environmental and GIS variables ($R^2 > 0.200$) with the component scores for each axis (Note: The variable Hydrologic Segment Length in Figure 4b is the nearest distance to a stream, lake or other hydrologic feature on a GIS hydrology map). For example, the intact chaparral community was generally further away from fire breaks than the iceplant-invaded chaparral community. MRPP tests showed that all community types were significantly different at the 95% level. Mantel tests showed that sites with similar species composition were also similar with respect to the environmental and GIS variables. In addition, Mantel tests also showed that sites with similar environmental conditions were also similar with respect to the GIS variables.

After establishing the relationships between species composition, the environmental conditions at the site and the more spatially extensive GIS parameters we used CART analyses to investigate the relationships between the presence of the jubata grass and iceplant with the GIS variables across the full extent of the flight path.
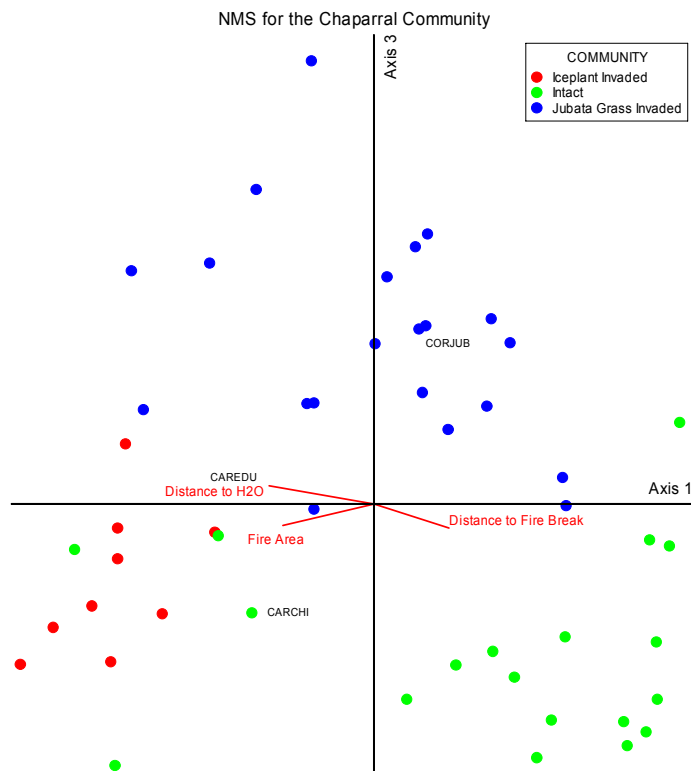
Figure 4a. Nonmetric multidimensional scaling ordination plot for the chaparral community showing sites, invasive weeds and significantly correlated variables.
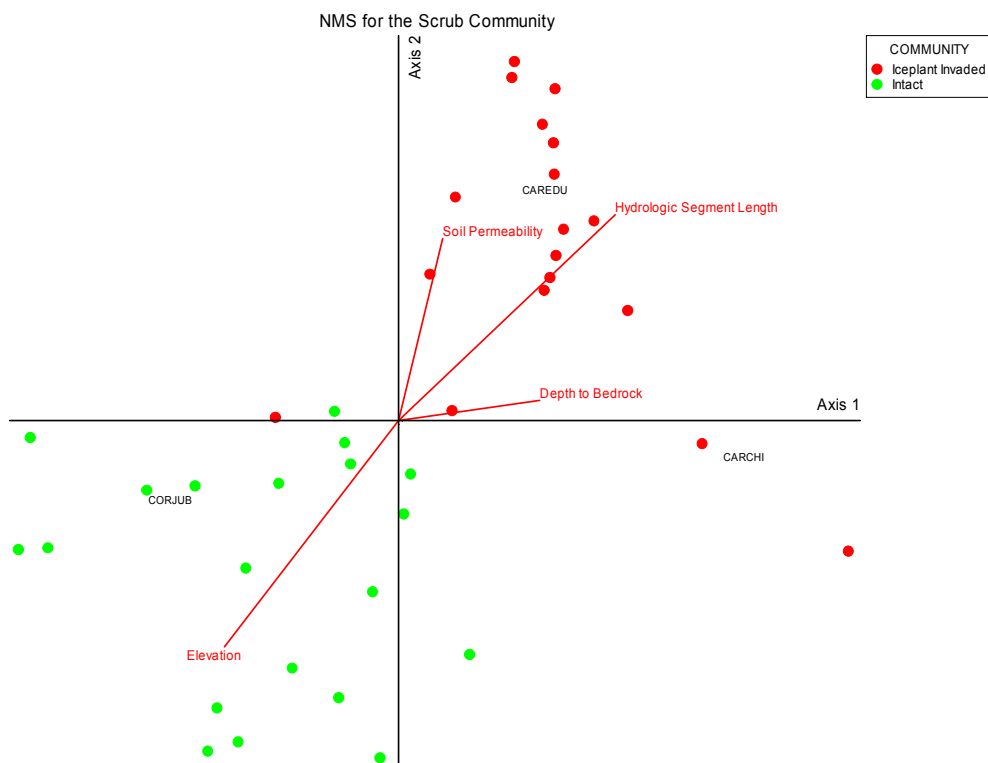

Figure 4b. Nonmetric multidimensional scaling ordination plot for the chaparral community showing sites, invasive weeds and significantly correlated variables.

4. CART Analyses

CART analysis has proven useful for description and predictions of ecological patterns and processes (Michaelson et al. 1994, De'ath and Fabricius 2000, Urban et al. 2002) and is a powerful tool for classifying multiple alternative environmental states. We chose CART for the reason that it can readily translate the predictor variables from the parameter space into a GIS where the results can be displayed geographically. The procedure offers a non-parametric, recursive approach well suited to complex, non-linear ecological data (De'ath and Fabricius 2000, Urban et al. 2002) including continuous, ranked and categorical variables. CART is tolerant of missing data and easy to interpret visually. CART analyses are performed using target species presence or abundance as the response variable and the environmental and GIS variables as explanatory variables.

CART trees explain the variation of a single response variable through repeated partitioning of a dataset into increasingly homogeneous groups using combinations of categorical or numeric explanatory variables (Breiman et al. 1984, Vayassieres et al. 2000). Trees are represented graphically beginning with the complete data set at the root node. Samples are divided into groups that form branches with each node characterized by a mean or typical value for the response variable, the number of samples in the group, and values of the explanatory variable defining the split that separates samples into the next lower branches (De'ath and Fabricius 2000, Urban et al. 2002). A single variable is identified at each branch and a variable can occur at multiple levels in the tree allowing for very complex interactions. Splitting continues until the tree is over-fitted to the data and the final groups occupy the leaves or terminal nodes of the diagram; the overlarge tree is then pruned back to the desired size using complexity plots (based on 10-fold cross-validation) and research goals (De'ath and Fabricius 2000, Urban et al. 2002). Pruning the tree minimizes over-generalizations often due to spurious or coincidental relationships peculiar to a sample set and not general to the population overall. The total percentage of correct classification is reported for the classification trees based on presence or absence of the target weeds.

To create the CART decision trees from which the rule-based models are derived we used the R statistical package (http://www.r-project.org). We used the decision tree module in ENVI to apply the CART rules to create invasion probability maps for the study area.

5. Development of the Uninvaded Plant Communities Map

Our ecological analysis indicated that the chaparral and scrub communities had different responses to the encroachment of the invasive weeds and should be modeled separately. Our first step in the modeling procedure was to develop a community-level map to use as a mask to separate the scrub areas from the chaparral areas during the modeling. We used the CART techniques with the ecological field plots as the dependent variable and the GIS layers as the independent variable.

Figure 5 shows the decision tree and resulting GIS image map depicting the spatial distribution of the scrub and chaparral plant communities in the area of the flight paths. This "uninvaded" map shows the distribution of the two communities without consideration of the target invasive species. The CART decision tree correctly classified 96.3% of the 644 plots (a combination of the field plots and ground-truthing plots where the plant community identification had been verified on the ground). Differences in elevation and soil type were significant predictors for the scrub and chaparral communities in this area. A rule-based model was constructed based on the set of "if-then-else" rules derived from the classification tree. Each pixel in the image was then input into the model and classified as to scrub or chaparral.

We visually compared our results for the uninvaded scrub and chaparral communities map based on the CART model with a field ecology map provided to us by VAFB personnel (Figure 6). The two maps are in remarkably close agreement.
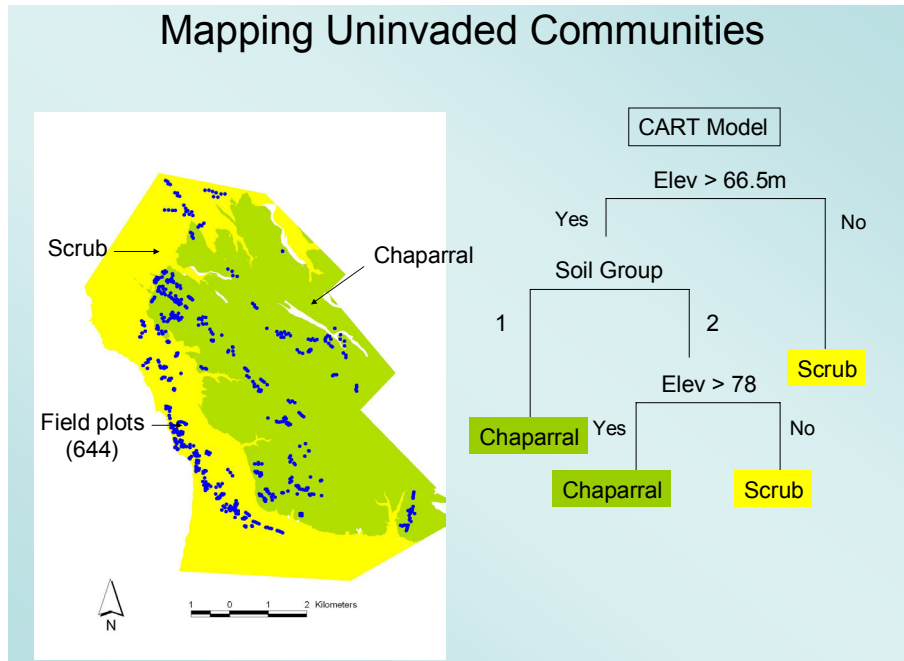
Mapping Uninvaded Communities

Figure 5. Predicted scrub and chaparral distribution map derived from the CART analysis decision tree.

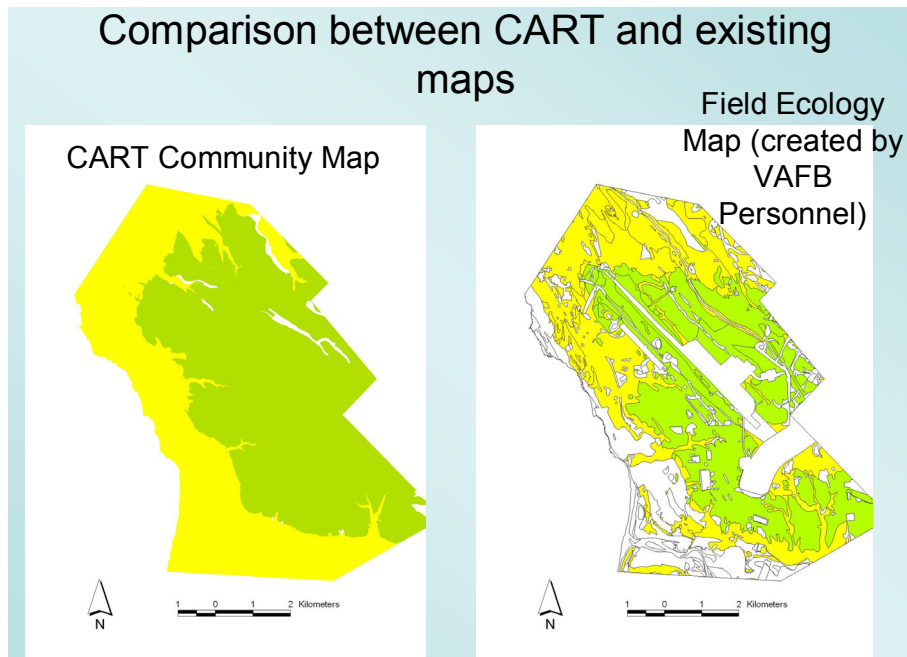## Comparison between CART and existing maps

Figure 6. Comparison of the predicted community map and a vegetation map for VAFB.

6. Development of the Hyperspectral Imagery Map

We used AVIRIS imagery (3.7 m pixels) collected on September 6, 2000 to create a map of the location of the pampas grass and the iceplant as described in Underwood et al, 2002. The classified map is shown in Figure 7. The classification was 70% successful in identifying pampas grass and 98% successful in identifying iceplant.

7. Development of a Map of Invasion Risk

We used the AVIRIS map as the dependent variable for the invasion risk modeling. Each pixel in the map has a possible value of "uninvaded", pampas, or ice plant. To create a statistical sampling set, we used a "virtual sampling" technique. We developed a sampling grid of points spaced 100 m apart that could overlaid on top of the AVIRIS to extract the value at each grid point as shown in Figure 8. We then used the same grid with the GIS layers to extract the independent (predictor) variables. This virtual
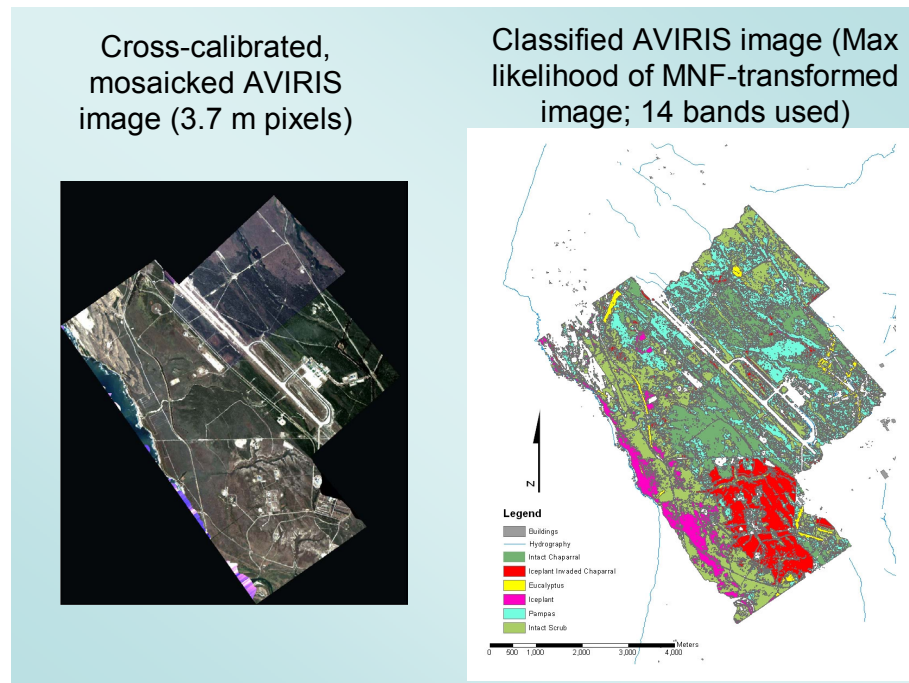

Figure 7. AVIRIS imagery and vegetation classification map for Vandenberg AFB.
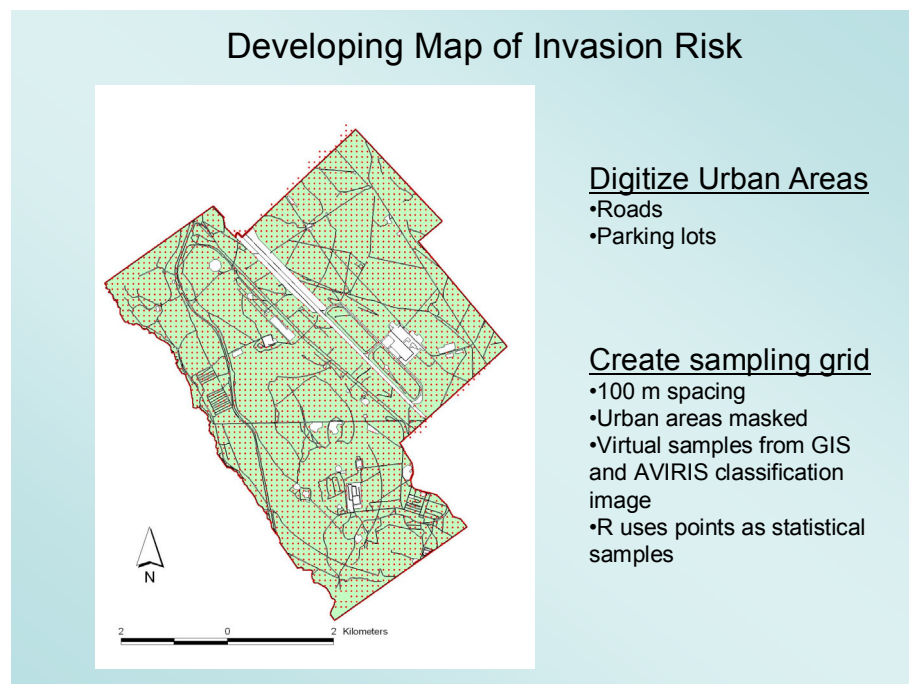

Figure 8. Virtual sampling technique for CART analysis.

sampling grid gave us complete coverage over the flight path areas. We digitized polygons around the urban areas to remove these grid points from the analysis.

   We hypothesized that the invasion of weeds could be predicted by two general classes of predictor variables. First are those parameters that are the natural landscape variables not under human control (Figure 9). This includes such things as elevation, soil type, soil permeability, slope, aspect, etc. The second class is those parameters that are anthropogenic (Figure 10). This second class includes, control burns, roads, buildings, pastures, ditches, etc. The analysis described below is that for the natural
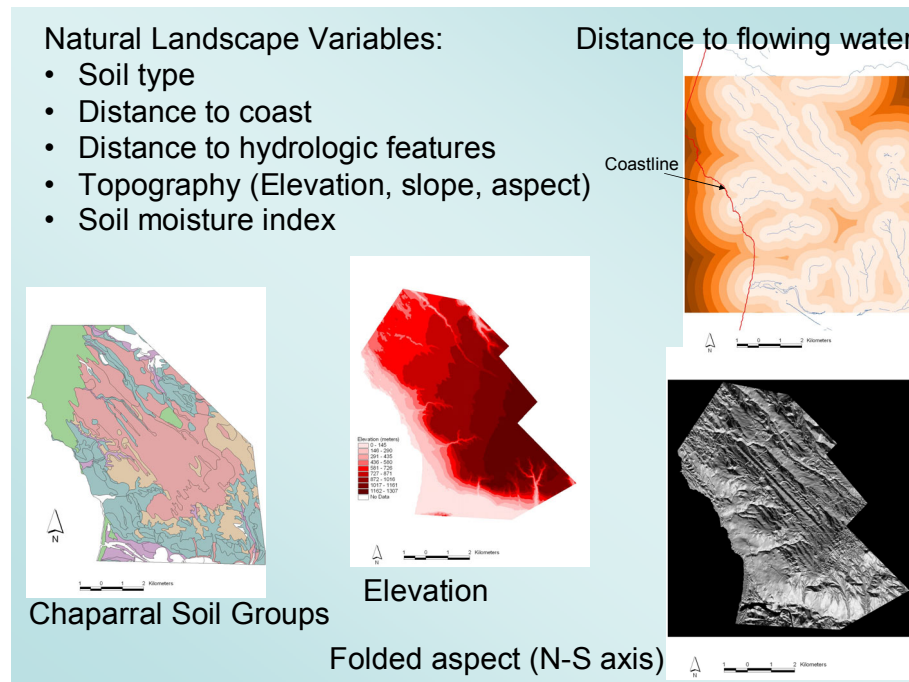

Figure 9. Examples of natural landscape GIS layers used in the CART analysis at Vandenberg AFB.
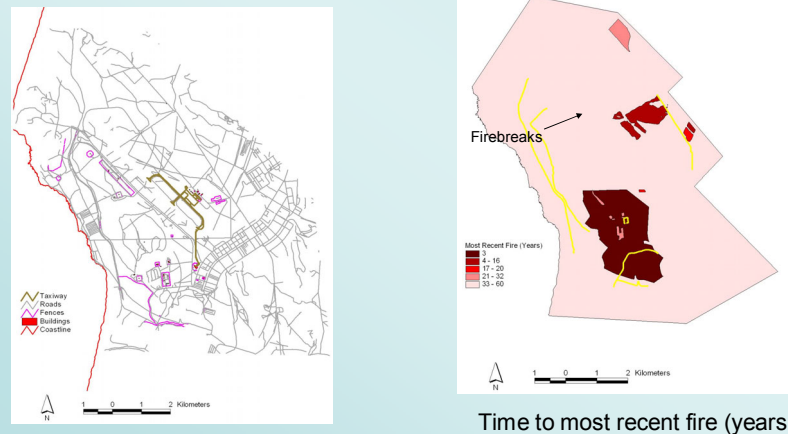

Figure 10. Examples of anthropogenic GIS layers to be used in the CART analysis at Vandenberg AFB.

landscape variables. We will be investigating the anthropogenic variables at a later date. Our approach was to first develop maps predicting the distribution of the invasive weeds using a CART model with the natural landscape variables and then investigate changes in the distribution after including the anthropogenic variables. Using points on the sampling grid we populated a database by first extracting the plant community predicted by the AVIRIS image and then extracted variables of interest from the various GIS layers provided by VAFB. Separate CART models were developed for the scrub and chaparral associated communities.

Figure 11 shows the classification decision tree resulting from the CART analysis for the scrub community. Percentages at the termination of each node represent the percentage of sites that follow that branch of the tree to its terminus. Of the sites that were within 245 m of the coast 76% of them were not invaded. The remaining sites beyond 245 m of the coast were separated using a complex suite of predictors that included the type of soil, distance to flowing water, elevation, percent slope and aspect. This decision tree correctly classified 86% of the 1068 sampling grid points.

Figure 12 shows the classification decision tree resulting from the CART analysis for the chaparral community. This tree is a complex interaction between the soil types, distance to coast, and elevation. Sixty-seven percent of the 1864 sampling grid points were correctly classified by this tree.

The CART rules shown in Figures 11 and 12 were used in the ENVI Decision Tree module as shown in Figure 13. Each pixel was assigned a probability of invasion based on which endpoint on the tree the pixel represents. A comparison between the original AVIRIS image and the CART results for iceplant and pampas grass is shown in Figures 14 and 15, respectively.

8. Summary

The CART modeling technique provides a powerful, highly intuitive method to look at spatial ecological data. Once the variables promoting weed invasion have been identified by the CART model, high risk areas can be plotted out in the GIS as in the examples shown in Figures 14 and 15. Alternative scenarios can be explored by modifying the GIS layers, then running the Decision Tree to see the effects of a planned action.
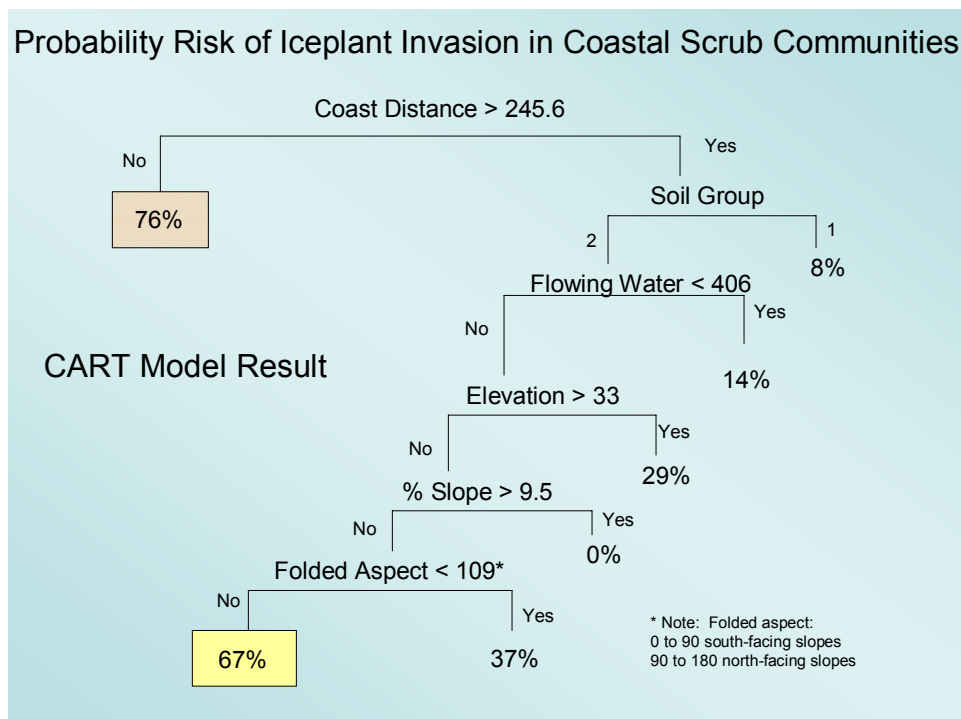

Figure 11: CART tree developed for iceplant invasion into scrub community at Vandenberg AFB.

CART Model for Invasion in Chaparral Communities

Chap Soil Grp = 1

Coast Dist > 3300   Soil Grp = 2

Ice 69%
Pamp 28%

Ice 7%
Pamp 79%

Elev < 100

Ice 10%
Pamp 29%

Coast Dist > 3355

Elev < 85

Ice 7%
Pamp 75%

Ice 68%
Pamp 21%

Ice 0%
Pamp 59%

Coast Dist > 2908

Soil Grp = 3

Elev > 106

Ice 9%
Pamp 60%

Ice 4%
Pamp 33%

Elev < 90

Ice 86%
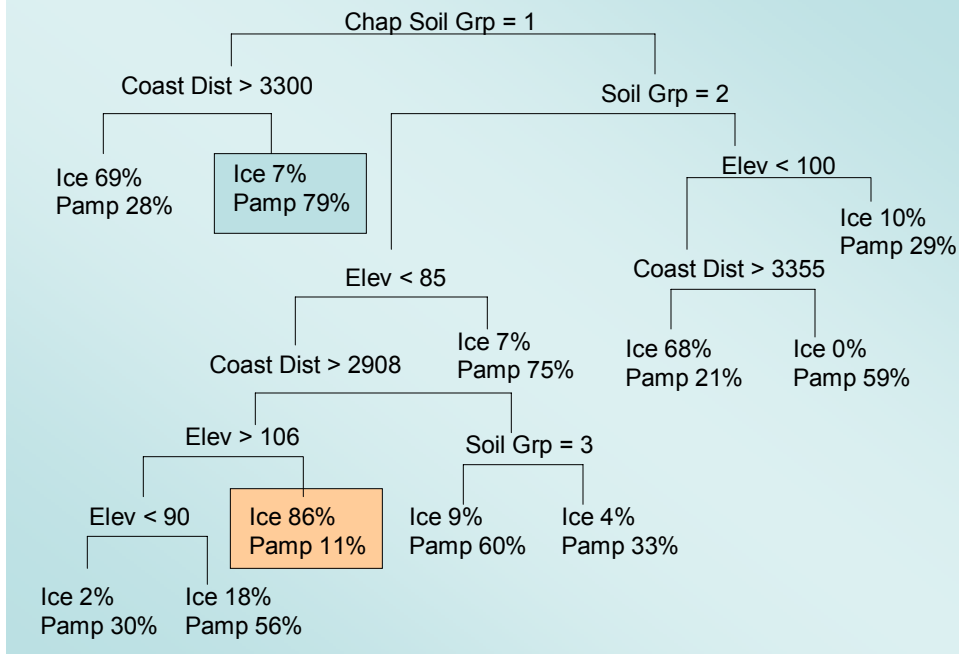Pamp 11%

Ice 2%
Pamp 30%

Ice 18%
Pamp 56%

Figure 12. CART tree developed for iceplant and pampas grass invasion into chaparral community at Vandenberg AFB.

Decision Tree (ENVI) Application of Classification Rules
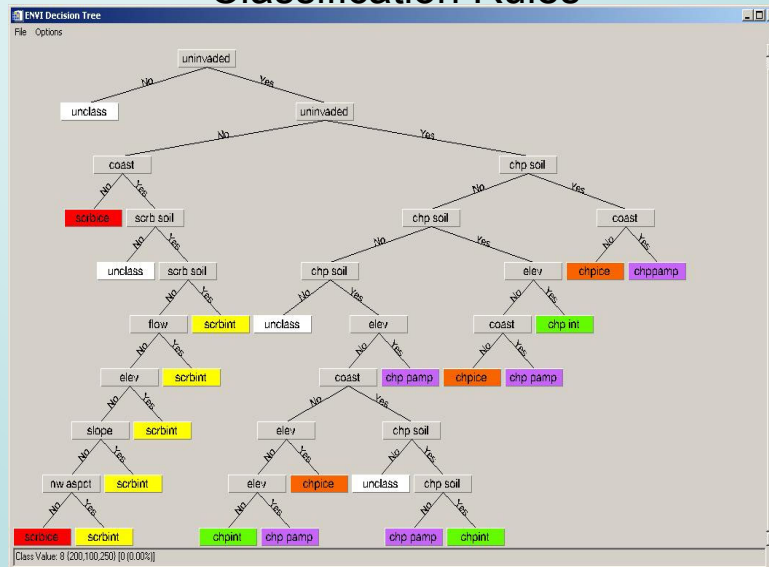
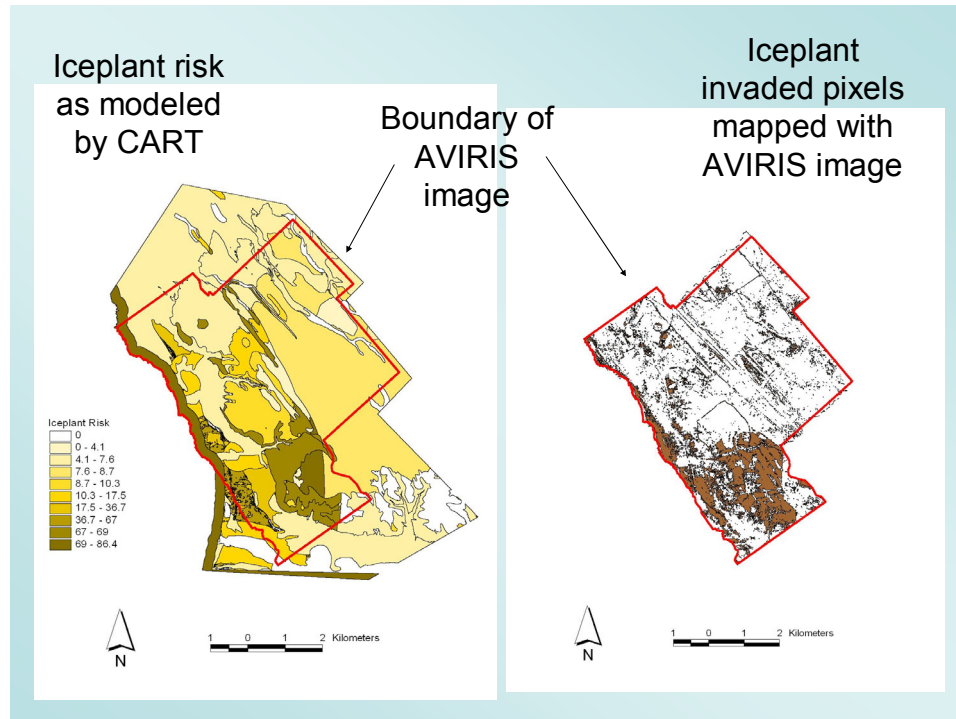Figure 13. Example of application of CART rules in the Decision Tree module of ENVI.

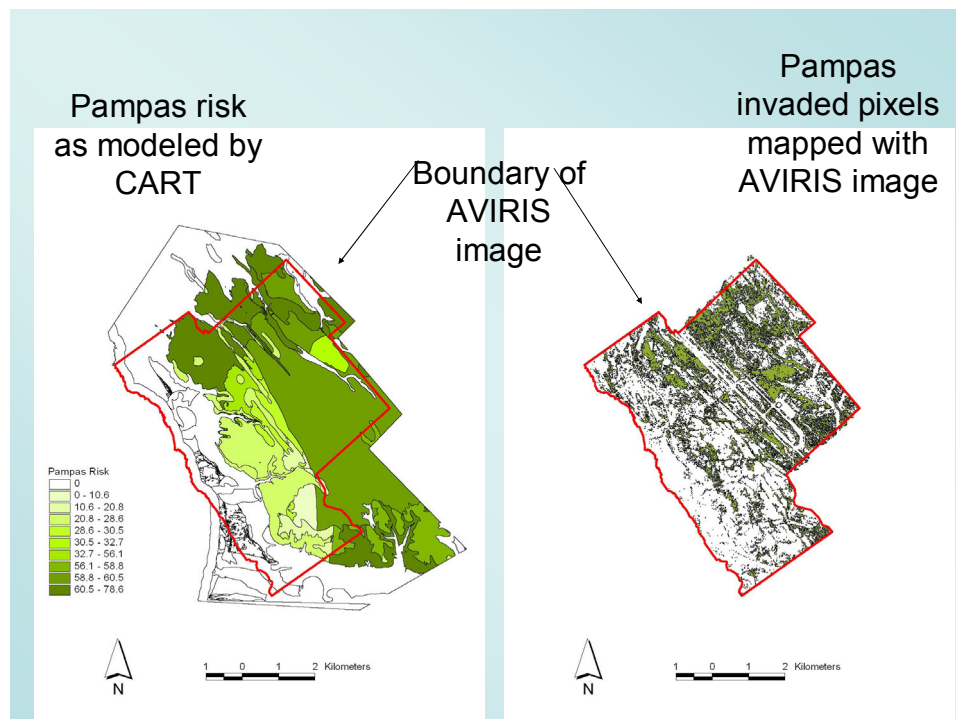Figure 14. Comparison between CART-derived iceplant invasion risk and original AVIRIS map.

Figure 15. Comparison between CART-derived pampas grass invasion risk and original AVIRIS map.

9. References

Babbitt, B. 1998. Statement by the Secretary of the Interior on invasive alien species. *Proc. Int. Weed Symp*. BLM Weed Page, April 8-10, 1998.

Breiman, L., J.H. Friedman, R.A. Olshen, and C.J. Stone. 1984. *Classification and regression trees*. New York: Chapman and Hall.

Coulombe, H.N. and C.F. Cooper. 1976. *Ecological Assessment of VAFB, California: Evaluation and Recommendations, Volume 1 and 2*. San Diego State University, Center for Regional Environmental Studies for U.S. Air Force. HQ, SAMSO, AFCEC-TR-76-15.

De'ath, G., and K.E. Fabricius. 2000. Classification and regression trees: a powerful yet simple technique for ecological data analysis. *Ecology* 81:3178-3192.

Keil, D.J., and V.L. Holland. 1998. *Documented flora of Vandenberg Air Force Base, Santa Barbara County, California*. The Nature Conservancy and Vandenberg Air Force Base

Michaelson, J., D.S. Schimel, M.A. Friedl, F.W. Frank and R.C. Dubayah. 1994. Regression tree analysis of satellite and terrain data to guide vegetation sampling and surveys. *Journal of Vegetation Science* 5:673-686.

Pimentel, D., McNair, S., Janecka, J., Wightman, J., Simmonds, C., O'Connell, C., Wong, E., Russel, L., Zern, J. Aquino, T., and T. Tsomondo. 2000. Economic and environmental threats of alien plant, animal and microbe invasions. *Agri. Ecosys. & Environ.* 84: 1-20.

TNC. 1991. *Fish and wildlife management plan for Vandenberg Air Force Base*; Revision Number 3 for Plan Period August 1991 to August 1996. The Nature Conservancy

Urban, D., S. Goslee, K. Pierce, and T. Lookingbill. 2002. Extending community ecology to landscapes. *Ecoscience* 9 (2):200-212.

Underwood E.C., S.L. Ustin and D. DiPietro. 2002. Mapping non-native plants (iceplant) using hyperspectral imagery. *11th Earth Science Airborne Workshop*, Jet Propulsion Laboratory, Pasadena, CA March 31-April 2, 2002.

Vayassieres, M.P., R.E. Plant, B.H. Allen-Diaz. 2000. Classification trees: an alternative non-parametric approach for predicting species distributions. *Journal of Vegetation Science* 11:679-694.

NONLINEAR NEURAL NETWORK MIXTURE MODELS FOR FRACTIONAL ABUNDANCE ESTIMATION IN AVIRIS HYPERSPECTRAL IMAGES

Javier Plaza,[1] Pablo Martínez, Rosa Pérez, and Antonio Plaza

1. Introduction

The interpretation of mixed pixels is a key factor in the analysis of hyperspectral imagery. Mixed pixels are a mixture of more than one distinct substance, and exist for one of two reasons. Firstly, if the spatial resolution of the sensor is not high enough to separate different materials, these can jointly occupy a single pixel, and the resulting spectral measurement will be a composite of the individual spectra that reside within the pixel. Secondly, mixed pixels can also result when distinct materials are combined into a homogeneous mixture [1]. This circumstance occurs independent of the spatial resolution of the sensor.

A commonly used approach to mixed pixel classification has been linear spectral unmixing, which uses a linear mixture model (LMM) to estimate the abundance fractions of spectral signatures lying within a mixed pixel [2]. Although the LMM has been demonstrated in numerous applications to be a useful technique for interpreting remote sensing data with high dimensionality, the question of whether linear or non-linear processes dominate spectral signatures of mixed pixels is still an unresolved matter. It has been reported that the reflectance spectrum of a mixture is a systematic combination of the component reflectance spectra in the mixture (usually called endmembers in the literature). The combination tends to be linear if components of interest in a pixel appear in spatially segregated patterns. If, however, the components are in intimate association, light typically interacts with more than one component as it is multiply scattered, and the mixing systematics between the different components are highly nonlinear. Nonlinear effects are an area of active research in particular applications such as vegetation and canopy studies [3] or water quality assessment [4–5], where LMM generally result in poor mixture analysis accuracy.

Artificial neural networks (ANNs) have been widely studied in the literature as a promising alternative to accomplish the difficult task of estimating fractional abundances of endmember materials in hyperspectral scenes [6]. The advent of ANN approaches in hyperspectral analysis is mainly due to their power in pattern recognition and classification [7]. The problem of mixed pixels has been tackled before from an ANN-based perspective, specifically, associative ANNs have been used in the past to establish a linear mixture model based on endmembers. Despite these attempts, ANN-based nonlinear mixing techniques remain largely unexplored for general-purpose applications. Only the pioneering work by Guilfoyle and Chang [8], which constructed a neural architecture based on radial basis function (RBF) neural networks, can be considered as a general model for ANN-based nonlinear unmixing independent of specific physical properties of the observed land-cover materials. Such specificity usually complicates nonlinear models in terms of both implementation and computational complexity, and prevents their generalization to different applications, which is one of the most powerful features of the LMM.

In this paper we describe a new methodology for inferring land cover fraction within hyperspectral scenes. The proposed methodology makes use of a modified multi-layer perceptron (MLP) neural network, whose entries are determined by a linear activation function provided by a Hopfield neural network (HNN). As a result, our combined HNN/MLP method uses the LMM to provide an initial abundance estimation in linear fashion, and then refines the linear estimation using a nonlinear mixing model. To the best of our knowledge, this is the first approach in the literature that integrates linear and

[1]Neural Networks & Signal Processing Group (GRNPS), Computer Science Dept. University of Extremadura, Spain
Contact e-mail: jplaza@unex.es, Phone: +34 927 257254, Fax: +34 927 257203

nonlinear unmixing concepts for fractional abundance estimation in hyperspectral imagery. The remainder of the paper is organized as follows. Section 2 describes an Automated Morphological Endmember Extraction algorithm that is used in this work to find adequate training samples for the proposed neural architecture. Section 3 describes the proposed HNN/MLP method. Section 4 conducts a series of experiments where simulated data, made up of real spectra collected by the NASA/JPL Airborne Visible and Infra-Red Imaging Spectrometer (AVIRIS), are used to investigate performance of our approach. The impact of noise, mixture complexity, and use of radiance/reflectance data on algorithm performance are investigated. Section 5 conducts experiments using nonlinearly mixed real data which consists of 13 data sets collected by a Relab spectrometer (a high resolution, bi-directional spectrometer at Brown University). Our results with simulated and real data indicate that the proposed methodology is useful, robust and efficient in the task of identifying land cover fractions from remotely sensed imagery at sub-pixel scales, in particular when nonlinear mixtures and/or low SNR conditions dominate the hyperspectral data. Section 6 summarizes our conclusions and provides hints at plausible future research.

2. Automated morphological endmember extraction

The algorithm used in this work to generate training samples for the proposed neural network architecture is the automated morphological endmember extraction (AMEE) algorithm [9]. It is the only available endmember extraction algorithm that makes simultaneous use of spatial and spectral information via multi-channel morphological processing [10]. The input to the AMEE method is the full image data cube, with no previous dimensionality reduction. Let $\boldsymbol{h}$ denote the input hyperspectral data cube and $\boldsymbol{h}(x, y)$ denote the pixel vector at spatial location (x, y). Similarly, let K be a kernel defined in the spatial domain of the image (the $x - y$ plane). This kernel, usually called structuring element (SE) in mathematical morphology terminology, is translated over the image. The SE acts as a probe for extracting or suppressing specific structures of the image objects, according to the size and shape of the SE. Having the above definitions in mind, the AMEE method is based on the application of multi-channel erosion and dilation operations to the data. The above operations are respectively defined as follows.

$$(\boldsymbol{h} \otimes K)(x, y) = \arg\_ \text{Min}_{(s,t) \in K} \left\{ \sum_s \sum_t \text{dist}(\boldsymbol{h}(x, y), \boldsymbol{h}(x + s, y + t)) \right\} \tag{1}$$

$$(\boldsymbol{h} \oplus K)(x, y) = \arg\_ \text{Max}_{(s,t) \in K} \left\{ \sum_s \sum_t \text{dist}(\boldsymbol{h}(x, y), \boldsymbol{h}(x - s, y - t)) \right\} \tag{2}$$

where dist is the spectral angle mapper (SAM). Multi-channel erosion (respectively, dilation) selects the pixel vector which minimizes (respectively, maximizes) a cumulative distance-based cost function, based on the sum of the SAM distance scores between each pixel in the spatial neighborhood defined by K and all the other pixels in the neighborhood. As a result, multi-channel erosion extracts the pixel vector that is more similar to its neighbors as opposed to multi-channel dilation, which extracts the most spectrally distinct pixel in the neighborhood (endmember candidate). It should be noted that, according to the definition of morphological erosion and dilation, the above operations are sensitive to the size and shape of the SE used in the computation. In our application, a morphological eccentricity index (MEI) is defined for each endmember candidate by calculating the SAM distance between the pixel provided by the dilation operation and the pixel provided by the erosion. This operation is repeated for all the pixels in the scene, using SEs with a range of different sizes, until a final MEI image is generated. A set of endmembers signatures $\{\boldsymbol{e}_i\}_{i=1}^N$ is found by a fully automated approach which consists of two steps [9]: 1) automated segmentation of the MEI image and 2) Spatial/spectral region growing of resulting regions.

202

3. Proposed neural network architecture for solving the nonlinear mixing problem

Once a set of endmember signatures $\{e_i\}_{i=1}^{N}$ has been extracted from the original image, our goal is to solve the mixing equation $h(x, y) = \sum_{i=1}^{N} c_i e_i$ for each hyperspectral image pixel $h(x, y)$. Let us denote by $e_i = [e_{1i}, e_{2i}, ..., e_{Li}]^T$ a pure endmember signature, where L is the number of spectral bands. Similarly, let $c_i = f(a_i)$ be the contribution of endmember signature e_i in the pixel given by a nonlinear mixing function f, where a_i is the real abundance fraction of e_i in the pixel. If we express the problem using a matrix notation, i.e. $E = [e_1, e_2, ..., e_N]$, $c = [c_1, c_2, ..., c_N]$ and $a = [a_1, a_2, ..., a_N]$, then our goal is to solve the equation $h(x, y) = Ec^T$ at each pixel. In this work, we propose to solve the linear part of the problem, i.e., $c^T = E^{-1}h(x, y)$, by a modified Hopfield neural network (HNN). On other hand, the nonlinear part of the problem related with the mixing equation, i.e., $a = f^{-1}(c)$, is solved by using a Multi-Layer Perceptron (MLP). The effectiveness of this approach has been demonstrated in previous work [4],[11].
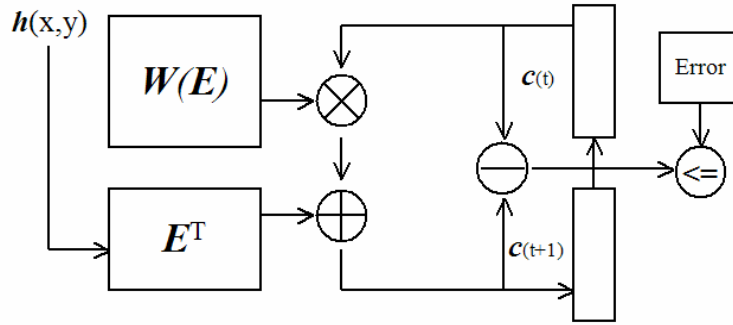

Figure 1. Schematic block diagram summarizing the performance of the HNN module.

3.1 Modified Hopfield neural network (HNN)

In order to solve the linear part of the mixing problem, we use a modified Hopfield neural network (HNN) with gradient descent learning based on error minimization (see Fig. 1). The number of input neurons is N, i.e., the dimension of the fractional abundance vector c. A weight matrix W is created by using the sample correlation matrix between AMEE-derived endmember materials $\{e_i\}_{i=1}^{N}$. The bias vector is dependent on the mixture spectrum under analysis. The proposed HNN is based on an iterative process where an initial abundance estimation $c(t)$ is refined by multiplying $c(t)$ by the weight matrix. The bias vector is then added and the result $c(t+1)$ is compared to that obtained at the previous iteration until a desired threshold condition is satisfied for convergence.

3.2 Multi-layer perceptron (MLP)

In order to refine the HNN-based linearly derived contribution estimations obtained in the previous subsection, we propose to use a Multi-layer perceptron (MLP) neural network. The entries to the MLP are the outputs of the HNN, which we denote by $c_{(HNN)}^i$, where $i = 1, ..., N$. The number of input neurons is the same as the number of output neurons (see Fig. 2). The number of hidden neurons can be adjusted depending on the problem, and is only important in terms of convergence time. In this work, we have

used a recently developed concept of virtual dimensionality (VD), which estimates the number of distinct signal sources in the input data, to optimize the number of hidden neurons. On the other hand, the training process is based on error back-propagation criteria, where the output nodes and the hidden nodes modify their respective weight matrices (W and V in Fig. 2) depending on a pre-defined error (Delta), the input data, and an adjustable learning parameter Alpha (see Fig. 3). The delta error of the output layer is calculated as the difference between the abundance estimation ouputs a_i , $i = 1,...,N$ provided by the network architecture in Fig. 2 and a set of desired outputs given by ground truth fractional abundances available for the training samples. The resulting error is back-propagated to the hidden nodes until convergence is reached.
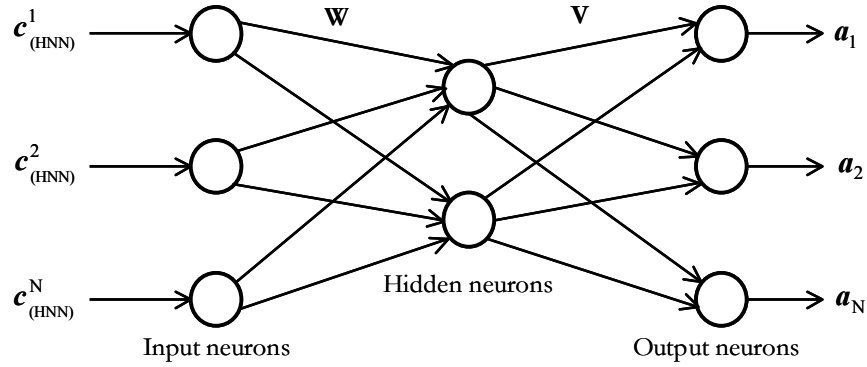
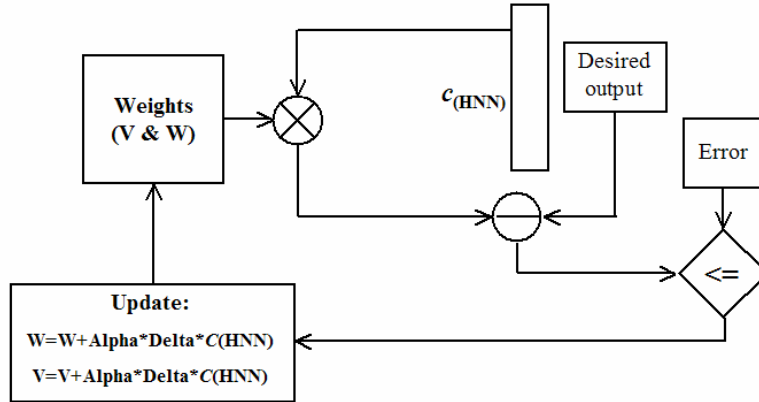

Figure 2. Architecture of the MLP module.

Figure 3. Schematic block diagram summarizing the performance of the MLP module.

4. Simulation experiments

One of the major problems involved in analyzing the quality of fractional abundance estimation methods in remotely sensed imagery is the fact that ground-truth information about the real abundances of materials at sub-pixel levels is very difficult (if not impossible) to obtain in real scenarios [10]. This fact has traditionally prevented the existence of comparative surveys using large databases of real images. In order to avoid this shortcoming, simulation of hyperspectral imagery has been suggested as a simple and intuitive way to perform a preliminary evaluation of analysis techniques [12]. The primary reason for the use of simulated imagery as a complement to real data analysis is that all details of the simulated images

are known. These details, such as noise, mixture complexity, and use of radiance/reflectance data, can be efficiently investigated because they can be manipulated individually and precisely. As a result, algorithm performance can be examined in a controlled manner.

In this section, we use simulated data based on real spectra collected by the AVIRIS imaging spectrometer [13] to accomplish the following experiments. Two AVIRIS imaging spectrometer datasets of the Jasper Ridge Biological Preserve (JRBP) in California have been selected for experiments. The datasets are available from http://aviris.jpl.nasa.gov. The datatets, acquired on April 1998, consist of 512x614 pixels and 224 spectral bands, with a nominal ground resolution of 20 m, spectral resolution of 10 nm, and 16-bit radiometric resolution. In a previous study of surface materials over JRBP, image endmembers were derived from the scenes above based on extensive ground knowledge. Fig. 4 plots spectral signatures associated with two of the main constituent materials at JRBP. These signatures, denoted as r_1 (soil) and r_2 (evergreen forest), will be used to construct two types of simulated data in this paper. Firstly, experiments with simulated linear mixtures are developed. These experiments will be mainly used to adjust input parameters such as Alpha and also to test the sensibility of the proposed HNN/MLP architecture against the signal-to-noise ratio (SNR). Secondly, nonlinear mixtures are simulated using a simple nonlinear function, the logarithmic function, to explore the accuracy of the proposed method in the presence of more complex mixtures. Simulation experiments will be used as a baseline to interpret results with real hyperspectral data, described in the following section. Next, we describe our simulation experiments.

4.1. Simulated linear mixtures

For this experiment, we have artificially mixed r_1 and r_2 in computer simulations to create a simulated scene containing linear mixtures. This scene, with a size of 100x100 pixels, is formed by 100 regions, $R_1,...,R_{100}$, of one-pixel width, representing linear mixtures between r_1 and r_2. Abundance fractions of r_1 at region R_i are assigned by $(i/100)$, while abundance fractions of r_2 at R_i are assigned by $1-(i/100)$, as depicted in Fig. 5(a) and 5(b). The scene represents a subtle mixing scenario where r_1 progressively infiltrates into r_2 and vice versa. Random noise was added to the scene above to simulate contributions from ambient (clutter) and instrumental sources. White gaussian noise was created by using numbers with a standard normal distribution obtained from a pseudorandom number generator and added to each pixel. For the simulations, we consider the SNR for each band as the ratio of the 50% signal level to the standard deviation of the noise, hence following the definition given by Harsanyi and Chang [14]. This results in noise standard deviation that is roughly proportional to the average signal, a phenomenon often observed in radiometric data. Thus, the simulated hyperspectral data were created, based on a simple linear mixture model, by the following expression:

$$s(x,y)=\left(\frac{\text{SNR}}{2}+n(x,y)\right)\cdot\left(\sum_{j=1}^{2}r_j\cdot\alpha_j(x,y)\right)\tag{3}$$

where s denotes a vector containing the simulated discrete spectrum at the pixel with spatial coordinates (x,y) of the simulated image, $\alpha_j(x,y)$ is the assigned fractional abundance of spectral signature at the pixel (x,y), and $n(x,y)$ is the noise factor. Abundance sum-to-one and non-negativity constraints have been imposed in the expression in order to provide the simulation with adequate physical meaning. Six different SNR values, i.e., 10:1, 30:1, 50:1, 70:1, 90:1 and 110:1, were considered in the simulations.
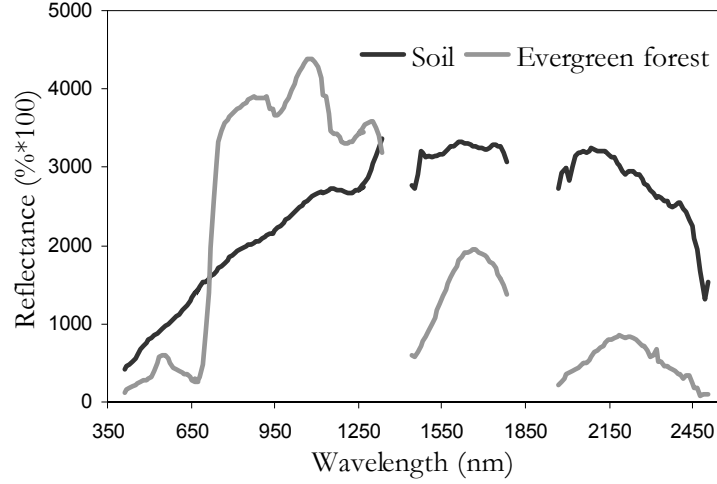
Figure 4. Spectral signatures associated with soil and evergreen forest constituents at AVIRIS Jasper Ridge scene.
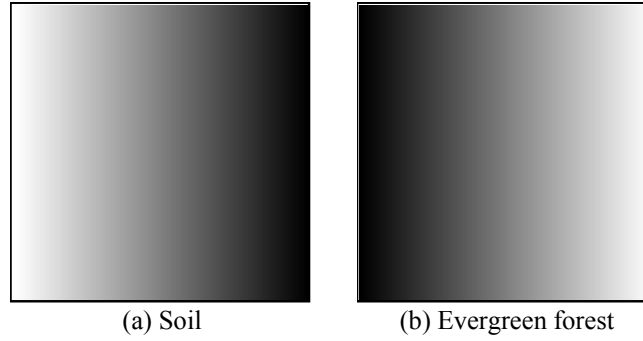

(a) Soil   (b) Evergreen forest

Figure 5. Fractional abundance maps for soil and evergreen forest in the simulated scene with linear mixtures.

Table 1 shows an experimental study of the sensitivity of unconstrained linear spectral unmixing (LMM) and the proposed HNN/MLP to SNR using the root mean square error (RMSE) as the error metric. Let us denote by N and M the total number of samples and lines in the simulated image. Similarly, let us denote by $\hat{\alpha}_j(x,y)$ the estimated fractional abundance of endmember material r_j in the pixel at spatial coordinates (x,y). Then, we can express the RMSE score associated to fractional abundance estimation of r_j by:

$$\text{RMSE}(r_j) = \left(\frac{1}{N \cdot M} \sum_{x=1}^{N} \sum_{y=1}^{M} \left[\alpha_j(x,y) - \hat{\alpha}_j(x,y) \right]^2 \right)^{1/2} \tag{4}$$

Regarding the training of HNN/MLP in this experiment, we used two different training sets. The first training set, designed as training set 1 (TS1), is composed of two AMEE-derived endmembers and 99 additional training samples corresponding to all possible mixtures between r_1 and r_2. The second training set, designed as training set 2 (TS2), is composed of two AMEE-derived endmembers and 9 additional training samples corresponding to nine representative mixtures between r_1 and r_2. As illustrated by equation (3), the LMM model is exclusively based on two AMEE-derived endmembers. As shown in Table 1, TS1 and TS2 resulted in very similar results in terms of RMSE in fractional abundance estimation for the considered HNN/MLP.

Table 1. Comparison of RMSE in fractional abundance estimation accuracy for simulated linear mixtures of r_1 and r_2 by LMM and HNN/MLP using the simulated image in Fig. 5.

Method	Material	No noise	SNR=110:1	SNR=90:1	SNR=70:1	SNR=50:1	SNR=30:1	SNR=10:1
HNN/MLP (TS1)	r_1	0	0.0019	0.0020	0.0023	0.0037	0.0061	0.0174
	r_2	0	0.0019	0.0019	0.0025	0.0033	0.0060	0.0164
HNN/MLP (TS2)	r_1	0	0.0015	0.0018	0.0024	0.0032	0.0054	0.0166
	r_2	0	0.0016	0.0019	0.0023	0.0032	0.0055	0.0164
LMM	r_1	0	0.0056	0.0065	0.0079	0.0106	0.0192	0.0514
	r_2	0	0.0023	0.0032	0.0046	0.0073	0.0158	0.0479

Results in Table 1 reveal that the proposed HNN/MLP neural model seems to be less sensitive than the commonly used LSU in fractional abundance estimation of r_1 (soil) and r_2 (vegetation). It is also worth noting that HNN/MLP performs considerably better than LSU when the SNR is low, thus revealing that our combined linear/nonlinear approach can outperform the unconstrained LMM method in a noisy environment. Due to the sensitivity of the HNN/MLP to the Alpha parameter, we have developed additional experiments using the simulated image in Fig. 5 in order to determine the influence of Alpha in the number of iterations and CPU time in seconds consumed by the proposed method. Specifically, Table 2 shows the number of iterations and subsequent CPU time for different values of Alpha, where the CPU time in seconds was measured in a specific computing environment based on a Personal Computer with Pentium V Processor at 1.6 GHz and 512 Mb of RAM. It should be noted that scores by HNN/MLP in Table 2 refer to experiments using training set TS2.

Table 2. Number of iterations and CPU time in seconds for different values of Alpha in the HNN/MLP method.

Alpha	10^{-5}	2×10^{-5}	3×10^{-5}	4×10^{-5}	5×10^{-5}	6×10^{-5}	7×10^{-5}	8×10^{-5}	9×10^{-5}	10^{-4}	10^{-3}	10^{-2}	10^{-1}
Iterations	470974	235495	157002	117757	94208	78510	67296	58887	52346	47112	4726	480	44
CPU time	166	108	79	76	76	76	66	64	69	55	62	48	50

As shown in Table 2, when low values are used for the Alpha parameter, both the number of iterations and the CPU time in seconds increase considerably. On other hand, if parameter Alpha is set to an appropriate value, both the number of iterations and processing time can be substantially reduced. Since the setting of the Alpha parameter only affects convergence rate, not the final estimation results, this simple experiment will be used to set the Alpha parameter accordingly in the following experiments, which involve both nonlinear mixture simulations and nonlinear mixtures collected in a real analysis scenario.

4.2. Simulated nonlinear mixtures

This subsection describes our experiments with simulated nonlinear mixtures. We have created a second simulated image with nonlinear mixtures of r_1 and r_2 using a simple logarithmic function. The 90x90-pixel scene consists of nine vertical regions $R_1,...,R_9$ of ten pixels in width, containing nonlinear mixtures between r_1 and r_2 . The abundances of r_1 and r_2 were assigned according to equation (5)

$$s(x, y) = \sum_{j=1}^{2} r_j \cdot c_j(x, y) \tag{5}$$

where $c_j(x, y) = \log \alpha_j(x, y)$ is the contribution of endmember r_j and $\alpha_j(x, y)$ is the fractional abundance of r_j. Table 3 shows the fractional abundances assigned to each of the nine simulated regions by means of

equation (5). It should be noted that all the pixels in the simulated scene are mixed in different proportions (there are no pure instances of any material).

Table 3. Abundance assignment for regions in a simulated scene with nonlinear mixtures.

Region	R_1	R_2	R_3	R_4	R_5	R_6	R_7	R_8	R_9
$\alpha_1(x, y)$	0.9	0.8	0.7	0.6	0.5	0.4	0.3	0.2	0.1
$\alpha_2(x, y)$	0.1	0.2	0.3	0.4	0.5	0.6	0.7	0.8	0.9

Table 4 shows an experimental study of the accuracy of linear spectral unmixing (LMM) and the proposed HNN/MLP approach in fractional abundance estimation using the simulated image with nonlinear mixtures described above. Four different training sets were used for the training of the network. The first one, TS1, is composed of nine spectral signatures that represent every possible mixture in the data set. The second one, TS2, uses five out of nine possible mixtures. The third one, TS3, only uses three out of nine possible mixtures. Finally, the fourth considered training set, TS4, uses two AMEE-derived endmembers from the simulated scene. It should be noted that, since there are no pure pixels in the scene, the AMEE algorithm extracted two endmembers that correspond to purest available samples, located in R_1 and R_9 regions, respectively. As reported by Table 4, the lowest RMSE score in abundance estimation was observed when the proposed HNN/MLP method was combined with training set TS1. However, it is also clear from Table 4 that results obtained by HNN/MLP using TS2 and TS3 were very similar in terms of accuracy to those found by HNN/MLP combined by TS1. When HNN/MLP was trained using only the two AMEE-derived endmembers (TS4), the RMSE score was slightly increased. The above result seems to indicate that endmember signatures alone may not be appropriate for training purposes. Although in this case endmember signatures are not completely pure (i.e., they are obtained as the purest available samples) they needed to be combined with additional mixed pixels in order to obtain a representative set of training samples for HNN/MLP. Finally, it is clear from Table 4 that the LMM clearly produced the worst scores in terms of RMSE.

Table 4. Fractional abundance estimation results for simulated nonlinear mixtures of r_1 and r_2 and resulting RMSE after applying the considered methods.

Material	Abundance	LMM	HNN/MLP (TS1)	HNN/MLP (TS2)	HNN/MLP (TS3)	HNN/MLP (TS4)
	0.9	0.975	0.872	0.869	0.873	0.747
	0.8	0.949	0.757	0.757	0.766	0.727
	0.7	0.920	0.673	0.676	0.687	0.705
	0.6	0.887	0.598	0.600	0.616	0.679
r_1	0.5	0.847	0.523	0.530	0.545	0.649
	0.4	0.799	0.440	0.452	0.468	0.612
	0.3	0.737	0.351	0.361	0.378	0.564
	0.2	0.649	0.230	0.242	0.261	0.497
	0.1	0.499	0.038	0.052	0.074	0.382
	0.9	0.975	0.867	0.869	0.874	0.747
	0.8	0.949	0.754	0.757	0.766	0.724
	0.7	0.920	0.671	0.676	0.687	0.705
	0.6	0.887	0.597	0.603	0.616	0.679
r_2	0.5	0.847	0.523	0.530	0.545	0.649
	0.4	0.799	0.444	0.452	0.468	0.612
	0.3	0.737	0.353	0.361	0.378	0.564
	0.2	0.649	0.233	0.242	0.261	0.497
	0.1	0.499	0.042	0.053	0.073	0.382
RMSE		0.1101	0.0014	0.0016	0.0021	0.0378

5. Real data experiments

Up to now, computer simulations were used to demonstrate the effectiveness of HNN/MLP in nonlinear spectral mixture analysis. In this section, real spectra collected from nonlinear mixtures will be analyzed. These data, available from Prof. John Mustard's laboratory at Brown University, consisted of 13 data sets collected using the RELAB spectrometer (a high-resolution, bi-directional spectrometer at Brown University). The measurement precision of the RELAB spectrometer is better than 0.25%, which makes it an ideal candidate to evaluate fractional abundance estimation accuracy. The data included spectra from individual endmembers such as Olivine, Enstatite and Magnetite [15], where Fig. 6 plots the three endmember spectra. Most importantly, the data also contained mixtures of these endmembers with abundances listed in Table 5. As a result, the mixture data were the spectra of true mixtures with known abundances for each endmember. In the available Mustard data samples for these mineral types, only nonlinear mixture spectra with associated abundance values were provided [16].

Table 5. Mustard's nonlinear mixture data sets.

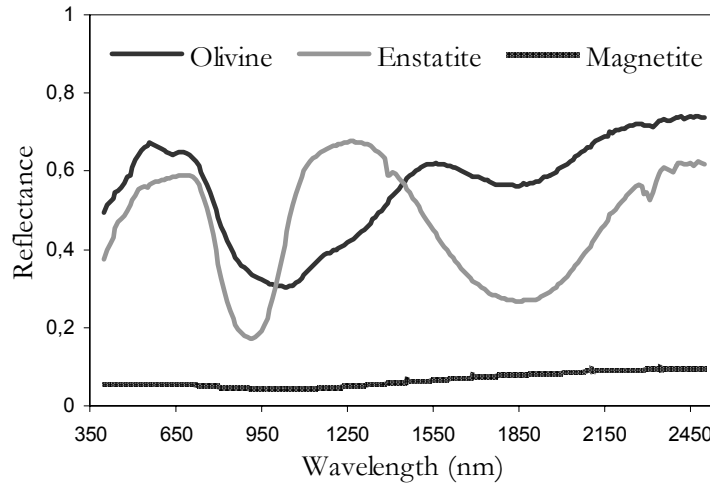| Olivine/Enstatite mixtures		Olivine/Magnetite mixtures	
Olivine abundance	Enstatite abundance	Olivine abundance	Magnetite abundance
0.90	0.10	0.95	0.05
0.75	0.25	0.90	0.10
0.50	0.50	0.75	0.25
0.25	0.75	0.50	0.50
0.10	0.90	0.25	0.75

Figure 6. Mustard's endmember spectra.

Tables 6 and 7 show an experimental study of the accuracy of linear spectral unmixing (LMM), Guilfoyle and Chang's previously developed nonlinear abundance estimation method which uses RBF neural networks, and the proposed HNN/MLP approach in the task of estimating fractional abundances using Mustard's data. Mixtures of Olivine/Enstatite and Olivine/Magnetite are respectively considered. While the training for RBF was accomplished as specified in the literature, three different training sets were used for the proposed HNN/MLP. The first training set (TS1) is composed of a representative spectrum of all possible mixtures. The second training set (TS2), is composed of three out of five possible mixtures. Finally, the third training set (TS3) contains no mixture data at all, only spectra corresponding to pure mineral signatures. For illustrative purposes, results obtained using the simple LMM as well as results obtained by using Guilfoyle and Chang's approach [8] based on RBF neural networks are also reported.

From experimental results in Tables 6 and 7, we can conclude that the proposed HNN/MLP model can accurately estimate the abundance of endmember materials in nonlinear mixtures, provided that the training set contains a representative set of mixed signatures. When nonlinear mixtures of Olivine and Enstatite were considered (see Table 6), we found that the HNN/MLP model trained only with spectral endmembers (TS3) cannot perform better than the simple LMM. However, when training sets made up of mixed signatures (TS1 and TS2) were used, the proposed HNN/MLP clearly outperformed both the LMM and Guilfoyle and Chang's RBF-based method. It is important to note that no significant difference was sought in the abundance estimation accuracy when TS1 or TS2 were used, a fact that reveals that a judicious selection of mixed spectra can help reduce the number of required training samples.

Table 6. Fractional abundance estimation results for real nonlinear mixtures of Olivine and Enstatite and resulting RMSE after applying the considered methods.

Material	Abundance	LMM	RBF	HNN/MLP (TS1)	HNN/MLP (TS2)	HNN/MLP (TS3)
Olivine	0.90	0.880	0.881	0.916	0.913	0.879
	0.75	0.704	0.700	0.736	0.730	0.703
	0.50	0.452	0.443	0.479	0.468	0.452
	0.25	0.244	0.210	0.266	0.251	0.244
	0.10	0.115	0.121	0.115	0.117	0.115
Enstatite	0.90	0.886	0.835	0.886	0.890	0.886
	0.75	0.727	0.761	0.731	0.721	0.725
	0.50	0.535	0.551	0.521	0.517	0.534
	0.25	0.298	0.295	0.263	0.267	0.298
	0.10	0.133	0.114	0.083	0.091	0.133
RMSE		0.0010	0.0012	0.0003	0.0003	0.0010

On other hand, when nonlinear mixtures of Olivine and Magnetite were considered, it is clear from Table 7 that Guilfoyle and Chang's RBF-based method performed the best, with the proposed HNN/MLP producing very close results in terms of abundance estimation when both TS1 and TS2 were used as training sets. Using only endmember signatures for training produced better results than those found by the standard LMM, but the overall accuracy in terms of RMSE decreased as compared to that found by RBF and HNN/MLP with other considered training sets.

Table 7. Fractional abundance estimation results for real nonlinear mixtures of Olivine and Magnetite and resulting RMSE after applying the considered methods.

Material	Abundance	LMM	RBF	HNN/MLP (TS1)	HNN/MLP (TS2)	HNN/MLP (TS3)
Olivine	0.95	0.843	0.946	1.000	0.965	1.000
	0.90	0.697	0.899	0.883	0.831	0.879
	0.75	0.457	0.765	0.651	0.599	0.608
	0.50	0.255	0.576	0.533	0.435	0.329
	0.25	0.102	0.300	0.411	0.298	0.138
Magnetite	0.75	0.895	0.693	0.643	0.708	0.995
	0.50	0.741	0.407	0.513	0.559	0.789
	0.25	0.533	0.199	0.184	0.187	0.271
	0.10	0.298	0.075	0.136	0.127	0.191
	0.05	0.153	0.031	0.053	0.030	0.059
RMSE		0.0429	0.0024	0.0057	0.0044	0.0285

Overall, experiments in Tables 6 and 7 demonstrate that nonlinear abundance estimation methods generated a substantially better mass fraction estimate than did the LMM in Mustard's data. These results, combined with those found in computer simulations, indicate that the proposed HNN/MLP method worked well on both linearly and nonlinearly mixed data, in particular, when an appropriate set of training samples was selected for the learning stage [17].

6. Conclusions and future research

This paper has described a combined HNN/MLP neural network for estimating the abundance of endmember materials in hyperspectral images. The proposed neural model integrates the concepts of linear and nonlinear unmixing. In a first stage, a rough estimation of concentrations is accomplished by HNN via LMM. This initial estimation is refined by MLP in a second step using nonlinear mixing concepts. The experiments conducted in this paper have shown that the proposed HNN/MLP model is a useful tool for performing abundance estimation in both simulated and real hyperspectral imagery data, in particular, when the data are dominated by nonlinear mixing effects. Since the HNN/MLP used in this analysis is a hybrid of linear and nonlinear estimators, it can be easily adapted to either the linear or nonlinear mixture model. An important issue for successful application of the combined HNN/MLP model is the selection of an appropriate set of training samples for supervised learning. In this work, we have explored different training sets composed by several combinations of endmember signatures as well as mixed signatures. From our experiments, we conclude that endmember signatures alone cannot define an appropriate training set for the network, which also requires other types of training samples such as mixed signatures for successful exploitation. Future work will investigate four different types of signatures: pure (endmember), mixed, anomalous and homogeneous to develop appropriate mechanisms to generate a set of good training samples for HNN/MLP in unsupervised mixed pixel classification [17]. Also, since the experiments presented in this paper only consisted of binary mixtures which were intended to show the usefulness of the proposed method, further experiments with ternary or quaternary mixtures are highly desirable.

Acknowledgements

References

[1] N. Keshava and J.F. Mustard, "Spectral unmixing," *IEEE Signal Processing Magazine*, vol. 19, pp. 44-57, 2002.

[2] C.-I Chang, *Hyperspectral imaging: spectral detection and classification*, Kluwer Academic/Plenum Publishers, New York, 2003.

[3] G.A. Carpenter, S. Gopal, S. Macomber, S. Martens and C.E. Woodcock, "A neural network method for mixture estimation for vegetation mapping," *Remote Sensing of Environment*, vol. 70, pp. 138-152, 1999.

[4] J. Plaza, P. Martínez, R. Pérez, A. Plaza, M.C. Cantero, "Nonlinear neural network-based mixture model for estimating the concentration of nitrogen salts in turbid inland waters using hyperspectral imagery," *SPIE Optics East Conference, Chemical and Biological Standoff Detection*, Philadelphia, Pennsylvania, USA, 2004.

[5] M.C. Cantero, R. Pérez, P. Martínez, P.L. Aguilar, J. Plaza and A. Plaza, "Analysis of the behaviour of a neural network model in the identification and quantification of hyperspectral signatures applied to the determination of water quality," *SPIE Optics East Conference, Chemical and Biological Standoff Detection*, Philadelphia, Pennsylvania, USA, 2004.

[6] R. Pérez, P. Martínez, A. Plaza and P.L. Aguilar, "Systolic array methodology for a neural model to solve the mixture problem," in *Neural Networks and Systolic Array Design*, World Scientific: Singapore, 2002.

[7] C.M. Bishop, *Neural networks for pattern recognition*, Oxford University Press: Oxford, 1995.

[8] K.J. Guilfoyle, M.L. Althouse and C.-I Chang, "A quantitative and comparative analysis of linear and nonlinear spectral mixture models using radial basis neural networks," *IEEE Transactions on Geoscience and Remote Sensing*, vol. 39, no. 8, Aug. 2001.

[9] A. Plaza, P. Martínez, R. Pérez and J. Plaza, "Spatial/spectral endmember extraction by multidimensional morphological operations," *IEEE Transactions on Geoscience and Remote Sensing*, vol. 40, pp. 2025-2041, 2002.

[10] A. Plaza, P. Martínez, R. Pérez and J. Plaza, "A quantitative and comparative analysis of endmember extraction algorithms from hyperspectral data," *IEEE Transactions on Geoscience and Remote Sensing*, vol. 42, no. 3, pp. 650-663, March 2004.

[11] J. Plaza, A. Plaza, P. Martínez and R. Perez, "Nonlinear mixture models for analyzing laboratory simulated-forest hyperspectral data," *SPIE Image and Signal Processing for Remote Sensing*, Barcelona, Spain, 2003.

[12] J. Plaza, A. Plaza, P. Martínez, R. Pérez, "H-COMP: A tool for quantitative and comparative analysis of endmember identification algorithms," *IEEE International Geoscience and Remote Sensing Symposium*, Toulouse, France, 2003.

[13] R.O. Green et al., "Imaging spectroscopy and the airborne visible/infrared imaging spectrometer (AVIRIS)," *Remote Sensing of Environment*, vol. 65, pp. 227–248, 1998.

[14] J. C. Harsanyi and C.-I Chang, "Hyperspectral image classification and dimensionality reduction: An orthogonal subspace projection approach," *IEEE Transactions on Geoscience and Remote Sensing*, vol. 32, pp. 779–785, 1994.

[15] K.J. Guilfoyle and C.-I Chang, "Application of linear and nonlinear mixture models for hyperspectral imagery analysis using radial basis function neural networks," *Ph. D. Dissertation*, University of Maryland, Baltimore County, 2001.

[16] J.F. Mustard and J.M. Sunshine, "Spectral analysis for earth science investigation," in *Remote Sensing for the Earth Sciences*, Wiley: New York, 1999.

[17] J. Plaza, C.-I Chang, P. Martínez, R. Pérez and A. Plaza, "On the generation of training samples for neural network-based mixed pixel classification," submitted to *SPIE Defense and Security Symposium*, Orlando, Florida, USA, 2005.

Mapping Weathering and Alteration Minerals in Virginia City, Nevada, with AVIRIS and HyperSpecTIR

R. Greg Vaughan[1,2] and Wendy M. Calvin[1]

[1] University of Nevada Reno, Department of Geological Sciences
[2] Present address: Jet Propulsion Laboratory, Pasadena CA (greg.vaughan@jpl.nasa.gov)

1. Introduction

1.1 Virginia City

Situated on the east side of the Virginia Range, Virginia City (Figure 1) is the home of the historic Comstock mining district and was mined as a source of Au and Ag between 1859 and the 1960's, with numerous underground workings and small open pit operations. The Virginia Range consists mostly of Oligocene to Miocene volcanic rocks that overlie Mesozoic metamorphic rocks (Mzvs) and Cretaceous granodiorite (Kgd) (Figure 2). Andesite to dacite flows, breccias and intrusives of the Alta Formation (Ta) (18-15 Ma) (Hudson, 2003) are overlain by intermediate volcanic, volcaniclastic and locally intrusive rocks of the Kate Peak Formation (Tk) (14.7-12 Ma) (Vikre, 1998; Hudson, 2003). Contemporaneous with the Alta Formation was the intrusion of the Davidson diorite (15.2 Ma) (Castor et al., 2002), which forms the bulk of Mt. Davidson just west of the town site. Hydrothermal alteration in the Comstock district is widespread, with several episodes of hydrothermal events and subsequent precious metal mineralization. Alteration mineral assemblages have been distinguished based on their dominant mineral constituents (Hudson, 1987; Hutsinpillar and Taranik, 1988; Vikre et al., 1988; Vikre 1998; Hudson, 2003).

The *alunitic* alteration assemblage consists of alunite + quartz + pyrite; the *alsic* zone consists of pyrophyllite + quartz + diaspore; the *kaolinitic* zone consists of kaolinite + quartz + pyrite; the *illitic* zone consists of illite + montmorillonite (mixed layered) + quartz + pyrite; the *sericitic* zone consists of sericite + quartz + pyrite; and the *propylitic* zone consists of chlorite + albite + epidote + calcite + illite/sericite + quartz + pyrite. Table 1 lists these alteration assemblages with their characteristic mineralogy and also indicates the minerals that display diagnostic spectral features in the VNIR/SWIR wavelength region.

The Alta Formation is generally more altered than the Kate Peak, and the accurate dating of the complex series of magmatic events and pulses of hydrothermal activity and mineralization is the subject of on-going study (S. Castor, pers. comm., 2004). Precious-metal mineralization in the Comstock district is concentrated along major north-northeast trending structures. The Comstock fault, which transects the town site, and the Occidental fault to the east, are two such structures that strike north-northeast, dip steeply to the east, and once provided pathways for mineralizing fluids. Another structural zone to the west of Mt. Davidson, the Jumbo zone (Vikre, 1998), displays acid-sulfate alteration and minor precious metal mineralization in adularia-sericite veins along an east-dipping fault. Recent studies indicate that alteration and mineralization events appear to have shifted from west of Virginia City (Jumbo), to the east (Comstock, then Occidental) with time (Castor et al., 2002; Vikre et al., 2003).

As a historic mining district with over 100 years of activity, much of the surface area in Virginia City (approximately 0.85 km^2) is covered with mine dumps. Mine dumps and tailings piles are composed of minerals like quartz, pyrite, and various clay minerals, and often contain anomalous concentrations of accessory elements such as Hg, As, Cd, Co, Cu, Mo, Ni, Pb, Zn, Se, and Sb. Iron sulfides, most commonly pyrite, exposed at the surface readily oxidize to form secondary Fe-bearing minerals, which are indicative of the chemical conditions under which they form (Swayze et al., 1998; Swayze et al., 2000; Jambor et al., 2000; Bigham and Nordstrom, 2000; Montero et al., 2004). Pyrite oxidation is a complex biogeochemical process involving hydration, oxidation, and microbial catalysis that results in the formation of acidic water (Bigham and Nordstrom, 2000). Acidic surface water, and water that percolates through the porous rock pile, contain dissolved heavy metals and travel away from the acid-generating source. Chemical reactions with other rocks and minerals partially neutralize the pH of the water, which
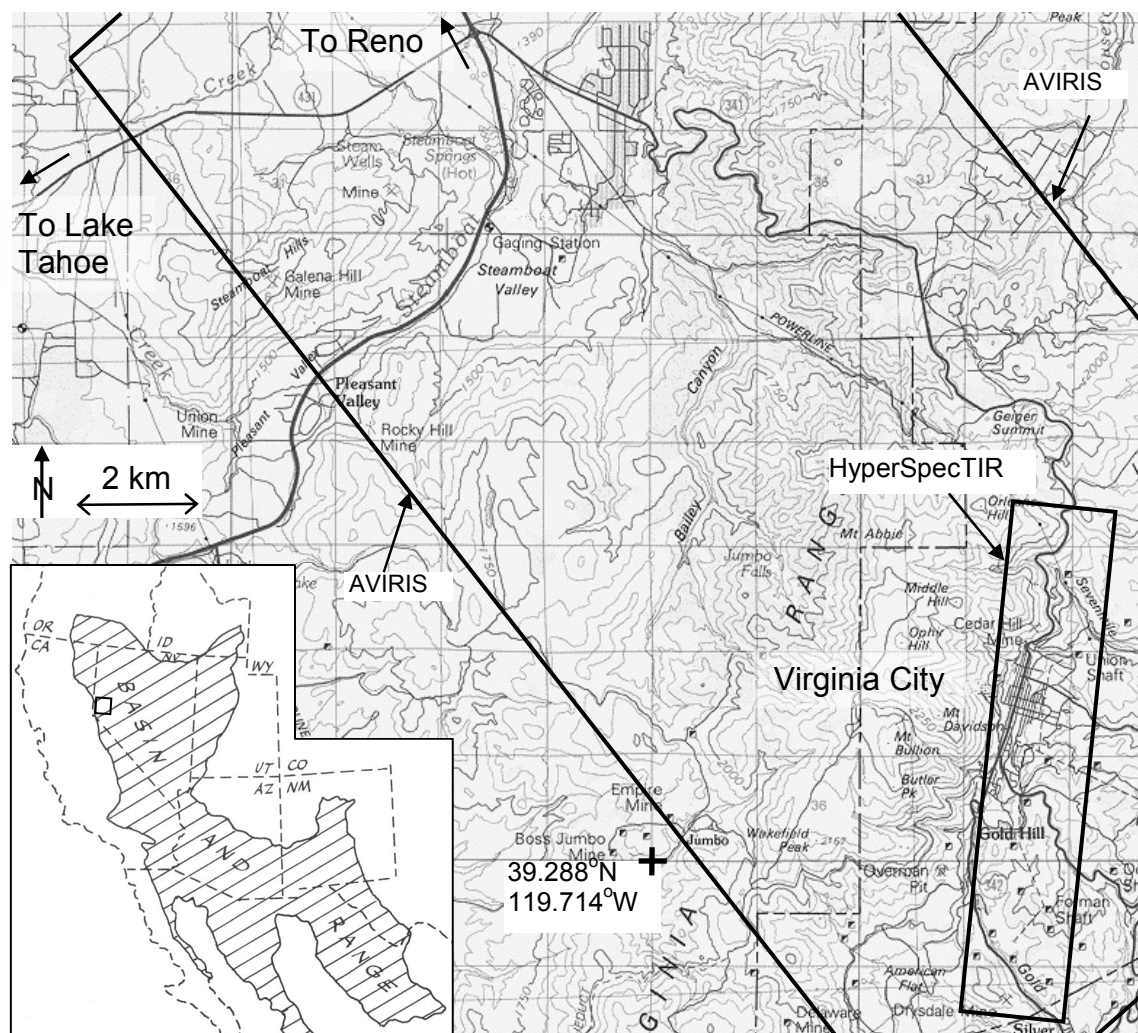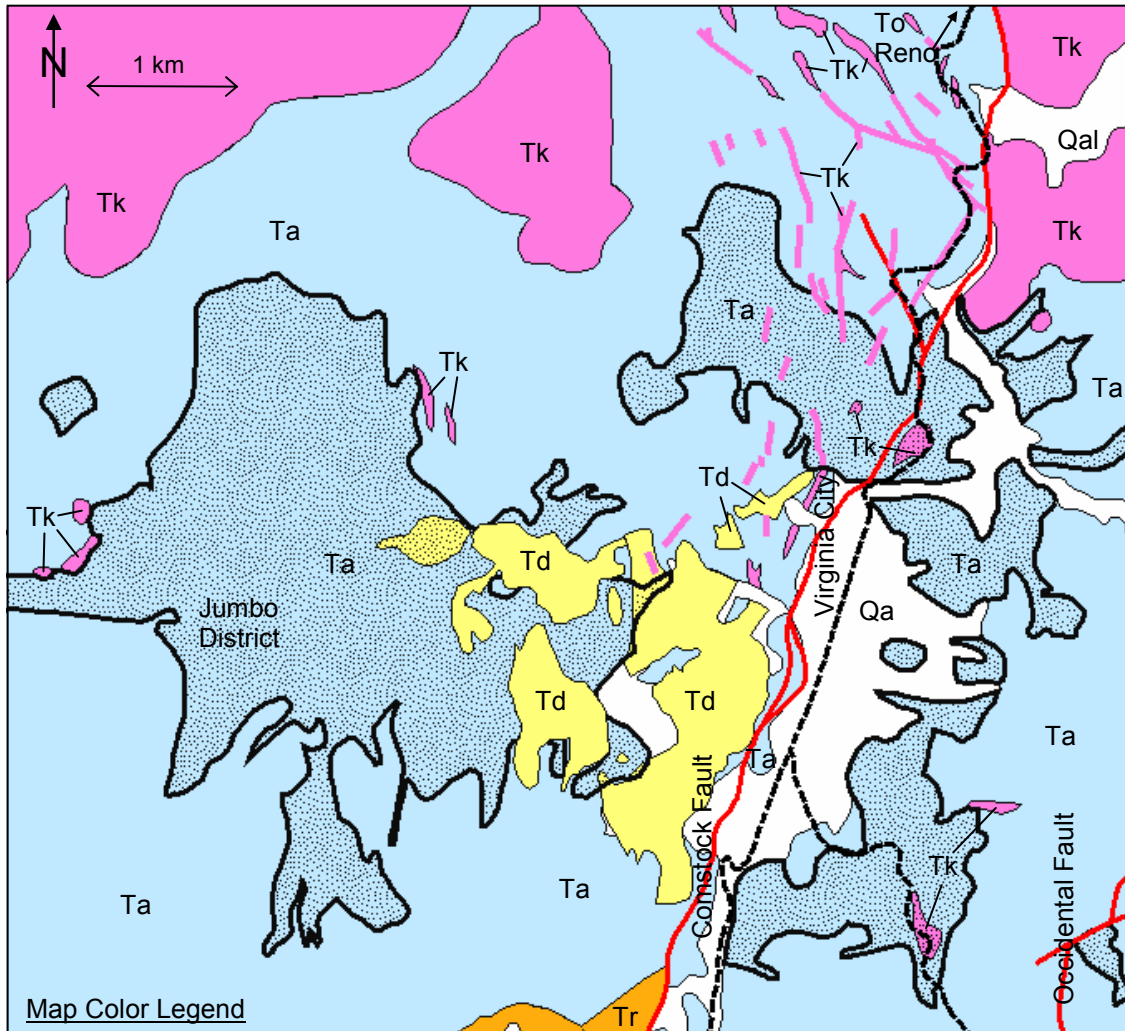
Figure 1. Map showing the location of Virginia City with respect to Nevada and the Basin and Range geologic province. Also shown are the outlines of the AVIRIS and HST data sets acquired. Inset figure from Fiero (1986).

leads to the precipitation of Fe-sulfates (e.g., jarosite, schwertmannite, or copiapite), Fe-oxyhydroxides (e.g., goethite), and Fe-oxides (e.g., hematite) that sometimes forms a spatial pattern around points of actively oxidizing sulfides (Montero et al., 2004). The occurrence of water-soluble sulfates on mine dumps is also indicative of acidic surface conditions. These sulfate salts can contain high concentrations of heavy metals within their crystal structure that can be rapidly released during increased water flow shortly after rainfall events (Jambor et al., 2000; Montero et al., 2004).

1.2. Background and Objectives

With a wide range of exposed weathering and alteration minerals, Virginia City has been the focus of numerous hyperspectral imaging spectroscopy studies (Ashley et al., 1979; Hutsinpillar and Taranik, 1988; Kruse and Huntington 1996; Yang et al., 1999). This study introduces a new hyperspectral imaging spectrometer to the family of sensors that have imaged Virginia City. The SpecTIR Corporation's airborne hyperspectral imager, HyperSpecTIR (HST) has been designed to acquire images with a very high-spatial resolution without significant loss of signal over noise. This

Figure 2. Simplified geologic map of the Comstock district and Virginia City (from Thompson and White, 1964; and Hudson, 2003).

study represents the first geological analysis of the new HST data and presents mineral mapping results of one of the highest-spatial resolution hyperspectral data sets acquired over Virginia City.

Table 1. Alteration mineral assemblages in the Geiger Grade and Comstock alteration zones (from Hudson, 1987).

Alteration Type	Mineral Assemblage	Absorption features in the VNIR/SWIR
Alunitic	alunite, quartz, pyrite	alunite
Alsic	pyrophyllite, quartz, diaspore, kaolinite, pyrite	pyrophyllite, diaspore, kaolinite
Kaolinitic	kaolinite, quartz, pyrite	kaolinite
Illitic	illite, quartz, pyrite, montmorillonite	illite, montmorillonite
Sericitic	sericite, quartz, pyrite	sericite
Propylitic	albite, chlorite, epidote, calcite, illite/sercite, quartz, pyrite	chlorite, epidote, calcite, illite/sercite

The purpose of this study was to use both AVIRIS and HST data to map weathering and alteration minerals in the Comstock region and relate the mineral maps to local geology and chemical conditions on the mine dumps. It is instinctive to compare and contrast two data sets with different spatial resolution, but also helpful to use them together to make use of the advantages of each instrument. To what extent do these mineral maps agree with and/or add information to current geologic maps and alteration models of this well-studied region? Is there potential for acid mine drainage from the mine dumps in Virginia City?

2. Data Collection and Atmospheric Correction

AVIRIS data were collected over Virginia City in July 1995 from the high-altitude ER-2 platform and have a swath of ~11 km and a spatial resolution of ~18 m. The signal-to-noise ratio (SNR) of the 1995 AVIRIS data has been reported as >600:1 in the VNIR channels (Swayze et al., 2003), and calculations of SNR from these Virginia City data using the mean/standard deviation method normalized to 50% reflectance yield a SNR of ~500:1 in the VNIR channels.

The HyperSpecTIR (HST) is a hyperspectral imaging spectrometer developed and operated by the Spectral Technology and Innovative Research (SpecTIR) Corporation. It measures solar reflected radiance in 227 continuous spectral channels between 0.45 and 2.45 µm with a spectral band pass that is selectable from 5 to 10 nm. It has an IFOV of 1 mrad and a TFOV that is selectable from 0 to 1 rad (57°) (Watts et al., 2001). The instrument is mounted on a tilting platform equipped with a "fast optical line-of-sight steering" system that allows for real-time compensation of aircraft motion (roll, pitch and yaw variations) in heavy turbulence (Watts et al., 2001). It also increases the dwell time over the target, thus increasing the amount of incoming signal. The SNR in the VNIR channels calculated using the mean/standard deviation method and normalized to 50% reflectance was ~250:1. Images were acquired in a series of overlapping frames rather than a single, continuous strip. HST data were acquired over Virginia City, Nevada in June 2002 from a Cessna 310 aircraft at an altitude of 2.5 km AGL. The images cover a ground swath of about 1.1 km and have a spatial resolution of ~2.5 m.

For the atmospheric correction of both AVIRIS and HST data a radiative transfer modeling approach was used. For the AVIRIS data, the "fast line-of-sight atmospheric analysis of spectral hypercubes" (FLAASH) method was used (Adler-Golden et al., 1998). The FLAASH method uses the latest version of the "moderate resolution atmospheric radiance and transmission" (MODTRAN) model (Berk et al., 1999) to calculate the atmospheric parameters needed to extract at-surface reflectance. For the MODTRAN calculations the average profile for a typical continental location at mid-latitudes during the summer was assumed. A visibility of 23 km and a typical aerosol profile model for a rural area were also assumed. In addition, a spectral "polishing" routine (using a running average across 9 adjacent channels) was used to eliminate spectral artifacts that remain after atmospheric correction and to account for random channel-to-channel noise (Boardman, 1998; Adler-Golden et al., 1998). For the HST data a similar atmospheric correction method was used that allows MODTRAN to calculate the atmospheric parameters and extract at-surface reflectance. In addition, spectral measurements of natural calibration targets in the field (a recently-paved parking lot, and a large dirt lot) were acquired concurrently with the

HST over flights and compared to image spectra to calculate gain and offset factors for an empirical line correction used to fine-tune SpecTIR's surface reflectance data product.

Retrieved surface reflectance spectra were directly compared to reference spectra for pure minerals that are archived in spectral libraries. Both the USGS and JPL have spectral libraries available via the Internet and contain VNIR/SWIR spectra for over 2000 minerals and rocks combined. The most recent version of the USGS digital spectral library can be found at: http://pubs.usgs.gov/of/2003/ofr-03-395/datatable.html and is described by Clark et al. (2003). The JPL ASTER spectral library is a compilation of spectra of rocks and minerals measured at JPL, JHU, and the USGS, and is described on the Website: http://speclib.jpl.nasa.gov.

Field sites were chosen to aid in the calibration of airborne data sets as well as for the validation of the remotely derived mineral maps. For calibration sites, large (multi-pixel), flat areas that were mineralogically homogeneous and free of vegetation were chosen for field spectrometer measurements. Field sites for validation were also chosen by locating areas in the images that were relatively free of vegetation and thus clearly measured by the remote sensing instrument. An Analytical Spectral Devices (ASD) FieldSpec FR was used in the field for mineral identification and calibration of remote sensing data sets, as well as in the laboratory for high-resolution characterization of field samples (Curtiss and Goetz, 1997). The data were calibrated to reflectance by measuring a dark current to define detector "noise" that contributes to the incoming signal, and by measuring the radiance from a white spectralon® (Labsphere, Inc.) reference panel of known reflectance. X-ray diffraction (XRD) analyses of bulk rock and mineral separate samples were performed at two different laboratories (the Nevada Bureau of Mines and Geology and the University of Georgia) for mineralogical verification.

3. Data Processing and Mineral Mapping

The series of processing steps described by Kruse and Huntington (1996), Kruse et al. (1999), and Kruse et al. (2003) has become standard in hyperspectral data analysis. These methods, shown schematically in Figure 3, yield reproducible results, although there are some subjective decisions required of the user. The purpose of this methodology is to focus only on the information that is relevant to characteristic mineralogic features within the image.

With the AVIRIS data, the MNF transformation was applied to a total of 192 channels of the surface reflectance data that correspond to wavelengths 0.41-1.35, 1.42-1.81, and 1.94-2.48 μm. This
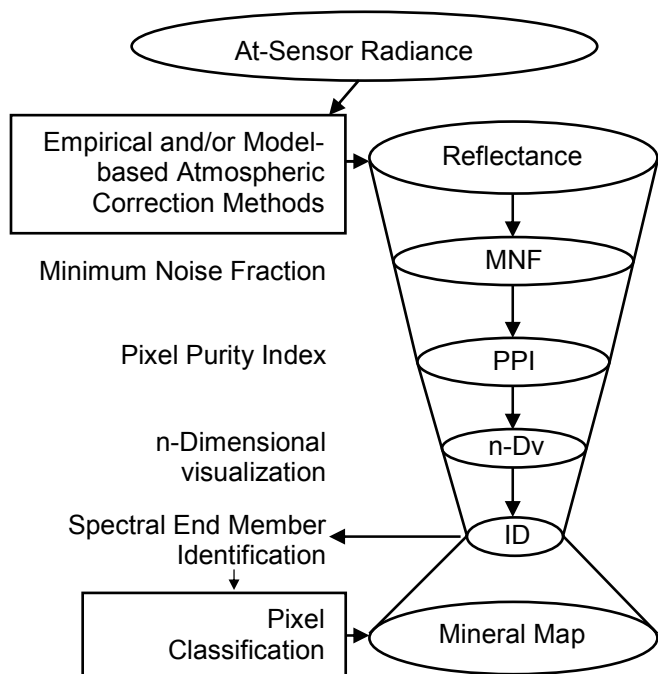

Figure 3. Flow chart illustrating data processing methods. Once the effects of the atmosphere are removed from the at-sensor radiance data, the spectral reflectance information can be extracted. The hyperspectral data processing steps serve to minimize noise and focus on information that is relevant to mineralogic features within the image.

eliminates the strong absorption bands caused by atmospheric H_2O around 1.4 and 1.9 μm. With the HST data, the MNF transformation was applied to a total of 167 channels of the surface reflectance data that correspond to wavelengths 0.49-0.89, 1.16-1.34, 1.43-1.80 and 1.95-2.40 μm. This eliminates the 1.4 and 1.9 μm H_2O bands as well as weak H_2O absorption features around 0.9 and 1.1 μm, which are also present in the HST surface reflectance data.

Reflectance data were used in three ways to find pixels that represent spectral end members. First, Pixel Purity Index (PPI) computation and spectral dimensionality analysis described by Boardman et al. (1995) were used to find spectrally "pure" pixels (target spectra), which represent compositionally distinct areas (Kruse and Huntington, 1996). This significantly reduces the number of pixels that need to be searched for mineralogic spectral information, but it also finds pixels that are not necessarily of geologic interest e.g. urban/ cultural features, and vegetation. The second method is similar, except the pure pixels were chosen by defining regions of interest around obvious geologic targets (e.g., non-vegetated and non-urban areas) and these pixel spectra were viewed as points in n-dimensional space to select the outliers. This helped reduce the number of chosen pixels that were not related to geologic diversity, e.g., vegetation, roads, roofs, and the occasional noisy scan line. Thirdly, spectral end member pixels were chosen based on a priori knowledge and sampling of the field area. In this case, just a few pixels were selected as end member spectra eliminating the need for n-dimensional analysis. Each spectral end member was used as a target spectrum, to "train" the pixel classification method described next.

Pixels were classified using two different supervised classification methods: 1) Spectral Angle Mapper (SAM) (Kruse et al., 1993) and Matched Filtering (MF) (Boardman et al., 1995). SAM classifies pixels together based on their spectral similarity by treating spectra as vectors in n-dimensional space and calculating the angle between them. The threshold angle used was 0.05 radians. MF generates proportional spectral end member abundance maps based on partial unmixing of image target spectra (Boardman et al., 1995). For each end member mapped, a region of interest (ROI) was defined by selecting a threshold range of values from the abundance maps that corresponded to the highest abundance. Each ROI was assigned to a unique color and displayed over a gray-scale image to produce a mineral classification map. The threshold value selection is somewhat subjective and can lead to slight variations in the final mineral map product. Threshold values can be chosen liberally such that many pixels are classified together that are not truly the same, i.e. results in the inclusion of false-positives in the class. Conversely, threshold values can be chosen conservatively, which results in the inclusion of false negatives, i.e. the classification misses some pixels that should be classified. Some background knowledge of the field area and a basic understanding of common geologic models are helpful, but not necessary. In practice, threshold values were chosen more conservatively to reduce the possibility of false-positives and only classify pixels with a high-confidence in the spectral identification. Finally, based on matching the spectra of classified pixels to the spectra of pure minerals from reference libraries, mineralogy was assigned to classified pixel regions to produce mineral maps.

4. Mineral Mapping Results

Around Virginia City, AVIRIS data mapped the hydrothermal alteration minerals alunite, kaolinite, pyrophyllite, montmorillonite/muscovite and chlorite, and also jarosite on some weathered mine dumps (Figure 4, top). In the spectral plots (Figure 4, bottom), four alteration minerals (alunite, pyrophyllite, kaolinite, and chlorite) are identified based on their spectral features between 2.2 and 2.4 μm, and jarosite is identified based on spectral features at 2.26 and μm.

The AVIRIS spectrum from an outcrop on the south side of a hill, in magenta (site 9a - left spectral plot) matches the USGS library reference spectrum for a linear mixture of kaolinite (60%) and hematite (40%). The field spectrum matches the AVIRIS spectrum and XRD data indicate the presence of quartz and kaolinite. The AVIRIS spectrum from an outcrop forming a tall, erosion-resistant knob, in blue (site 9b – left spectral plot) matches the USGS library reference spectrum for a linear mixture of alunite (60%) and cheat grass (40%). The outcrop is relatively small from an aerial perspective and
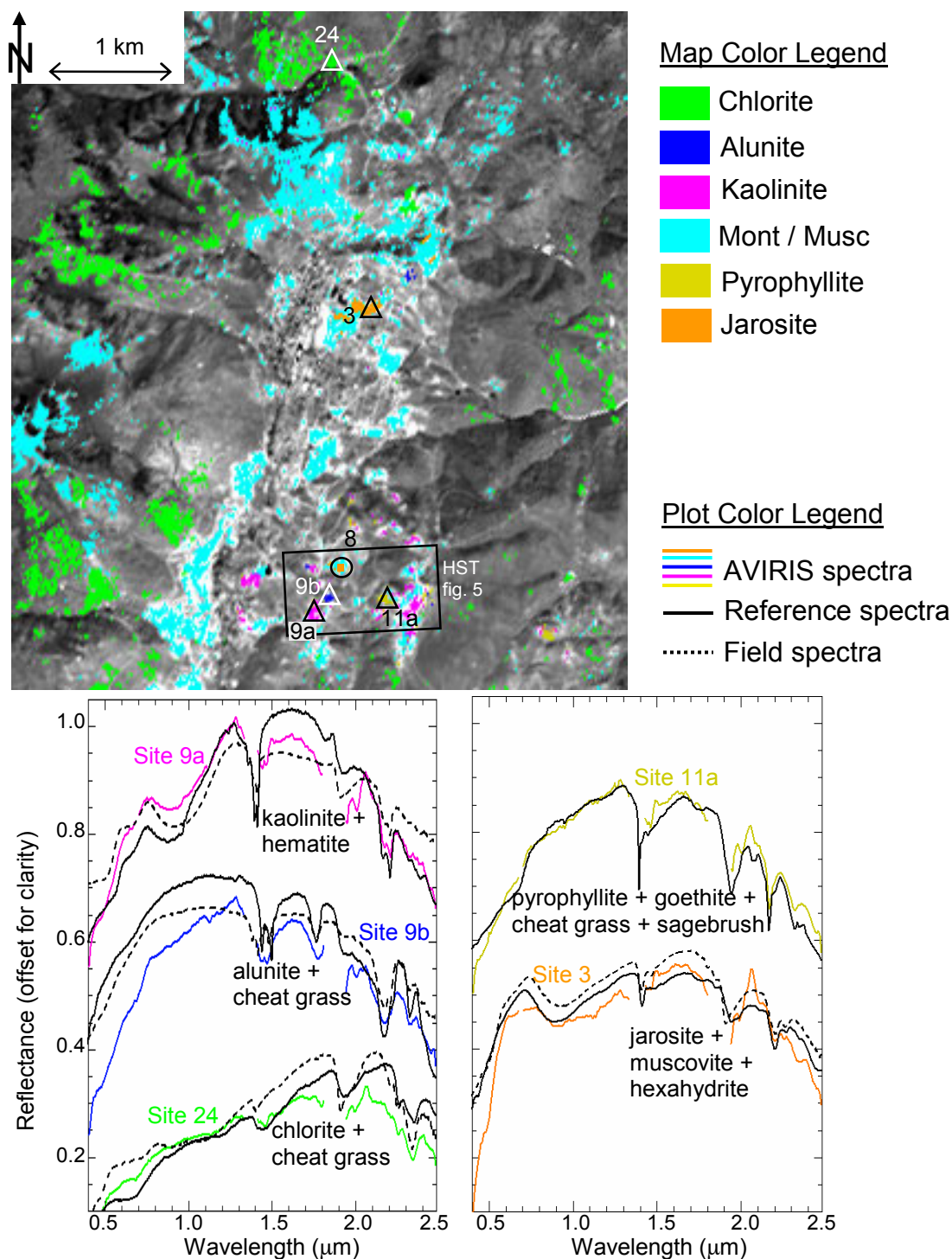
Figure 4. AVIRIS mineral map over Virginia City (top). The five regions mapped are distinguished by their dominant mineralogy and noted in the legend. AVIRIS spectra from representative field sites (3, 9a, 9b, 11, and 24 - marked with triangles on map) are color coordinated to the map legend. The spatial resolution for the AVIRIS image is 18 m.

surrounded by vegetation. The field spectrum matches the AVIRIS spectrum and XRD data from bulk rock samples indicate the presence of quartz, Na-alunite, minamiite, and trace kaolinite. The AVIRIS spectrum from talus material on the side of a hill, on either side of a road cut, in dark yellow (site 11a - right spectral plot) matches the USGS library reference spectrum for a linear mixture of pyrophyllite

(40%), goethite (10%), sage brush (25%) and cheat grass (25%). Based on the narrow feature at 2.17 μm pyrophyllite was identified as the principal clay mineral among an area dominated by vegetation. Bulk rock XRD data from site 11a indicate the presence of quartz, pyrophyllite, and minor kaolinite. The AVIRIS spectrum from a talus slope next to the road, in green (site 24 - left spectral plot) matches the USGS library reference spectrum for a mixture of the chlorite mineral clinochlore (60%) and cheat grass (40%), and corresponds to a zone of propylitic alteration around Virginia City. Clinochlore was identified by the unique spectral feature around 2.34 μm, as well as the very low reflectance below 1.5 μm. The field spectrum matches the AVIRIS spectrum and bulk rock XRD data indicate the presence of quartz, clinochlore, albite, and epidote. Finally, the AVIRIS spectrum from a mine dump, in orange (site 3 - right spectral plot), matches the USGS library reference spectrum for a mixture of jarosite (45%), muscovite (40%) and hexahydrite (15%).

Site 3, as well as other areas mapped in orange (e.g., site 8) are all located on top of mine dumps. Jarosite forms coatings on the rocks around these dumps, and hydrous sulfate salt crusts like hexahydrite and gypsum form in small depressions on top of many weathering mine dumps. The 2.26-μm feature is indicative of jarosite, but this feature is relatively weak as it is mixed with muscovite, which has a stronger feature around 2.20 μm. The presence of jarosite is also implied by the broad 0.9-μm absorption feature and the relatively high reflectance peak around 0.7 μm. However, hematite and goethite also have broad absorption features in the 0.9 μm region, thus the identification of jarosite by AVIRIS with 18-m pixels is somewhat ambiguous. The ASD field spectrum from site 3 matches the AVIRIS spectrum. XRD data from multiple samples of this dump indicate the presence of jarosite, muscovite, quartz, albite, chlorite and white crusts of hydrous Mg-sulfate (hexahydrite), with minor alunogen and gypsum. The dump at site 8 contains dominantly gypsum; the presence of small amounts of gypsum and hexahydrite was identified by field sampling and XRD measurements.

The HST mineral map in Figure 5 (top) is shown to zoom in on a section of Virginia City where there is particularly diverse suite of exposed minerals, including hydrothermal alteration minerals (alunite, kaolinite, montmorillonite/muscovite, and pyrophyllite), as well as a dump containing jarosite and gypsum. In the spectral plot (right), the HST spectrum from the dump, in orange (site 8a) matches the USGS library reference spectrum for a linear mixture of jarosite (40%), muscovite (45%), and gypsum (15%). The ASD field spectrum matches the HST spectrum and XRD data from field samples indicate the presence of quartz, jarosite, and muscovite; and from the sulfate crusts at site 8b, gypsum. The HST spectrum from a resistant outcrop, in blue (site 9b) matches the USGS library reference spectrum for a mixture of alunite (50%), goethite (30%) and cheat grass (20%). XRD data indicate the presence of quartz, Na-alunite, minamiite, and minor kaolinite. The HST spectrum from the talus down hill from a road cut, in dark yellow (site 11a) matches the USGS library reference spectrum for a mixture of pyrophyllite (40%), goethite (40%) and cheat grass (20%). The ASD field spectrum matches the HST spectrum and XRD data indicate the presence of quartz, pyrophyllite, and minor kaolinite. The HST spectrum from an outcrop on a south facing hill, in magenta (site 9a) matches the USGS library reference spectrum for a mixture of kaolinite (55%), hematite (30%) and cheat grass (15%). The ASD field spectrum matches the HST spectrum and XRD data indicate the presence of quartz and kaolinite.

5. Data Interpretation and Discussion

5.1. Hydrothermal Alteration in the Comstock Region

Figure 6 is a mineral map of the Comstock region derived primarily from the AVIRIS data that shows the distribution of large hydrothermal alteration zones. The geologic units from the geology map in Figure 2 are shown in pale, partly transparent colors. The mineral assemblages mapped are shown in solid, opaque colors. Acid-sulfate zones (alunitic, alsic, and kaolinitic assemblages) are shown in magenta, illite/sericite zones in cyan, and propylitic zones in green.

Hydrothermal alteration generally falls within the areas mapped as "bleached" on the original geologic map, and is dominated by widespread propylitic and illitic/sericitic zones, notably on the west
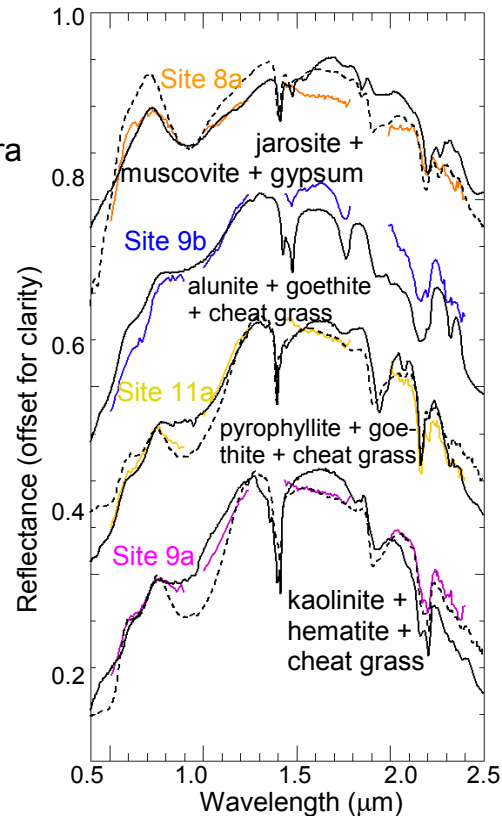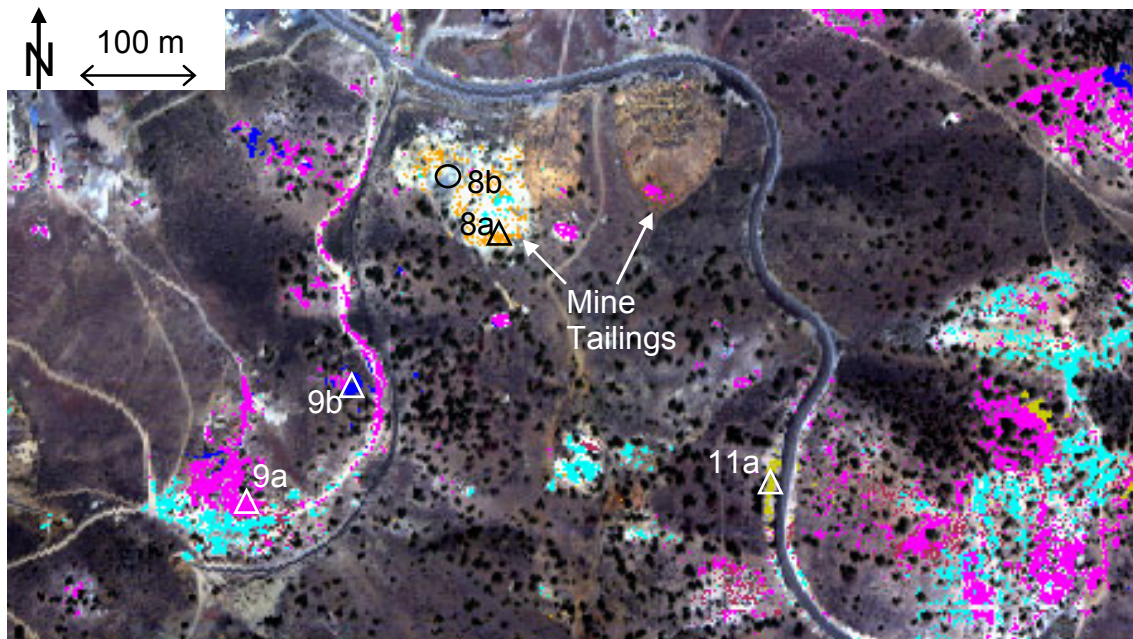
Figure 5. HST mineral map over Virginia City (top). The five regions mapped are distinguished by their dominant mineralogy and noted in the legend. HST spectra from representative field sites (8a, 9a, 9b, and 11a - marked with triangles on map) are color coordinated to the map legend. The spatial resolution for the HST image is 2.5 m.

side (foot wall) of the Comstock fault. Pods of acid-sulfate alteration (alunitic, alsic, and kaolinitic zones) occur on the east side (hanging wall) of the Comstock fault around the Virginia City town site. Also, an acid-sulfate alteration zone (alsic + kaolinitic) is mapped in the hanging wall of the Occidental fault. The areas mapped as "bleached" on the original geologic map generally do not include rocks that are propylitically altered. For example, the Davidson diorite (Td) ranges from relatively unaltered to propylitic and illitic/sericitic alteration in some areas. Other propylitic zones occur along the Comstock and Occidental faults. Hudson (2003) differentiates three different types of propylitic alteration based on
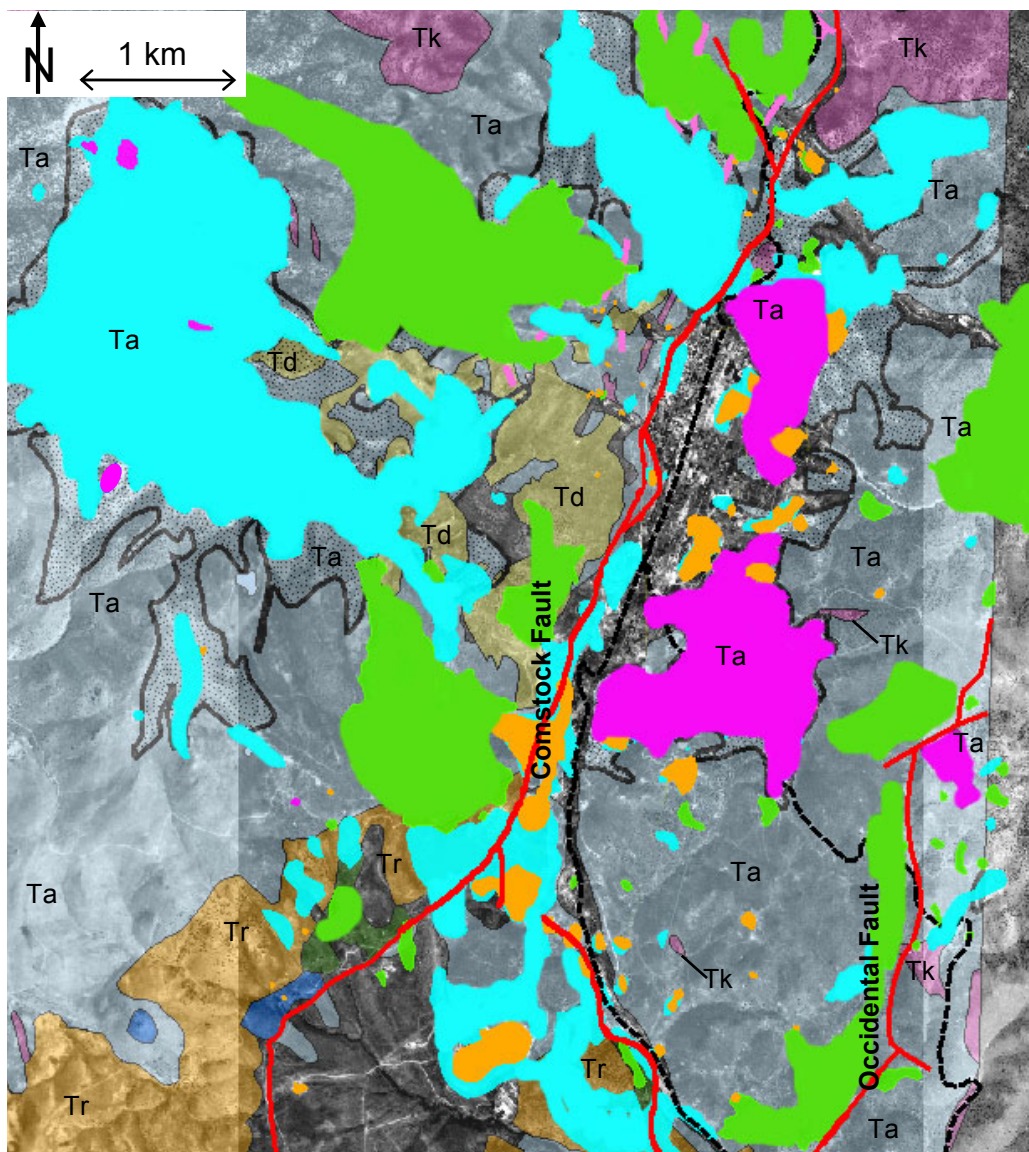
Geologic Map Color Legend

Tk — Kate Peak Andesite

Td — Davidson Diorite

Ta — Alta Andesite

Tr — Hartford Hill Rhyolite

Bleached Rocks

Kate Peak intrusive dikes

Faults

Roads

Mineral Map Color Legend

Propylitic Zones

Illitic/Sericitic Zone

Acid-Sulfate Zones

Mine Tailings

Figure 6. Mineral map of the Comstock district around Virginia City showing the regional-scale distribution of hydrothermal alteration mineral assemblages. The colored lines and polygons are overlain on a gray scale DOQ image.

the relative abundance of epidote, calcite, and albite in the assemblage. Although these minerals were identified by XRD and laboratory spectroscopy, the remote mineral maps classify all propylitic alteration together. The centrality of the Davidson diorite intrusive to intensely altered areas implicates this intrusive body as a heat source (and possibly fluid source) for hydrothermal fluid flow during this time. Geochemical data from these rocks support this assumption, but there may have been other acid-sulfate systems associated with later emplacement of small intrusions and dikes associated with Kate Peak volcanism (Vikre, 1998; Castor et al., 2002; Vikre et al., 2003; Hudson, 2003). In the mineral map it is clear that the widespread propylitic alteration is found in the foot wall blocks of the Comstock and Occidental fault zones, and also proximal to these structures along which mineralized adularia-sericite veins are found. The pervasive acid-sulfate alteration zones, found in the hanging wall blocks, were cut by these younger structures. This is consistent with new radiometric dates from alteration minerals indicate that the acid-sulfate alteration zones pre-date ore-grade mineralization along the Comstock and Occidental faults by ~1-2 million years, and bear only incidental spatial relationship to the ore veins (Vikre et al., 1988; Vikre, 1998; Castor et al., 2002; Hudson, 2003).

Figure 7 is a subset of the Comstock region showing the distribution of alteration mineral zones mapped by HST data on a smaller scale. The rocks here are mostly hydrothermally altered andesite of the Alta Formation (Ta), with one small Kate Peak intrusive plug (Tk) in the southeast part of the image. Several small outcrops of alunitic alteration are mapped (dark blue). These quartz + alunite assemblages are more resistant to erosion and commonly form topographic ridges and small pinnacles (see upper photograph). There are also small resistant pinnacles that are composed of dominantly quartz + kaolinite (see lower photograph) that look very similar.   Some of the alunitic zones appear to follow ~northeast-southwest structures, which have not been mapped previously. In agreement with the model of Hudson (1987), the alunitic zones (blue) grade outward into kaolinitic zones (magenta), and then into illitic/sericitic zones (cyan); also, alsic zones rich in pyrophyllite (yellow) grade into kaolinitic and illitic/sericitic zones.

5.2. Secondary Weathering Minerals on Mine Dumps

Figure 8 is a mineral map of the Virginia City area showing the distribution of mine dumps, and some open pit exposures. Jarosite (orange), mapped primarily by the HST data, is indicative of conditions with pH <3 (Montero et al., 2004). Other hydrous sulfate minerals (hexahydrite, alunogen and gypsum) were mapped in the
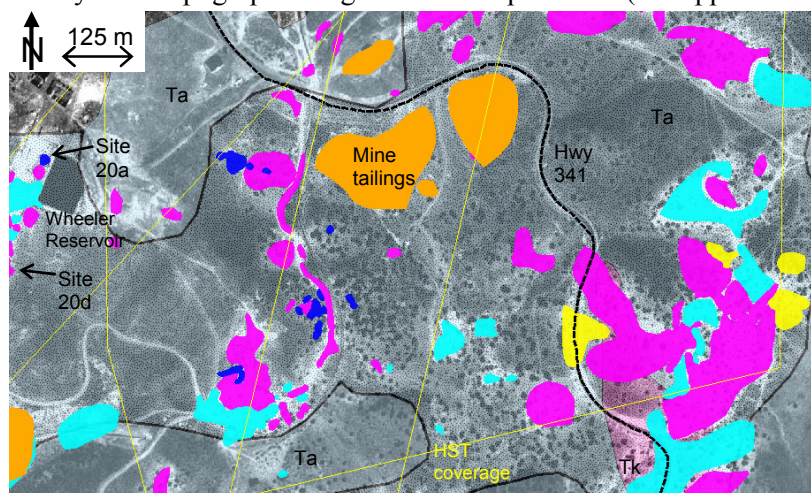
Geologic and Mineral Map Legend

Tk	Kate Peak Andesite
Ta	Alta Andesite
	Bleached Rocks
••••••	Roads
—	Faults
	Image Data Coverage
	Illitic/Sericitic Zone
	Kaolinitic Zone
	Alsic Zone
	Alunitic Zone
	Mine Tailings

Site 20a: resistant quartz-alunite outcrop.

Site 20d: resistant quartz-kaolinite outcrop.

Figure 7. Mineral map of an area within Virginia City showing the small-scale distribution of hydrothermal alteration mineral assemblages.

field and occur as hard, white crusts precipitating in small depressions on top of some of the dumps. The presence of hydrous Ca-Mg-Al sulfate salts on the surface is indicative of pH values between 3 and 5 (C. Alpers pers. comm., 2004). On one dump where both jarosite and hexahydrite had been identified, a pH of 3.5 was measured in a small puddle formed after a recent rain storm. On the edges of the puddle, a white sulfate crust of hexahydrite was beginning to precipitate. This field measurement is in agreement with the range of pH values predicted based on the mapped surface mineralogy.

Jarosite is considered to be the most important mineral to map to locate potential sources of acid mine drainage. The zoning of goethite and hematite away from oxidizing Fe-sulfide-rich waste rock piles that has been observed by others (Montero et al., 2004; Swayze et al., 2000) is of secondary importance because these minerals can be found in many other environments and are not necessarily indicative of acid drainage potential. For example, the soils and hydrothermally altered volcanic rocks in the

Map Color Legend

■ Jarosite (mixed with quartz & muscovite)

□ Mine tailings

Figure 8. Mineral map of the Virginia City area showing the distribution of mine tailings with jarosite and hydrous sulfate salts. The spatial resolution of the DOQ in the background is 1 m.

surrounding area contain hematite and goethite nearly ubiquitously. The distribution of jarosite on the flanks of the mine dumps and the lack of distal jarosite deposits indicate that acidic waters are confined to the dump environment and not found down stream.
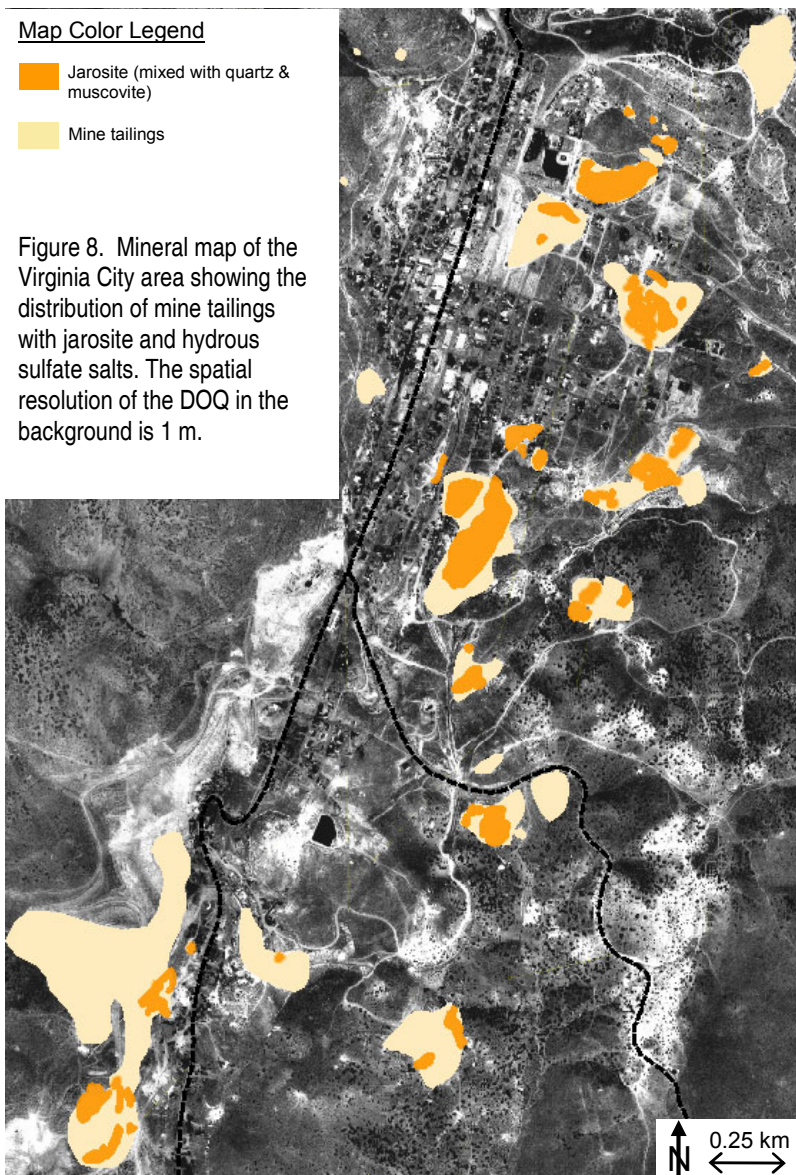
6. Summary and Conclusions

6.1. Weathering and Alteration Mineral Maps

All of the significant base and precious metal deposits in the Virginia Range are located within, or proximal to, acid-sulfate alteration zones in Miocene volcanic rocks (Vikre, 1998). The Comstock region however, appears to be unique. Over a period of ~6 million years multiple episodes of magmatic activity were accompanied by, or followed by, different types of hydrothermal alteration and mineralization. The mineral maps show the distribution of these large alteration zones from which relative timing can be inferred. The maps also show small-scale zoning of alteration minerals. Of particular importance is alunite, which, 1) is an indicator of acid-sulfate systems, 2) tends to delineate structures, and 3) is a hydrous K-bearing sulfate mineral that can be analyzed by a number of geochemical

224

methods to provide information about the geochemical and temperature environment, and timing of hydrothermal activity.

Of the approximately 0.35 km^2 of tailings piles in Virginia City that were mapped, about 30% of that area contained jarosite mineralization on the surface and an estimated 5% contained water-soluble Mg-, Al- and Ca-sulfate salt deposits. Although no known reports of acid mine drainage problems from the town site have been published, there are clearly acid-generating source materials dispersed around the town site and acidic surface water has been observed after short rainfall events. The acidic source areas identified in this study could serve in future reclamation efforts should acid mine drainage become a serious problem.

6.2. Remote Sensing

The zonation of hydrothermal alteration minerals commonly observed in the field was also evident in the spectral mineral mapping at both large (AVIRIS) and small (HST) scales. The high-altitude AVIRIS data were better for looking at the Comstock alteration zones on a district-wide scale (10x10 km), while the high-spatial resolution HST data mapped some smaller alunite veins in structural orientations not previously recognized, and was more effective than the 18-m AVIRIS data for the detailed mapping of secondary weathering minerals on the mine dumps. It is important to note that the hydrous sulfate salts on the mine dumps were identified in the field and not by remote VNIR/SWIR imaging spectroscopy, and the unique identification of jarosite is sometimes ambiguous due to its mixture with other minerals like muscovite. The fact that HST mapped more jarosite occurrences than AVIRIS is purely a function of the higher spatial resolution. Even though the estimated SNR for the HST data is lower than for AVIRIS, it was still sufficient to uniquely map the important weathering and alteration minerals in this area.

Since HST data were acquired as a series of overlapping frames, one of the challenges to working with the HST data was the lack of geo-coding information and the need to correct and process each HST frame separately to avoid spectral analysis of re-sampled pixels. Mineral map data products were then warped to a 1-m resolution USGS digital orthophoto quad by choosing 30-50 ground control points per frame, and then stitched together. The lack of geo-coding information is unique to this initial 2002 data set, however, and recent improvements to the HST instrument and data products have addressed some these challenges (see http://www.spectir.com). Both high- and low-altitude airborne imaging spectrometer data should continue to occupy distinct and complementary niches for geoscience remote sensing applications.

References

Adler-Golden, S., Berk, A., Bernstein, L.S., Richtsmeier, S.C., Acharya, P.K., and Matthew, M.W. (1998). FLAASH, A MODTRAN 4 Atmospheric Correction Package for Hyperspectral Data Retrievals and Simulation. *Proceedings of the 7th JPL Airborne Earth Science Workshop*, JPL.

Ashley, R.P., Goetz, A.F.H., Rowan, L.C., and Abrams, M.J. (1979). Detection and Mapping of Hydrothermally Altered Rocks in the Vicinity of the Comstock Lode, Virginia City, Nevada, Using Enhanced Landsat Images. *USGS Open File Report*, 79-960, 41 pp.

Berk, A., Anderson, G.P., Bernstein, L.S., Acharya, P.K., Dothe, H., Matthew, M.W., Adler-Golden, S., Chetwynd, J.H. Jr., Richtsmeier, S.C., Pukall, B., Allred, C.L., Jeong, L.S., and Hoke, M.L. (1999). MODTRAN4 Radiative Transfer Modeling for Atmospheric Correction. *Proceedings of the 8th JPL Airborne Earth Science Workshop*, JPL Publication 99-17.

Bigham, J.M. and Nordstrom, D.K. (2000). Iron and Aluminum Hydroxysulfates from Acid Sulfate Waters. Ch 7 in: *Reviews in Mineralogy and Geochemistry*, *v. 40, Sulfate Minerals: Crystallography, Geochemistry, and Environmental Significance*, C.N. Alpers, J.L. Jambor, and D.K. Nordstrom editors, Mineralogical Society of America, Washington, D.C., pp. 351-403.

Boardman, J. W., Kruse, F. A., and Green, R. O. (1995). Mapping Target Signatures Via Partial Unmixing of AVIRIS Data. *Proceedings of the Fifth JPL Airborne Earth Science Workshop*, JPL Publication 95-1 (1), pp. 23-26.

Boardman, J.W. (1998). Post-ATREM Polishing of AVIRIS Apparent Reflectance Data Using EFFORT: A Lesson in Accuracy versus Precision. *Summaries of the 7th JPL Airborne Earth Science Workshop*, JPL Publication 97-21.

Castor, S.B., Garside, L.J., Henry, C.D., Hudson, D.M., McIntosh, W.C., and Vikre, P.G. (2002). Multiple Episodes of Magmatism and Mineralization in the Comstock District, Nevada. *Abstracts with Programs*, Geological Society of America, 34(6), p. 185.

Clark, R.N., Swayze, G.A., Wise, R., Livo, K.E., Hoefen, T.M., Kokaly, R.F., and Sutley S.J. (2003). USGS Digital Spectral Library splib05a. *USGS Open File Report*, 03-395.

Curtiss, B. and Goetz, A.F.H. (1997). Field Spectrometry: Techniques and Instrumentation. *Analytical Spectral Devices FieldSpec^{TM} User's Guide*, Appendix A, pp. 45-62.

Fiero, B. 1986. *Geology of the Great Basin*. University of Nevada Reno Press, Reno, NV.

Hudson, D.M. (1987). Steamboat Springs Geothermal Area, Washoe County, Nevada. In: *Bulk Mineable Precious Metal Deposits of the Western United States*, J.L. Johnson editor, Geological Society of Nevada field trip guidebook, pp. 408-412.

Hudson, D.M. (2003). Epithermal Alteration and Mineralization in the Comstock District, Nevada. *Economic Geology*, 98, pp. 367-385.

Hutsinpiller, A. and Taranik, J.V. (1988). Spectral Signatures of Hydrothermal Alteration at Virginia City, Nevada. In: Bulk Mineable Precious Metal Deposits of the Western United States, Robert W. Schafer editor, Geological Society of Nevada Symposium Proceedings, pp. 505-530.

Jambor, J.L., Nordstrom, D.K., and Alpers, C.N. (2000). Metal-Sulfate Salts from Sulfide Mineral Oxidation. Ch 6 in: *Reviews in Mineralogy and Geochemistry*, *v. 40, Sulfate Minerals: Crystallography, Geochemistry, and Environmental Significance*, C.N. Alpers, J.L. Jambor, and D.K. Nordstrom editors, Mineralogical Society of America, Washington, D.C., pp. 303-350.

Kruse, F.A., Lejkoff, A.B., Boardman, J.W., Heidebrecht, K.B., Shapiro, A.T., Barloon, P.J., and Goetz, A.F.H. (1993). The Spectral Image Processing System (SIPS) - Interactive Visualization and Analysis of Imaging Spectrometer Data. *Remote Sensing of Environment*, 44, pp. 145-163.

Kruse, F.A. and Huntington, J.F. (1996). The 1995 AVIRIS Geology Group Shoot. *Proc. of the Sixth JPL Airborne Earth Science Workshop*, JPL Publication 96-4 (1), Pasadena, CA, pp. 155-164.

Kruse, F.A., Boardman, J.W., and Huntington, J.F. (1999). Fifteen Years of Hyperspectral Data: Northern Grapevine Mountains, Nevada. In: *Proceedings of the 8th JPL Airborne Earth Science Workshop*, JPL publication 99-17, pp. 247-258.

Kruse, F.A., Boardman, J.W. and Huntington, J.F. (2003). Comparison of Airborne Hyperspectral Data and EO-1 Hyperion for Mineral Mapping. In: *Special Issue, IEEE Transactions on Geoscience and Remote Sensing*, 41 (6), pp. 1388-1400.

Montero, I.C., Brimhall, G.H., Alpers, C.N., and Swayze, G.A. (2004). Characterization of Waste Rock Associated with Acid Drainage at the Penn Mine, CA, by Ground-based Visible to Short-wave IR Reflectance Spectroscopy Assisted by Digital Mapping. *Chemical Geology*, in review.

Swayze, G.A., Clark, R.N., Smith, K.S., Hageman, P.L., Sutley, S.J., Pearson, R.M., Rust, R.S., Briggs, P.H., Meier, A.L., Singleton, M.J., and Roth, S. (1998). Using Imaging Spectroscopy to Cost-Effectively Locate Acid-Generating Minerals at Mine Sites: An Example From the California Gulch Superfund Site in Leadville, Colorado. Proceedings of the 7th Airborne Earth Science Workshop, JPL publication 97-21 (1), pp. 385-389.

Swayze, G.A., Smith, K.S., Clark, R.N., Sutley, S.J., Pearson, R.M., Vance, J.S.,. Hugeman, P.L, Briggs, P.H., Meier, A.L., Singleton, M.J., Roth, S. (2000). Using Imaging Spectroscopy to Map Acidic Mine Waste. Environ. Sci. Technol. 34, 47-54.

Swayze, G.A., Clark, R.N., Goetz, A.F.H., Chrien, T.G., and Gorelick, N.S. (2003). Effects of Spectrometer Band Pass, Sampling, and Signal-to-Noise Ratio on Spectral Identification Using the Tetracorder Algorithm. *Journal of Geophysical Research*, 108 (E9), pp. 9-1 - 9-30.

Thompson, G.A. and White, D.E. (1964) Regional Geology of the Steamboat Springs Area, Washoe County, Nevada. *USGS Professional Paper* 458-A, 52 pp.

Vikre, P.G., McKee, E.H., and Silberman, M.L. (1988). Chronology of Miocene Hydrothermal and Igneous Events in the Western Virginia Range, Washoe, Storey, and Lyon Counties, Nevada. *Economic Geology*, 83, pp. 864-874.

Vikre, P.G. (1998). Quartz-Alunite Alteration in the Western Part of the Virginia Range, Washoe and Storey Counties, Nevada. *Economic Geology*, 93, pp. 338-346.

Vikre, P.G., Garside, L.J., Castor, S.B., Henry, C.D., Hudson, D.M., and McIntosh, W.C. (2003). Multiple Episodes of Magmatism, Quartz-Alunite Alteration, and Adularia-Sericite Precious Metal Mineralization, Western Virginia Range, Nevada. *Abstracts with Programs*, Geological Society of America, 35 (6), p. 401.

Watts, L.A., Davis, R.O., Granneman, R.D., LaVeigne, J.D., Chandos, R.A., Russell, E.E., and Cairns, B. (2001). Unique VISNIR-SWIR Hyperspectral and Polarimeter Measurements. In: *Proceedings of the 5th Airborne Remote Sensing Conference*, San Francisco, CA.

Yang, K., Huntington, J.F., Boardman, J.W., and Mason, P. (1999). Mapping Hydrothermal Alteration in the Comstock Mining District, Nevada, Using Airborne Hyperspectral Data. *Australian Journal of Earth Sciences*, 46, pp. 915-922.